

FLOW OF POLYMER SOLUTIONS THROUGH POROUS MEDIA

Stroming van polymeeroplossingen
door poreuze media

FLOW OF POLYMER SOLUTIONS THROUGH POROUS MEDIA

Stroming van polymeeroplossingen
door poreuze media

Proefschrift

ter verkrijging van de graad van doctor
aan de Technische Universiteit Delft,
op gezag van de Rector Magnificus prof.dr.ir. J.T. Fokkema,
voorzitter van het College voor Promoties,
in het openbaar te verdedigen

op dinsdag 18 november 2003 te 15:30 uur

door

Karl Filip Jerome DENYS

materiaalkundig ingenieur
geboren te Mohammadia, Algerije

Dit proefschrift is goedgekeurd door de promotor:
Prof. dr. ir. A. Posthuma de Boer

Samenstelling promotiecommissie:

Rector Magnificus	Technische Universiteit Delft, voorzitter
Prof. dr. ir. A. Posthuma de Boer	Technische Universiteit Delft, promotor
Dr. ir. K. te Nijenhuis	Technische Universiteit Delft, toegevoegd promotor
Prof. dr. ir. P. Currie	Technische Universiteit Delft
Prof. dr. S. Picken	Technische Universiteit Delft
Prof. dr. ir. C. Harris	Imperial College and Shell
Prof. dr. ir. J. van Turnhout	Technische Universiteit Delft, reservelid
Dr. A. Zaitoun	Institut Français du Pétrole
Dr. P. Zitha	Technische Universiteit Delft

Published and distributed by: DUP Science

DUP Science is an imprint of
Delft University Press
P.O. Box 98
2600 MG Delft
The Netherlands
Telephone : +31 15 27 85 678
Telefax : +31 15 27 85 706
E-mail : info@library.tudelft.nl

ISBN 90-407-2441-5

Keywords: polymer solutions, rheology, water shut-off

Copyright © 2003 by Karl Denys

All rights reserved. No part of the material protected by this copyright notice may be reproduced or utilised in any form or by any means, electronic or mechanical, including photocopying, recording or by any information storage and retrieval system, without written permission from the publisher:
Delft University Press

Printed in The Netherlands

Aan mijn ouders

Most of the research in this thesis was performed at two faculties of Delft University of Technology: the faculty of Applied Sciences (TNW) in the Polymer Materials and Engineering section, and the faculty of Civil Engineering and Geosciences (CITG) in the Petroleum Engineering section. The work described in Chapter 7 was performed at Institut Français du Pétrole in Rueil-Malmaison (France) in the Reservoir Engineering department in a European Community funded research project.

CONTENTS

CHAPTER 1 - INTRODUCTION	1
1.1 WATER SOLUBLE POLYMERS IN OIL RECOVERY	1
1.2 SCOPE OF THE PRESENT STUDY.....	3
1.3 THESIS OUTLINE	3
CHAPTER 2 - FLOW THROUGH POROUS MEDIA	6
2.1 INTRODUCTION	6
2.2 FLOW OF NEWTONIAN FLUIDS THROUGH POROUS MEDIA	8
2.2.1 <i>The creeping flow regime</i>	8
2.2.2 <i>The inertial and turbulent flow regime</i>	10
2.3 PERMEABILITY MODELS.....	12
2.3.1 <i>Introduction</i>	12
2.3.2 <i>Capillary models</i>	13
2.3.3 <i>Deterministic permeability models</i>	15
2.3.4 <i>Hydraulic diameter models</i>	16
2.4 FLOW OF POLYMER SOLUTIONS THROUGH POROUS MEDIA.....	20
2.4.1 <i>Introduction</i>	20
2.4.2 <i>Low permeability porous media</i>	20
2.4.3 <i>High permeability porous media</i>	21
2.4.4 <i>Intermediate permeability porous media</i>	24
2.5 SUMMARY.....	26
CHAPTER 3 - FLOW THROUGH PACKED BEDS OF MONODISPERSE SPHERES	29
3.1 INTRODUCTION	29

3.2	STRUCTURE OF ORDERED PACKED BEDS OF MONODISPERSE SPHERES	29
3.3	PERMEABILITY OF ORDERED PACKED BEDS OF MONODISPERSE SPHERES	35
3.4	DISORDERED PACKED BEDS OF MONODISPERSE SPHERES.....	39
3.5	SUMMARY.....	41

CHAPTER 4 - ELONGATIONAL DISSIPATION IN POROUS MEDIA; CORRUGATED CAPPILARY

BUNDLE MODELS.....	43	
4.1	INTRODUCTION	43
4.2	MATHEMATICAL FORMULATION.....	44
4.2.1	<i>Basic equations</i>	44
4.2.2	<i>Phenomenological relations</i>	46
4.2.3	<i>Lubrication approximation</i>	47
4.2.4	<i>Example fluids</i>	48
4.3	PRESSURE DROP PREDICTIONS	49
4.3.1	<i>The widening tube</i>	49
4.3.2	<i>The sinusoidal tube</i>	54
4.4	POROUS MEDIA MODELS	60
4.4.1	<i>The widening/converging capillary bundle model</i>	60
4.4.2	<i>The sinusoidal capillary bundle model</i>	62
4.5	DISCUSSION	64
4.6	SUMMARY.....	66

CHAPTER 5 - CORRUGATED CAPILLARY BUNDLE MODELS: PREDICTIONS BY A NEW LUBRICATION

APPROXIMATION METHOD.....	68	
5.1	INTRODUCTION	68
5.2	PRESSURE DROP PREDICTIONS	69

5.2.1	<i>The widening tube</i>	69
5.2.2	<i>The sinusoidal tube</i>	75
5.3	POROUS MEDIA MODELS	79
5.3.1	<i>The linear widening/converging capillary model</i>	79
5.3.2	<i>The sinusoidal capillary model</i>	80
5.3.3	<i>Comparison of both models</i>	81
5.4	DISCUSSION	82
5.4.1	<i>The linear widening/converging tube</i>	82
5.4.2	<i>The sinusoidal tube</i>	83
5.5	SUMMARY.....	85

CHAPTER 6 - PERMEABILITY MODIFICATION AND RHEOLOGY OF AQUEOUS POLYACRYLAMIDE

SOLUTIONS.....87

6.1	WATER SHUT-OFF TREATMENTS.....	87
6.1.1	<i>Introduction</i>	87
6.1.2	<i>Full-blocking treatments</i>	90
6.1.3	<i>DPR treatments</i>	92
6.2	CHARACTERISATION OF POLYACRYLAMIDE/BRINE SOLUTIONS	94
6.2.1	<i>Polymer and polymer solution preparation</i>	94
6.2.2	<i>Polymer solution characterisation</i>	95
6.2.3	<i>Rheological characterisation</i>	99
6.3	STATIC ADSORPTION EXPERIMENTS	101
6.4	COREFLOOD EXPERIMENTS.....	104
6.4.1	<i>Coreflood set-up</i>	104
6.4.2	<i>Experimental procedure</i>	108
6.4.3	<i>Definitions</i>	108
6.4.4	<i>Coreflood results</i>	109
6.5	SUMMARY.....	114

CHAPTER 7 - NEW INSIGHTS ON POLYMER RETENTION AND RHEOLOGY IN POROUS MEDIA; THE GELANT DIVERSION PROCESS	117
7.1 INTRODUCTION	117
7.2 EXPERIMENTAL.....	120
7.2.1 <i>Brine and polymer solution</i>	120
7.2.2 <i>Coreflood set-up and procedures</i>	121
7.3 COREFLOOD RESULTS.....	123
7.3.1 <i>CPAM1 experiments</i>	123
7.3.2 <i>CPAM2 experiments</i>	124
7.4 UNSTEADY-STATE PLUGGING BEHAVIOUR; FLOW-INDUCED ADSORPTION	131
7.5 SUMMARY.....	136
CHAPTER 8 - ON THE PERMEABILITY REDUCTION DUE TO ADSORBED POLYELECTROLYTES	138
8.1 INTRODUCTION	138
8.2 POLYMER SOLUTION CHARACTERISATION	139
8.2.1 <i>PAA solution preparation</i>	139
8.2.2 <i>PAA conformation in the dilute state</i>	140
8.2.3 <i>PAA titrations</i>	144
8.2.4 <i>Rheological measurements</i>	146
8.3 COREFLOOD STUDIES.....	154
8.3.1 <i>Set-up, materials and procedures</i>	154
8.3.2 <i>Coreflood results</i>	156
8.4 DOWNHOLE APPLICATION AS REVERSIBLE BARRIER.....	160
8.5 SUMMARY.....	161
CHAPTER 9 - CONCLUSIONS.....	163
APPENDIX A COIL-STRETCH TRANSITION.....	166

APPENDIX B	ELASTIC EFFECTS	169
APPENDIX C	TWO-PHASE IMMISCIBLE FLOW	175
APPENDIX D	CARREAU PARAMETERS	178
APPENDIX E	COREFLOOD SET-UP	179
APPENDIX F	DYNAMIC ADSORPTION	183
NOMENCLATURE	184
PUBLICATION LIST	189
SUMMARY	190
SAMENVATTING	192
DANKWOORD	195
CURRICULUM VITAE	196

CHAPTER 1 - INTRODUCTION

1.1 Water soluble polymers in oil recovery

Nowadays about 85% of world energy demand is delivered by fossil energy and oil's share in world demand is more than 30% [1]. World oil consumption per year has increased from 3.2 billion m³ in 1975 to 4.4 billion m³ in 2000 and it is expected to increase up to 5.2 billion m³ in 2010 [2]. The last decade has seen a progressive increase in global discovery volumes. This is mainly due to two reasons: 1) access to some very prospective resource areas, e.g. the former Soviet-Union and 2) advances in technology allowing the production of previously uneconomic reserves.

Actually it is estimated that there is still oil for about 60 years [3]. Consequently leading energy companies are investing increasing amounts of money into gas concessions and related production- and storage facilities. In addition, much money is invested into the development of non-fossil energy alternatives like wind-, solar- and biomass energy and forestry. However, these new sources of energy are not yet competitive on a large scale. Therefore, apart from the continuous search for new findings, companies are persisting in developing techniques to make energy recovery and consumption more efficient. In this way they intend to stretch the life span of the fossil resources. The work in this thesis should be seen in this perspective.

The overall efficiency of conventional oil recovery, including pressure maintenance by water flooding, is usually smaller than 40% of the oil originally in place. Technically it is possible to improve this efficiency by applying Enhanced Oil Recovery (EOR) processes, of which polymer flooding, steam injection and surfactant flooding are examples [4]. EOR processes intend to improve the sweep efficiency by reducing the mobility ratio between injected and in-situ fluids¹ and/or to improve the displacement efficiency by reducing the capillary- and interfacial forces. Polymer flooding is an enhanced water flooding process in which the water/oil mobility ratio is lowered by adding water-soluble polymers the water to increase its viscosity.

¹ The water/oil mobility ratio is defined as the ratio between permeability to water k_w and permeability to oil k_o times the ratio between viscosity of oil η_o and viscosity of water η_w .

Additionally, polymer adsorption decreases the permeability to water, also reducing the mobility ratio. Consequently sweep efficiency improves resulting in a higher oil recovery at breakthrough. Polymer flooding was popular in the seventies and eighties corresponding to increasing oil prices and low oil stocks [5]. Due to its high costs, typically sixty dollars per m³ of incremental oil, and the access to new easy exploitable reserves, polymer flooding nearly disappeared in the nineties. Currently it is applied in specific field situations, e.g. in the USA, but its worldwide scale is small. In future, as oil becomes scarcer, polymer flooding might well revive again.

Operators of mature oil and gas fields are more and more faced with a high water production coming from an underlying natural water source or from previous stimulation attempts involving water injection. For example, Shell's water production has increased steadily from about 350.000 m³/day in 1990 to more than 1.000.000 m³/day in 2000, nearly matching Shell's oil production [6]. Water production decreases oil production, results in large amounts of water that need to be disposed and gives extra costs related to oil/water separation, handling and lifting. Related problems include the increased tendency for the formation of emulsions, scale² and corrosion. Generally treatment costs of produced water range from \$0.15 per m³ to \$15 per m³ depending on volumes, contamination and location. Therefore oil industry is putting a lot of effort and money in developing techniques to decrease water-handling costs and to reduce water production. An important technology to minimise water production is to shut off water producing layers, by polymer gels or cements, or to reduce water flow by making use of relative permeability modifiers, usually aqueous polymer solutions or gels. Essential for a successful shut-off treatment are the knowledge of the reservoir structure (i.e. which layers produce water and are they interconnected) and the control of polymer placement. Important issues for the latter are polymer rheology (i.e. its flow behaviour) and its retention behaviour upon injection in the porous rocks. Apart from the above-mentioned technologies, which are the most relevant to this thesis, water-soluble polymers are also used to stimulate well production. Today approximately two-thirds of the wells worldwide are hydraulically fractured [7]. This stimulation technique consists of high-pressure fluid

² Scale is a term used in the oil industry for mineral precipitates, which can form during production when pressure and temperature change or when brines with different compositions are mixed.

injection to fracture the rock and create high permeability paths near the well bore allowing oil or gas to be produced more easily. This is effective since most of the reservoir pressure drop takes place in the vicinity of the well bore due to its radial nature and the near well-bore damage. Generally the fracturing fluid contains polymers to provide the viscosity required for transport of the proppants, which are solid particles in the fluid needed to keep the fracture open after the operation. Water-soluble polymers are also applied during the drilling phase as an addition to the drilling mud to influence its rheological properties and filter cake formation. During primary cementing of a casing, polymers are added to cement to decrease its water loss, which is known to cause brittleness. A last example is the use of polymer additives to decrease scale formation and/or its deposition on tubing and pumps.

1.2 Scope of the present study

The objective in this work was to gain knowledge on the flow and retention of polymer solutions through porous media. Although much scientific work has been done, the field is still not well understood. The main reason for this is the complex relation between polymer rheology and polymer retention. Both depend strongly on the porous medium structure and are often very different from bulk behaviour. The aim was thus to contribute to the understanding of this field. While the emphasis is on trying to understand what happens physically, oil recovery applications and implications are dealt with.

1.3 Thesis outline

Chapter 2 is a review of flow through porous media. It discusses the different flow regimes encountered for Newtonian fluids and gives an introduction on the main topic of this thesis, the flow of polymer solutions through porous media.

Chapter 3 deals with the relation between the permeability and packing structure in packed beds of monodisperse spheres. It shows that, even for Newtonian fluids,

dissipation is a complex function of parameters like wall- and internal friction, velocity gradients and tortuosity, all strongly related to flow path geometry.

Chapters 4 and 5 deal with predicting the pressure drop for flow of Newtonian fluids and the more complex polymeric fluids through tubes with diameter variations in the axial direction. A bundle of these tubes form a much better model for a porous medium than the normally used bundle of straight capillary tubes, as the presence of diameter variations gives the possibility to account for elongational dissipation contributions. This mechanism is relevant to porous medium flow due to the complex flow field in the pores including continuous accelerations and slow-downs. The predictions obtained are purely based on bulk fluid flow behaviour.

The last three chapters describe experimental work, both rheological studies and coreflows, on the flow of polymer solutions through porous media. They show that apart from the bulk flow behaviour the pressure drop over a porous medium is determined by polymer retention effects and specific porous medium rheology.

Chapter 6 describes studies on aqueous Polyacrylamide solutions in sandstone-like, SiC grain packs. This polymer is the most widely applied system in polymer flooding and in water shut-off.

Chapter 7 describes studies on aqueous Cationic Polyacrylamide solutions in SiC packs and Berea sandstone's. A lot of attention is paid to porous medium rheology and to the influence of permeability and flow rate on the polymer retention mechanisms occurring. The aim of this work was to explore whether there is scope for a new water shutoff process called two-step gelant diversion.

Chapter 8 describes studies on aqueous Polyacrylic acid solutions. Since Polyacrylic acid is a polyelectrolyte, both its rheology and adsorption behaviour are strongly dependent on pH and salinity. Particularly interesting is the fact that after polymer adsorption, the permeability of the porous medium can be regulated by changing pH and/or ionic strength of the injected fluid.

Chapter 9 summarises the main conclusions of the thesis.

References (Chapter 1)

1. www.deo.org (website USA Department of Energy)
2. Speech by A. Wood, head Shell Global Exploration (2000)
3. Speech by J. van der Veer, president Royal Dutch Shell (2001)
4. A. Carcoana, "Applied Enhanced Oil Recovery", Prentice Hall, New Jersey (1992)
5. K. Sorbie, "Polymer-Improved Oil Recovery", Blackie and Son, Glasgow (1991)
6. Z. Khatib, Changes, magazine Shell International Exploration and Production, September 2001
7. L. Britt, J. of Petroleum Technology, March 2000

CHAPTER 2 - FLOW THROUGH POROUS MEDIA

2.1 Introduction

It is not often realised that porous media govern our daily life. For example textile, leather, coffee filters, bricks, paper towels and snow all consist of numerous voids and pores resulting in unique properties like breathing, insulation, capillary suction and filtration. However, reality is even more drastic; our life depends on porous media like lungs, bones and skin.

A porous medium contains small open spaces, voids and pores, distributed throughout a solid matrix. Although most solids have small interstitial spaces of the size of the molecules, which can be penetrated by diffusion, pores in porous media generally have a larger size. Generally a close relationship exists between the pore structure of a porous medium and many of its macroscopic properties. Those properties, which are solely determined by the pore structure, are called pore structure parameters (PSP's) [1]. Microscopic PSP's describe the shape, size and connectivity of the pores³. Macroscopic PSP's represent the average behaviour of a sample containing many pores. Familiar examples of macroscopic PSP's are the porosity, the specific surface and the permeability. The permeability describes the conductivity of a porous medium with respect to fluid flow.

Another important macroscopic PSP is the macroscopic homogeneity. A porous medium is macroscopically homogeneous when all samples of a size comparable to the size of the medium have the same permeability, porosity etc. Most natural porous media however contain areas with a spatial variability in the morphology (packing structure, porosity and particle size) and are thus macroscopically heterogeneous. Those media, which are homogeneous on a macroscopic scale, often show heterogeneity's on a smaller scale. A frequently encountered problem in this respect is how to translate information describing the behaviour of a quantity on the microscopic scale into an effective macroscopic value; an up-scaling procedure must

³ An often-used method to gather information is to interpret microscope pictures of a porous medium cross-section by means of stereology.

include the selection of a statistically representative sample of the ‘right’ size. A sample too small may contain the behaviour of only the solid- or the open space; a sample too large may lead to loss of interesting details [2].

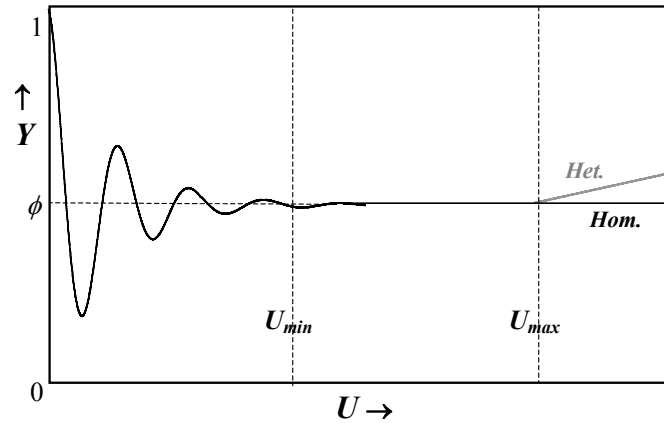


Figure 2.1 The representative elementary volume [2]

The above-mentioned effect is demonstrated in Figure 2.1, which shows the relation between the volumetric ratio $Y = U_v/U$ and U . Here U is the volume of a sphere centred at an arbitrary point in the porous medium. U_v is the volume of the void space within U . Initially, when the value of U is of the same order of magnitude as the pore size, large fluctuations in the volumetric ratio occur. These fluctuations, which occur around a constant value, the porosity ϕ , become small at $U = U_{min}$. At $U = U_{max}$ the decay of the fluctuation amplitude stops and a systematic variation in the volumetric ratio is observed. Above $U = U_{max}$ macroscopic heterogeneity's may appear (curve *Het.* in Figure 2.1). The representative elementary volume should have a size in between U_{min} and U_{max} [2]. In fact the smallest possible size of the representative elementary volume can be considered as a measure for the degree of homogeneity.

This chapter deals with single-phase flow through a porous medium. It is meant as a comprehensive introduction to the remainder of the thesis. Section 2.2 discusses the different flow regimes encountered during porous medium flow of a Newtonian fluid. Besides, the main parameters determining the permeability are considered. In Section 2.3 some important permeability models from literature are shortly reviewed. Section 2.4 introduces the main subject, polymer solution flow through porous media.

2.2 Flow of Newtonian fluids through porous media

2.2.1 The creeping flow regime

Most simple fluids obey Newton's law of viscosity i.e. their flow behaviour can be characterised by a constant viscosity η . The relationship between the pressure drop ΔP and the flow rate Q for isothermal, steady state, creeping flow⁴ of a Newtonian fluid through a porous medium (permeability k) was established empirically in 1856 by Darcy [3]. Its most simple form, for unidirectional and horizontal flow, is:

$$\frac{\Delta P}{L} = \frac{\eta u}{k} \quad (2.1)$$

where L is the porous medium length, u ($= Q/S$) the filtration or Darcy velocity and S the cross-sectional area of the porous medium.

As the understanding of porous media flow is important in fields like geohydrology, powder metallurgy, mechanical-, chemical- and petroleum engineering, the prediction of the permeability of a porous medium is a problem which has intrigued many scientists since long. This task is especially complex for natural porous media (e.g. sandstone) since their invisible internal pore structure evolved from geological processes like gravity separation and cementation of widely sized grains. Many theoretical and experimental studies have used packed beds of particles like spheres or fibres as models for porous media. The application of these synthetic porous media is attractive because their network structure may easily result in a reproducible macroscopically homogeneous medium providing a better opportunity to gain insight and to deduce general laws. Until now, experiments on these media have resulted in semi-empirical relations, which provide a reasonable estimation of the permeability of packed beds [1].

⁴ Flow at a small velocity, a regime where the viscous forces dominate the inertial forces.

It is nowadays accepted that the main parameters determining the permeability of a porous medium are:

- specific surface
- porosity
- particle parameters: size, shape and roughness and their distributions
- packing structure
- macroscopic homogeneity/heterogeneity

However these parameters are not independent from one another. For example, the porosity and the packing structure are closely related. The packing structure gives information on the spatial arrangement of particles with respect to one another. Monodisperse spheres for example, can be packed in an ordered⁵ or in a disordered⁶ manner [4,5] resulting in a different pore structure, porosity and permeability (see Chapter 3).

The establishment of a general non-empirical law to predict the permeability of packed beds has been hindered by the inability to define independent quantities. Besides, little is known about the nature of the interstitial velocities. Experimental difficulties include the quantification of the complex geometry and the inability to measure the interstitial velocity in porous media. Also, the problem of solving fluid mechanics through a porous medium has proved analytically intractable. Therefore, most likely, empirical correlations with universal quantities and properties easy to measure will be the upper limit to reach. Permeametry, which is the technique to measure the permeability, will consequently remain indispensable.

As an extension from classical fluid mechanics, the dimensionless quantities Reynolds number and friction factor are frequently used in the literature on flow through porous media. Although their definitions are somewhat different than for tube flow, their physical meaning is similar; the Reynolds number describes the ratio

⁵ The packing is established according to a crystallographic unit cell (see Chapter 3).

⁶ Frequently called haphazard or random packing. The term random is in fact incorrect because the distribution in space in such a packing is not random, since each sphere excludes other spheres from its own space.

between the inertial and viscous forces⁷. The friction factor equals the additional force associated with the kinetic behaviour of the fluid divided by the wetted surface and the kinetic energy per unit volume. The most common definitions for Reynolds number and friction factor in literature are respectively:

$$Re_p = \frac{\rho_f u D_p}{\eta} \quad (2.2)$$

$$f_p = \frac{\Delta P}{L} \frac{D_p}{\rho_f u^2} \quad (2.3)$$

where D_p is a characteristic length scale for the internal structure⁸ and ρ_f is the mass density of the fluid. The flow resistance Λ_p is the product of Re_p and f_p and describes the ratio between the pressure loss and flow rate in a dimensionless way:

$$\Lambda_p = Re_p f_p = \frac{\Delta P}{L} \frac{D_p^2}{\eta u} \quad (2.4)$$

It has been established by experiments that Darcy's law (Eq. 2.1) remains valid, i.e. Λ_p is constant, as long as $Re_p \leq 1$. This implies for the permeability:

$$k = \frac{D_p^2}{\Lambda_p} \quad (2.5)$$

2.2.2 The inertial and turbulent flow regime

Since the nineteenth century it has been known that large deviations from Darcy's law (Eq. 2.1) occur at high flow rates. These deviations are caused by the increasing contribution of inertial effects. In 1901 Forchheimer [6] proposed the following empirical law to account for the inertial effects:

⁷ The subscript p stands for: 'in porous media flow'

⁸ For packed beds this is usually the average particle diameter

$$\frac{\Delta P}{L} = \alpha_l \eta u + \beta_l \rho_f u^2 \quad (2.6)$$

where $\alpha_l (= k^{-1})$ is the Darcy parameter and β_l is the inertia parameter. Although not always supported by experiments, β_l is often considered constant for a specific porous medium. Combining Eqs. 2.2, 2.3 and 2.6 gives the following dimensionless form of Forchheimer's law:

$$A_p = \alpha^* + \beta^* Re_p \quad (2.7)$$

where $\alpha^* = \alpha_l D_p^2$ and $\beta^* = \beta_l D_p$. After analysing experiments from literature, Macdonald et al. [7] concluded that deviations from Darcy's law⁹ start in the range $1 \leq Re_p \leq 15$.

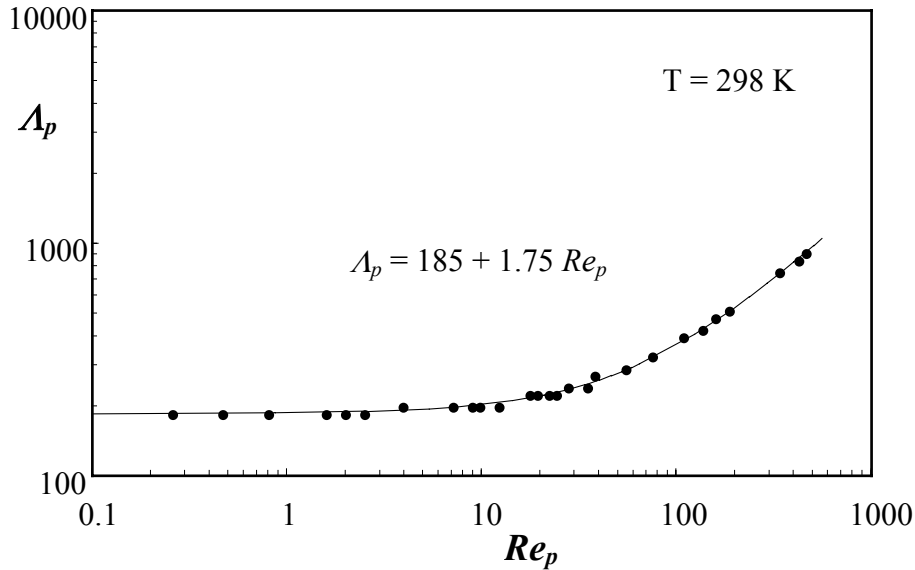


Figure 2.2 A_p vs. Re_p for flow of water in a disordered packed bed of monodisperse glass spheres [8]

Figure 2.2 shows a typical graph of A_p vs. Re_p for flow of water in a disordered packed bed of monodisperse glass spheres [8]. Many researchers have confirmed the gradual nature of the increase in A_p above $Re_p \approx 1$ [9-11]. Dybbs et al. [12] performed

⁹ Because the author used another definition of the Reynolds number, the values have been corrected.

laser anemometry- and flow visualisation studies on disordered packed beds of monodisperse spheres over a wide range of Reynolds numbers. These authors observed the development of boundary layers at $Re_p \approx 1$. On increasing the flow rate up to $Re_p \approx 10$ the boundary layers became more pronounced and an “inertial core” developed. This is a region in between the boundary layers with a velocity distribution resembling plug flow. Dybbs et al. [12] concluded that the development of “inertial core” flow was the reason for the non-linear relationship between pressure drop and flow rate. Upon further increasing the flow rate the size of the “inertial core” increased. This steady non-linear flow regime, called the inertial regime, persisted up to $Re_p \approx 150$. An unsteady flow regime was observed above $Re_p \approx 150$ which was characterised by the occurrence of wake oscillations in the pores. At $Re_p \approx 250$ vortices developed which persisted up to $Re_p \approx 300$. At higher values of Re_p a highly chaotic and unsteady flow resulted, which resembled turbulent flow. Happel et al. [13] stated: “Failure of Darcy’s law results when the distortion that occurs in the streamlines owing to changes in the direction of motion is great enough that inertial forces become significant compared with viscous forces. The incidence of turbulence will occur at much higher Reynolds numbers (if indeed such a phenomenon occurs at all)”. However, other authors have provided evidence that turbulence can occur during flow through porous media [14,15].

2.3 Permeability Models

2.3.1 Introduction

During many years scientists have attempted to predict the permeability of porous media by using models, which simplify the complex pore structure. This section gives a short overview of some important models from literature. Dullien [1] distinguishes two approaches, namely models based on flow inside conduits and models based on flow around submerged objects. The last category has only been successful at high porosity, which is not relevant for this thesis. The overview here is restricted to the first approach and deals with capillary models (Section 2.3.2), deterministic models (Section 2.3.3) and hydraulic diameter models (Section 2.3.4).

2.3.2 Capillary models

In capillary models the pores are described as a bundle of tubes, which are placed in parallel. The simplest form is the model with identical tubes, which means that the tubes are straight, cylindrical, and of equal radius R (Figure 2.3a). Darcy's law (Eq. 2.1) combined with the Hagen-Poiseuille law [16] gives the following relationship for the permeability:

$$k = \frac{\phi R^2}{8} \quad (2.8)$$

where ϕ is the porosity ($=N_t \pi R^2/S$), N_t is the number of tubes and S the normal cross-sectional area of the model. Eq. 2.8 is often used for a quick and rough estimation of the average pore diameter after having measured the permeability and porosity of a packed bed. However, the use of Eq. 2.8 to estimate the permeability of a real porous medium is not easy as the model includes a pore radius, which is difficult to extract from an analysis on the complex pore geometries. In addition, the model neglects the topology of the pore space and the heterogeneity of the medium can be an issue.

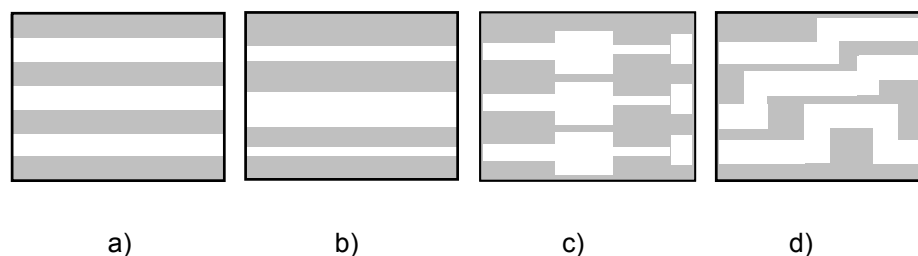


Figure 2.3 Longitudinal cross-section of different capillary models. The white sections indicate the tubes

Different paths have been walked to include a more realistic picture of the pore geometry into the capillary model by accounting for:

1. Non-uniformity of the parallel type

The presumption that the porous medium consists of cylindrical tubes of just one radius is of course not realistic. When introducing n_t tubes of different radii R_i in the capillary model (Figure 2.3b), the following result is obtained:

$$k = \frac{\phi \sum_{i=1}^{n_t} R_i^4}{8 \sum_{i=1}^{n_t} R_i^2} = \frac{\pi}{8S} \sum_{i=1}^{n_t} R_i^4 \quad (2.9)$$

where $\phi = \pi(\sum_{i=1}^{n_t} R_i^2)/S$ is the porosity. It follows from Eq. 2.9 that addition of one extra tube always results in an increase of the permeability. In general capillary models with non-uniformity of the parallel type are very sensitive to errors in the large pore size region when introducing an experimentally determined pore size distribution¹⁰.

II. Non-uniformity of the serial type

In an attempt to account for the complex pore geometry of throats and bodies, serial capillary models have been developed. The pores in these models (length L) consist of N_s cylindrical tube segments with varying radius R_i and length l_i (Figure 2.3c). This yields the following equation for the permeability¹¹:

$$k = \frac{\phi \left(\sum_{i=1}^{N_s} l_i \right)^2}{8 \sum_{i=1}^{N_s} R_i^2 l_i \sum_{i=1}^{N_s} l_i / R_i^4} = \frac{\pi}{8S} \frac{L}{\sum_{i=1}^{N_s} l_i / R_i^4} \quad (2.10)$$

where $\phi = \pi(\sum_{i=1}^{N_s} R_i^2 l_i)/SL$ is the porosity. In general, when using measured pore size distributions, serial models tend to underestimate permeability because they are very sensitive to errors in the small pore size region. Of course a combination of parallel and serial non-uniformity's is again a step closer to a real porous medium geometry.

¹⁰ Frequently pore size distributions obtained by a capillary pressure method have been attempted

¹¹ Pressure losses due to elongational deformation gradients are neglected here.

III. Three dimensions

A limitation of the capillary model is that it is unidirectional, i.e. the model provides only permeability in one direction. A simple modification is to put 1/3 of the tubes in each of the three dimensions. It results in a decrease of the permeability from Eqs. 2.8 - 2.10 by a factor 3.

IV. Tortuosity

The fact that the flow path in a porous medium is not straight but tortuous implies that a fluid particle has to travel an effective flow path of length L_e which is larger than the porous medium length L (Figure 2.3d). Introducing this in the capillary model at constant pressure drop results in a decrease of the effective pressure gradient by a factor L/L_e and an increase of the volume to be passed¹² by a factor L_e/L . Consequently the permeability obtained by Eqs. 2.8 - 2.10 decreases by a factor $\tau = (L_e/L)^2$, where τ is the tortuosity factor. This factor is a parameter to account for 3-D effects in a 1-D model. However, tortuosity is a fundamental property of the streamlines in the conducting pores. It is a measure for the deviation from the macroscopic flow direction of the fluid during flow [1]. Of course a more realistic capillary model should account for all four mentioned aspects and implement information concerning the pore geometry correctly. However the general opinion is that the representation of the pore geometry by capillary tubes is too simplistic to give good permeability predictions. The reason for this is that the model does not include vital characteristics of the pore space network structure, like the connectivity between pores or excess dissipation due to convergent-divergent velocity components. The value of capillary models will therefore remain the provision of a clear, elementary insight in important aspects controlling porous media flow.

2.3.3 Deterministic permeability models

In deterministic permeability models the porous medium is represented as a parallel sequence of tubes with periodically varying diameter. The relation for the permeability is obtained either by fully solving the continuity- and Navier-Stokes

¹² Consequently the effective velocity decreases by a factor L_e/L

equations by a numerical scheme or by making use of the lubrication approximation [16,17]. An advantage over the previous treated models is that deterministic models can account for dissipation due to the convergent-divergent nature of porous media flow¹³. A disadvantage is the difficulty of correlating the resulting model solution with the actual pore geometry present in a porous medium. A description of the deterministic models available in literature [18-22] is beyond the scope of this chapter. In Chapter 4 and 5 the lubrication approximation [17] is used to obtain pressure drop predictions for flow through linear widening/converging tubes and sinusoidal tubes. By making use of Darcy's law (Eq. 2.1) the pressure drop over one tube can be converted into an expression for the permeability of a porous medium consisting of these tubes placed in parallel.

2.3.4 Hydraulic diameter models

In the hydraulic diameter model or Carman-Kozeny model [23-25] it is assumed that a porous medium (length L) is a parallel sequence of pores (length L_e) of which the cross sectional area has a complicated shape (tortuosity factor τ) but on the average a constant area. For laminar flow through the above described medium application of the Hagen-Poiseuille law [16] yields:

$$v_i = \frac{\Delta P D_h^2}{16 K_o \eta L_e} \quad (2.11)$$

where v_i is the average interstitial velocity, which is the average velocity in the porous medium, D_h is the hydraulic diameter¹⁴ and K_o is a factor depending on the cross-sectional shape¹⁵. The Dupuit-Forchheimer assumption [1] states that the average interstitial velocity v_i is related to the Darcy velocity by:

¹³ Elongational and radial velocity gradients

¹⁴ The hydraulic diameter equals four times the cross-sectional area divided by the wetted perimeter

¹⁵ $K_o = 2$ for a cylindrical tube, $K_o = 1.78$ for a square channel, $K_o = 1.68$ for a equilateral triangle [2]

$$u = \frac{v_i \phi}{\sqrt{\tau}} \quad (2.12)$$

For the porous medium described above, the hydraulic diameter equals four times the void volume per unit volume divided by the wetted surface per unit volume (S_u):

$$D_h = \frac{4\phi}{S_u} = \frac{4\phi}{S_v(1-\phi)} \quad (2.13)$$

where S_v is the volumetric specific surface. By defining a mean particle diameter D_p as the diameter of a hypothetical sphere with the same volumetric specific surface as the particle, one obtains:

$$S_v = \frac{6}{D_p} \quad (2.14)$$

Combining Eqs. 2.11 - 2.14 results in:

$$u = \frac{\Delta P}{L} \frac{D_p^2}{36K\eta} \frac{\phi^3}{(1-\phi)^2} \quad (2.15)$$

where $K (= K_o \tau)$ is a constant, which accounts for pore shape and tortuosity. Combining Eqs. 2.1 and 2.15 yields the Carman-Kozeny equation for the permeability of packed beds:

$$k = \frac{D_p^2}{A} \frac{\phi^3}{(1-\phi)^2} \quad (2.16)$$

where $A = 36K$.

Carman [24,25] stated that $K = 5$, yielding $A = 180$ is the most realistic value for packed beds. For a medium approximated by cylindrical tubes ($K_o = 2$) this results in a tortuosity factor $\tau \approx 2\frac{1}{2}$. Flow experiments on disordered packed beds of monodisperse spheres have resulted in values for A in between 150 and 185 (see Table 2.1). Since the Carman-Kozeny equation (Eq. 2.16) is commonly reproduced with an inserted value for A , it is sometimes considered as being purely

phenomenological. However, this correlation has proven to hold for a variety of porous media. Experimental literature shows that the Carman-Kozeny relation can be used for dense, disordered packed beds, irrespective of particle size and shape, suggesting a general physical basis [25-28]. While not using any capillary bundle assumption, Thies-Weese et al. [29] have shown that Eq. 2.16 can be deduced from a scaling analysis in which the only assumption is that the porous medium is dense and isotropic.

Authors	Fluids	A	Authors	Fluids	A
Sadowski, Bird [30]	Water, Glycerine	180	Hanna et al. [34]	Water	180
Kozicki et al. [31]	Water	173	Mishra et al. [35]	Water, Oil	150
Kemblowski, Mertl [32]	Water, Glycerine	150	Kulicke, Haas [36]	Water, Ethylene Glycol	185
Brea et al. [33]	Water, Glycerine	160	Michele [37]	Water, Glucose	180

Table 2.1 Literature values of Carman-Kozeny constant A (Eq. 2.16) for disordered packed beds of monodisperse spheres

Based on Eq. 2.16 Leva [38] proposed the following equation for the permeability of a packed bed of solid particles, a definition which is frequently used in the field of chemical engineering:

$$k = \frac{D_p^2 H^2}{200} \frac{\phi^3}{(1-\phi)^2} \quad (2.17)$$

where H is a parameter dependent on the shape of the particles.

In this approach the shape factor H equals the ratio between the area of a sphere equivalent to the volume of the particle and the actual surface of the particle. In Table 2.2 some experimentally determined values for H from literature are given for various packing materials of different shape [38].

Packing material	H	Packing material	H
Mica flakes	0.28	Sand (angular)	0.73
Crushed glass (jagged)	0.65	Sand (rounded)	0.83
Wilcox Sand (jagged)	0.60	Ottawa sand (spherical)	0.95

Table 2.2 Values for the shape factor H for various packing materials [38]

For monodisperse spheres ($H = 1$), Eq. 2.17 results in slightly smaller permeability values than the Carman-Kozeny equation. Another difference is that the value of the empirical factor H is attributed solely to the shape of the packing materials, neglecting the influence of tortuosity. Generally, by taking K or H values from literature in combination with a Carman-Kozeny type of relationship, reasonable permeability predictions for synthetic porous media can be obtained [1]. Exact predictions remain difficult due to the fact that K and H are functions of shape, size distribution and specific packing structure. The influence of the latter is discussed in the next chapter. The appreciation of the hydraulic diameter theory has lead to another frequently used definition of the Reynolds number and the friction factor for flow through porous media [39]:

$$Re_{p2} = \frac{\rho_f u D_p}{\eta(1-\phi)} \quad (2.18)$$

$$f_{p2} = \frac{\Delta P}{L} \frac{D_p}{\rho_f u^2} \frac{\phi^3}{(1-\phi)} \quad (2.19)$$

$$\Lambda_{p2} = f_{p2} Re_{p2} = A + B Re_{p2} \quad (2.20)$$

where B is a parameter related to the inertial part of the flow resistance.

Eq. 2.20 is known as the Ergun equation [39]. Macdonald et al. [8] have tested this equation extensively using various data sets from literature involving different packing materials. The conclusion was that the best fit was obtained by $A = 180$, $B = 1.8$ for smooth particles and by $A = 180$, $B = 4.0$ for rough particles.

2.4 Flow of polymer solutions through porous media

2.4.1 Introduction

Contrary to Newtonian fluids, the viscosity of polymer solutions is usually a function of flow rate and time. This is caused by the fact that a dissolved polymer molecule, lying as a 3D-coil in the solvent, can be easily deformed during flow, yielding differences in the monomer-solvent friction i.e. the energy dissipation. The flow behaviour of polymer solutions, their rheology, depends on the type of flow field imposed. Frequently shear-thinning flow behaviour, a viscosity decrease with shear rate, is measured in a rheometer imposing a pure shear flow (i.e. velocity gradient is perpendicular to flow direction). A thickening behaviour, an elongational viscosity increase with elongational rate, often results when imposing a pure elongational flow field (i.e. velocity gradient is in the flow direction) [17]. Besides, polymer molecules can be retained during flow by e.g. adsorption on the wall or by other retention mechanisms. This decreases the polymer concentration and thus the bulk viscosity and causes a decrease in the cross-section available for flow.

This paragraph introduces the main subject of this thesis, the flow of polymer solutions through porous media. This complex topic, governed by polymer rheology and retention behaviour, is still not understood very well. Based on the experimental evidence in literature it is possible to define three different regimes by considering the ratio between the characteristic polymer coil radius, i.e. the hydrodynamic coil radius (R_h) and the characteristic pore radius (R_p). In the following the occurring retention mechanisms in low permeability porous media ($R_p < 3R_h$), high permeability porous media ($R_p > 50R_h$) and intermediate permeability porous media ($3R_h < R_p < 50R_h$) will be discussed respectively.

2.4.2 Low permeability porous media

The retention mechanism, in which polymer molecules are filtered out when passing constrictions in the porous medium smaller than the polymer coil size, is called mechanical entrapment. Figure 2.4 shows a schematic representation of the limiting case. A polymer coil can just enter a cylindrical pore, which has been pre-adsorbed.

The latter means that due to adsorption an adsorbed polymer layer (thickness $2R_h$) covers the pore walls¹⁶. When assuming that this adsorbed layer reduces the pore size effectively, it follows that mechanical entrapment can occur as $R_p < 3R_h$. If one assumes $R_h = 0.10 \mu\text{m}$ (high molecular weight polymer) and porosity $\phi = 0.40$ before adsorption, one can estimate the criterion for this regime: $k < 5 \times 10^{-15} \text{ m}^2$ (Eq. 2.8).

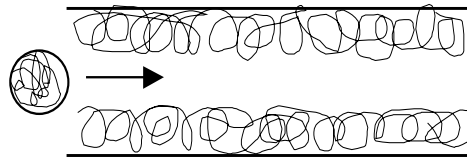


Figure 2.4 A polymer coil enters a cylindrical pore which has been pre-adsorbed

Some characteristics of mechanical entrapment are [40]: 1) The retention occurs at any flow rate, 2) The retention rate increases with flow rate, 3) The level of retained polymer is largest close to the core entrance and 4) The mechanism can take place both under adsorption and non-adsorption conditions.

2.4.3 High permeability porous media

The criterion of $R_p > 50R_h$ is based on experimental evidence [41-43]. When using $R_h = 0.10 \mu\text{m}$ and $\phi = 0.40$ as before, one obtains as permeability criterion: $k > 1.2 \times 10^{-12} \text{ m}^2$ (Eq. 2.8). In this regime, the average pore diameter is large compared to the polymer coil size and retention by filtration on pore throats is negligible. Polymer retention can only occur by adsorption, if the polymer has a tendency to adsorb on the porous medium. After complete saturation of the surface available by adsorption, polymer injection at a certain flow rate Q_s results in stationary flow conditions and a constant mobility reduction R_m , where

$$R_m = \frac{\Delta P_p}{\Delta P_{s0}} \quad (2.21)$$

¹⁶ Adsorption occurs if the difference in free energy of segment/surface contacts and that of the solvent/surface contacts is sufficiently negative. Important parameters are the adsorbed amount and the adsorbed layer thickness. For more details see Fleer et al. [44].

Here ΔP_p is the pressure drop during polymer solution flow at Q_s after adsorption. ΔP_{s0} is the pressure drop during solvent flow at Q_s before adsorption. In this regime, the mobility reduction R_m is a function of the (in-situ) viscosity, which depends on the flow rate and the permeability reduction R_k of the porous medium due to adsorption. The latter is defined by:

$$R_k = \frac{\Delta P_{s1}}{\Delta P_{s0}} \quad (2.22)$$

where ΔP_{s1} is the pressure drop during solvent flow at Q_s after adsorption. For high permeability porous media, the permeability reduction R_k is usually independent of Q . R_k depends on the ratio between the adsorbed layer thickness and the pore radius.

Since the (in-situ) rheological behaviour is a function of the deformation rates in the medium, an estimation of these parameters would be valuable. This is however impossible though due to the unknown structure. Therefore a macroscopic description is often used, which describes the porous medium as a capillary bundle model (Section 2.3.2) having N_t pores of radius R_p (Eq. 2.8). Under laminar flow conditions, an average shear rate follows by assuming that the shear rate equals the shear rate at the wall of a tube with radius R_p :

$$\dot{\gamma}_p = \alpha_g \frac{4u}{\phi R_p} \quad (2.23)$$

where $u = Q/S$ and the shift factor α_g is added to take into account the porous medium structure.

When comparing apparent viscosity data from the porous medium with rheometer data, Chauveteau [45] found that the rheological curves of the polymer solutions correlated well when using Eq. 2.23 and taking $\alpha_g = 1.7$ for packed beds of spheres and $\alpha_g = 2.5$ for packed beds of angular grains. James and McLaren [46] have confirmed that α_g should exceed one in order to match data. The fact that $\alpha_g > 1$ implies that the shear rate in a porous medium is underestimated by the regular capillary bundle model.

Zitha et al. [41,42] found after injection of a 0.37 g/l Polyacrylamide/brine solution in a high permeability grain pack of 110 μm SiC grains ($k = 3.2 \times 10^{-12} \text{ m}^2$), a

permeability reduction $R_k = 1.2$ after surface saturation independent of the flow rate. When varying the effective shear rate (i.e. the flow rate) while injecting the polymer solution, three different flow regimes could be identified. Newtonian flow behaviour was observed at small shear rates (no coil deformation), shear-thinning flow behaviour at higher shear rates (coil deformation) and thickening behaviour above a critical shear rate of $\dot{\gamma}_p = 110 \text{ s}^{-1}$ (coil stretching) (Figure 2.5). The measurements were fully reversible and the initial value of the permeability reduction R_k had not changed at the end of the experiment.

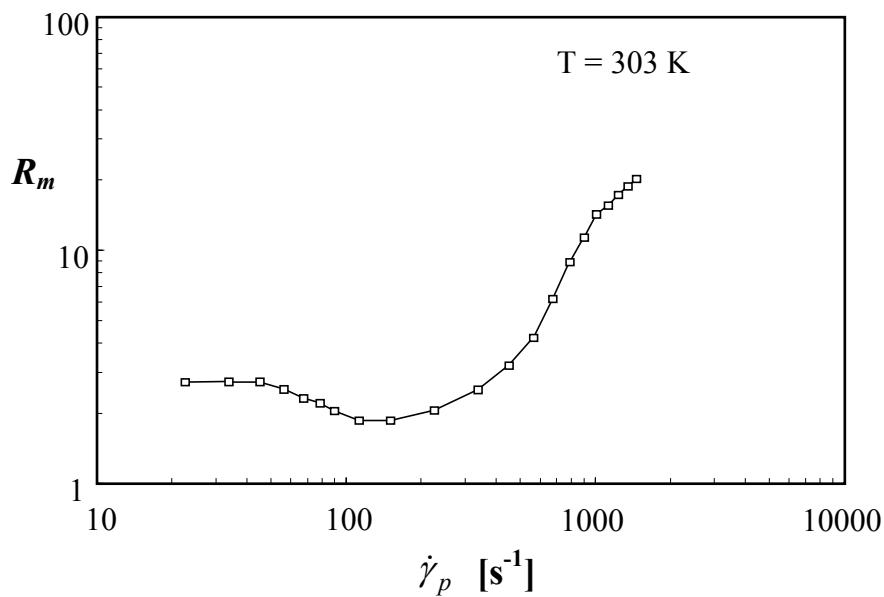


Figure 2.5 The mobility reduction vs. shear rate for injection of a 0.37 g/l PAM/brine solution in a 110 μm SiC grain pack [41,42]

In a conventional shear rheometer only the first two regimes can be measured. The thickening regime is a consequence of the extension of polymer coils to a stretched state, resulting in a large increase in polymer-solvent friction [17]. This coil-stretch transition is induced by the elongational deformation gradients present during porous medium flow. At large enough flow rates, also mechanical degradation i.e. chain breakage can occur in the thickening regime [8]. More information on the coil-stretch transition and its relevance in porous media flow is given in Appendix A.

The above-sketched behaviour is typical for flow of polymer solutions through high permeability porous media. The value of the permeability reduction after adsorption

R_k is small and does not vary with the solvent flow rate. The value of the mobility reduction R_m is governed by the rheological properties of the polymer solution.

2.4.4 Intermediate permeability porous media

Since a few years experimental evidence has been found for the existence of a retention mechanism specific to intermediate permeability cores [41,42,47,48]. Zitha et al. [41,42] found a critical shear rate when injecting a dilute Polyacrylamide/brine solution in 18 μm SiC grain packs ($k = 1.4 \times 10^{-13} \text{ m}^2$). Below this rate only a small permeability reduction resulted due to polymer adsorption. Above this rate R_m increased continuously in time during injection (Figure 2.6).

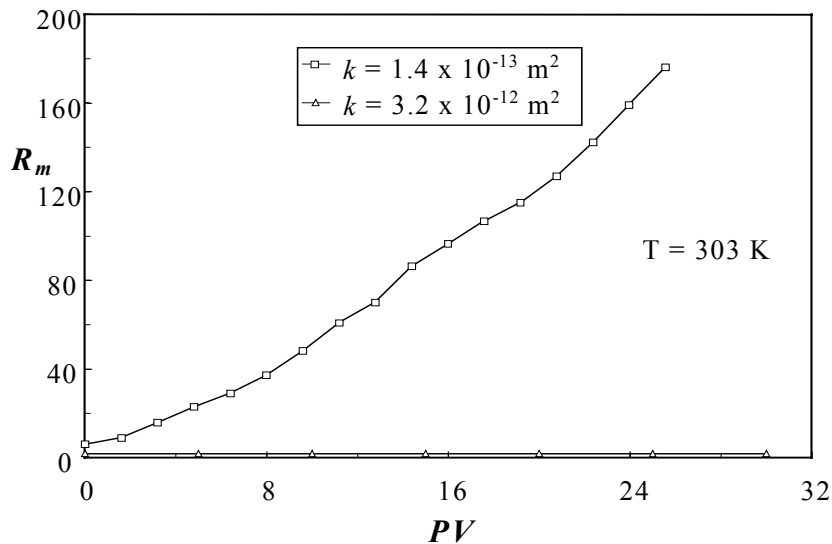


Figure 2.6 The mobility reduction vs. number of injected pore volumes (PV) for a 0.37 g/l PAM/brine solution in 18 μm and 110 μm SiC grain packs [41]

The authors proposed the following mechanism. At the critical flow rate the polymer coils can stretch due to the fact that the elongational deformation rates have become high enough. The stretched chains can bridge pore throats by adsorption. This bridging process, resulting in a continuous permeability reduction, can last as long as still free adsorption sites around the pore throat are available. The retention mechanism was called bridging adsorption. Other experimental findings [41,42] are: (1) The plugging rate (i.e. $\delta R_m / \delta PV$) is larger when injecting solutions of higher polymer concentration, (2) The plugging rate increases with decreasing core

permeability, (3) The plugging phenomenon is absent under non-adsorbing conditions. (4) The polymer is usually retained in the first part of the core.

Not only the retention mechanism, but also the rheology of polymer solutions in porous media is dependent on the permeability. Chauveteau and Sorbie [49] have shown that in the vicinity of a solid interface, polymer properties differ strongly from bulk properties. These authors found for polymer solutions under non-adsorbing conditions, that the apparent viscosity in the porous medium is smaller than the viscosity measured in a rheometer due to polymer depletion. The differences in viscosity become larger when decreasing the pore radius, i.e. the permeability or increasing the polymer concentration. This phenomenon is caused by the fact that the polymer molecules are hindered by the pore wall due to their size at distances smaller than the coil size. Consequently the concentration in the vicinity of the wall is locally smaller than the bulk concentration. As a result, during flow, the average polymer velocity is slightly larger than that of the solvent [49].

Another well-known phenomenon is the fact that the value of the permeability reduction, after surface saturation by polymer adsorption, can increase with the flow rate. This is a result of deformation of the adsorbed layer and generally results in a non-linearity in the volume rate vs. pressure drop relation [50]. This effect usually becomes stronger when decreasing the permeability. At much higher rates, when the flow is exerting enough drag on the adsorbed polymer molecules, polymer desorption has been witnessed [51].

2.5 Summary

1. In the creeping flow regime, the relation between the pressure drop and the flow rate is linear and is described by Darcy's law (Eq 2.1). Above a certain flow rate, corresponding with $Re_p \approx 1$ (Eq. 2.2), deviations occur due to inertia resulting in an increasing dissipation. The transition from the creeping flow regime to the inertial regime has usually a very gradual character.
2. The main parameters determining the permeability of a porous medium are the specific surface, the porosity, the particle parameters (size, shape, roughness, distributions), the packing structure and macroscopic homogeneity/heterogeneity. The establishment of a general non-empirical law to predict the permeability of packed beds is hindered by the inability to define independent quantities. Predictions based on fluid mechanics fail due to the great complexity of the pore geometry.
3. Over the years scientists have attempted to predict the permeability of porous media by using models, which simplify the complex pore structure. In literature various types of permeability models are developed, including capillary models, deterministic models and hydraulic diameter models. For practical purposes, the last type has been the most successful.
4. The field of polymer solution flow through porous media is governed by a combination of polymer retention and rheology phenomena. Both depend strongly on the ratio between the hydrodynamic polymer coil radius (R_h) and characteristic pore radius (R_p). Based on the experimental evidence in literature, three different regimes can be distinguished.

References (Chapter 2)

1. F. Dullien, "Porous Media, Fluid Transport and Pore Structure", Academic Press Inc. , San Diego (1992)
2. J. Bear, "Dynamics of Fluids in Porous Media", Dover Publications Inc., New York (1988)
3. H. Darcy, "Les Fontaines Publiques de la Ville de Dijon", Dalmont, Paris (1856)
4. P. Franzen, *Rheol. Acta* **18**, 392 (1979)
5. P. Franzen, *Rheol. Acta* **18**, 518 (1979)
6. P. Forchheimer, *Z. Ver. Deutsch. Ing.* **45**, 1782 (1901)
7. I. MacDonald, M. El-Sayed, K. Mow, F. Dullien, *Ind. Eng. Chem. Fundam.* **18**, 199 (1979)
8. R. Haas, PhD thesis, University of Karlsruhe (1982)
9. A. Gupte, PhD thesis, University of Karlsruhe (1970)
10. C. Kyan, D. Wasan, R. Kintner, *Ind. Eng. Chem. Fundamentals* **9**, 596 (1970)
11. J. Savins, *Ind. Eng. Chem.* **61**, 18 (1969)
12. A. Dybbs, R. Edwards in "Fundamentals of Transport Phenomena in Porous Media", Dordrecht, 199 (1984)
13. J. Happel, H. Brenner, "Low Reynolds Number Hydrodynamics, with Special Application to Particulate Media", Prentice-Hall, Englewood Cliffs (1965)
14. C. Kyle, R. Perrine, *Can. J. Chem. Eng.* **40**, 19 (1971)
15. C. Dudgeon, *Houille Blanche* **7**, 785 (1966)
16. R. Bird, W. Stewart, E. Lightfoot, "Transport Phenomena", John Wiley & Sons, New York (1960)
17. R. Bird, R. Armstrong, O. Hassager, "Dynamics of Polymeric Liquids", Vol. 1, John Wiley and Sons, New York (1987)
18. A. Payatakes, C. Tien, R. Turian, *AICHE J.* **19**, 67 (1973)
19. E. Christiansen, S. Kelsey, T. Carter, *AICHE J.* **18**, 372 (1972)
20. M. Azzam, F. Dullien, *Chem. Eng. Sci.* **32**, 1445 (1977)
21. J. Deiber, W. Schowalter, *AICHE J.* **25**, 638 (1979)
22. F. Trouton, *Proc. Roy. Soc.* **A77**, 426 (1906)
23. J. Kozeny, Royal Academy of Science, Vienna, *Proc. Class. I* **136**, 271 (1927)
24. P. Carman, *J. Soc. Chem. Ind.* **57**, 225 (1938)
25. P. Carman, *Trans. Inst. Chem. Eng. (London)* **15**, 150 (1937)
26. A. Scheidegger, "The Physics of Flow through Porous Media", University of Toronto Press, Toronto, 1974
27. G. Scherer, R. Swiatek, *J. Non-Cryst. Solids* **113**, 119 (1989)
28. A. Philipse, C. Pathmamanoharan, *J. Colloid Interface Sci.* **159**, 96 (1993)
29. D. Thies-Weesie, A. Philipse, *J. Colloid Interface Sci.* **162**, 470 (1994)
30. T. Sadowski, R. Bird, *Trans. Soc. Rheol.* **9**, 243 (1965)
31. W. Koziicki, C. Hsu, C. Tiu, *Chem. Eng. Sci.* **22**, 487 (1967)
32. Z. Kemblowski, J. Mertl, *Chem. Eng. Sci.* **29**, 213 (1974)

33. F. Brea, M. Edwards, W.L. Wilkinson, *Chem. Eng. Sci.* **31**, 329 (1976)
34. M. Hanna, W. Kozicki, C. Tiu, *Chem. Eng. J.* **13**, 93 (1977)
35. P. Mishra, D. Singh, I. Mishra, *Chem. Eng. Sci.* **30**, 397 (1975)
36. W. Kulicke, R. Haas, *Ind. Eng. Chem. Fundam.* **23**, 308 (1984)
37. H. Michele, *Rheol. Acta* **16**, 413 (1977)
38. A. Leva, *Chem. Eng.* **56**, 115 (1949)
39. S. Ergun, *Chem. Eng. Prog.* **48**, 98 (1952)
40. K. Sorbie, "Polymer-Improved Oil Recovery", Blackie and Son, Glasgow (1991)
41. P. Zitha, PhD thesis, University Paris VI (1994)
42. P. Zitha, G. Chauveteau, A. Zaitoun, SPE conference paper 28955, San Antonio (1995)
43. K. Denys, unpublished results (1999)
44. G. Fleer, M. Cohen Stuart, J. Scheutjens, T. Cosgrove, B. Vincent, "Polymers at Interfaces", Chapman & Hall, London (1993)
45. G. Chauveteau, *J. Rheol.* **26**, 111 (1982)
46. D. James, D. McLaren, *J. Fluid Mech.* **70**, 733 (1975)
47. P. Zitha, C. Botermans, SPE conference paper 36665, Denver (1996)
48. A. Zaitoun, G. Chauveteau, SPE conference paper 39674, Tulsa (1998)
49. G. Chauveteau, K. Sorbie, "Mobility Control by Polymers in Basic Concepts in Oil Recovery Processes", Elsevier (1991)
50. P. Gramain, P. Myard, *Macromolecules* **14**, 180 (1981)
51. J. Lee, G. Fuller, *Macromolecules* **17**, 375 (1984)

CHAPTER 3 - FLOW THROUGH PACKED BEDS OF MONODISPERSE SPHERES

3.1 Introduction

A packed bed is an assembly of contacting particles. Packed beds are applied and studied in various fields like geology, biology, physics and many other engineering disciplines [1]. Scientists, studying transport properties through porous media, often prefer to apply synthetic packed beds instead of natural porous media. Their simpler structure, macroscopic homogeneity and reproducibility permit a better possibility for interpretation. Popular packed beds are those of monodisperse (MD) spheres i.e. spheres having one specific diameter. The permeability and porosity of these beds are known to depend strongly on the specific packing structure, i.e. the spatial arrangement of particles with respect to one another.

This chapter deals with the relation between the permeability and packing structure for ordered and disordered packed beds of MD spheres. It combines data available in the literature in an attempt to give a concise synopsis.

3.2 Structure of ordered packed beds of monodisperse spheres

Contrary to disordered beds, an ordered packed bed is built up according to a certain repeating unit, the unit cell. A first subdivision of these beds can be made upon layer type, i.e. the angle of intersection of the sets of rows¹⁷ in the layer¹⁸. In fact numerous layer types with intermediate intersection angle are possible. However the most common are the limiting cases, the square layers (intersection at 90°) and the simple rhombic layers (intersection at 60°). For each layer type, three more or less stable

¹⁷ A row is an aggregate of uniform spheres arranged with their centres along a straight line and successively spaced at a distance D_s , the sphere diameter.

¹⁸ A layer is a parallel arrangement of rows in the same plane and spaced in such a manner that the spheres in each row are tangent to the corresponding spheres in adjacent parallel rows.

ways of stacking layers upon each other can be distinguished. The six main packing types (I-VI) and their nomenclature are shown in Figure 3.1 [2-4].

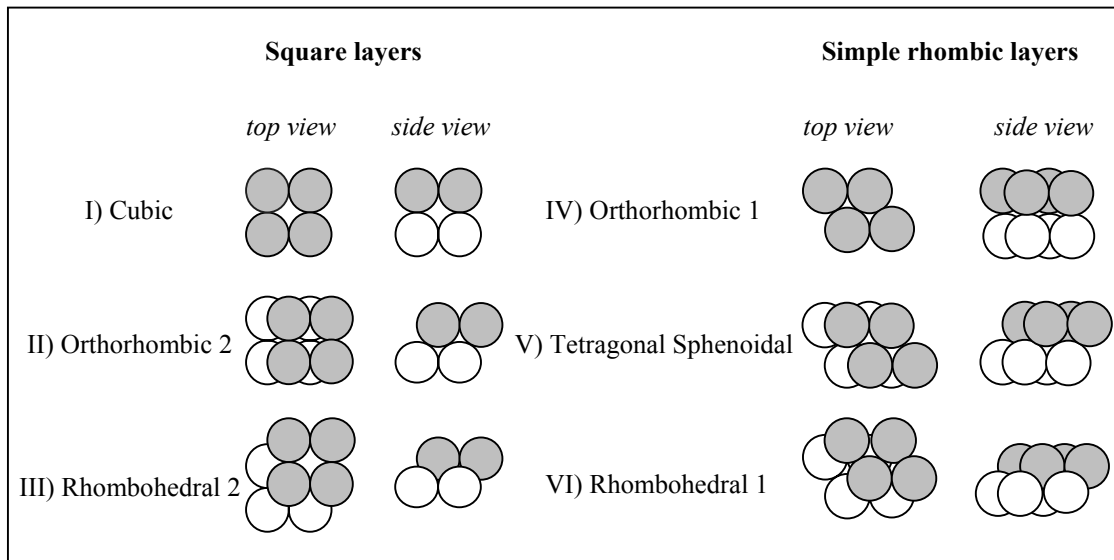


Figure 3.1 The six main packing types

In packing types I and IV the spheres in the second layer are placed vertically over those in the first layer. In packing types II and V, the spheres in the second layer horizontally offset by a distance $\frac{1}{2}D_s$ with respect to the spheres of the first layer in one of the three principal directions. In packing types III and VI, the spheres in the second layer horizontally offset in a direction bisecting the angle between two sets of rows, by a distance $\frac{1}{2}\sqrt{2}D_s$ for packing III and $\frac{1}{3}\sqrt{3}D_s$ for packing VI. Frequently in the literature other names are used than those shown in Figure 3.1. Packing type I is also called simple cubic packing (scp). Packing type III is called face cubic centred (fcc). Packing IV is equivalent to simple hexagonal packing (shp) and packing VI to hexagonal close packing (hcp).

The smallest sample of ordered packing, which gives a complete representation of the manner of packing and the distribution of voids, is called the unit cell. Each unit cell is a parallelepiped with six sides (edge length D_s) containing parts of eight adjacent spheres. Summation of the volume of all sphere parts gives the equivalent of exactly one sphere. The unit cells of the packing types from Figure 3.1 are shown in Figure 3.2. Here it was tacitly assumed that the unit cell should also represent the orientation of the void distribution in the packing. Without this criterion the shape of the unit cell

of packing II, IV and V would be a trigonal prism corresponding in volume to half a sphere.

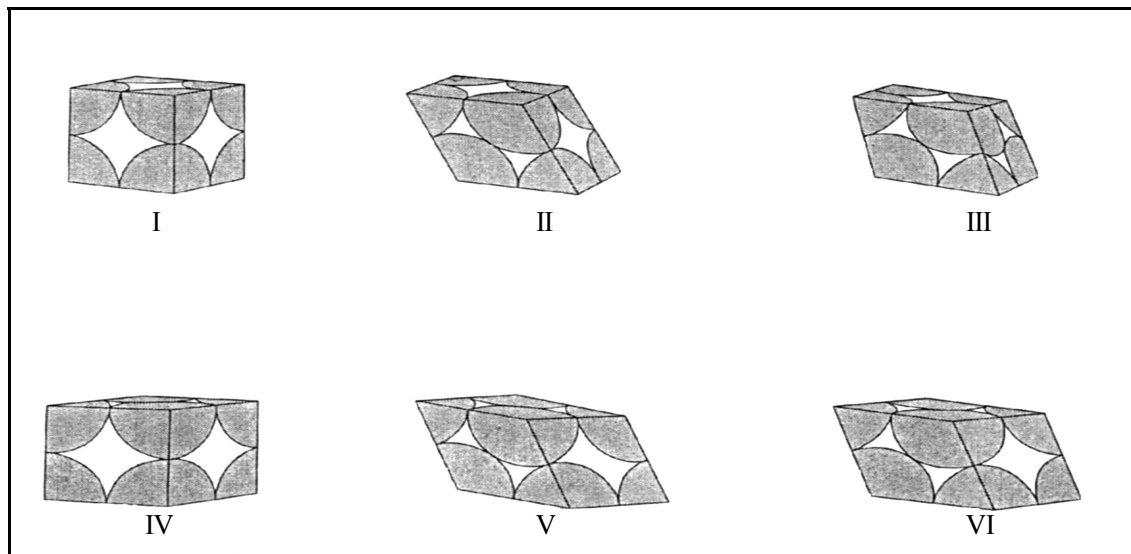


Figure 3.2 The unit cell of the six packing types (from Graton and Fraser [2])

Table 3.1 shows some geometrical parameters of the unit cells. It includes the co-ordination number, i.e. the number of neighbour spheres touched by each sphere, the interfacial angles, i.e. the angles between the sides of the interfacial planes of the unit cell, and the unit cell volume, the unit void volume and the porosity.

The co-ordination number is important with respect to the packing stability. In general, packing, which is jarred, has the tendency to translate into a packing of higher stability. This tendency is counteracted by lateral support, which prevents the toppling of spheres. A sphere acted upon by gravity, which is supported from below, needs at least three points of support to acquire a stable position. Packing types III and VI are fully stable arrangements in this respect. Packing types II and V, which have two support points, are less stable. Packing types I and IV are relatively unstable since they possess only one support point. In general the packing stability increases with increasing co-ordination number, decreasing porosity and decreasing vertical layer spacing. In ordered sphere packings all voids are interconnected and form a network structure. If one considers the unit cells of Figure 3.2 and removes all the spheres, one obtains the unit voids. These are 3-D complex shaped bodies bounded by eight spherical and six plane surfaces [2].

Type of packing	CN	Z [°]	CV (*D _s ³) [m ³]	VV (*D _s ³) [m ³]	φ
I) Cubic	6	{90,90} (3x)	1	1 - 1/6π	0.4764
II) Orthorhombic 2	8	{60,120} & {90,90} (2x)	1/2√3	1/2√3 - 1/6π	0.3954
III) Rhombohedral 2	12	{90,90} & {60,120} (2x)	1/2√2	1/2√2 - 1/6π	0.2595
IV) Orthorhombic 1	8	{60,120} & {90,90} (2x)	1/2√3	1/2√3 - 1/6π	0.3954
V) Tetragonal Sphenoidal	10	{63.4,116.6} & {60,120} (2x)	3/4	3/4 - 1/6π	0.3019
VI) Rhombohedral 1	12	{90,90} & {60,120} (2x)	1/2√2	1/2√2 - 1/6π	0.2595

Table 3.1 Geometrical parameters of the various packing structures. CN = the coordination number, Z = the interfacial angles, CV = the unit cell volume, VV = the unit void volume, φ = the porosity [2-4]

The unit void geometry can be characterised in terms of the area porosity ξ , which is the ratio of the area of the sectioned voids in a cross section to the total sectioned area¹⁹. The area porosity depends on the place in the unit cell. We therefore define a dimensionless place co-ordinate $z_d = z/D_s$ ($0 \leq z_d \leq 1$). z_d is directed in a principal direction, perpendicular to two opposing interfacial planes of the unit cell.

The area porosity ξ of the six unit cells of Figure 3.2 can be described by [5]:

$$\xi = 1 + J_1 (4z_d^2 - 1) \quad \text{for } 0 \leq z_d \leq J_2 - 1/2 \quad (3.1)$$

$$\xi = 1 + J_1 (8z_d^2 - 8z_d J_2 + 4J_2^2 - 2) \quad \text{for } J_2 - 1/2 \leq z_d \leq 1/2 \quad (3.2)$$

¹⁹ The area porosity provides information on the magnitude of the cross-section, but not on the shape

$$\xi = 1 + J_1 (4z_d^2 - 8z_d J_2 + 4J_2^2 - 1) \quad \text{for } \frac{1}{2} \leq z_d \leq J_2 \quad (3.3)$$

where J_1 and J_2 are constants which characterise the pore geometry.

Packing type	Conduit element	NP	J_1	J_2
I	A	3	$\frac{1}{4}\pi$	1
II & IV	B	2	$\frac{1}{4}\pi$	$\frac{1}{2}\sqrt{3}$
	C	1	$\frac{1}{6}\pi\sqrt{3}$	1
V	D	2	$\frac{1}{6}\pi\sqrt{3}$	$\frac{1}{2}\sqrt{3}$
	E	1	$\frac{1}{8}\pi\sqrt{5}$	$\frac{3}{8}\sqrt{5}$
III & VI	F	2	$\frac{1}{6}\pi\sqrt{3}$	$\frac{1}{3}\sqrt{6}$
	G	1	$\frac{1}{4}\pi$	$\frac{1}{2}\sqrt{2}$

Table 3.2 J_1 and J_2 values of the conduit elements present in the packing types (Eqs. 3.1 - 3.3). NP is the number of principal directions containing this conduit element

For most ordered packing types, the area porosity depends on which principal direction is considered. From this perspective it is useful to regard the unit void as a body containing three characteristic pores, the conduit elements, each having a different principal direction. In fact each unit cell from Figure 3.2 contains two different conduit elements since the pore geometry is identical in two principal directions and is different in the other principal direction. Packing type I, however, contains only one type of conduit element. Table 3.2 shows for each packing type the constants J_1 and J_2 of Eqs. 3.1 - 3.3, which describe the area porosity of its conduit elements. Figure 3.3 shows the resulting curves of ξ vs. z_d for all conduit elements.

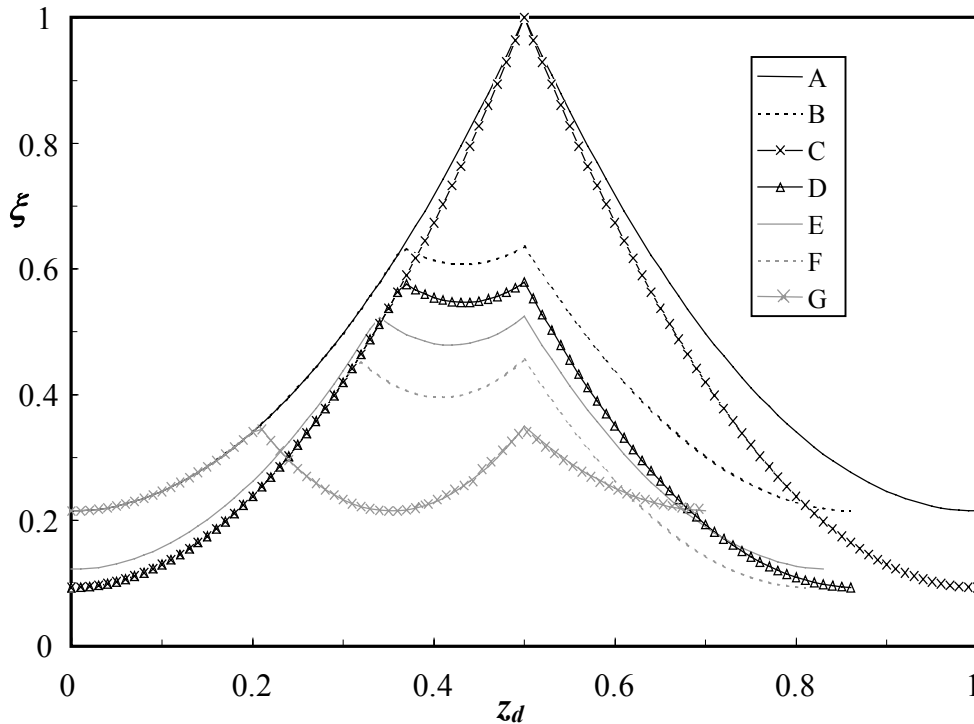


Figure 3.3 The area porosity ξ as a function of z_d for the conduit elements in the different packing types

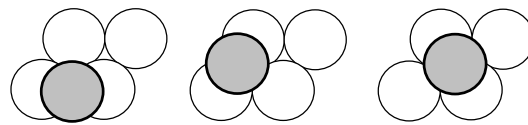


Figure 3.4 The three alternatives in layer stacking for packing V. The grey sphere is the position of one sphere in the layer above [2]

Table 3.2 implies that the conduit elements in packing types II & IV and in packing types III & VI are identical. This would mean that we have to distinguish only four packing types instead of six. However, in packing types II, V and VI layers can be stacked in different ways while still fulfilling the conditions of Table 3.1. It appears that packing types II and VI offer two alternatives in layer stacking, while packing type V offers three. This effect, which is called twinning, is shown schematically in Figure 3.4 for packing V. Twinning does not change the number, size and shape of the voids, nor the porosity. It stiffens the structure and changes the void orientation [2]. Note that twinning does not occur for packing types I, III and IV, since only one manner of stacking the layers is possible.

3.3 Permeability of ordered packed beds of monodisperse spheres

The pore network structure present in these beds can be considered as parallel placed, equally oriented, conduit channels²⁰ connected at regular intervals to the four neighbouring channels. Though during flow there will exist a general flow direction, the connections permit divisions and reunions by hopping over to and from neighbour conduit channels. In general flow along one of the principal directions is preferred. However, if the position of flow inlet and outlet differs markedly from any principal direction, the resulting flow may not necessarily follow these favoured paths. The outcome is a compromise between the tendency to hold the axis of the maximum cross section, resulting in a zigzag path, and the tendency to hold the shortest path, resulting in a straighter, more constricted path. Note that only for conduit elements A and C (Table 3.2) a straight central line represents the direction of easiest flow. For all other conduit elements the central line is curved and fluid elements have to adopt a tortuous flow path [2,5].

The relationship between the flow field in a porous medium and the resulting permeability is not very well understood. Since unit cells contain different conduit elements, ordered packed beds of MD spheres show anisotropy in the permeability. Even the permeability of packing type I, which only contains one type of conduit element, has direction dependency due to the fact that the flow path changes due to the connectivity. As a result of this, a measured permeability is always an effective value resulting from a sorted averaging of permeability's in many directions. The value of any of these permeability's is determined by the flow path, which provides the minimum dissipation. This dissipation is a complex function of parameters like wall friction, internal friction, velocity gradients and tortuosity, all strongly related to the flow path geometry.

Since the fabrication of ordered packed beds of spheres is far more time consuming than that of disordered packed beds, their permeability data in literature are scarce. Franzen [6] has performed the only systematic study on this topic. Although he obtained measurements over a wide range of flow rates, only the permeability

²⁰ A serial placement of conduit elements having the same orientation is called a conduit channel. The same orientation means that the channel can be described by one combination of J_1 and J_2 (Table 3.2).

measurements in the creeping flow regime are considered here. In this range the flow resistance A_p (Eq. 2.7) was always constant and equal to α^* . Note that the permeability of the packed bed $k_p = D_s^2/\alpha^*$. The measured $1/\alpha^*$ values for the different packed beds are shown in Table 3.3. Included are resulting values for the Carman-Kozeny constant A (Eq. 2.16). Table 3.3 shows that the permeability's of the square layer based conduit elements A and B are much larger than those of the rhombic layer based conduit elements. Conduit element G, also based on a square layer, forms an exception. Note that the values of the Carman-Kozeny constant A for conduit elements A, F and G are of the same order of magnitude as the value in disordered packed beds (Table 2.1).

Type of packing	Conduit element	$1/\alpha^*$ (x 10 ⁻⁴)	A
I	A	23.8	166
II & IV	B	16.7	101
	C	2.94	575
V	D	2.33	242
	E	-	-
III & VI	F	1.89	169
	G	2.27	140

Table 3.3 The measured $1/\alpha^*$ values for the different packed beds. Included are the corresponding values for the Carman-Kozeny constant A (Eq. 2.16) [6]

Franzen [6] obtained a good prediction of these permeability results by applying the following empirical expression:

$$k_p = 0.00698 \phi^{1.5} A_c^2 D_s^2 \quad (3.4)$$

where A_c is the dimensionless inflow cross-section²¹. Eq. 3.4 shows again the scaling of the permeability with D_s^2 .

²¹ $A_c = 1$ for square layer based tubes, $A_c = \frac{1}{4}\sqrt{3}$ for rhombic layer based tubes

Concerning the geometry of conduit element G, Franzen noted the following [6]: “While for each type of packing the number of enclosed pore cross-sections is identical to the number of pore openings in the upper sphere layer, this type of packing contains two enclosed pore cross-sections per dimensionless inflow cross-section. Therefore a triangular characteristic inflow-cross section of $A_c = \frac{1}{2}$ (Eq. 3.4) must be applied”²².

Type of packing	Conduit element	$1/\alpha^*$ (x 10 ⁻⁴)	k_p/k_t
I	A	43.5	0.55
II & IV	B	37.7	0.44
	C	5.56	0.53
V	D	5.00	0.47
	E	-	-
III & VI	F	4.55	0.41
	G	25.0	0.09

Table 3.4 The measured values of $1/\alpha^*$ for the tubes and the permeability ratio k_p/k_t between packed beds and tubes [5,6]

In another publication Franzen compared the results for packed beds with flow resistance measurements on six models of equally shaped parallel placed tubes of periodically varying diameter [5]. Each model was fabricated in such a way that the cylindrical cross-section of the tubes equalled exactly the area porosity of the studied conduit element in the corresponding ordered packed bed of spheres²³. Also the periodicity of the tubes and the total open volume were kept equal to those found in the corresponding ordered packed beds. The results are reproduced in Table 3.4.

From Table 3.4 it follows that the square layer based tubes (conduit elements A, B and G) have higher permeability's than the rhombic layer based tubes (conduit elements C, D and F). Besides, the permeability of the packed beds equals about half the value of the permeability of the corresponding tube (Table 3.4). Again conduit

²² Translated from German

²³ According to Eqs. 3.1-3.3 and Table 3.2

element G forms an exception with its small permeability ratio of $k_p/k_t = 0.09$. Logically, the smaller permeability of the packed beds is caused by the different shape of the pores and the pore network topology (tortuosity, connectivity). Franzen [6] proposed the following relation between the permeability of the packing and that of the corresponding tube:

$$\frac{k_p}{k_t} = \frac{d_t \tau_t}{d_p \tau_p} \quad (3.5)$$

where d_p and d_t are shape factors of respectively packed bed and tube and τ_p and τ_t are their tortuosity factors

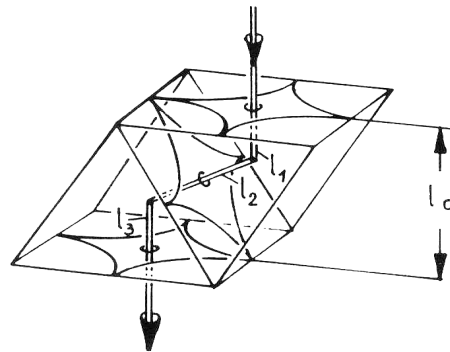


Figure 3.5 The procedure to estimate the tortuosity factor τ_p [6]

Type of packing	Conduit element	τ_p	d_p
I	A	1	1.8
II & IV	B	1.3	1.7
	C	1	1.9
V	D	1.3	1.6
III & VI	F	1.5	1.6
	G	1.7	6.4

Table 3.5 The values for the tortuosity factor τ_p and the shape factor d_p (Eq. 3.5) for all conduit elements.

For each conduit element the tortuosity factor τ_p can be estimated by summation of the flow path length over the central line and subsequent division by the distance between the sphere layers (l_o) [6] (Figure 3.5). The tortuosity factor and shape factor of the tubes, τ_t and d_t , were assumed to be equal to 1. Table 3.5 contains the values of τ_p and d_p for all conduit elements. The latter is obtained by using the measured values from Tables 3.3 and 3.4 in combination with Eq. 3.5. Except for the unexplainable large d_p value of conduit element G, Eq. 3.5 gives reasonable predictions when using $d_p \approx 1.7$.

3.4 Disordered packed beds of monodisperse spheres

In disordered packed beds the packing structure cannot be described by one or more unit cells (Table 3.2). Another characteristic is that the area porosity of the porous medium is usually more or less independent on the place of the cross-section or the direction considered [7]. In fact the structure can only be characterised by statistics i.e. probability distributions [7-9]. Experiments have shown that the porosity of disordered packed beds of MD spheres varies in the range $0.375 < \phi < 0.391$ [4].

In practice disordered packed beds develop naturally when spheres are poured into a container, explaining their popularity as model cores. It is therefore important to notify how these packed beds develop and which parameters determine their ultimate structure. When dropping MD spheres on a horizontal flat starting surface, the tendency to form a first layer with a simple rhombic pattern is large [2]. However the second layer, which has to start on a surface of regularly spaced hoppers and hummocks, contains two times as many hoppers as available spheres. Besides, the interval between two neighbour hoppers is too small to contain two spheres. The continuation of the rhombic pattern in the second layer now depends on whether each sphere settles in a 'right' or in a 'wrong' hopper. If the spheres do not chose every alternate hopper, the regularity of the simple rhombic layer will be broken. If this occurs disorder will aggravate in the next layers and a pyramidal colony of packing VI develops (Table 3.1) with a share of haphazard packing increasing upwards. Since the hoppers are identical in shape and size, in principal the chance should be even to choose a 'right' or a 'wrong' one. Graton [2] discusses reasons why the chance of

choosing a ‘right’ one is much better though. However, when spheres are poured on a flat surface, they are often isolated initially. This results in different nuclei for colony growth of the simple rhombic arrangement. While pouring, growing colonies start to interfere with each other resulting in an interruption of the ordered arrangement and the development of regions with a different, frequently haphazard arrangement. Within these regions the arrangement in different zones may vary from extremely disordered to fully ordered colonies according to other packing types of Table 3.1. In general the colony size of packing types with a low stability is small²⁴. Packing type III has a very strong tendency to continue growth in the vertical direction, because of its large stability and the fact that each hopper is a ‘right’ one. However the chance of development of packing type III is much smaller than that of packing type VI, in particular when the starting surface is non-planar. It can thus be concluded that the packing structure of disordered packed beds usually consists of 3-D ordered colonies dispersed in a matrix of haphazard arrangement which consistence cannot be forecast easily. Colonies other than packing VI exist, but they are relatively small in size. Packing type III dominates among these [2]. The ratio of occurrence between ordered colonies of packing type VI and haphazard zones depends on many parameters like the inclination of the starting surface, the pouring rate, the manner and direction of assembly, the elasticity of the spheres and the shape and contacting angle of present container walls. From this it can be understood that the large variation in packing structure explains the large range in permeability values measured for disordered packed beds of MD spheres (Table 2.1).

²⁴ In general the stability of a packing increases with decreasing porosity and vertical layer spacing and increasing co-ordination number and number of vertical supporting points. Consequently the stability of the packing types of Table 3.1 increases in the following order: I, IV, II, V, VI and III.

3.5 Summary

1. The permeability of ordered packed beds depends strongly on the packing structure since this determines the pore geometry i.e. the area porosity and the shape of the pores. Although the porosity is also dependent on the packing structure, this parameter is of smaller importance for the resulting permeability.
2. A measured permeability is always an effective value resulting from a sorted averaging of permeability's in many directions. The value of any of these permeability's is determined by the flow path, which provides the minimum dissipation. This dissipation is a complex function of parameters like wall- and internal friction, velocity gradients and tortuosity, all strongly related to the flow path geometry.
3. Due to different area porosity characteristics, ordered packed beds of MD spheres show a larger permeability anisotropy than disordered beds. Also the permeability of a type I ordered packed bed, which only contains one type of conduit element (Table 3.2), has direction dependency due to the fact that the flow path changes as a result of the pore connectivity.
4. Generally, for ordered packed beds of MD spheres, the permeability of the square layer based conduit elements is much larger than that of the rhombic layer based conduit elements (Table 3.3). Franzen [5,6] found that the permeability of a certain packed bed equals about half the value of the permeability of the equivalent tube model (Table 3.4). The smaller permeability of the ordered packed beds is caused by the different pore shape, connectivity and tortuosity.
5. The packing structure of disordered packed beds of MD spheres usually consists of 3-D ordered colonies, i.e. usually packing type VI, dispersed in a matrix of haphazard arrangement. Their ratio of occurrence is strongly dependent on the conditions and manner of bed fabrication. As a result of this, the permeability values of packed beds show a large spreading. The porosity values however vary only slightly.

References (Chapter 3)

1. F. Dullien, "Porous Media, Fluid Transport and Pore Structure", Academic Press Inc. , San Diego (1992)
2. L. Gratton, H. Fraser, *J. Geol.* **43**, 785 (1935)
3. J. Hrubisek, *Kolloid Beihefte* **53**, 385 (1941)
4. D. Haughey and G. Beveridge, *Can. J. Of Chem. Eng.* **47**, 130 (1969)
5. P. Franzen, *Rheol. Acta* **18**, 392 (1979)
6. P. Franzen, *Rheol. Acta* **18**, 518 (1979)
7. S. Debbas, H. Rumpf, *Chem. Eng. Sci* **21**, 583 (1966)
8. G. Mason, *J. of Colloid Interface Sci.* **35**, 279 (1971)
9. M. Yanuka, F. Dullien, D. Elrick, *J. of Colloid Interface Sci.* **112**, 24 (1986)

CHAPTER 4 - ELONGATIONAL DISSIPATION IN POROUS MEDIA; CORRUGATED CAPILLARY BUNDLE MODELS

4.1 Introduction

It has been known since long that the pressure losses for laminar flow through a cylindrical tube with a varying diameter are exceeding the predictions by the Hagen-Poiseuille law, based upon the assumption of a simple shear flow [1-3]. This excess dissipation, caused by elongational deformation gradients, is often overlooked in literature on porous medium flow. The neglect has been favoured by the fact that for laminar flow of a Newtonian fluid, both shear- and elongational pressure drop terms are proportional to the flow rate and are usually measured as a single pressure drop during coreflow experiments. Nevertheless its relevance is clear regarding the highly irregular pore geometries present and their large influence on the resulting permeability (Chapter 3) [4,5]. For example the strong sudden increase of the flow resistance for laminar flow of dilute polymer solutions through high permeability porous media above a critical flow rate (see Figure 2.5) is a clear proof of the importance of elongational deformation effects. More background on this phenomenon is given in Appendix A.

Notwithstanding the fact that usually shear is the main dissipation mechanism, it is conceptually incorrect from this perspective to translate a permeability measurement on a porous medium into an average pore diameter by using the straight tube capillary bundle model from Section 2.3. A capillary model of tubes with a varying cross-section, a corrugated capillary bundle model, is a much better candidate when trying to approach porous medium flow conditions.

This chapter is concerned with the problem of predicting the pressure drop for laminar flow of Newtonian- and more complex fluids through a cylindrically shaped tube with diameter variations in the axial direction. Figure 4.1 shows a typical example, the sinusoidal tube. The analytical methods applied here make use of the Lubrication Approximation Method (LAM), i.e. a process of locally adapting the results for a

uniform geometry to a slowly varying geometry. Bird et al. [2] state: “LAM is a very powerful technique for estimating the flow rate vs. pressure drop relation in many complex flows”. The chapter is organised as follows. In Section 4.2 the mathematical formulation of the method is given in terms of cylindrical co-ordinates. Section 4.3 discusses the resulting pressure drop predictions for the following geometries, the widening tube and the sinusoidal tube. In Section 4.4 the pressure drop predictions are converted in porous media models, i.e. two capillary bundle models which do account for elongational dissipation. In Sections 4.5 and 4.6 the results are discussed and conclusions are drawn.

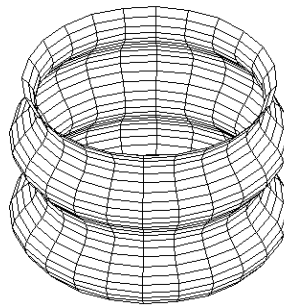


Figure 4.1 Schematic representation of the sinusoidal tube

4.2 Mathematical formulation

4.2.1 Basic equations

Let us consider a cylindrically shaped tube with a varying cross-section in the axial direction z (radius $R = R(z)$). Since this tube has rotation symmetry with respect to the z -axis, the flow problem is reduced to two dimensions. By using cylindrical co-ordinates and assuming incompressibility, the equation of continuity reads:

$$\frac{v_r}{r} + \frac{\partial v_r}{\partial r} + \frac{\partial v_z}{\partial z} = 0 \quad (4.1)$$

where r is the radial place co-ordinate, z is the axial place co-ordinate and v_r and v_z are the velocity components in these directions. The equations of motion for steady-state flow can be expressed as:

$$\rho_f \left(v_r \frac{\partial v_r}{\partial r} + v_z \frac{\partial v_r}{\partial z} \right) = - \left[\frac{1}{r} \frac{\partial (r T_{rr})}{\partial r} + \frac{\partial T_{zr}}{\partial z} \right] - \frac{\partial P}{\partial r} \quad (4.2)$$

$$\rho_f \left(v_z \frac{\partial v_z}{\partial z} + v_r \frac{\partial v_z}{\partial r} \right) = - \left[\frac{1}{r} \frac{\partial (r T_{rz})}{\partial r} + \frac{\partial T_{zz}}{\partial z} \right] - \frac{\partial P}{\partial z} \quad (4.3)$$

where ρ_f is the fluid density, $\frac{\partial P}{\partial r}$ and $\frac{\partial P}{\partial z}$ are components of the gradient of the fluid pressure and T_{zr} , T_{zz} etc. are components of the stress tensor \underline{T} . This tensor describes the (external) contact forces acting on a volume element via its surface, which are functions of the fluid flow behaviour. The imposed deformation rates in a flow field [1] can be described by the rate of deformation tensor \underline{D} :

$$\underline{D} = \begin{bmatrix} \frac{\partial v_z}{\partial z} & \frac{1}{2} \left(\frac{\partial v_z}{\partial r} + \frac{\partial v_r}{\partial z} \right) \\ \frac{1}{2} \left(\frac{\partial v_z}{\partial r} + \frac{\partial v_r}{\partial z} \right) & \frac{\partial v_r}{\partial r} \end{bmatrix} = \begin{bmatrix} \dot{\varepsilon} & \frac{1}{2}(\dot{\gamma} + \dot{\gamma}_r) \\ \frac{1}{2}(\dot{\gamma} + \dot{\gamma}_r) & \dot{\varepsilon}_r \end{bmatrix} \quad (4.4)$$

where $\dot{\gamma}$ is the shear rate, $\dot{\varepsilon}$ is the elongational rate, $\dot{\gamma}_r$ is the radial shear rate and $\dot{\varepsilon}_r$ is the radial elongational rate. Because LAM is restricted to geometries with a slowly changing diameter, the influence of $\dot{\gamma}_r$ compared to $\dot{\gamma}$ is small and will be neglected in the following²⁵. The following form of the stress tensor [1] has been assumed²⁶:

$$\underline{T} = \begin{bmatrix} T_{zz} & T_{zr} \\ T_{rz} & T_{rr} \end{bmatrix} = \begin{bmatrix} \sigma_{elo} + N_1 + N_2 & \sigma_{sh} \\ \sigma_{sh} & N_2 \end{bmatrix} \approx \begin{bmatrix} \eta_{elo} \dot{\varepsilon} + \psi_1 \dot{\gamma}^2 & \eta_{sh} \dot{\gamma} \\ \eta_{sh} \dot{\gamma} & 0 \end{bmatrix} \quad (4.5)$$

where $\sigma_{elo} = \eta_{elo} \dot{\varepsilon}$ is the elongational stress, η_{elo} is the elongational viscosity, $\sigma_{sh} = \eta_{sh} \dot{\gamma}$ is the shear stress, η_{sh} is the shear viscosity, $N_1 = \psi_1 \dot{\gamma}^2$ is the first normal stress difference, ψ_1 is the first normal stress coefficient and N_2 is the second normal stress difference. The stress tensor of Eq. 4.5 results when assuming additivity of stresses

²⁵ Besides, the relation between the viscosity and the radial shear rate is unknown for polymeric fluids.

²⁶ N_1 , N_2 and ψ_1 are only relevant for elastic fluids. Since for a polymeric liquid the value of N_2 is usually much smaller than 10% of N_1 , the N_2 term has been neglected in the right term of Eq. 4.5.

due to shear- and elongational flow. The tensor is exact in the two extremes of simple shear flow and uniaxial extensional flow and was described in literature before [6]. Also there is numerical evidence in literature to suggest that such additivity may indeed be approximately valid [7,8]. Note that this stress tensor expresses time independent fluid flow behaviour and that elasticity is associated with normal stress differences resulting from shear.

Generally for a polymeric liquid η_{elo} , η_{sh} and ψ_I are functions of the deformation rates, while for a Newtonian fluid η_{elo} and η_{sh} are constants ($\psi_I = 0$) [2]. By making use of the mechanical energy balance for steady incompressible flow [1,3] the pressure drop ΔP_{tot} during laminar flow through such a tube (length L) can be calculated by summation of the dissipation over the volume:

$$\Delta P_{tot} = \frac{I}{Q} \left(\int_V (\underline{T} : \underline{D}) dV - \int_S \underline{T} \cdot \underline{v} \cdot \underline{n} dS \right) = \frac{I}{Q} \left(\int_{z=0}^L \int_{r=0}^R (\underline{T} : \underline{D}) 2\pi r dr dz - \int_S \underline{T} \cdot \underline{v} \cdot \underline{n} dS \right) \quad (4.6)$$

where $\underline{T} : \underline{D}$ denotes the double contraction of the stress tensor and the rate of deformation tensor. The negative term in Eq. 4.6 is the surface term, which describes the difference in the surface forces at $z = 0$ and $z = L$. This term is only relevant for elastic liquids. Note that \underline{n} is the outwardly directed normal unit vector on dS .

4.2.2 Phenomenological relations

The assumption is made that the fluid flow behaviour can be described by the following rheological equations:

$$\eta_{elo} = g |\dot{\epsilon}|^{h-1} \quad (4.7)$$

$$\eta_{sh} = m |\dot{\gamma}|^{n-1} \quad (4.8)$$

$$\psi_I = p |\dot{\gamma}|^{q-1} \quad (4.9)$$

Eqs. 4.7 - 4.9 are phenomenological laws, which are frequently used to describe the flow properties of concentrated polymer solutions and polymer melts [2]. By variation of their parameters a wide scope of rheological properties can be described. For a Newtonian fluid holds: $h = 1$, $n = 1$ and $p = 0$. Shear-thinning and strain-thinning flow behaviour can be described by $n < 1$ and $h < 1$ respectively. Strain-thickening phenomena can be expressed by $h > 1$. Elasticity can be introduced by assigning finite values to p and q . By making use of Eqs. 4.7 – 4.9 one obtains for the double contraction of $\underline{\underline{T}}$ and $\underline{\underline{D}}$:

$$\underline{\underline{T}} : \underline{\underline{D}} = \sum_{i,j} T_{ij} D_{ji} = g|\dot{\epsilon}|^{h+1} + m|\dot{\gamma}|^{n+1} + p|\dot{\gamma}|^{q+1} \dot{\epsilon} \quad (4.10)$$

The first term at the right hand side of Eq. 4.10 can be associated with elongational dissipation, the second with shear dissipation and the third with elastic storage or release.

4.2.3 Lubrication approximation

For geometries with slowly varying diameter the flow field can be approximated by the Lubrication Approximation Method (LAM). This method is based on locally adapting the result for a uniform geometry to a slowly varying geometry [2,3]. This yields for flow of a power law fluid with non-slip conditions at $r = R$ for the velocity in the z -direction:

$$v_z = \frac{3n+1}{n+1} \frac{Q}{\pi R^2} \left(1 - \beta^{1+\frac{1}{n}} \right) \quad (4.11)$$

where Q is the flow rate and $\beta = \frac{r}{R}$

By making use of the continuity equation (Eq. 4.1), one obtains:

$$v_r = \beta v_z R_z \quad (4.12)$$

where $R_z = \frac{dR}{dz}$

Expressions of the main deformation rates, components of the rate of deformation tensor (Eq. 4.4), can be derived by differentiating Eq. 4.11 towards z and r respectively:

$$\dot{\epsilon} = \frac{3n+1}{n+1} \frac{Q}{\pi R^3} \left(\frac{3n+1}{n} \beta^{1+\frac{1}{n}} - 2 \right) R_z \quad (4.13)$$

$$\dot{\gamma} = -\frac{3n+1}{n} \frac{Q}{\pi R^3} \beta^{\frac{1}{n}} \quad (4.14)$$

4.2.4 Example fluids

All pressure drop predictions in this chapter are demonstrated by considering the flow of three example fluids; a Newtonian fluid, a Power Law fluid and a Boger fluid. The parameters describing their rheological behaviour are given in Table 4.1.

Nr	Fluid type	g [Pa s ^h]	h	m [Pa s ⁿ]	n	p [Pa s ^{q+1}]	q
I	Newtonian	30	1	10	1	0	-
II	Power Law	30	0.8	10	0.8	0	-
III	Boger	30	1.3	10	1	1	1

Table 4.1 The rheological parameters of the example fluids

Here we define the parameter f_e :

$$f_e = \frac{g}{m} \quad (4.15)$$

f_e is a fluid property, which is a function of the type of elongational flow field. For example in a steady biaxial elongational flow $f_e = 6$ while in a simple uniaxial elongational flow $f_e = 3$ [1]. Because the elongational deformation in a cylindrical tube of varying cross-section resembles most simple uniaxial elongation/ compression flow, we applied $f_e = 3$ for the example fluids.

Figure 4.2 shows the resulting viscosity vs. deformation rate relations for the three example fluids.

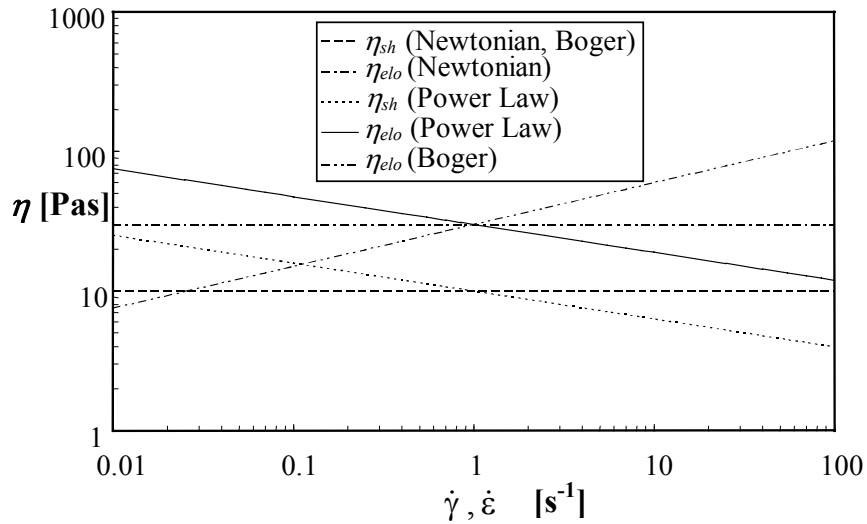


Figure 4.2 The shear viscosity η_{sh} and elongational viscosity η_{elo} of the example fluids as a function of the deformation gradients

4.3 Pressure drop predictions

4.3.1 The widening tube

The geometry of a widening tube which radius increases linearly ($R = R_{min}$ at $z = 0$ and $R = R_{max}$ at $z = L$) can be described by:

$$R = R_{min} + z \tan\Theta \quad (\text{for } 0 < z < L) \quad (4.16)$$

where Θ is the widening angle for which holds $\tan\Theta = \frac{R_{max} - R_{min}}{L}$.

For this geometry LAM can be applied²⁷ provided that:

$$W = \frac{R_{min}}{L} \left[1 - \frac{R_{min}^2}{R_{max}^2} \right] = \alpha (1 + \alpha) \tan \Theta \ll 1 \quad (4.17)$$

and:

$$\frac{\rho_f Q W}{\pi \eta_{sh} R_{min}} \ll 1 \quad (4.18)$$

where $\alpha = \frac{R_{min}}{R_{max}}$

Note that α and $\tan \Theta$ are mutually dependent, meaning that a change of one while keeping the other constant is equivalent to a change in the tube length (Figure 4.3).

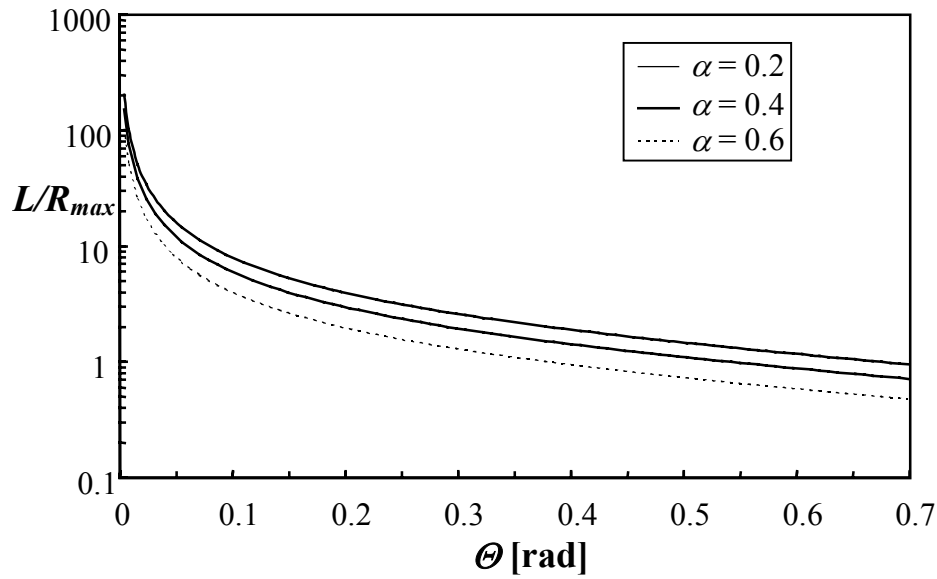


Figure 4.3 The ratio L/R_{max} vs. Θ for different values of α

Figure 4.4 shows values for α as a function of Θ in order to satisfy $W = 0.1$ and $W = 0.3$ (Eq. 4.17). This figure shows decreasing α values for larger angles, indicating that the length of the tube must increase when increasing Θ in order for LAM to be applicable. Of course, also the flow rate may not be too large (Eq. 4.18).

²⁷ Eqs. 4.17 and 4.18 can be obtained from an order of magnitude analysis of the different Navier-Stokes terms [1].

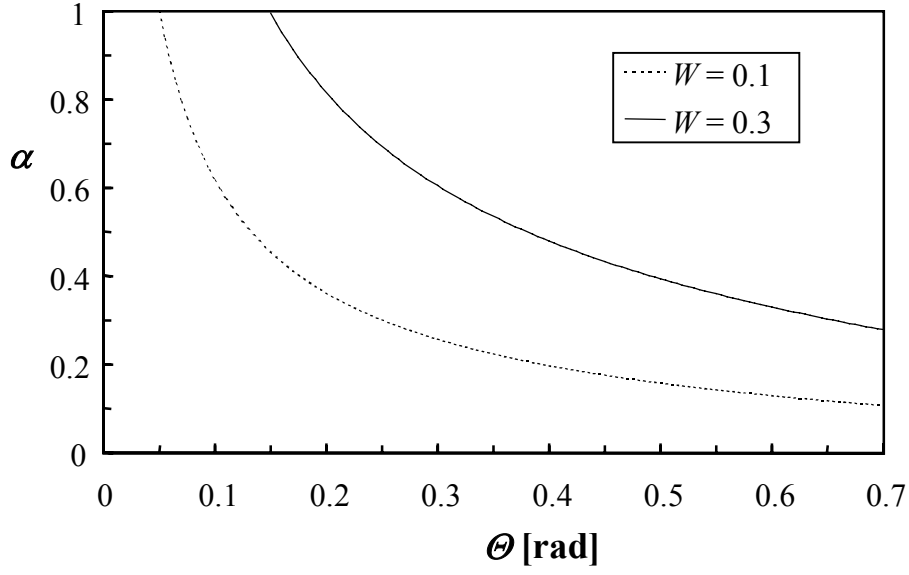


Figure 4.4 Values for α as a function of Θ in order to satisfy $W = 0.1$ and $W = 0.3$ (Eq. 4.17)

By combining Eqs. 4.6 and 4.10 we find that the total pressure drop ΔP_{tot} consists of four different terms: ΔP_{elo} , ΔP_{sh} , ΔP_{ela} and ΔP_{sur} . Carrying out the integration of Eq. 4.6 over the volume yields:

Elongational term:

$$\Delta P_{elo} = \frac{4g\kappa^2 \left(1 - \kappa^{1+\frac{1}{n}}\right) (\tan \Theta)^h}{3h} \left(\frac{3n+1}{n+1}\right)^{h+1} \left(\frac{Q}{\pi R_{min}^3}\right)^h (1 - \alpha^{3h}) \quad (4.19)$$

where $\kappa = \frac{n+1}{n} \sqrt{\frac{2n}{3n+1}}$

Shear term:

$$\Delta P_{sh} = \frac{2m}{3n \tan \Theta} \left(\frac{3n+1}{n}\right)^n \left(\frac{Q}{\pi R_{min}^3}\right)^n (1 - \alpha^{3n}) \quad (4.20)$$

Elasticity term:

$$\Delta P_{ela} = \frac{2pn}{3(3n+q+2)(2n+q+1)} \left(\frac{3n+1}{n} \right)^{q+2} \left(\frac{Q}{\pi R_{min}^3} \right)^{q+1} (1 - \alpha^{3q+3}) \quad (4.21)$$

Surface term:

$$\Delta P_{sur} = -3n\Delta P_{ela} \quad (4.22)$$

From Eqs. 4.19 - 4.22 it follows that the elongational term is a function of the parameters g , h and n , the shear term is a function of m and n , while the elastic terms are functions of p , q and n .

If we consider the analogue problem of flow through a linear converging tube (same R_{max} , R_{min} and L), it follows that all terms remain the same except for the elastic terms (Eqs. 4.21 and 4.22), which only change in sign. In the remainder of Section 4.3.1 we will consider pressure drop predictions for flow of the example fluids through a linear widening tube ($R_{min} = 0.02$ m, $L = 0.20$ m) at a flow rate $Q = 1 \times 10^{-4}$ m³/s. Note that at this rate the criteria (Eqs. 4.17 and 4.18) are met for all angles considered.

I. The Newtonian fluid

The expression for ΔP_{sh} of the Newtonian fluid (Eq. 4.20 with $n = 1$) has been derived earlier by Bird et al. [2]. Combining Eqs. 4.19 and 4.20 ($h = 1$, $n = 1$, $p = 0$) yields for the total pressure drop:

$$\Delta P_{tot} = \left(\frac{4g \tan \Theta}{3} + \frac{8m}{3 \tan \Theta} \right) \frac{Q}{\pi R_{min}^3} (1 - \alpha^3) \quad (4.23)$$

Figure 4.5a shows the influence of the widening angle Θ on the pressure drop terms for flow of the Newtonian fluid through the widening tube. It shows that ΔP_{sh} decreases strongly when increasing Θ due to the fact that the mean tube radius augments. The elongational pressure drop ΔP_{elo} increases progressively as a result of

the increasing (negative) elongational gradients. The grey lines represent the contribution of the shear- and elongational pressure drop to the total pressure drop. Note that at $\Theta = 0.70$ rad ($W \approx 0.1$) the contribution of ΔP_{elo} to ΔP_{tot} exceeds 50%.

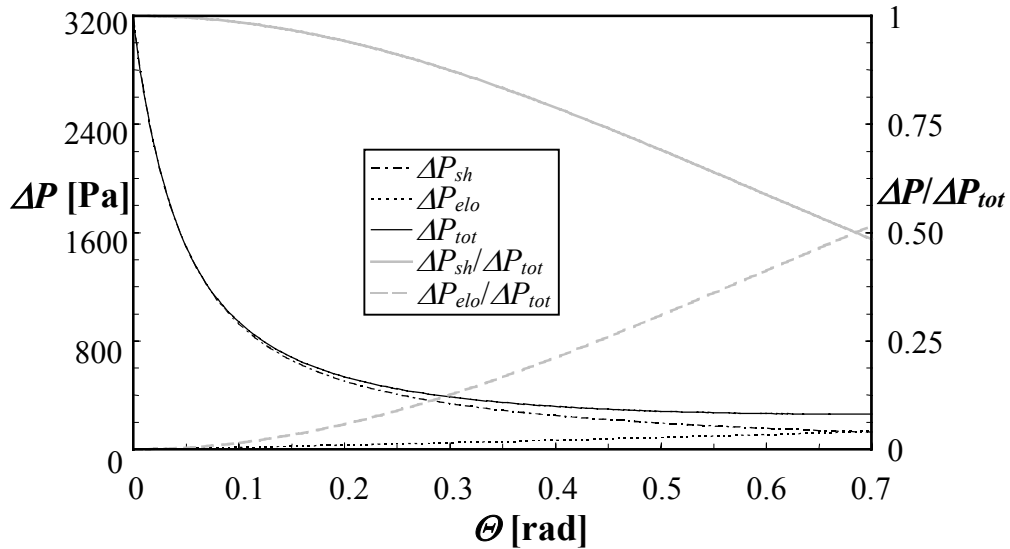


Figure 4.5a The pressure drop terms for flow of the Newtonian fluid through the widening tube as a function of Θ

II. The Power Law fluid

Because of the thinning character (Figure 4.5b) both pressure drop terms are smaller than for the Newtonian fluid. However, the trends found are consistent with this fluid.

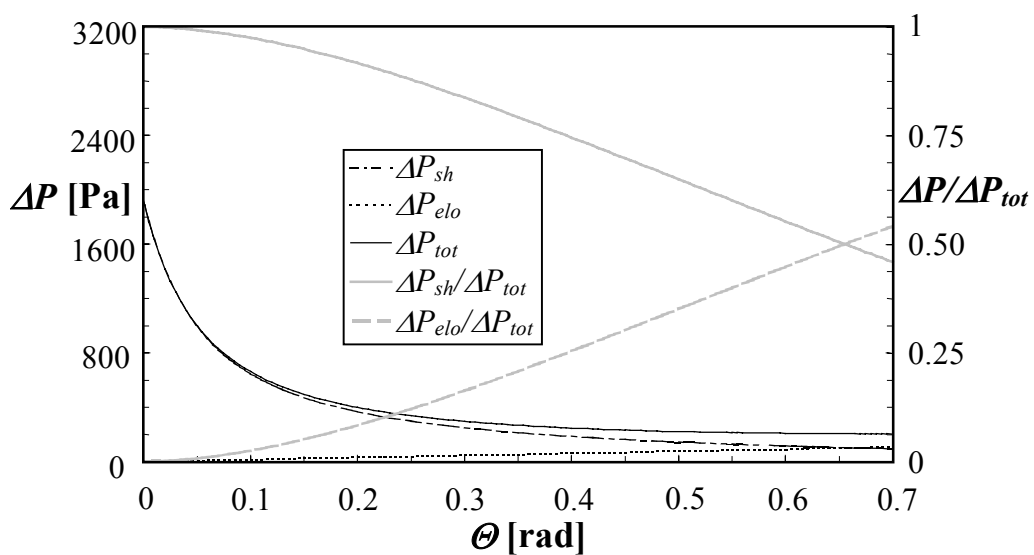


Figure 4.5b The pressure drop terms for flow of the Power Law fluid through the widening tube as a function of Θ

III. The Boger Fluid

Due to the strain-thickening character of this fluid (Figure 4.5c) ΔP_{elo} is larger than for the Newtonian fluid. However the sum of the elastic components ($\Delta P_{elast} = \Delta P_{ela} + \Delta P_{sur}$) gives a negative contribution to ΔP_{tot} . Therefore, in this case, the strain-thickening behaviour does not cause a significant increase in ΔP_{tot} at large Θ values.

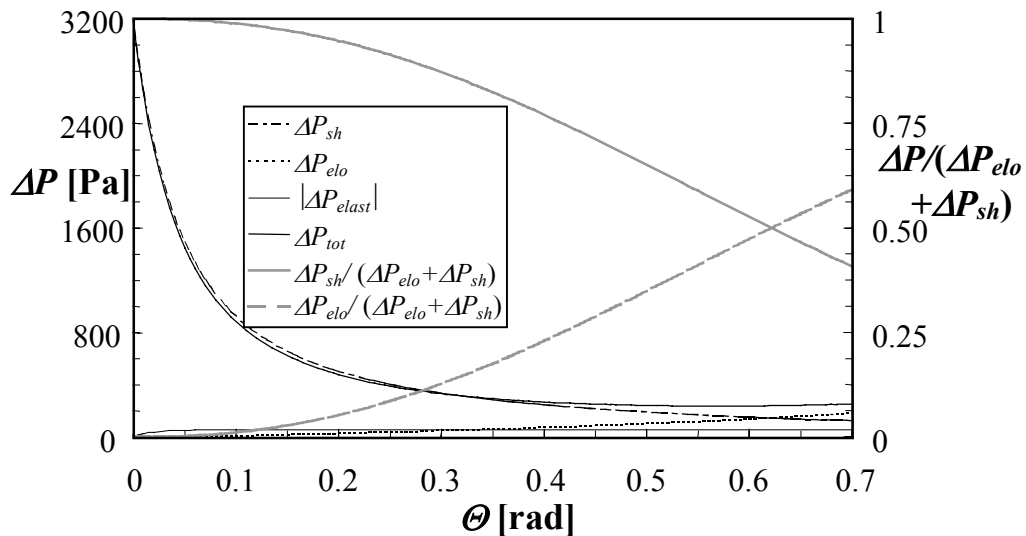


Figure 4.5c The pressure drop terms for flow of the Boger fluid through the widening tube as a function of Θ

4.3.2 The sinusoidal tube

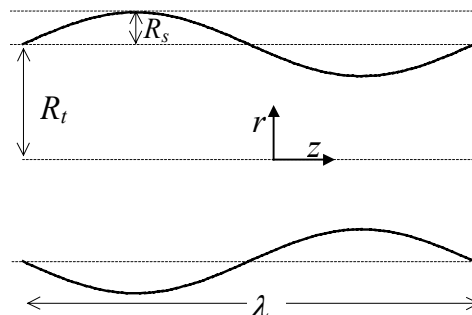


Figure 4.6 The sinusoidal tube

The geometry of a sinusoidal tube (Figure 4.6) can be expressed as:

$$R = R_t \left(1 + a \sin \left(\frac{2\pi z}{\lambda} \right) \right) \quad (4.24)$$

where R_t is the average tube radius, a ($= R_s/R_t$) is the normalised amplitude, R_s is the amplitude of the distortion and λ is the wavelength.

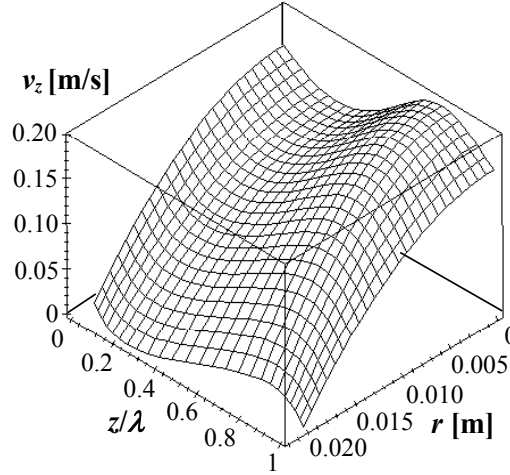


Figure 4.7 The v_z profile for flow of a Newtonian fluid through the sinusoidal tube

Figure 4.7 shows the v_z profile (Eqs. 4.11 and 4.24) for flow of a Newtonian fluid with $Q = 1 \times 10^{-4} \text{ m}^3/\text{s}$ through a sinusoidal tube ($R_t = 0.02 \text{ m}$, $a = 0.10$). The velocity profile is parabolic at constant z and yields the maximum velocity in the centre of the tube at the smallest tube diameter ($z/\lambda = 3/4$). By using an order of magnitude analysis of the Navier-Stokes terms [1,2] we find for the criteria under which LAM holds:

$$W = \frac{8a}{b(1+a)^2(1-a)^2} \ll 1 \quad (4.25)$$

and

$$\frac{\rho_f Q W}{\pi \eta_{sh} R_t} \ll 1 \quad (4.26)$$

where $b = \frac{\lambda}{R_t}$

As expected, the approximation becomes better, i.e. W decreases, when a decreases or b increases i.e. when approaching the straight tube geometry. Figure 4.8 shows the sinusoidal tube geometries, expressed by combinations of a and b , which satisfy $W = 0.1$ and $W = 0.3$ (Eq. 4.25).

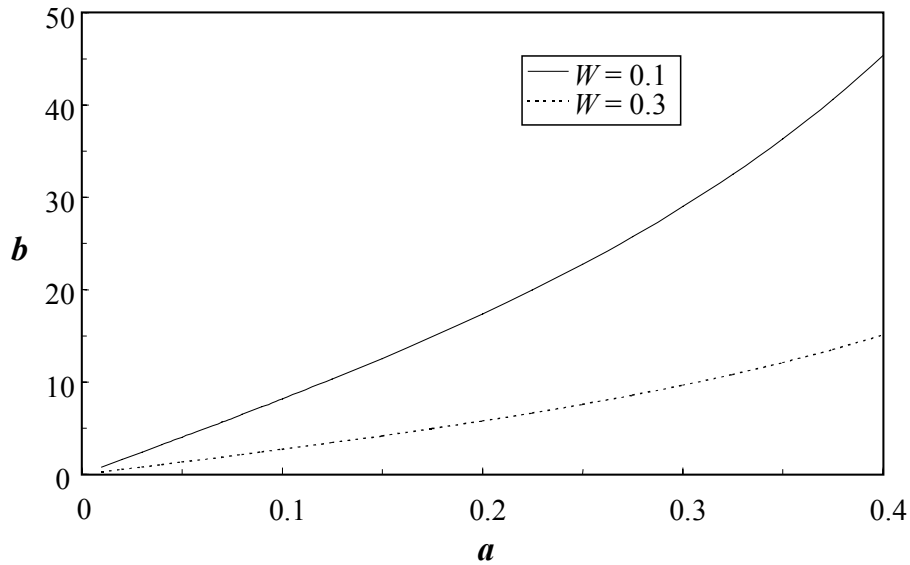


Figure 4.8 Sinusoidal tube geometries which satisfy $W = 0.1$ and $W = 0.3$ (Eq. 4.25)

Combining Eqs. 4.6 - 4.14 and 4.24 results in an expression for the total pressure drop ΔP_{tot} during flow through a sinusoidal tube of total length λ . Elastic contributions cancel out because the energy needed for elastic deformation in a contraction is released when flowing through a decontraction. So ΔP_{tot} only consists of two terms:

Elongational term:

$$\Delta P_{elo} = 4g \left(\kappa^2 - \kappa^{\frac{3n+1}{n}} \right) \left(\frac{2\pi a R_t}{\lambda} \right)^{h+1} \left(\frac{3n+1}{n+1} \right)^{h+1} \left(\frac{Q}{\pi R_t^3} \right)^h \frac{I_a}{R_t} \quad (4.27)$$

where $\kappa = \frac{n+1}{n} \sqrt{\frac{2n}{3n+1}}$

Shear term:

$$\Delta P_{sh} = 2m \left(\frac{3n+1}{n} \right)^n \left(\frac{Q}{\pi R_t^3} \right)^n \frac{I_b}{R_t} \quad (4.28)$$

where I_a and I_b are the following integrals:

$$I_a = \int_{z=0}^{\lambda} \frac{|\cos\left(\frac{2\pi z}{\lambda}\right)|^{h+1}}{\left(1 + a \sin\left(\frac{2\pi z}{\lambda}\right)\right)^{3h+1}} dz \quad (4.29)$$

$$I_b = \int_{z=0}^{\lambda} \frac{1}{\left(1 + a \sin\left(\frac{2\pi z}{\lambda}\right)\right)^{3n+1}} dz \quad (4.30)$$

Eq. 4.27 shows that ΔP_{elo} cancels out when the normalised amplitude a approaches zero, i.e. when going to the limit of the cylindrical tube geometry. In the remainder of Section 4.3.2 we will consider pressure drop predictions for flow of the example fluids through a sinusoidal tube ($\lambda = 0.12$ m, $R_t = 0.02$ m, total length $L = 0.48$ m, $b = 6$) at a flow rate $Q = 1 \times 10^{-4}$ m³/s.

1. The Newtonian fluid

For the Newtonian fluid ($h = 1$, $n = 1$, $p = 0$) I_a and I_b can be solved analytically by using residue method in function analysis [9]. This gives:

$$I_a = \lambda \frac{\frac{1}{2}}{\left(1 - a^2\right)^{\frac{5}{2}}} \quad (4.31)$$

$$I_b = \lambda \frac{1 + \frac{3}{2}a^2}{\left(1 - a^2\right)^{\frac{7}{2}}} \quad (4.32)$$

The expression for ΔP_{sh} of the Newtonian fluid, when combining Eqs. 4.28 and 4.32, has been obtained earlier by Deiber et al. [10]. Bird et al. [2] derived $I_b = \lambda(1+5a^2)$ which is a first order Taylor expansion of the solution given in Eq. 4.32. The total pressure drop for the Newtonian fluid can now be expressed by:

$$\Delta P_{tot} = Q \left(\frac{16\pi g a^2 I_a}{R_t^2 \lambda^2} + \frac{8mI_b}{\pi R_t^4} \right) \quad (4.33)$$

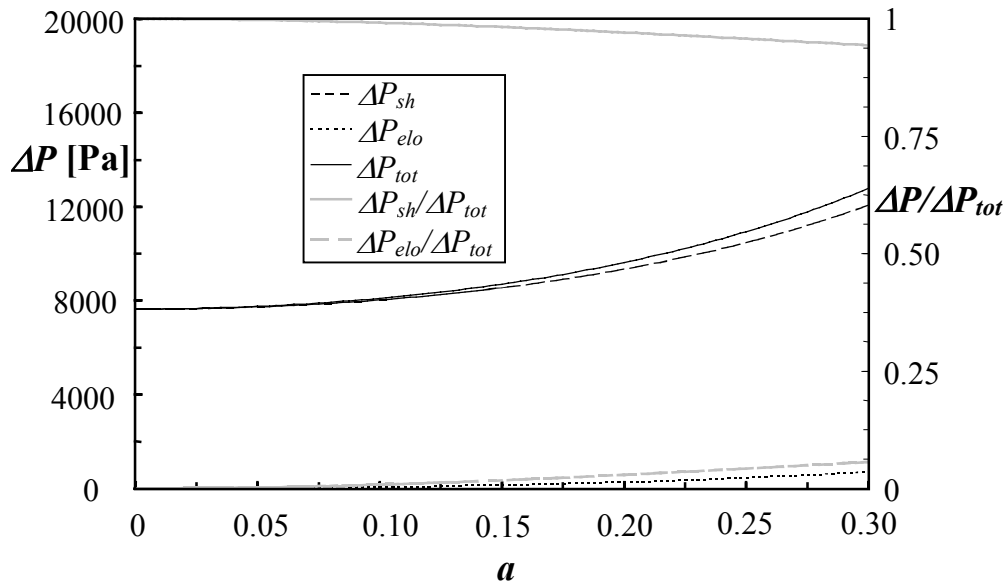


Figure 4.9a The pressure drop terms for flow of the Newtonian fluid through the sinusoidal tube ($b = 6$)

Figure 4.9a shows the pressure drop predictions for the Newtonian fluid (Table 4.1) as a function of a . As can be seen both contributions, ΔP_{sh} and ΔP_{elo} , increase with a . At small values of a , ΔP_{elo} is negligible, while at $a = 0.30$ its contribution is about 6% to the total pressure drop ΔP_{tot} .

II. The Power Law fluid

For the Power Law fluid I_a and I_b (Eqs. 4.29 and 4.30) have to be solved numerically. Figure 4.9b shows the prediction of the different pressure drop terms as a function of a for flow of the Power Law fluid (Table 4.1) through the earlier-described sinusoidal

tube. As expected, all pressure drop terms are smaller than for the Newtonian fluid. Note that the contribution of ΔP_{elo} to ΔP_{tot} is larger than for the Newtonian fluid i.e. more than 8% at $a = 0.30$.

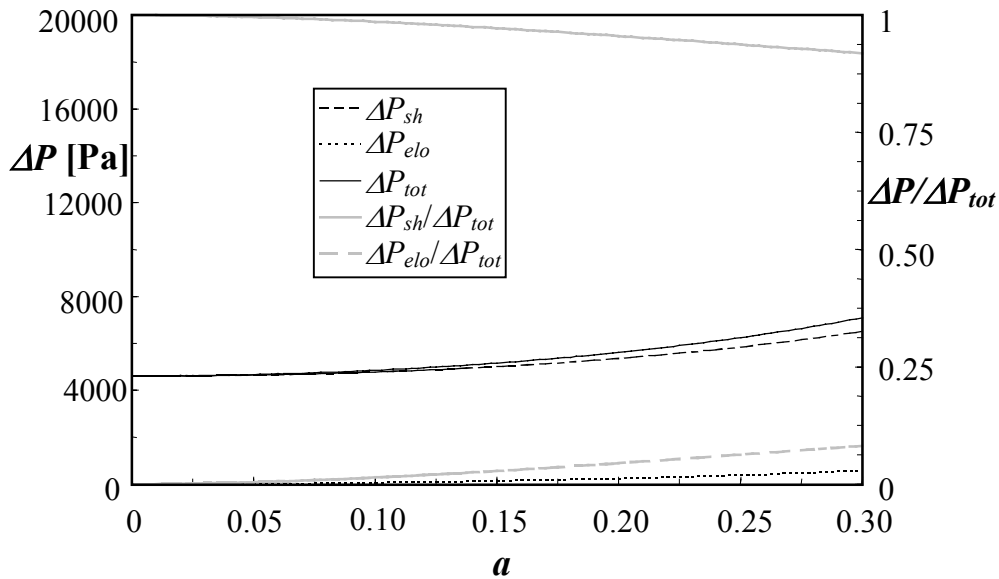


Figure 4.9b The pressure drop terms for flow of the Power Law fluid through the sinusoidal tube ($b = 6$)

III. The Boger fluid

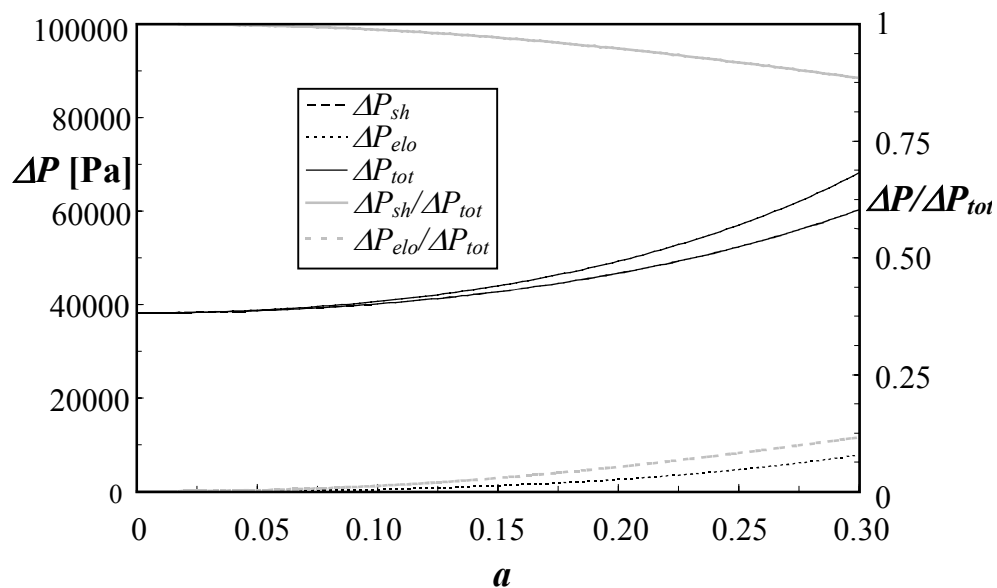


Figure 4.9c The pressure drop terms for flow of the Boger fluid ($Q = 5 \times 10^{-4} \text{ m}^3/\text{s}$) through the sinusoidal tube ($b = 6$)

The integral I_b is given by Eq. 4.32, while I_a has to be solved numerically. It follows that at $Q = 1 \times 10^{-4} \text{ m}^3/\text{s}$ the pressure drop terms for the Boger fluid are practically the same as for the Newtonian fluid ($\Delta P_{elo}/\Delta P_{tot}$ equals more than 7% at $a = 0.30$). At this flow rate strain-thickening effects are still very small. Figure 4.9c shows the pressure drop terms at a higher flow rate ($Q = 5 \times 10^{-4} \text{ m}^3/\text{s}$) as a function of a . As can be seen the ratio $\Delta P_{elo}/\Delta P_{tot}$ at $a = 0.30$ has now increased to over 11%. Note that in all examples given in Figure 4.9, the criterion of $W = 0.3$ (Eq. 4.25) is exceeded above a normalised amplitude of $a = 0.20$ meaning that the predictions by LAM may become somewhat less accurate.

4.4 Porous media models

As stated in the introduction, elongational dissipation is often disregarded in literature on porous media flow. From this perspective, the direct translation of permeability measurements into an average pore diameter by the straight tube capillary bundle model is conceptually incorrect due to the fact that all dissipation is considered to be a result of shear deformation only. In this section we will consider the influence of the main geometrical parameters on the pressure drop for flow of a Newtonian fluid through the widening/converging tube and through the sinusoidal tube. To clarify effects the pressure drop predictions are represented by dimensionless functions i.e. ratios between the pressure drop for a specific geometry divided by the pressure drop for an equivalent straight tube. In addition, the predictions are converted in terms of capillary bundle models, which do account for elongational dissipation effects.

4.4.1 The widening/converging capillary bundle model

Let us consider the ratio F_I between the total pressure drop for flow of a Newtonian fluid through a linear widening/converging tube (Eq. 4.23) and a straight tube having the average radius $R_{av} = \frac{l}{2}(R_{min} + R_{max})$. A rearrangement yields the following dimensionless function:

$$F_1 = \frac{(\alpha^2 + \alpha + 1)(1 + \alpha)^4}{48\alpha^3} \left(1 + \frac{1}{2} f_e \tan^2 \Theta\right) \quad (4.34)$$

where f_e is defined by Eq. 4.15

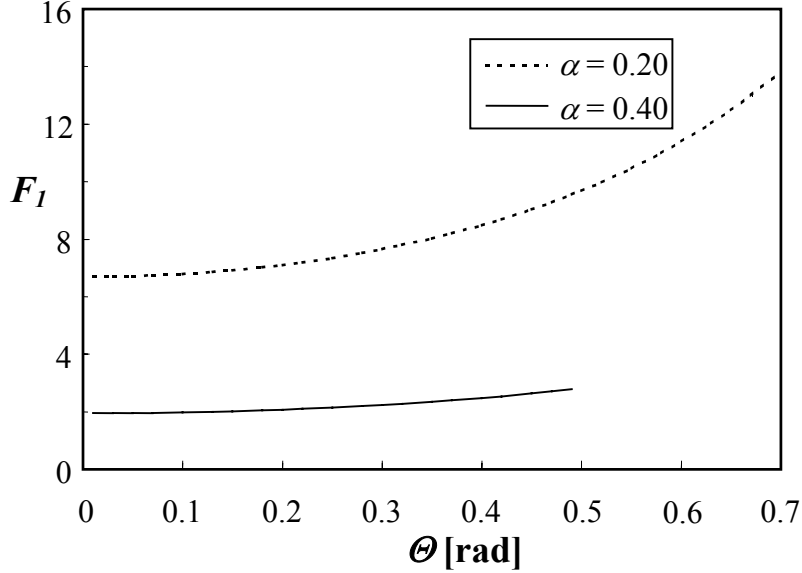


Figure 4.10 F_1 vs. Θ for $\alpha = 0.20$ and $\alpha = 0.40$

It follows that the term associated with shear dissipation in F_1 is only a function of α , while the term associated with elongational dissipation is a function of α and Θ . Note that $\alpha = 1$ yields $F_1 = 1$, the result for the straight tube. Figure 4.10 shows the dimensionless function F_1 vs. Θ for $\alpha = 0.20$ and $\alpha = 0.40$. At increasing values of Θ , and constant α , F_1 increases as a result of augmenting elongational dissipation. Both curves are confined by Eq. 4.17 where $W = 0.3$ was used as criterion.

The pressure drop predictions for this geometry can be easily converted in a linear widening/converging capillary bundle model. Suppose N_a tubes (length L) are placed in parallel, each consisting of Ω alternatively widening and converging segments (length l , mean radius R_{av} , α , Θ). Then the total pressure drop ΔP_m over this model is:

$$\Delta P_m = \frac{\Omega}{N_a} \Delta P_{tot} = \frac{8mQL}{N_a \pi R_{av}^4} F_1 \quad (4.35)$$

where F_l is defined by Eq. 4.34. By equalising this to Darcy's law (Eq. 2.1) one obtains for the permeability:

$$k = \frac{N_a \pi R_{av}^4}{8 S F_l} \quad (4.36)$$

For a constant angle Θ (constant N_a , R_{min} and S) Eq. 4.36 predicts that the permeability increases when decreasing the value of α , resulting in a longer tube with a larger mean radius. The porosity ϕ of the model can be calculated by taking the ratio between the (average) total cross-sectional area occupied by the tubes and the total cross-sectional area S :

$$\phi = \frac{N_a \pi R_{av}^2 A_l}{S} \quad (4.37)$$

where the average cross-sectional area equals $\pi R_{min}^2 A_l$. For this geometry holds $A_l = 4(\alpha^2 + \alpha + 1)/(3(\alpha + 1)^2)$. By combining Eqs. 4.36 and 4.37, one obtains:

$$k = \frac{\phi R_{av}^2}{8} G_l \quad (4.38)$$

where $G_l = (F_l A_l)^{-1}$

This equation reduces to the well-known capillary bundle model prediction (Eq. 2.8) in the limit of the straight tube ($\alpha = 1$).

4.4.2 The sinusoidal capillary bundle model

If we consider the ratio between the total pressure drop for flow of a Newtonian fluid through a sinusoidal tube of length λ (Eq. 4.33) and a straight tube (radius R_t , length λ) we obtain the following dimensionless expression:

$$F_2 = \frac{\pi^2 f_e a^2}{(1-a^2)^{\frac{5}{2}} b^2} + \frac{1 + \frac{3}{2} a^2}{(1-a^2)^{\frac{7}{2}}} \quad (4.39)$$

Here the first term on the right hand side is associated with elongational dissipation, the second with shear dissipation. Note that both the elongational term and the shear term increase with increasing a .

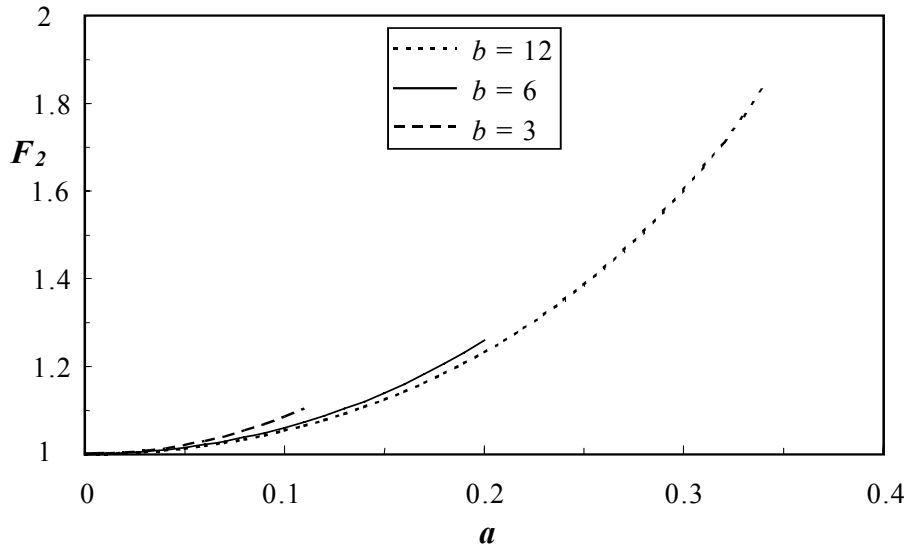


Figure 4.11 F_2 vs. a for $b = 3$, $b = 6$ and $b = 12$

Of course $F_2 = 1$ when a goes to zero, the straight tube limit. Figure 4.11 shows the dimensionless function F_2 vs. a for $b = 3$, $b = 6$ and $b = 12$. Again $W = 0.3$ (Eq. 4.25) has been used as criterion.

Suppose N_a sinusoidal tubes (length $L = \Omega\lambda$, average tube radius R_t , normalised amplitude a) are placed in parallel. The total pressure drop over the model and its permeability are expressed by Eqs. 4.35 and 4.36 when substituting F_2 for F_1 and R_t for R_{av} . The porosity is expressed by Eq. 4.37 when substituting R_t for R_{av} and $A_2 = 1 + \frac{1}{2} a^2$ for A_1 . Combination of all these equations yields for the permeability:

$$k = \frac{\phi R_t^2}{8} G_2 \quad (4.40)$$

where $G_2 = (F_2 A_2)^{-1}$

4.5 Discussion

In this chapter pressure drop predictions have been derived for flow through tubes with a slowly varying diameter by making use of the Lubrication Approximation Method. For the Newtonian fluid the predictions have been converted into capillary models, which do account for elongational dissipation effects.

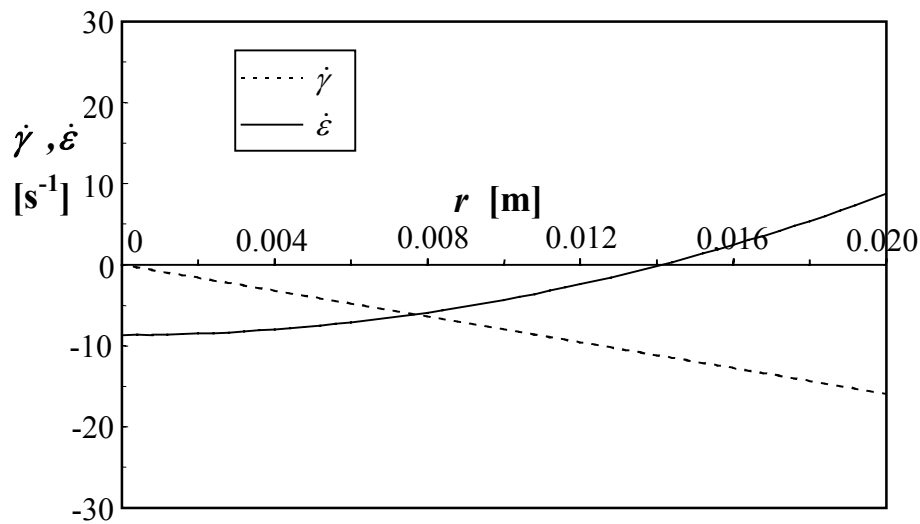


Figure 4.12 The shear- and elongational rate profile (at $z = 0$) for Newtonian flow through a widening tube as predicted by using LAM with cylindrical co-ordinates

Although LAM [2] is an established method in literature, the resulting deformation rates are approximations, which tend to be not fully correct. This is well demonstrated in Figure 4.12 which shows the shear- and elongational rate profile at $z = 0$ for flow of a Newtonian fluid at $Q = 1 \times 10^{-4} \text{ m}^3/\text{s}$ through a widening tube ($R_o = 0.02 \text{ m}$, $\Theta = 0.50 \text{ rad}$). Logically one expects the elongational rate to be negative in the whole flow domain for this geometry, except at the tube edges where it should be equal to zero. Surprisingly, we find by LAM (Eq. 4.13 and 4.24) that the elongational rate becomes positive close to the tube wall. This anomaly is caused by the fact that the main directions in the co-ordinate system do not match very well with the direction of streamlines in the flow problem. Another consequence of the same problem is that a radial shear rate component $\dot{\gamma}_r = \partial v_r / \partial r$ appears in the equations. Due to the unknown relation between viscosity and the radial shear rate and the logical reasoning

that this contribution must be small, the radial shear rate contribution has been neglected (see Eq. 4.5). Actually, the predictions are obtained by approximating the deformation gradients by the shear rate $\dot{\gamma} = \partial v_z / \partial r$ and the axial elongational rate $\dot{\epsilon} = \partial v_z / \partial z$. This approximation becomes worse at higher values of \mathcal{O} .

Nevertheless, LAM is valuable from a practical point of view due to its simplicity, its analytical solutions and the reasonable pressure drop predictions, which can be obtained. The latter is caused by the fact that shear is the main dissipation mechanism and that this prediction is generally fairly good. A limitation of the method is the fact that it can only be used under creeping flow conditions for geometries with a slowly varying diameter. It is not appropriate to give predictions at large values of W (Eq. 4.17 and 4.25), the regime where one expects larger elongational pressure drops.

In the next chapter we will discuss a new LAM, based on spherical co-ordinates, which gives improved predictions and which shows, more convincingly, that elongational dissipation can be significant. Note that changes in the pore cross-section in real porous media are usually more drastic and consequently elongational contributions are expected to be higher. Comparisons of the pressure drop predictions with experimentally measured values are also described in the next chapter.

4.6 Summary

1. Although generally disregarded, elongational dissipation contributes to the measured permeability of a porous medium. Therefore, the incorporation of this effect can improve the classical, straight tube capillary model (Eq. 2.8), while preserving its simple, easy applicable nature.
2. It is conceptually incorrect to model the flow through a porous media by a straight tube capillary model. The permeability and also the porosity are misinterpreted by this approach.
3. Pressure drop predictions for different corrugated tubes and for different type of fluids have been derived by combining LAM and the energy balance i.e. by integration of the dissipation over the volume. This procedure gives fully analytical expressions for the Newtonian fluid. The solutions for the Power Law- and Boger fluid involve integrals, which have to be solved numerically. The solutions for the Newtonian fluid have been converted into capillary bundle models, which do take into account elongational dissipation effects.
4. Since in the classical LAM the main directions of the cylindrical co-ordinate system do not match with the direction of streamlines in the flow problem, the resulting deformation gradients are approximations, which in general become less good at increasing values of Θ . The method is nevertheless valuable due to its simplicity and the analytical solutions and reasonable predictions which can be obtained. A limitation of the method is the fact that it can only be used under creeping flow conditions for geometries with a slowly varying diameter.
5. The pressure drop predictions in this chapter are purely based on stationary fluid flow behaviour i.e. neglecting polymer retention effects and time dependent flow behaviour. This means that the solutions are valid under non-adsorbing conditions or in the case retention has a negligible impact e.g. at high permeabilities.
6. When applying Darcy's equation for two-phase flow, the permeability to each phase is accounted for by the relative permeability concept (see appendix C). The use of capillary bundle models, which include diameter variations in the axial direction, can improve the application of this concept to real porous media [11].

References (Chapter 4)

1. R. Bird, W. Stewart, E. Lightfoot, "Transport Phenomena", John Wiley & Sons, New York (1960)
2. R. Bird, R. Armstrong, O. Hassager, "Dynamics of Polymeric Liquids", John Wiley & Sons, New York (1987)
3. V. Streeter, "Handbook of Fluid Dynamics", McGraw-Hill Book Company, New York (1961)
4. F. Dullien, "Porous Media, Fluid Transport and Pore Structure", Academic Press Inc. , San Diego (1992)
5. J. Bear, "Dynamics of Fluids in Porous Media", Dover Publications Inc., New York (1988)
6. A. Collyer, "Techniques in Rheological measurement", Chapter 1, p. 18, Chapman & Hall (1993)
7. B. Debbaut, M. Crochet, H. Barnes and K. Walters, Proc. Xth Int. Cong. Rheol., 2, 291 (1988)
8. B. Debbaut, M. Crochet, J. Non-Newtonian Fluid Mech. **30**, 169 (1988)
9. P. Schaum, "Complex Functions" , Los Angeles (1992)
10. J. Deiber, W. Schowalter, A.I.Ch.E.J. **25**, 638 (1979)
11. P. Zitha, F. Vermolen, H. Bruining, SPE conference paper 54737, The Hague (1999)

CHAPTER 5 - CORRUGATED CAPILLARY BUNDLE

MODELS: PREDICTIONS BY A NEW LUBRICATION APPROXIMATION METHOD

5.1 Introduction

It was shown in the preceding chapter that the approximation of the deformation rates in the cylindrical co-ordinate system becomes worse when the diameter change per length unit increases. Also the appearance of a radial shear rate is uncomfortable and its functional dependence with respect to viscosity is unknown.

In order to improve the prediction of the deformation gradients, a new description has been developed using a spherical co-ordinate system [1]. Figure 5.1 shows the application of a spherical co-ordinate system (ρ, θ) for the widening tube.

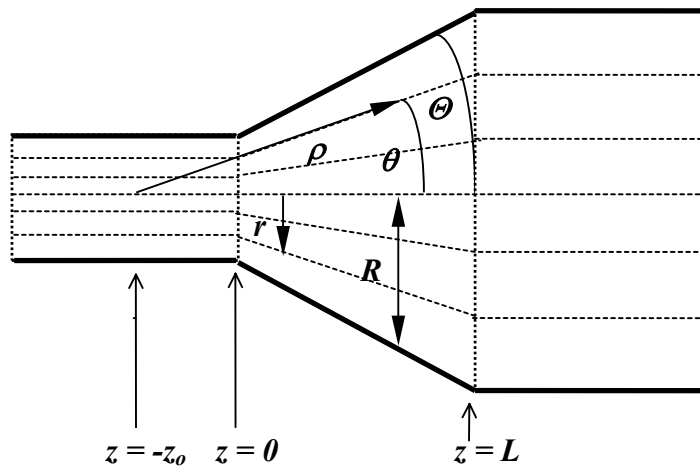


Figure 5.1 Schematic representation of the spherical co-ordinate system in a widening tube

As the flow problems considered in this chapter are invariant with respect to rotation, the rotational angle ϕ is irrelevant here. Except for the different co-ordinate system, the mathematical formulation of the method is the same as described in Section 4.2.

This chapter is organised as follows. In Section 5.2 pressure drop predictions are obtained for fluid flow through the widening- and sinusoidal tube by the new Lubrication Approximation Method (LAM). In Section 5.3 the predictions for

Newtonian flow are converted into porous media models, i.e. capillary models that do take into account elongational dissipation. In Section 5.4 the results are discussed and compared with measurements and predictions from literature. In Section 5.5 conclusions are drawn.

5.2 Pressure drop predictions

5.2.1 The widening tube

For flow through a widening tube, the spherical description yields for the velocity in the ρ direction:

$$v_\rho(\rho, \vartheta) = \frac{3n+1}{n+1} \frac{Q}{\pi \tan^2 \Theta} \left(1 - \beta^{\frac{n+1}{n}}\right) \frac{1}{\rho^2 \cos^3 \vartheta} \quad (5.1)$$

where $\beta = \frac{r}{R} = \frac{\tan \vartheta}{\tan \Theta}$ and $\rho = \frac{r}{\sin \vartheta}$

The rates of elongation and shear are now defined as $\dot{\varepsilon} = \frac{\partial v_\rho}{\partial \rho}$ and $\dot{\gamma} = \frac{1}{\rho} \frac{\partial v_\rho}{\partial \vartheta}$

respectively. This combined with Eq. 5.1 yields:

$$\dot{\varepsilon} = \dot{\varepsilon}(\rho, r) = \frac{2Q}{\pi \rho^3 \tan^2 \Theta} \left(-\frac{3n+1}{n+1} \frac{1}{\cos^3 \vartheta} \left(1 - \beta^{\frac{n+1}{n}}\right) \right) \quad (5.2)$$

$$\dot{\gamma} = \dot{\gamma}(\rho, r) = \frac{Q}{\pi \rho^3 \tan^2 \Theta} \frac{3n+1}{n+1} \frac{1}{\cos^3 \vartheta} \left(3 \left(1 - \beta^{\frac{n+1}{n}}\right) \tan \vartheta - \frac{n+1}{n} \frac{\beta^{\frac{1}{n}}}{\tan \Theta \cos^2 \vartheta} \right) \quad (5.3)$$

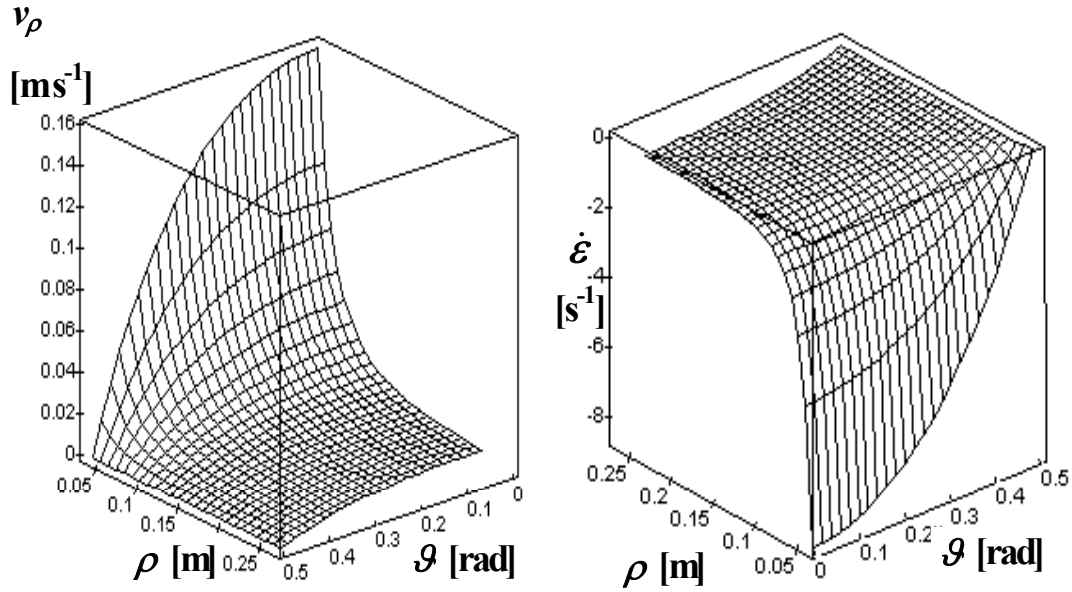


Figure 5.2 The velocity- and elongational rate profile for flow of a Newtonian fluid through a widening tube. Different ρ and ϑ scale directions are applied to obtain better visubility

Figure 5.2 shows the velocity- and elongational rate profiles resulting from the spherical co-ordinate system for flow of the Newtonian fluid through a widening tube at $Q = 1 \times 10^{-4} \text{ m}^3/\text{s}$ ($R_{min} = 0.02 \text{ m}$, $L = 0.20 \text{ m}$, $\Theta = 0.50 \text{ rad}$). Note that except at the tube edge ($\theta = \Theta$) where $\dot{\epsilon} = 0$, the elongational rate is negative everywhere. This result, which we did not obtain when using the cylindrical description (see Figure 4.12), is what is to be expected for this geometry. It is a consequence of the better definition of the deformation rates in the spherical system. The rate of deformation tensor [2] is now given by:

$$D = \begin{bmatrix} \frac{\partial v_\rho}{\partial \rho} & \frac{1}{2\rho} \frac{\partial v_\rho}{\partial \vartheta} \\ \frac{1}{2\rho} \frac{\partial v_\rho}{\partial \vartheta} & \frac{v_\rho}{\rho} \end{bmatrix} = \begin{bmatrix} \dot{\epsilon} & \frac{\dot{\gamma}}{2} \\ \frac{\dot{\gamma}}{2} & \frac{v_\rho}{\rho} \end{bmatrix} \quad (5.4)$$

The double contraction of the stress tensor (Eq. 4.5) and the rate of deformation tensor (Eq. 5.4) results in Eq. 4.10. However, the deformation rates are now given by Eqs. 5.2 and 5.3.

The total pressure drop can be calculated by integration of the dissipation over the volume of the flatted cone:

$$\Delta P_{tot} = \frac{2\pi}{Q} \int_{z=0}^L \int_{\vartheta=0}^{\Theta} \left(\frac{T}{D} (z + z_o)^2 \frac{\sin \vartheta}{\cos^3 \vartheta} \right) d\vartheta dz \quad (5.5)$$

where $z_o = \frac{R_{min}}{\tan \Theta}$ and $\rho = \frac{z + z_o}{\cos \vartheta}$

This gives the following expressions for the different pressure drop terms:

Elongational term:

$$\Delta P_{elo} = \frac{2g}{3h} \left(\frac{n}{n+1} \right) \left(\frac{6n+2}{n+1} \right)^{h+1} (\tan \Theta)^h B \left(\frac{2n}{n+1}, h+2 \right) \left(\frac{Q}{\pi R_{min}^3} \right)^h (1 - \alpha^{3h}) \quad (5.6)$$

where $B(x,y)$ is the beta function defined as $\int_0^1 j^{x-1} (1-j)^{y-1} dj$ [3] and $\alpha = \frac{R_{min}}{R_{max}}$

Shear term:

$$\Delta P_{sh} = \frac{2m}{3n} \left(\frac{3n+1}{n+1} \right)^{n+1} (\tan \Theta)^{n-2} \left(\frac{Q}{\pi R_{min}^3} \right)^n (1 - \alpha^{3n}) I_c \quad (5.7)$$

Elasticity term:

$$\Delta P_{ela} = -\frac{4p}{3q+3} \left(\frac{3n+1}{n+1} \right)^{q+2} (\tan \Theta)^{q-1} \left(\frac{Q}{\pi R_{min}^3} \right)^{q+1} (1 - \alpha^{3q+3}) I_d \quad (5.8)$$

Surface term:

$$\Delta P_{sur} = -2p \left(\frac{3n+1}{n+1} \right)^{q+2} (\tan \Theta)^{q-1} \left(\frac{Q}{\pi R_{min}^3} \right)^{q+1} (1 - \alpha^{3q+3}) I_e \quad (5.9)$$

where

$$I_c = \int_{\vartheta=0}^{\Theta} \left(w^{n+1} \frac{\sin \vartheta}{\cos^3 \vartheta} \right) d\vartheta \quad (5.10)$$

$$I_d = \int_{\vartheta=0}^{\Theta} \left(w^{q+1} \left(1 - \beta^{\frac{n+1}{n}} \right) \frac{\sin \vartheta}{\cos^3 \vartheta} \right) d\vartheta \quad (5.11)$$

$$I_e = \int_{\vartheta=0}^{\Theta} \left(w^{q+1} \left(1 - \beta^{\frac{n+1}{n}} \right) \frac{\sin \vartheta}{\cos^4 \vartheta} \right) d\vartheta \quad (5.12)$$

and

$$w = \left| 3 \left(1 - \beta^{\frac{n+1}{n}} \right) \tan \vartheta - \frac{n+1}{n} \frac{\beta^{\frac{1}{n}}}{\tan \Theta \cos^2 \vartheta} \right| \quad (5.13)$$

The equations for ΔP_{sh} and ΔP_{elo} of a widening tube (Eqs. 5.6 and 5.7) remain exactly the same for the problem of flow through a converging tube (same R_{min} , R_{max} and L). However, the elastic pressure drop terms (Eqs. 5.8 and 5.9) only change in sign for the latter geometry. Let us consider again the influence of Θ on the pressure drop terms for flow of the example fluids (Table 4.1) through a widening tube ($R_{min} = 0.02$ m, $L = 0.20$ m, $Q = 1 \times 10^{-4}$ m³/s).

1. The Newtonian fluid

Combining Eqs. 5.6 and 5.7 ($n = 1$, $h = 1$) yields for the total pressure drop:

$$\Delta P_{tot} = \left(\frac{16g \tan \Theta}{9} + \frac{8mI_c}{3 \tan \Theta} \right) \frac{Q}{\pi R_{min}^3} (1 - \alpha^3) \quad (5.14)$$

where the analytical solution of the integral I_c is:

$$I_c = 1 + \frac{1}{3}\tan^2 \Theta + \frac{3}{8}\tan^4 \Theta \quad (5.15)$$

Comparison of the results for the Newtonian fluid shows that the spherical co-ordinate system gives an elongational pressure drop ΔP_{elo} , which is a factor $\frac{4}{3}$ larger than ΔP_{elo} in the cylindrical system (Eq. 4.23). The shear pressure drop ΔP_{sh} in this spherical system is a factor I_c (Eq. 5.15) larger than ΔP_{sh} in the cylindrical system (Eq. 4.20). This factor I_c increases from about 1.01 at $\Theta = 0.20$ rad. to 1.43 at $\Theta = 0.70$ rad. The larger dissipation can be attributed to the fact that the absolute values of the deformation rates, $\dot{\gamma}$ and $\dot{\epsilon}$, are larger in the spherical co-ordinate system. This is caused by the fact that this description allows a correct definition of the deformation rates, while in cylindrical description the deformation rates are approximated by its axial components, neglecting radial contributions.

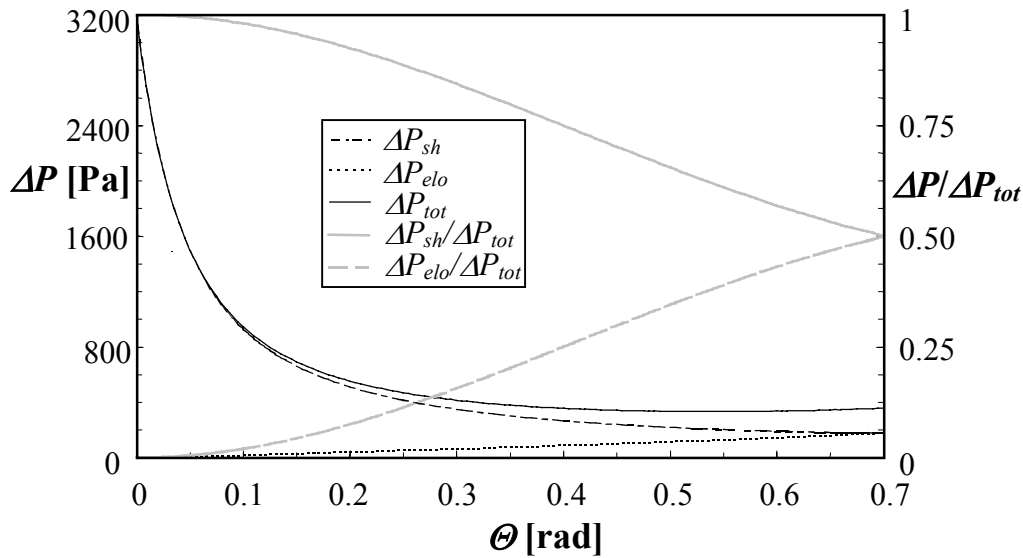


Figure 5.3a The pressure drop terms for flow of the Newtonian fluid through the widening tube as a function of Θ

Figure 5.3a shows the pressure drop terms for flow of the Newtonian fluid through a widening tube vs. the widening angle Θ . The curves show the same trends as discussed in Section 4.3.1.

II. The Power Law fluid

For this fluid I_c (Eq. 5.10) has to be solved numerically. Figure 5.3b shows the predictions for flow of the Power Law fluid through the widening tube. The pressure drop terms are here also larger than in the cylindrical description (Figure 4.5b).

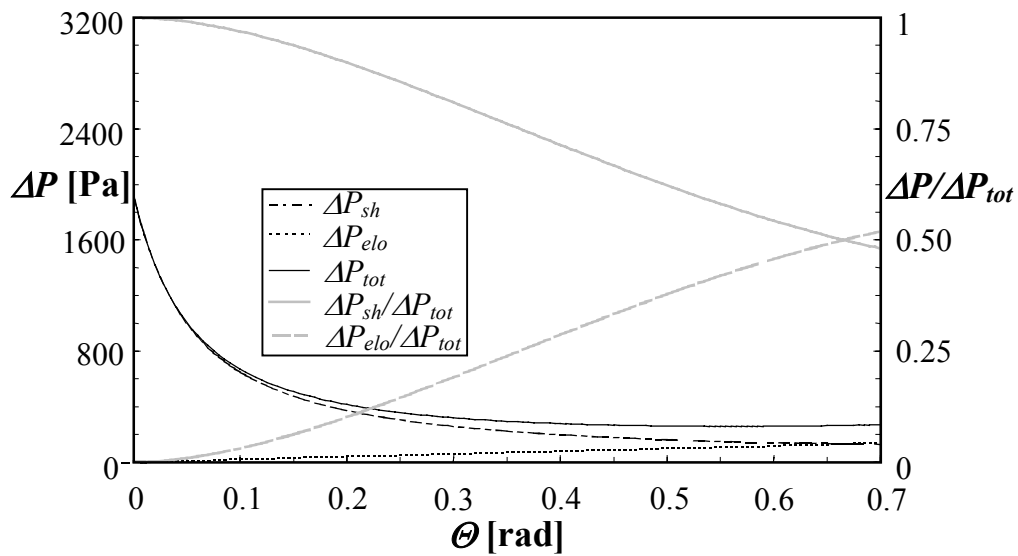


Figure 5.3b The pressure drop terms for flow of the Power Law fluid through the widening tube as a function of Θ

III. The Boger fluid

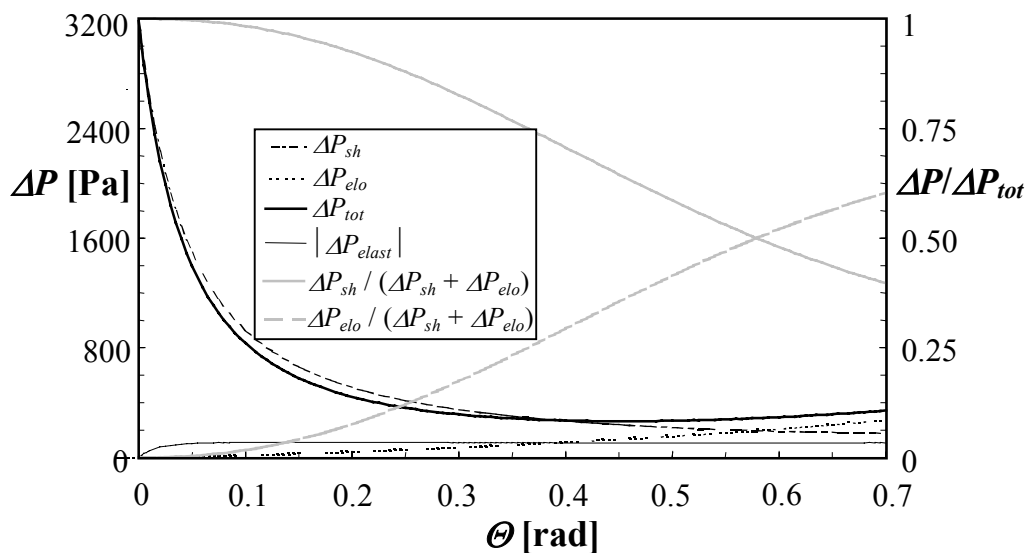


Figure 5.3c The pressure drop terms for flow of the Boger fluid through the widening tube as a function of Θ

Here the integral I_c is given by Eq. 5.15, while I_d and I_e have to be solved numerically. Figure 5.3c shows the pressure drop terms for flow of the Boger fluid through the widening tube as a function of the widening angle Θ . Both shear- and elongational pressure drop terms are larger than in the cylindrical approach (Figure 4.5c). The same is true for the absolute value of the elastic terms $|\Delta P_{elast}|$ and the total pressure drop.

5.2.2 The sinusoidal tube

By implementing the following substitutions in Eqs. 5.2 and 5.3, $\rho = R/(R_z \cos \vartheta)$, $\tan \Theta = R_z$ and $\tan \vartheta = \beta R_z$, the deformation rates during flow through the sinusoidal tube are given by:

$$\dot{\varepsilon} = -\frac{3n+1}{n+1} \frac{2Q}{\pi R^3} \left(1 - \beta^{\frac{n+1}{n}}\right) R_z \quad (5.16)$$

$$\dot{\gamma} = \frac{3n+1}{n+1} \frac{Q}{\pi R^3} \left(3\beta R_z^2 - \frac{n+1}{n} \beta^{\frac{1}{n}} - \frac{4n+1}{n} \beta^{\frac{2n+1}{n}} R_z^2\right) \quad (5.17)$$

where R is defined by Eq. 4.24 and $R_z = \frac{dR}{dz}$. The pressure drop during flow can be now be calculated by making use of Eq. 4.6. This yields the following pressure drop terms over one wavelength λ :

Elongational term:

$$\Delta P_{elo} = 2g \left(\frac{n}{n+1}\right) \left(\frac{3n+1}{n+1}\right)^{h+1} B\left(\frac{2n}{n+1}, h+2\right) \left(\frac{4\pi a R_t}{\lambda}\right)^{h+1} \left(\frac{Q}{\pi R_t^3}\right)^h \frac{I_a}{R_t} \quad (5.18)$$

where $B(x,y)$ is the beta function and I_a is the integral given by Eq. 4.29

Shear term:

$$\Delta P_{sh} = 2m \left(\frac{3n+1}{n+1} \right)^{n+1} \left(\frac{Q}{\pi R_t^3} \right)^n \frac{I_f}{R_t} \quad (5.19)$$

where,

$$I_f = \int_{z=0}^{\lambda} \frac{I_g}{\left(1 + a \sin \frac{2\pi z}{\lambda} \right)^{3n+1}} dz \quad (5.20)$$

$$I_g = \int_0^1 \left(3\beta^{\frac{n+2}{n+1}} - \frac{4n+1}{n} \beta^{\frac{2n+1}{n(n+1)+2}} \right) R_z^2 - \frac{n+1}{n} \beta^{\frac{2n+1}{n(n+1)}} \Big|^{n+1} d\beta \quad (5.21)$$

Let us consider again the predictions for flow of the example fluids ($Q = 1 \times 10^{-4}$ m³/s) through the sinusoidal tube ($\lambda = 0.12$ m, $R_t = 0.02$ m and total length $L = 0.48$ m).

1. The Newtonian fluid

The total pressure drop ΔP_{tot} can be calculated by:

$$\Delta P_{tot} = Q \left(\left[g \frac{64\pi a^2}{3R_t^2 \lambda^2} I_a \right]_{elo} + \left[m \left(\frac{8}{\pi R_t^4} I_b + \frac{32\pi a^2}{3R_t^2 \lambda^2} I_a + \frac{48\pi^3 a^4}{\lambda^4} I_h \right) \right]_{sh} \right) \quad (5.22)$$

where I_a and I_b are given by Eqs. 4.29 and 4.30. Note that it is indicated in Eq. 5.22 which terms are due to elongational- and which due to shear dissipation. By making use of the residue theorem [1] the integral I_h can be solved:

$$I_h = \int_{z=0}^{\lambda} \frac{\cos^4\left(\frac{2\pi z}{\lambda}\right)}{\left(1 + a \sin \frac{2\pi z}{\lambda} \right)^4} dz = \frac{\lambda}{a^4} \left(1 + \frac{\frac{3}{2}a^2 - 1}{(1-a^2)^{\frac{3}{2}}} \right) \quad (5.23)$$

Figure 5.4a shows the predictions of the pressure drop terms for flow of the Newtonian fluid through the sinusoidal tube as a function of a . Both contributions,

ΔP_{sh} and ΔP_{elo} , increase with a and are larger than their equivalents in the cylindrical system. Also for this geometry ΔP_{elo} is a factor $\frac{4}{3}$ larger than in the cylindrical description (Figs. 4.9a). At small values of a , ΔP_{elo} is negligible, while at $a = 0.30$ its contribution raises to over 7% of the total pressure drop ΔP_{tot} .

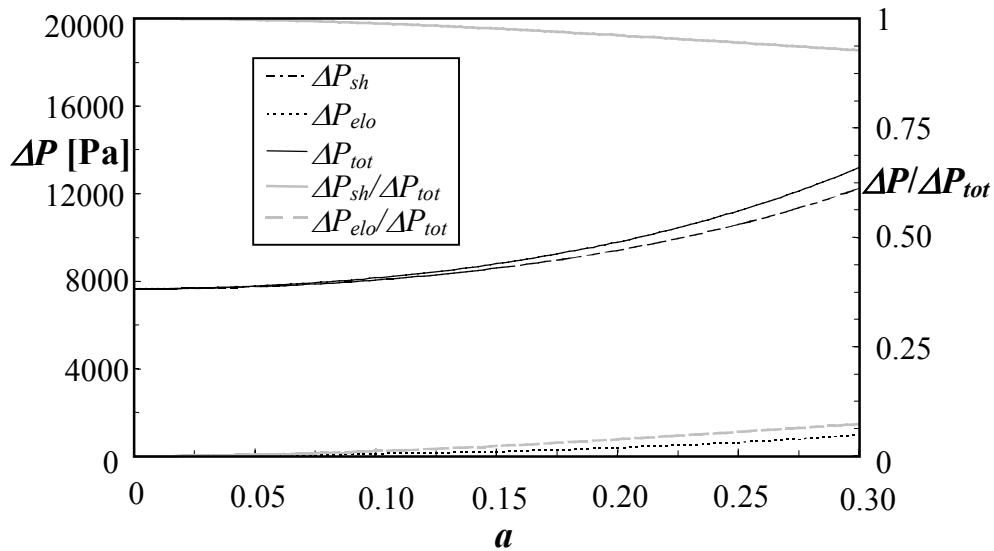


Figure 5.4a The pressure drop terms for flow of the Newtonian fluid through the sinusoidal tube ($b = 6$)

II. The Power Law fluid

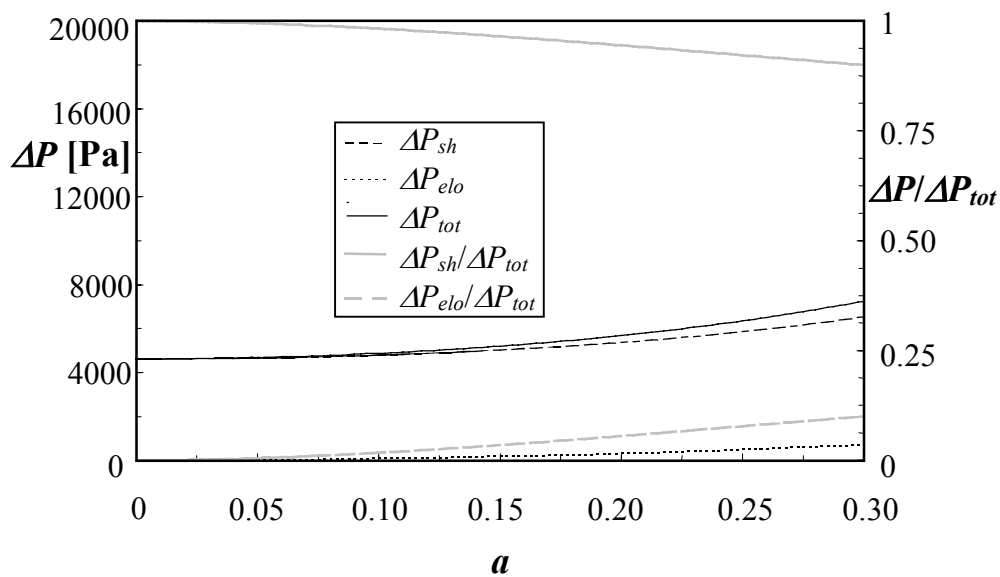


Figure 5.4b The pressure drop terms for flow of the Power Law fluid through the sinusoidal tube ($b = 6$)

Figure 5.4b shows the prediction of the pressure drop terms for flow of the Power Law fluid through the sinusoidal tube as a function of a for $b = 6$. The integrals I_a and I_f (Eqs. 4.29, 5.20 and 5.21) have to be solved numerically for this fluid. All pressure drop terms are slightly larger than for the cylindrical approach. As for the Newtonian fluid ΔP_{elo} is negligible at small values of a , while its contribution is almost 10% of ΔP_{tot} at $a = 0.30$.

III. The Boger Fluid

The elongational pressure drop ΔP_{elo} from Eq. 5.18 has to be solved numerically while ΔP_{sh} is expressed by the shear term in Eq. 5.22. At $Q = 1 \times 10^{-4} \text{ m}^3/\text{s}$ the ratio $\Delta P_{elo}/\Delta P_{tot}$ is about 10% since strain-thickening effects are relatively small. Figure 5.4c shows the pressure drop terms as a function of a at a higher flow rate ($Q = 5 \times 10^{-4} \text{ m}^3/\text{s}$). The ratio $\Delta P_{elo}/\Delta P_{tot}$ at $a = 0.30$ has increased to up to 16%. Both pressure drop terms are larger than in the cylindrical approach (Figure 4.9c).

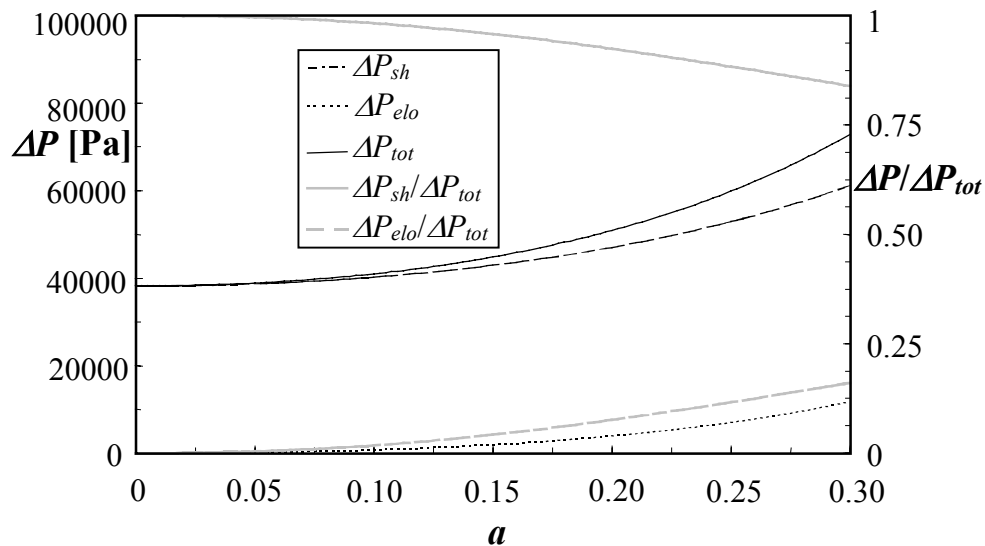


Figure 5.4c The pressure drop terms for flow of the Boger fluid through the sinusoidal tube ($b = 6$)

5.3 Porous media models

In this section we consider the influence of the main geometrical parameters on the pressure drop for flow of a Newtonian fluid through the widening tube and through the sinusoidal tube. To clarify effects the predictions are represented by dimensionless functions i.e. ratios between the pressure drop for a specific geometry divided by the pressure drop for an equivalent straight tube. In addition, the predictions are converted into capillary models, which do account for elongational dissipation effects.

5.3.1 The linear widening/converging capillary model

Let us consider the ratio between the total pressure drop for flow of a Newtonian fluid through a linear widening or converging tube (Eqs. 5.14 and 5.15) and a straight tube having the average radius $R_{av} = \frac{1}{2}(R_{min} + R_{max})$. This results in the following dimensionless function:

$$F_3 = \frac{(\alpha^2 + \alpha + 1)(1 + \alpha)^4}{48\alpha^3} \left(1 + \frac{1}{3}\tan^2 \Theta + \frac{3}{8}\tan^4 \Theta + \frac{2}{3}f_e \tan^2 \Theta \right) \quad (5.24)$$

where f_e is defined by Eq. 4.15

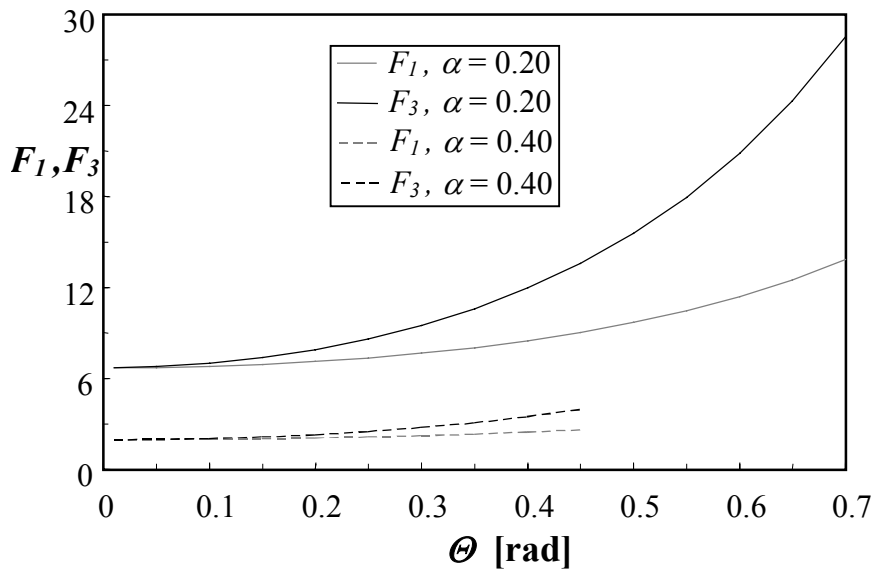


Figure 5.5 F_1 and F_3 vs. Θ for $\alpha = 0.20$ and $\alpha = 0.40$

In Eq. 5.24 the first three terms of the angle function on the right hand side are related to shear dissipation, while the last term is associated to elongational dissipation. It follows thus that both shear- and elongational dissipation are functions of α and Θ .

Figure 5.5 shows the dimensionless functions F_1 (Eq. 4.34) & F_3 (Eq. 5.24) vs. Θ for $\alpha = 0.20$ and $\alpha = 0.40$. At increasing values of Θ , both functions increase as a result of augmenting shear and elongational dissipation. At large angles both curves are confined by Eq. 4.17. Figure 5.5 shows clearly that the dissipation predicted by the spherical system is larger than predicted by the cylindrical system. It follows that at $\Theta = 0.10$, F_3 is only about 1% larger than F_1 for both values of α . However at $\Theta = 0.30$, F_3 is already 7 % larger than F_1 . This percentage grows at larger values of Θ .

The pressure drop predictions for this geometry can be converted into a linear widening/converging capillary model. The approach is fully similar to the one described in Section 4.4.1. This model is obtained by replacing in Eqs. 4.35, 4.36 and 4.38 F_1 by F_3 (Eq. 5.24) and arbitrarily A_1 by A_3 and G_1 by G_3 in Eq. 4.38.

5.3.2 The sinusoidal capillary model

For the ratio between the total pressure drop for flow of a Newtonian fluid through a sinusoidal tube (Eqs. 5.22 and 5.23) and a straight tube of radius R_t we obtain the following dimensionless expression:

$$F_4 = \frac{6\pi^4}{b^4} + \frac{\frac{6\pi^4\left(\frac{3}{2}a^2 - 1\right)}{b^4} + \frac{2\pi^2 a^2(1 + 2f_e)}{3b^2(1 - a^2)} + \frac{1 + \frac{3}{2}a^2}{(1 - a^2)^2}}{(1 - a^2)^{\frac{3}{2}}} \quad (5.25)$$

Figure 5.6 shows that for the Newtonian fluid the dissipation predicted by the spherical system is slightly larger than that predicted by the cylindrical system. It follows that at $a = 0.11$, F_4 is over 2% larger than F_2 for $b = 3$. At smaller values of a , this percentage is smaller. At $a = 0.20$, F_4 is less than 2% larger than F_2 for $b = 6$. Larger differences occur for higher values of W (Eq. 4.25). Note that we used here as criterion $W = 0.3$.

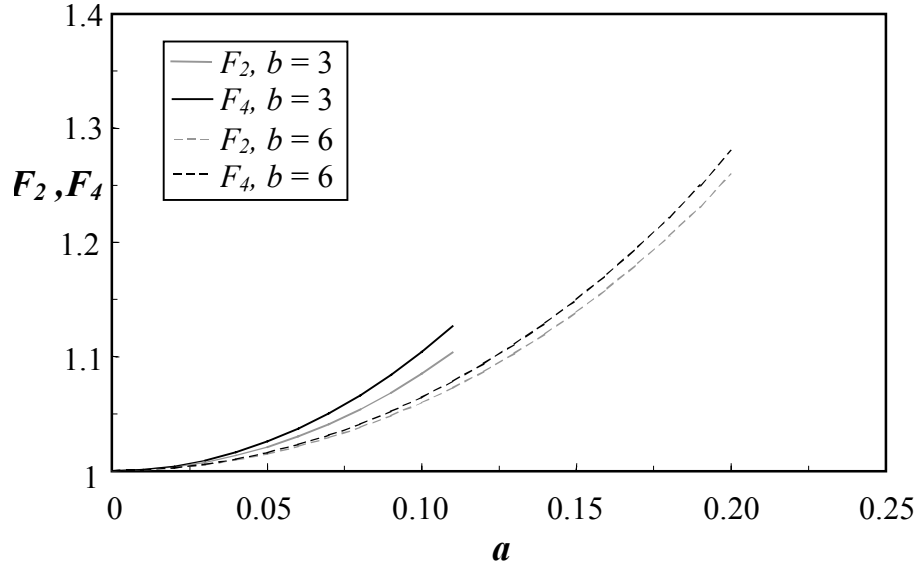


Figure 5.6 F_2 and F_4 vs. a for $b = 3$ and $b = 6$

Suppose N_a sinusoidal tubes (length $L = \Omega\lambda$, average tube radius R_t , normalised amplitude a) are placed in parallel. The total pressure drop over the model and its permeability are now expressed by Eqs. 4.35 and 4.36 when substituting F_4 for F_1 and R_t for R_{av} . The porosity is expressed by Eq. 4.37 when substituting R_t for R_{av} and $A_4 = 1 + \frac{1}{2}a^2$ for A_1 . This yields for the permeability:

$$k = \frac{\phi R_t^2}{8} G_4 \quad (5.26)$$

where $G_4 = (F_4 A_4)^{-1}$

5.3.3 Comparison of both models

Consider a linear widening/converging capillary model (R_{av} , α , $\tan\Theta$) and a sinusoidal capillary model (R_t , a , b) which have the same mean radius ($R_{av} = R_t$). When approaching the geometry of the first model in terms of parameters of the second we obtain:

$$\alpha = \frac{l+a}{l-a} \quad (5.27)$$

$$\tan \Theta = \frac{2a}{b} \quad (5.28)$$

When substituting these equations into F_1 (Eq. 4.34) and F_3 (Eq. 5.24) we can compare all results. Figure 5.7 shows the comparison of all F-functions using $W = 0.3$ as the criterion. For similar geometries one finds that $F_1 < F_2$ and that $F_3 < F_4$. The higher dissipation found for the sinusoidal geometry compared to the widening/converging geometry is a result of the presence of higher elongational rates in its flow field.

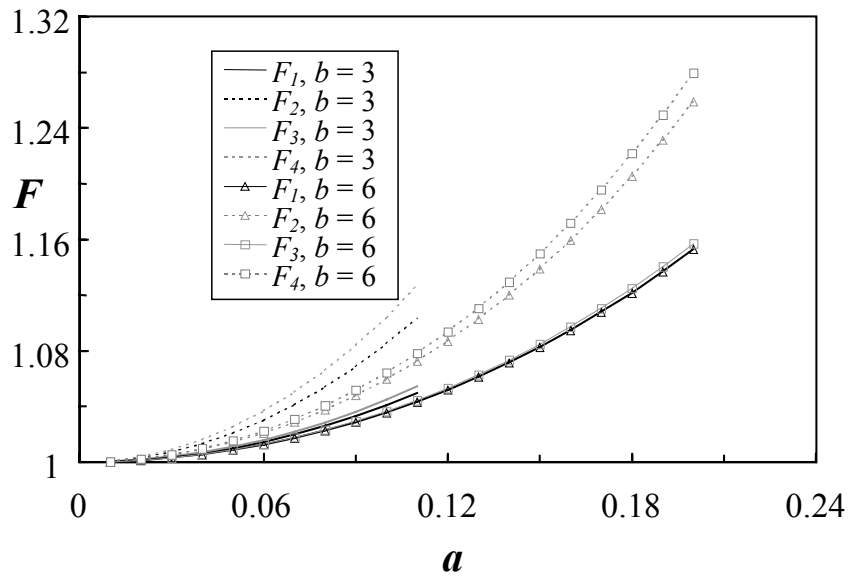


Figure 5.7 Comparison of the F-functions

5.4 Discussion

5.4.1 The linear widening/converging tube

In this chapter pressure drop predictions for fluid flow through a widening/converging tube have been established by making use of a new LAM approach; The flow problem has been described by a spherical co-ordinate system, which allows a better description of the deformation rates present (Section 5.2.1). Generally, for all fluids in both geometries the new description results in larger pressure drops than the

predictions by the classical LAM approach (Chapter 4). This is caused by the fact that the deformation rates in this system are larger due to the fact that all contributions can be taken into account. For the Newtonian fluid, the shear pressure drop ΔP_{sh} from the spherical system (Eq. 5.7) is a factor I_c (Eq. 5.15) larger than ΔP_{sh} from the cylindrical system (Eq. 4.20). The elongational pressure drop ΔP_{elo} (Eq. 5.6) is a factor $\frac{4}{3}$ larger than the result for the cylindrical system (Eq. 4.19).

5.4.2 The sinusoidal tube

For the Newtonian fluid the elongational pressure drop ΔP_{elo} (Eq. 5.18) is a factor $\frac{4}{3}$ larger than the result for the cylindrical system (Eq. 4.27). Generally the shear pressure drop (Eq. 5.19) is also larger, but a simple relation with respect to the cylindrical system (Eq. 4.28) cannot be given.

Author & Reference	F	Remarks
Huzarewicz et al. [5]	1.59	Experimental
Deiber et al. [6]	1.57	Experimental
Lahbabi et al. [7]	1.65	Numerical Navier-Stokes solution
Plitsis et al. [8]	1.65	Numerical Navier-Stokes solution
Tilton et al. [9]	1.66	Numerical Navier Stokes solution
Zitha et al. [10]	1.65	Numerical Stokes solution
Bird et al. [3]	1.58	Traditional LAM = shear term F_2 (Eq. 4.39)
this work [2]	1.66	new LAM, F_2 (Eq. 4.39)
this work [2]	1.71	new LAM, F_4 (Eq. 5.25)

Table 5.1 Pressure drop measurements and predictions for flow of a Newtonian fluid through a sinusoidal tube ($a = 0.30$, $b = 2\pi$)

Table 5.1 shows pressure drop measurements, numerical predictions and LAM predictions from literature²⁶ for flow of a Newtonian fluid through a sinusoidal tube with $a = 0.30$ and $b = 2\pi$. The LAM predictions from Chapter 4 and 5 are also included. The results are expressed in terms of F , which is the dimensionless factor

²⁶ In literature measurements and numerical predictions are available only for this specific geometry.

with which the Hagen-Poiseuille law [3] has to be multiplied to obtain the pressure drop over one wavelength λ of sinusoidal tube. Tab. 5.1 shows that the measurements [5-6] result in somewhat smaller pressure drops than the numerical predictions [7-10]. The pressure drop prediction from the cylindrical LAM approach gives a pressure drop prediction, which is about 5% larger than the average experimental value and equal to the value of the numerical solutions. For this geometry the spherical LAM approach gives a pressure drop prediction, which is about 8% larger than the average experimental value and about 4% larger than the value of the numerical solutions. It can be concluded from Table 5.1 that for this specific geometry both methods give reasonable pressure drop predictions.

The predictions in Chapters 4 and 5 are obtained by doing some model assumptions to simplify the problem of porous media flow of polymer solutions: The rheology is supposed to be time independent. No adsorption occurs in the porous medium (or its influence is negligible). The pores have a well defined geometry. Despite these simplifications, many of the pressure drop expressions given have been obtained after quite extensive mathematical derivations. More background information on the importance of time dependency is given in Appendices A and B. Information on the coil-stretch transition and its relevance to porous media flow is given in Appendix A. Appendix B provides the summary of an experimental study on the influence of the flow rate on the pressure drop for flow of dilute Polyacrylamide/water solutions in high permeability packed beds of glass beads.

5.5 Summary

1. The LAM description in terms of spherical co-ordinates allows a better definition of the deformation rates present during flow (Figure 5.2) and consequently it allows more accurate pressure drop predictions. The method is therefore a clear improvement over the classical LAM and its application is recommended.
2. The predictions resulting from the spherical system result in larger pressure drops than those from the cylindrical system. This is caused by the fact that also radial contributions can be taken into account.
3. The predictions obtained for flow of the Newtonian fluid in the sinusoidal tube are in good agreement with both measured and numerical predictions (Table 5.1).
4. The predictions have been converted in porous media models, i.e. capillary models which do take into account elongational dissipation. Apart from the prediction of pressure drops, these corrugated capillary models can also be useful for the description of two phase immiscible flow problems, e.g. to account for capillary pressure effects in oil/ water flow (see appendix C).
5. For comparable geometries the sinusoidal capillary model geometry gives a higher dissipation than the widening/converging capillary model. This is caused by the inherently higher elongational rates in its flow field.

References (Chapter 5)

1. K. Denys, K. te Nijenhuis, paper in preparation on widening/converging tube flow
2. K. Denys, K. te Nijenhuis, P. Zitha, paper in preparation on sinusoidal tube flow
3. R. Bird, R. Armstrong, O. Hassager, "Dynamics of Polymeric Liquids", John Wiley & Sons, New York (1987)
4. P. Schaum, "Complex Functions", Los Angeles (1992)
5. S. Huzarewicz, R. Gupta, R. Chhabra, *J. Rheol.* **35**, 221 (1991)
6. J. Deiber, W. Schowalter, *A.I.Ch.E.J.* **25**, 638 (1979)
7. A. Lahbabi, H. Chang, *Chem. Eng. Sci.* **41**, 2487 (1986)
8. S. Plitsis, A. Souvaliotis, A. Beris. *J. Rheol.* **35**, 605 (1991)
9. J. Tilton, A. Payatakes, *A.I.Ch.E.J.* **30**, 1016 (1984)
10. P. Zitha, F. Vermolen, H. Bruining, SPE conference paper 54737, The Hague (1999)

CHAPTER 6 - PERMEABILITY MODIFICATION AND RHEOLOGY OF AQUEOUS POLYACRYLAMIDE SOLUTIONS²⁷

6.1 Water shut-off treatments

6.1.1 Introduction

Many operators of mature oil and gas fields are faced with a high water production coming from an underlying natural water source or from previous stimulation attempts involving water injection. This water production causes huge economic and operational problems. It decreases oil production, results in large amounts of water that need to be disposed and gives extra costs related to oil/water separation, handling and lifting. Other problems include the increased tendency for the formation of emulsions, precipitates and corrosion. Consequently, water production decreases the economical lifetime of an oil well and thus there is a need to reduce it. The water production problems encountered can be classified as either near-wellbore related or reservoir related [1]. Typical examples of the first category are breakdown of a natural barrier due to pressure differences during production or stimulation attempts, leaks in the casing by corrosion or high local stresses or channels behind the casing, which usually result from a poor cementing job. Typical reservoir related problems are:

- Fingering (Figure 6.1a), which occurs when the mobility of the displacing fluid is higher than that of the displaced fluid. In this case instabilities at the displacement front may lead to the growth of fingers. In water flooding operations recoverable oil reserves can become bypassed by these fingers resulting in poor sweep efficiency and an early water breakthrough in the production well.

²⁷ A part of the work described in this chapter has been published in a SPE paper: P. Zitha, K. van Os, K. Denys, SPE 39675, Tulsa, 1998

- Channeling (Figure 6.1b) occurs when high permeability channels exist between a water source and the production well. Reservoirs suffering from channelling generally show an early water breakthrough and poor sweep efficiency irrespective of the type of driving mechanism.
- Coning (Figure 6.1c) is the attraction of water from an adjacent connected zone towards the well bore due to a reduced pressure caused by production. Eventually this leads to water breakthrough in the perforated sections replacing hydrocarbon production. On a global scale channeling and coning are the main causes for excessive water production.

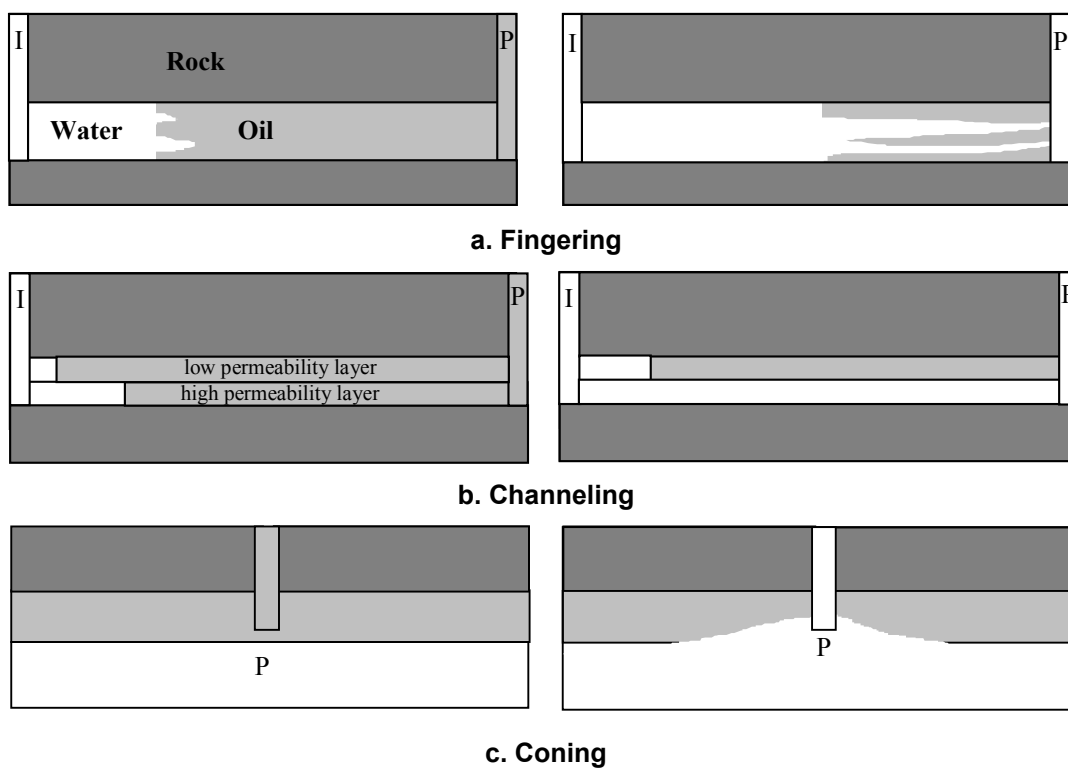


**Figure 6.1 Sketches of reservoir related water production problems
(I = Injection well, P = production well)**

The technology, which intends to reduce water production, is called *water shut-off* or *conformance*. It can be subdivided into separation-, mechanical- or chemical methods. An example of the first category is downhole separation, which comprises oil/water separation in the well near the producing interval using a hydro cyclone [2,3]. The oil-rich stream is sent upwards, while the disposal water stream is reinjected in zones, which do not contact the oil-producing zones directly. This technology is still in the development and field trial stage.

Mechanical methods are based on the principle of hindering flow by placing mechanical barriers within the wellbore. One example is the inflatable packer, which is a tool, which, after lowering to the required setting depth, can be inflated to form a seal against the casing. An advantage is that it can be used in vertical and horizontal wells, in open and in a cased hole. An important limitation is the fact that the maximum pressure differential the inflatable packer can hold is around 100 bar.

The concept in chemical methods is that injected materials interact with the rock material of water-producing layers resulting in a decrease of water production or in full plugging. The aim is to reduce the water cut or to divert water into unswept oil-saturated layers. Classically the following distinction is made regarding the chemical treatments to be used to tackle the water problem [4]:

- If water and hydrocarbon zones are clearly separated, permanent barriers, which are placed in the water-producing zones, should be applied. Note that an important condition is that the productivity of the pay zone is not affected by the chemical treatment. These *full-blocking treatments* can be done by cements, resins or strong polymer gels.
- If hydrocarbon and water zones are not clearly distinguishable or there is a high level of cross-flow between layers, the use of total shut-off is risky. In this case disproportionate permeability reducers (DPR's), usually polymer solutions or weak polymer gels should be applied. The aim is to reduce water flow selectively while not influencing oil flow. The effectiveness of *DPR treatments* is based on the fact that adsorption of hydrophilic polymers can strongly decrease the relative permeability to water while having little effect on the relative permeability to oil (see Appendix C).

Initially DPR systems were considered to be “magic products” i.e. systems that can be pumped downhole without the requirement for zonal isolation and which will reduce the water production no matter the reservoir conditions. However, the poor initial track record of these systems, typically a 30% success rate, has triggered studies to better understand the mechanisms and the conditions under which DPR systems have optimal performance (see section 6.1.3). For example the WELGEL consortium between several research institutions and oil companies intends to develop optimised

DPR systems [5]. Polymer treatments are nowadays used on a regular base and the application is expected to grow in future, as water production is an increasing problem [6-12]. An important advantage of polymer systems over cements is their lower viscosity and their non-particle nature, which enable penetration in the formation at larger depths and smaller permeabilities. Moreover, they can be easily removed from the borehole by water recirculation. Also the flexibility in the permeability modification is an advantage; Cements can only accomplish full blocking, while the impact of polymer treatments can be controlled by changing the formulation. Although most polymer shut-off treatments are usually done at the production well, injector treatments also exist. Usually their aim is to direct injected fluids to the desired oil-bearing zones bypassed in previous water flooding operations. Production well treatments are more popular since their effect is faster and their impact on the oil/water ratio is generally larger. The advantage of injector treatments is that there is no need to stop production and that failures have a larger chance of correction.

6.1.2 Full-blocking treatments

As mentioned before, these treatments aim at fully sealing off watered-out zones with strong gels placed by using mechanical tools (coiled tubing, packers etc.). In most cases this will be a water-producing layer, but also a block at the bottom to prevent water coning is regularly applied.

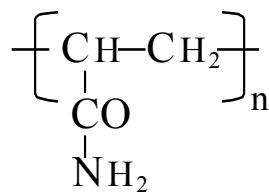


Figure 6.2 Molecular structure of non-ionic Polyacrylamide

The desirable characteristics of the gelants, the gel forming fluids, are good injectivity, programmable gelation delay, good polymer and cross-linker propagation, insensitivity of cross-linking chemistry to fluid-rock and fluid-fluid interactions and good gel stability under reservoir conditions. The main gelants currently employed in industry are based on the Polyacrylamide (PAM)/ Chromium (Cr^{3+}) system [9,13]

(see Figure 6.2). This relatively cheap system is reliable and robust and has a good track record for use up to temperatures of 70°C [14]. Above this temperature problems exist:

- At 70°C the system undergoes gelation in a few hours, while at 100°C gelation occurs within a few minutes, which is too fast for shut-off treatments [15].
- The polymer has a tendency to hydrolyse in time. This decreases its solubility, especially in hard brines, and leads to precipitation or gel syneresis, the contraction of a gel under expulsion of water. Hydrolysis is faster at high temperatures [16].
- Propagation studies indicate that retention of the Cr^{3+} crosslinker in porous media can be a serious problem due to the formation of insoluble colloids. The tendency of these Cr^{3+} complexes to precipitate increases with pH and temperature [17].

Various methods have been studied to address the above-mentioned problems. A method to delay the fast gelation reaction is cooling the formation with a pre-flush [18]. A method to reduce Cr^{3+} retention is to add a chelating ligand, e.g. acetate, which stabilises Cr^{3+} by complex formation and retards the porous media induced pH rise [19]. New developments include copolymers of acrylamide with improved thermal stability [20] and the use of the less toxic zirconium as cross-linking agent [21]. Concerning gel placement, the most ideal location for the gel in a water producing layer is far from the wellbore, typically 5-15 m., aiming to reduce water channeling and to avoid an unacceptable loss of well productivity. Also the lower drawdown pressure far from the wellbore allows weaker formulations i.e. smaller polymer- and crosslinker concentrations. Gel treatments are most effective when the gel penetration is restricted to the watered-out layers and leak-off to low permeability oil containing layers can be avoided. Gel placement is therefore critical and much effort has been put into developing techniques to control it [22-24]. Important aspects for this are the gelant rheology and the methodology used to obtain zonal isolation.

A recent development is gel technology to obtain zonal isolation in horizontal wells. Starting in the 1980s, horizontal well drilling has gained enormous popularity on a global scale. This is caused by the fact that the productivity index of these wells is usually much higher. Generally horizontal producers are the best choice for thin

reservoirs ($h < 20$ m) or for thicker reservoirs with good vertical permeability. However, due to their long production intervals and open annulus, these wells are more likely to suffer from water inflow. Currently fit for purpose gels and placement technologies are being developed to provide shut-off in horizontal wells [25].

6.1.3 DPR treatments

Often for a well engineer injecting the polymer treatment without any zonal isolation, i.e. bullheading, is the only valid option. Frequent causes are a poor identification of the different zones around the wellbore, a multi-layered production, an unfavourable completion (e.g. gravel packs or slotted liners) or excessive workover costs (e.g. offshore wells, marginal wells). Also the development of horizontal wells calls for more bullhead treatments. The DPR systems are considered to be attractive bullhead systems since it they do not harm the permeability of the pay zones. Indeed studies indicate that, both for polymer solutions and gels, adsorption decreases the relative permeability to water with little effect on the relative permeability to oil [26-30].

An extensive study on the DPR phenomenon was done by Barreau et al. [27]. These authors used water-wet sandstone cores and oil-wet sandstone cores, rendered oil-wet by a silane treatment, to study the influence of PAM adsorption on the two-phase flow properties (see appendix C). For both type of cores the authors confirmed the DPR phenomenon. For the water-wet cores the authors measured a ratio between the water relative permeability before and after polymer adsorption, at residual oil saturation S_{or} , equal to 22. For the oil relative permeability, at irreducible water saturation S_{wi} , this ratio was equal to 1.6. In addition, after polymer adsorption the authors observed: i) no change in S_{or} ; ii) an increase in S_{wi} from 0.33 to 0.49 and iii) a strong increase in the capillary pressure P_c . The increase in S_{wi} was attributed to the increased amount of polymer hydration water. The increase in P_c was attributed to pore throat size reduction. For the oil-wet cores the authors measured a ratio between the water relative permeability before and after polymer adsorption, at S_{or} , equal to 4.3. For the oil relative permeability, at S_{wi} , this ratio was equal to 2.3. After polymer adsorption i) S_{or} decreased strongly from 0.54 to 0.17, ii) S_{wi} increased from 0.32 to 0.49 and iii) P_c increased dramatically from negative to positive values. Both changes in S_{or} and P_c were attributed to a change in wettability. The increase in S_{wi} was attributed to the

increased amount of polymer hydration water. Barreau et al. [27] believe that wall effects are the cause for the DPR effects. The explanation for the DPR phenomenon continues to be a matter of debate in literature. Three mechanisms are often cited but there is no consensus on which mechanism is actually occurring:

- Polymer swelling/shrinking. The adsorbed polymer swells in the presence of water and shrinks in the presence of oil [30].
- Fluids partitioning. Oil and water flow through separate channels. The polymer preferentially penetrates the water paths reducing the water mobility [32].
- Wall effects. Polymer adsorption induces steric-, lubrication- and wettability effects [26,33]. Steric effects refer to pore flow cross-section reduction. Lubrication effects deal with oil flow lubrication as a result of the larger water film at the walls. Wettability effects are related to wettability changes due to polymer adsorption.

Concerning the required reservoir conditions to apply DPR systems, it is currently generally accepted that these systems only work when water and oil are produced from separate layers. If the water and oil come from the same layer, the DPR will cause a decrease in the water production in the near wellbore. As a result the water will accumulate further away where it will act as a choke causing a reduction in the permeability for oil and thus having a negative impact on oil production.

It is clear that knowledge of polymer propagation- and retention mechanisms in porous media is indispensable to the development of effective shut-off- and polymer flooding treatments. In the following rheological-, static adsorption- and coreflood experiments on aqueous PAM solutions in synthetic cores packed by silicon carbide (SiC) grains are discussed. PAM and its derivatives are popular in both DPR- and polymer flooding operations due to their low cost and long time experience available²⁸. Owing to their chemical similarity, packed SiC grains are frequently used as a model system for sandstone in lab studies. The goal of this study was to obtain information on polymer rheology and retention behaviour in sandstone-like porous media and in particular on the influence of polymer concentration and molecular weight on the mobility reduction and the permeability reduction to water and to oil.

²⁸ Already in the end sixties Polyacrylamides have been applied in polymer flooding operations.

6.2 Characterisation of Polyacrylamide/brine solutions

6.2.1 Polymer and polymer solution preparation

Non-ionic Polyacrylamide (PAM) (see Figure 6.2) is an amorphous polymer whose appearance is white, wool-like, when freeze dried and glassy, hard and partly transparent when precipitated in methanol²⁹. Table 6.1 shows some physical properties of PAM. In the experiments two PAM samples of different molecular weight have been used. Table 6.2 shows product information on the molecular weight, the degree of hydrolysis (*DH*, determined by titration) and water content of the solid polymer (*WC*, by freeze drying). Note that the degree of hydrolysis is the percentage of monomers, which possess an OH group instead of a NH₂ group (Figure 6.2).

PAM	
Monomer weight	71.1 g/mole
Density	1302 kg/m ³
Glass temperature	438 K
Solvents	Water, formamide, ethylene glycol

Table 6.1 Some physical properties of PAM

Polymer	Manufacturer & sample ref.	M_w [10 ⁶ g/mole]	M_w/M_n	<i>DH</i> [%]	<i>WC</i> [wt.%]
PAM1	Polysciences 02806	5	2.2	0.1	10.5
PAM2	SNF Floerger VHM 920	10	2.1	0.2	10.4

Table 6.2 Product information on the PAM's used.

²⁹ Non-ionic means here that the monomer groups do not carry any free charges, i.e. the polymer is not a polyelectrolyte. In practice, however, for non-ionic PAM usually a finite but small degree of hydrolysis always exists (Table 6.2).

The PAM/brine solutions were obtained by dissolution of the solid polymer particles in brine. This brine was prepared by adding 0.34 M sodium chloride (NaCl) and 0.006 M sodium azide (NaN₃) to double distilled water. Sodium azide was added to inhibit polymer degradation by bacteria. Subsequently the brine was filtered through a 0.22 µm Millipore™ filter. After preparation, the brine was stirred and a vortex was created. The polymer was added in a slow manner to the vortex in order to avoid polymer agglomeration. After addition the fluid was cautiously stirred during 15 hours to complete the dissolution process. This time span was enough to obtain homogeneous polymer solutions in equilibrium. Before injection into the cores the polymer solutions were filtered at 6 ml/h through a set of Millipore™ membranes (pore diameter 8, 3 and 1.2 µm in series) in order to remove microgels. This procedure did not result in a notable change in polymer concentration.

6.2.2 Polymer solution characterisation

In order to gain information on the coil size in solution and the molecular weight distribution, gel permeation chromatography (GPC) has been attempted using water as driving fluid. This measuring technique however gave huge problems due to the high affinity of the polymer to adsorb on the column material, a well-known problem for high molecular weight hydrophilic polymers. Besides, at molecular weights of 1 x 10⁶ g/mole and larger, light scattering on PAM/water becomes highly unreliable since the Zimm diagram shows curved angular dependencies [34,35]. A choice was made to comply with coil size estimations by combining intrinsic viscosity measurements with information on PAM from literature. Rheological measurements have been conducted on the PAM/brine solutions using a Couette type rheometer, a Contraves LS40™. This rheometer is well suited to measure viscosities as low as the water viscosity (typically 1 mPas at room temperature). By performing viscosity measurements at small shear rates the intrinsic viscosity $[\eta]$, which characterises the ability of a polymer to increase the solvent viscosity after dissolving (Eq. 6.1), was determined:

$$[\eta] = \lim_{c \rightarrow 0} \frac{\eta_{sp}}{c} = \lim_{c \rightarrow 0} \frac{\eta_p - \eta_s}{\eta_s c} \quad (6.1)$$

where η_{sp} is the specific viscosity, η_p is the polymer solution viscosity, η_s is the solvent viscosity and c is the polymer concentration. Apart from temperature, the intrinsic viscosity depends on molecular weight, the interaction between the specific polymer/solvent system and chain rigidity. Figure 6.3 shows the curves for η_{sp}/c vs. c for both PAM's. Extrapolation to $c = 0$ yields intrinsic viscosities for PAM1 and PAM2 of respectively 0.82 l/g and 1.84 l/g. Logically, the intrinsic viscosity of PAM1 is much smaller due to its smaller molecular weight.

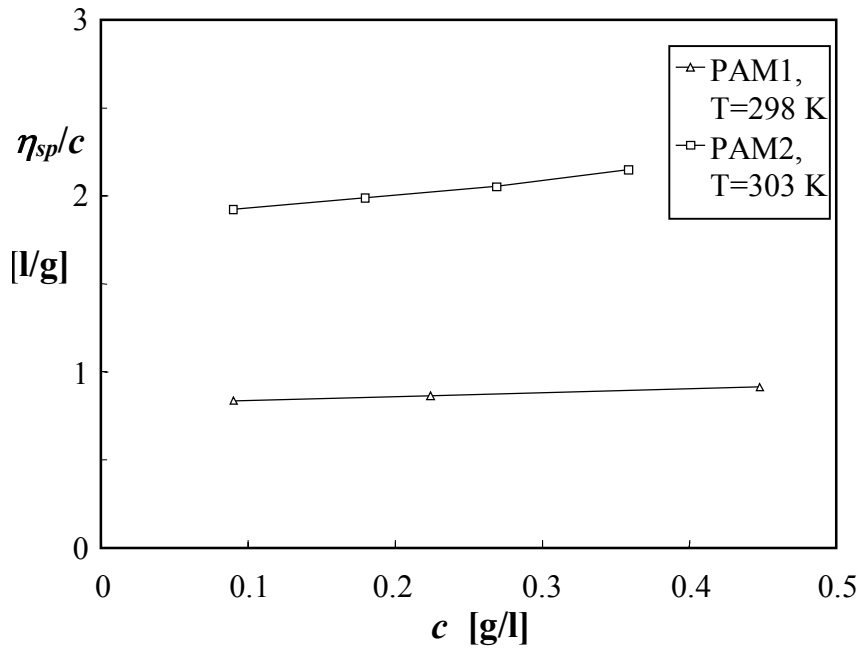


Figure 6.3 η_{sp}/c vs. c for both PAM's

The average conformation of a dissolved polymer coil can be described using statistic mechanics. Let us assume N chain units (length b_c) are linked to each other with both bonding and rotational restrictions. The root mean square radius of gyration ($\langle R_g^2 \rangle_o^{1/2}$), which equals the average value of the square of the distance of the segments from the centre of mass³⁰, can now be calculated by:

$$\left(\langle R_g^2 \rangle_o \right)^{1/2} = \left(\frac{N}{6} C_\infty \right)^{1/2} b_c \quad (6.2)$$

³⁰ Assuming the end-point distribution is Gaussian

where C_∞ is a rigidity constant, which accounts for all bonding and rotational restrictions. Note that for vinyl polymers like PAM, $N = 2M/M_m$. Here M_m is the molar mass of the monomer unit and b_c equals 0.154 nm, the C-C bonding length. The subscript o in Eq. 6.2 denotes the unperturbed state dimension. This is the dimension, which the polymer molecule adopts, when it is free of external constraints such as an applied force and when attractive and repulsive interactions cancel out.

The root mean square radius of gyration $(\langle R_g^2 \rangle)^{1/2}$ is an important property since it is generally used as a measure of the size of the polymer coil in solution. C_∞ can be determined experimentally by light scattering. Values for C_∞ are typically in between 3 and 20 and are widely available in literature. Predictions can be obtained by the group contribution method of Van Krevelen [36]. Light scattering studies³¹ have resulted in $C_\infty \approx 13$ for PAM [37].

Real polymer solutions also show long-range interactions, which can be subdivided in attractions due to dispersive forces and repulsions due to the inability to occupy the same point in space. In the dilute state interactions between different polymer molecules can be ignored, but interactions between different segments of the same polymer molecule cannot be neglected. This type of steric hindrance is called the excluded-volume effect. Flory and Fox [38] corrected the unperturbed mean square end-to-end distance for long range interactions by introducing an empirical factor α_i :

$$(\langle R_g^2 \rangle)^{1/2} = \alpha_i (\langle R_g^2 \rangle_o)^{1/2} \quad (6.3)$$

In a good solvent the attraction between polymer segments and solvent molecules is larger than the attraction in between polymer segments. Consequently, the coil will be swollen ($\alpha_i > 1$). In a poor solvent the reverse is true and the coil is in a collapsed state ($\alpha_i < 1$). In between a good and a poor solvent is the Θ -solvent, where the effect of the attractive forces cancels the effect of the physical excluded volume ($\alpha_i = 1$). Thus under Θ -conditions Eq. 6.2. is valid.

³¹ Using its Θ -solvent 59/41 water/methanol at 294 K

Kirkwood and Riseman [39] obtained for the intrinsic viscosity of a polymer coil under Θ -conditions with maximum interaction between the segments i.e. the so-called non-free draining limit:

$$[\eta]_{\Theta} = \frac{\Phi \langle R_g^2 \rangle_{\Theta}^{3/2}}{M} = K_{\Theta} M^{1/2} \quad (6.4)$$

where Φ is a constant with the dimension mole^{-1}

This equation gives a direct relation between the intrinsic viscosity and the coil size. Experiments have confirmed that $[\eta]_{\Theta} \sim M^{1/2}$ over a large molecular weight range. Values for Φ have been found in the range $2.9 \times 10^{24} < \Phi < 4.0 \times 10^{24}$, although $\Phi = 3.75 \times 10^{24} \text{ mole}^{-1}$, the value found for the model system Polystyrene in cyclohexane at 307 K, is considered as more or less universal i.e. valid for all systems. Combination of Eq. 6.2 and 6.4 gives $K_{\Theta} = 2.06 \times 10^{-4} \text{ l}^3 \text{ mole}^{1/2} \text{ g}^{-3/2}$ for PAM. From literature is known that brine is a reasonably good solvent for PAM, i.e. the coils are swollen ($\alpha_i > 1$ in Eq. 6.3). Kulicke and Haas [40] found $[\eta] \sim M^{0.70}$ in 0.34 M NaCl brine by light scattering at $T = 298 \text{ K}$. Combination of Eq. 6.3 and 6.4 yields:

$$\alpha_i = \left(\frac{[\eta]}{K_{\Theta} M_v^{1/2}} \right)^{1/3} \quad (6.5)$$

Eq. 6.5 is an expression for polydisperse polymers. Instead of the molecular weight M , a viscosity average molecular weight M_v is used³². Usually M_v is slightly smaller than the weight average molecular weight M_w . Table 6.3 shows the predictions of the radius of gyration under Θ -conditions and in brine for the PAM's studied.

³² For a Flory distribution ($M_w/M_n=2$) holds: $M_v = \frac{1}{2} M_w \left((1 + a_m) \Gamma(1 + a_m) \right)^{\frac{1}{a_m}}$. Here $\Gamma(x)$ is the Gamma function and a_m is the Mark-Houwink index. This index was determined to equal 0.70 for PAM in brine [40]. This value has been used in Table 6.3.

Polymer	$(\langle R_g^2 \rangle)^\ominus$ [nm] (Eq. 6.2)	$[\eta]^\ominus$ [l/g] (Eq. 6.4)	α_i (Eq. 6.5)	$(\langle R_g^2 \rangle)^{1/2}$ [nm] (Eq. 6.3)
PAM1	85	0.46	1.22	104
PAM2	120	0.65	1.43	172

Table 6.3 Predictions of the radius of gyration $(\langle R_g^2 \rangle)^{1/2}$ under \ominus -conditions and dissolved in brine for the PAM's studied

6.2.3 Rheological characterisation

Figure 6.4 shows measurements of the stationary viscosity vs. the shear rate for PAM1/brine solutions at different polymer concentrations. Included are fits of the measurements by the Carreau model [41]:

$$\frac{\eta_p - \eta_{p\infty}}{\eta_{p0} - \eta_{p\infty}} = \left(1 + \lambda_l^2 \dot{\gamma}^2\right)^{\frac{n-1}{2}} \quad (6.6)$$

where $\eta_{p\infty}$ is the infinite shear rate viscosity, η_{p0} is the zero shear rate viscosity, λ_l is a relaxation time and n is a power law constant. The fits were made by assuming that $\eta_{p\infty} = \eta_s$ while using linear regression with the least square method. In this way for each concentration a combination of λ_l and n was determined (see appendix D).

Figure 6.5 shows measurements of the stationary viscosity vs. the shear rate for PAM2/brine solutions at different polymer concentration. Included are fits of the measurements by the Carreau model [41] (see appendix D).

Increasing the polymer concentration decreases the distance between different polymer coils. The coils start to overlap when exceeding the critical concentration c^* . The Simha criterion, $[\eta]c^* \approx l$, is frequently used to mark the transition towards the semi-dilute regime. This yields here: c^* (PAM1) \approx 1.2 g/l and c^* (PAM2) \approx 0.5 g/l.

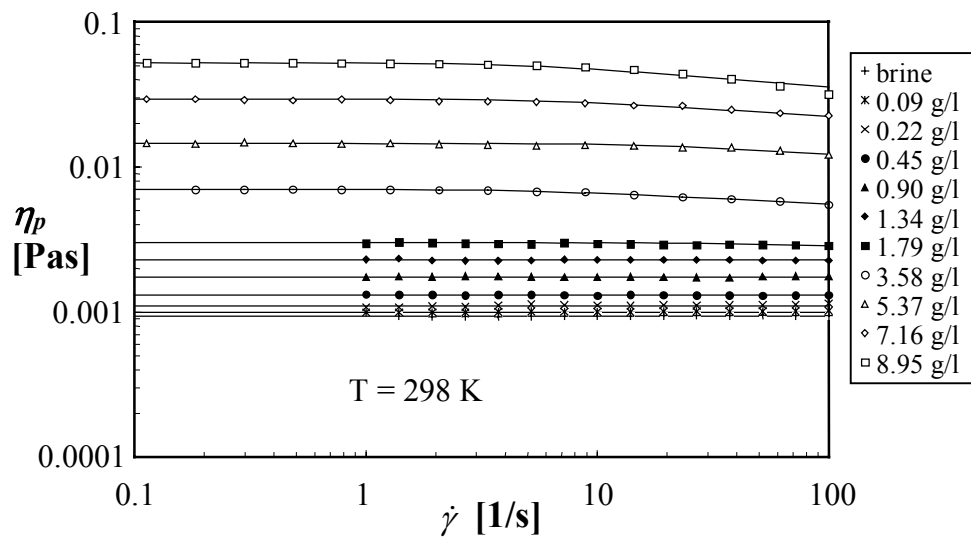


Figure 6.4 Measurements of the viscosity vs. the shear rate for PAM1/brine solutions. Included are fits by the Carreau model

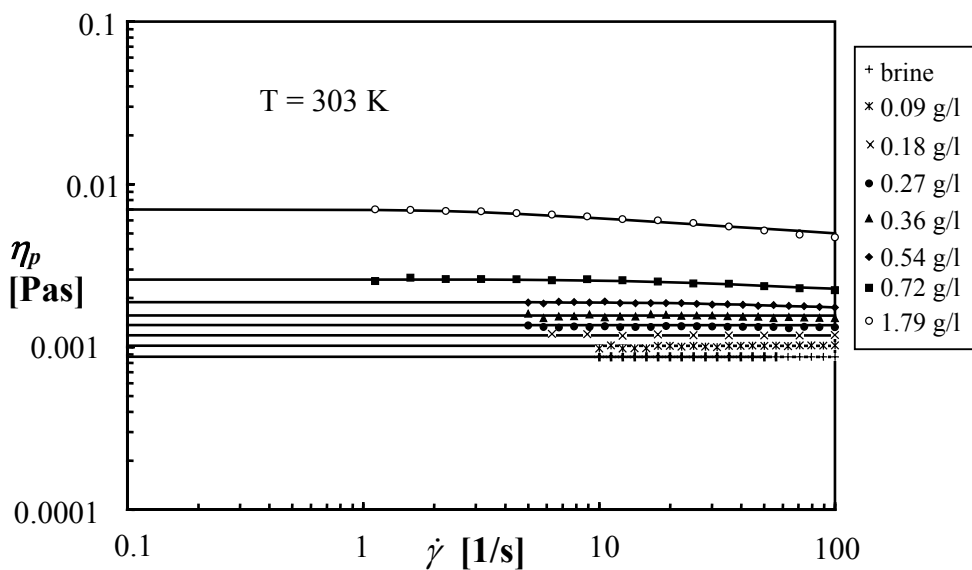


Figure 6.5 Measurements of the viscosity vs. the shear rate for PAM2/brine solutions. Included are fits by the Carreau model

The PAM1/brine solutions behave shear-thinning at a concentration of 1.79 g/l and higher (Figure 6.4), the PAM2/brine solutions at 0.54 g/l and higher (Figure 6.5). The shear-thinning behaviour can be associated with coil deformation (dilute regime) or the presence of entanglements (semi-dilute regime). For both PAM systems shear-thinning behaviour becomes more pronounced, and it starts at smaller shear rates, at higher concentrations. It is more prominent for the high molecular weight PAM2 system.

6.3 Static adsorption experiments

The advantage of the use of synthetic cores to study porous media flow problems with respect to natural rock, is the ease in obtaining a rather homogeneous pack and the relatively simple core reproduction. The coreflood experiments described in this chapter have been performed on unconsolidated porous media, obtained by packing silicon carbide (SiC) grains in a core holder. SiC is an abrasive, angular material, which is used in industry to polish materials. Figure 6.6 shows scanning electron microscope (SEM) pictures of 30 μm SiC grains [42].

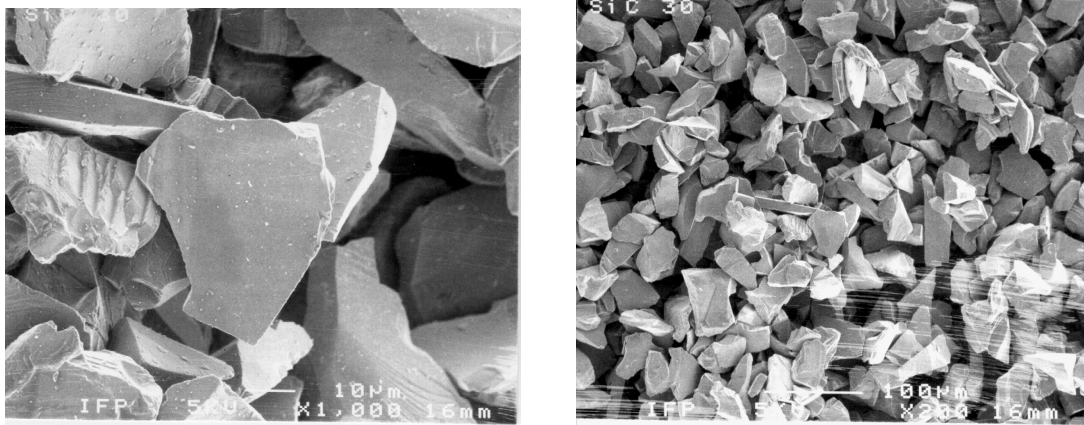
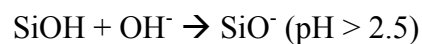


Figure 6.6 SEM pictures of 30 μm SiC grains from Zitha [42]

SiC is an interesting core material because of its chemical resemblance to sandstone. From literature it is known that SiC is covered by a thin oxidised layer, which carries silicon hydroxide groups (SiOH) giving it more or less similar properties as sand (SiO_2) [43]. The proportion of silica groups on the surface is known to equal about 30% [44]. The surface charge of silicon carbide is governed by the ionisation reactions of the SiOH groups at the surface:



In our experiments the SiC surface charge was always negative ($\text{pH} \approx 7$). Before use, the SiC grains have been submerged in a 1 M HCl bath to dissolve initially present carbonates or iron impurities. Then the grains were rinsed in double distilled water

until a neutral pH was reached. The SiC grains, as supplied by the Peter Wolters company (density 3220 kg/m³), contain very fine particles with a size $\approx 0.1 \mu\text{m}$, which have to be removed since they cause a dramatic increase in the specific area. The following procedure was applied: SiC grains were added to a bottle of double distilled water, which was placed in an ultrasonic bath for 15 minutes. The suspension was then shaken vigorously and allowed to settle during 20 seconds. Subsequently the unsettled suspension of fines was removed. Fresh water was added and the procedure was repeated until the water above remained clear, usually after 20 seconds of settling. The cleaned SiC suspension was then put in a furnace at 313 K in order to dry for 2 days.

Static adsorption experiments have been conducted to determine the quantity of PAM adsorbed on SiC. In these experiments 30 μm SiC grains have been used. Zitha [42] found an average grain size of 36 μm and a specific area of 0.19 m²/g for the same sample material. An average grain size of 32 μm by light scattering and a specific surface of 0.13 m²/g by the BET adsorption method have been found here.

The amount of PAM, adsorbed on SiC was determined by the indirect method [45]. In this method a separation of the surface layer and polymer solution is accomplished after equilibrium adsorption has been reached. Subsequently the supernatant is analysed to determine the polymer concentration. The adsorbed amount per unit surface area follows from:

$$\Gamma = \frac{\Delta c V_p}{A_s} \quad (6.7)$$

where Δc is the change in polymer solution concentration, V_p is the polymer solution volume used and A_s is the total area available for adsorption.

In the experiments SiC grains have been added to the polymer solution. The suspension was kept for 10 hours under mechanical shaking. From literature is known that equilibrium adsorption for this system is reached after about 5 hours [44]. Subsequently the supernatant was analysed using a DohrmanTM Total Organic Carbon analyser. Note that TOC measures the amount of organic carbon in the solution i.e. the PAM concentration is a factor 71/36 higher (Figure 6.2). Typical amounts of 20 g SiC in 20 ml polymer solution were used in the experiments. Figure 6.7 shows the results of the static adsorption experiments. It shows the plateau adsorption values

were already reached at the smallest polymer concentrations measured. This resulted in $\Gamma(\text{PAM1}) = 0.49 \text{ mg/m}^2$ and $\Gamma(\text{PAM2}) = 0.55 \text{ mg/m}^2$. One may conclude that the adsorbed quantity varies only slightly with molecular weight. This result, predicted by theory for high molecular weight polymers under good solvent conditions [45], has been confirmed for different polymer solution/substrate systems [46,47]. The adsorbed amounts are in good agreement with 0.50 mg/m^2 found by Lecourtier et al. [44] for adsorption of a $7.5 \times 10^6 \text{ g/mole}$ PAM onto SiC grains.

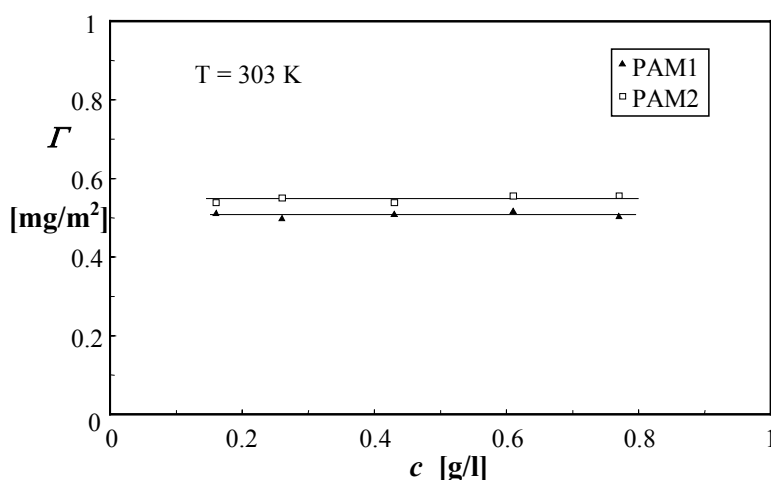


Figure 6.7 The adsorption isotherms of PAM1 and PAM2

PAM adsorption onto minerals was long time thought to be governed only by hydrogen bonding [48-50]. However, van der Waals bonding of the apolar PAM backbone is nowadays considered to be important, especially for hydrophobic surfaces. Broseta and Medjahed [51] studied the influence of hydrophobicity on the adsorption of PAM onto sand. The substrates were rendered hydrophobic by a silane treatment. The hydrophobicity was analysed by contact angle measurements on slides (water drops contacting substrate and dodecane), which yielded 10° for silica, 50° for sand, 120° for the short chain silane treated sand and $>170^\circ$ for the long chain silane treated sand. The adsorption of PAM increased with increasing hydrophobicity: $\Gamma = 0.15 \text{ mg/m}^2$ on silica, $\Gamma = 0.40 \text{ mg/m}^2$ on sand, $\Gamma = 0.49 \text{ mg/m}^2$ on sand with a short chain silane and $\Gamma = 0.72 \text{ mg/m}^2$ on sand treated with a long chain silane. With increased hydrophobicity, when water and hydrophylic polymer parts have decreased surface affinities, van der Waals interaction becomes more important. Note that PAM adsorption on siliceous surfaces is independent of brine salinity [45,49,51].

6.4 Coreflood experiments

6.4.1 Coreflood set-up

A new coreflood set-up is developed which is able to perform accurate pressure drop measurements over a wide range of flow rates. The decision was made to build this set-up after having gained experience with a previous system. Appendix E gives information on the modifications and the procedures applied to perform measurements.

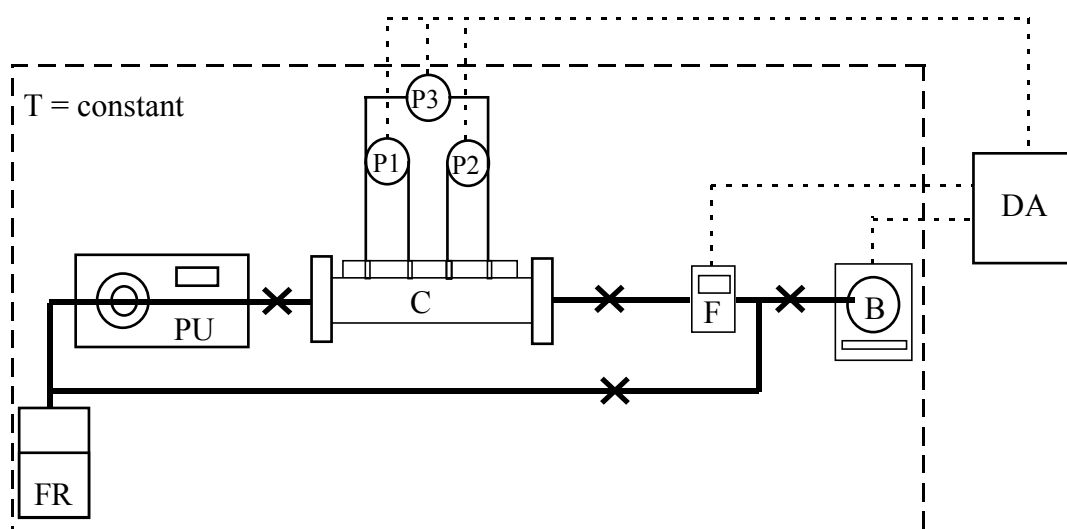


Figure 6.8 The coreflood set-up. FR = Fluid reservoir, PU = pump, C = Core-holder, F = Flow meter, B = Balance, P1-P3 = Differential pressure transducers, DA = Data acquisition system

The coreflood set-up (Figures 6.8 and 6.9) consists of i) a core-holder, ii) two pumps, iii) four differential pressure transducers, iv) two flow meters and one balance, v) a temperature control system, vi) a data acquisition system and vii) tubing, valves and connectors.

- i. The main parts of the core-holder are a cylindrical hollow core made of polymethylmethacrylate (PMMA) and two end pieces of polychlorotrifluoroethylene (PCTFE) and steel (Figures 6.10 and 6.11). The core has an internal diameter of 2.62 cm and a total length of 12 cm. Upon the core a solid PMMA block is glued in which four straight pressure point channels (A, B, C & D) of 0.20 cm diameter have been pierced perpendicular to the core wall and through it.

The aim of the pressure point channels is to enable separate measurement of the pressure drop over three core sections ($S1 = AB$, $S2 = BC$ and $S3 = CD$) (Figures 6.10 and 6.11). The pressure point channels are pierced at a distance of 2.67 cm from each other. So the maximum distance over which the pressure drop can be measured was equal to 8.00 cm. On top of each pressure point channel, Swagelok™ connectors are fitted. Inside the core four polycarbonate (PC) filters are glued on the four holes of the pressure point channels. The aim of these filters is to transfer the local fluid pressure through the channels while avoiding loss of packing material from the core. The end pieces consist of a PCTFE part in which a fluid flow channel of 0.32 cm. diameter is pierced. This PCTFE part, which can be mounted inside a piece of steel (Figures 6.10 and 6.11) has Swagelok™ connectors at one side. By means of rubber O-rings the core can be clamped in the end-pieces. To avoid loss of packing material PC filters are fixed in between the packing material and the end-pieces.

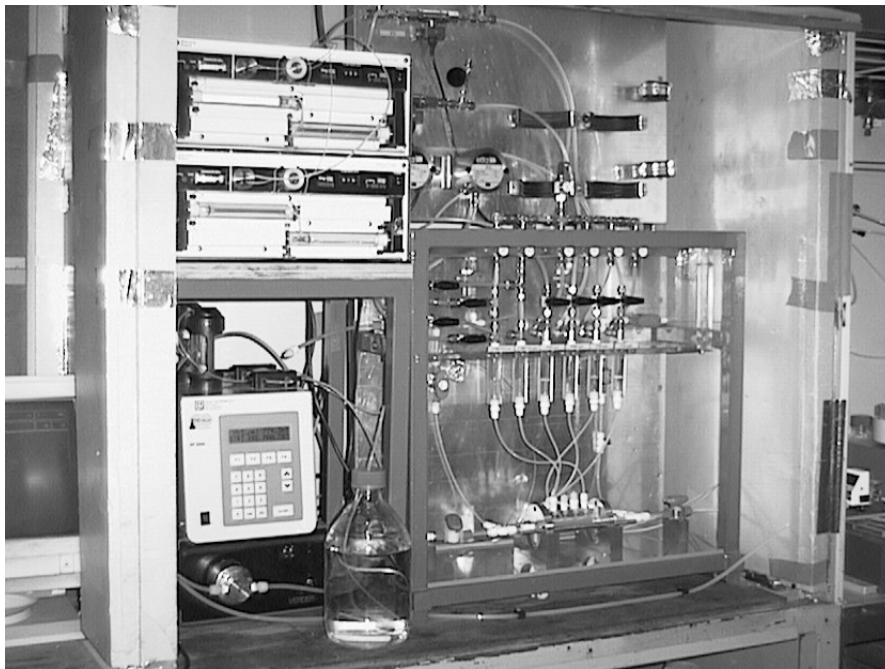


Figure 6.9 A photo of the coreflood set-up

- ii. During measurement only one pump was used (Figure 6.8). The pumps available complement each other in flow rate range. The first pump is a Desaga™ KP 2000 positive displacement pump equipped with two compensating pistons, which

allows to impose continuous flow with an accuracy of 0.1%. All parts of the pump contacting the liquid are made of borosilicate glass (cylinder) or PTFE (valve, piston and tubes). This pump is used for volumetric flow rates of 1-1000 ml/h. The second pump is a Verder™ 2030 gear-wheel pump, which can be equipped with a V 4.16 or a V 15.12 pump head. The internal of the pump head is made of graphite. This pump gives flow without any pulse and can deliver volumetric flow rates of 200-15000 ml/h.

- iii. Differential pressure transducers are used to measure pressure differences over the core sections (Figure 6.8). Transducers are available in the ranges: 0-50 mbar (Effa™), 0-1 bar (Effa™), 0-2 bar (Druck™). Every differential pressure transducer obtains the signal of two pressure point channels from the core. The pressure signals are passed towards the pressure transducers by small PTFE tubes with water as signal fluid. Since the membranes of the pressure transducers cannot withstand water, the signal fluid changed from water to oil before reaching the transducer. This is done in tubes made of PMMA. The few and tiny air bubbles emerging in the pressure measurement system during coreflows are removed carefully in order to avoid their delaying influence on the reaction of the pressure transducers. Generally, small air bubbles do not change the absolute value of the pressure drop measurement. In this set-up there is a full flexibility in the choice which pressure transducer to use for which core section. All pressure transducers are connected to the data acquisition system.

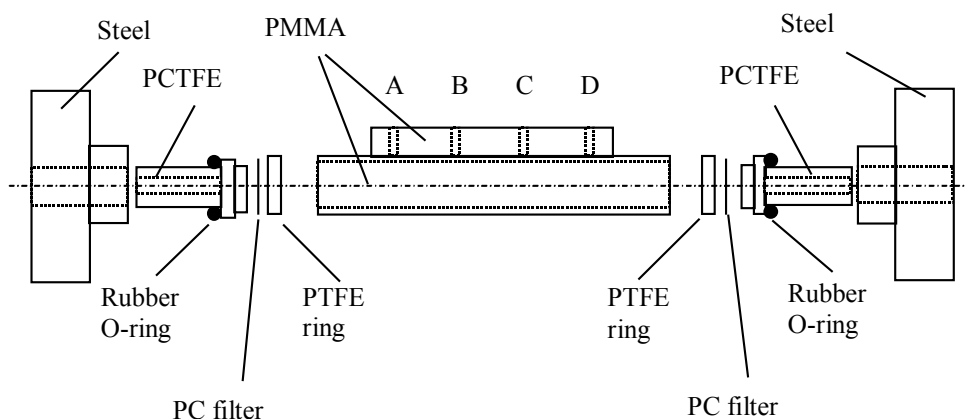


Figure 6.10 Schematic representation of the core-holder. The core sections are respectively S1 (AB), S2 (BC) and S3 (CD)

- iv. Because the flow rate delivered by the gear-wheel pump is dependent on the total system resistance (and thus core permeability) determination of the resulting flow rate is necessary. The flow rate is determined using either a Sartorius™ balance or a McMillan™ propeller flow meter (Figure 6.8). The balance measures the mass of the barrel placed on it. The difference in fluid mass over a certain time interval combined with the fluid density gives the volumetric flow rate. Measuring over long time intervals (typically 20-60 s) reduces drop effects significantly. Adding oil to the barrel, covering the open surface, eliminates water evaporation effects. Because of its better accuracy, the balance is used up to volumetric flow rates of 2000 ml/h. Above this flow rate a McMillan™ flow meter is used which action is based on propeller rotation by fluid drag. The two flow meters available in the set-up (type 111, respectively type 3 and 5) complement each other in the range of measurement. The first flow meter can measure volumetric flow rates up of 1200-6000 ml/h. The second flow meter is able to measure up to flow rates of 6000-15000 ml/h. Both balance and flow meter are connected to the data acquisition system.

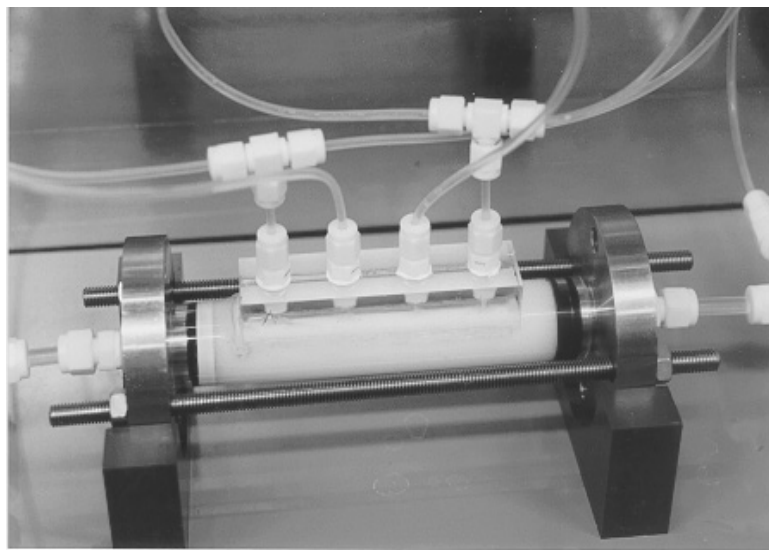


Figure 6.11 A photo of the core-holder

- v. The set-up is placed in a thermally isolated cell into which heated air is injected, which is warmed by a heat exchanger connected to a thermostatic bath. During measurements the sliding doors of the cell remain closed. By this method the temperature can be controlled with an accuracy of 0.5 K. In the set-up and

thermostatic bath, thermocouples are placed to obtain temperature data. These are connected to the data acquisition system.

- vi. The data-acquisition system consists of an amplifier, an AD-converter and a computer equipped with LabtechTM software.
- vii. All tubing, SwagelokTM valves and connectors in the set-up are made of PTFE. This inert material is chosen to eliminate ion release effects known to occur with steel tubing. Release of ions can affect measurements in an uncontrolled manner. This is especially necessary when performing measurements on polyelectrolyte systems, whose adsorption and rheological behaviour can depend strongly on the ionic strength present (see Chapter 8).

6.4.2 Experimental procedure

The coreflood experiments consisted of injections of PAM solutions into 30 μm SiC packs by using the described coreflood set-up. Before use the SiC grains were treated as described in the Section 6.3. The packs were prepared by dry packing SiC grains into the core holder (see Appendix E). By weighing the core before and after packing and taking into account its dimensions and SiC density, the porosity ϕ was determined to be 0.43, meaning that one pore volume (PV) equalled about 18.5 cm^3 . After core saturation the permeability k was determined by brine flow (Eq. 2.1). In these experiments only one pressure transducer was used over the full length of 8.0 cm. The polymer injections were performed at a flow rate of 10 ml/h. After injection of about 15 PV polymer solution, brine was injected at the same flow rate and temperature to determine the permeability reduction. Into some packs, after polymer injection, oil has been injected (at 10 ml/hr) to obtain estimations of the permeability to oil after adsorption. The oil used was Shell TellusTM with a viscosity of 10 mPas at $T = 298 \text{ K}$.

6.4.3 Definitions

In the following the definitions of the permeability reduction, mobility reduction and average shear rate in the porous medium are used as given in Eqs. 2.21 – 2.23. The hydrodynamic adsorbed layer thickness ε_h can be deduced from the permeability

reduction R_k when assuming that the pore radius R_p (Eq. 6.9) is reduced by an uniform impermeable polymer layer:

$$\varepsilon_h = R_p \left(1 - R_k^{-0.25}\right) \quad (6.8)$$

Since these SiC packs are generally very homogeneous porous media, an effective pore radius R_p can be defined by making use of the capillary bundle model:

$$R_p = \alpha_s \sqrt{\frac{8k}{\phi}} \quad (6.9)$$

where k is the permeability, ϕ the porosity and α_s is a geometrical factor, which depends on the porous medium structure. Note that $\alpha_s \approx 1.15$ for angular particles like SiC grains.

6.4.4 Coreflood results

By making use of Eq. 2.23 one finds for the effective shear rate during polymer solution injection $\dot{\gamma}_p \approx 30 \text{ s}^{-1}$, meaning that the deformation rates are small and that adsorption is the retention mechanism to be expected. Figure 6.12 and 6.13 show the mobility reduction R_m as a function of PV for PAM1 and PAM2 injections at different polymer concentrations. In all curves, except at the highest concentrations, three sections can be distinguished. At first R_m is equal to one, as the polymer solution has not yet reached the first pressure drop point of the core. Then R_m increases more or less linearly with PV . This is a result of the combined action of brine displacement by a polymer solution with a higher viscosity and polymer adsorption inducing a permeability reduction. Finally, R_m levels off to a plateau value R_{mp} when adsorption is fully accomplished and thermodynamic equilibrium is reached. The time to reach a real plateau is long as R_m continues to increase very slowly in time due to rearrangement of the adsorbed layer. This involves the replacement of small polymer chains, which diffuse and adsorb faster, by larger polymer molecules. The kinetics of

this exchange process are slow, especially under dilute conditions as the osmotic pressure forms an energy barrier.

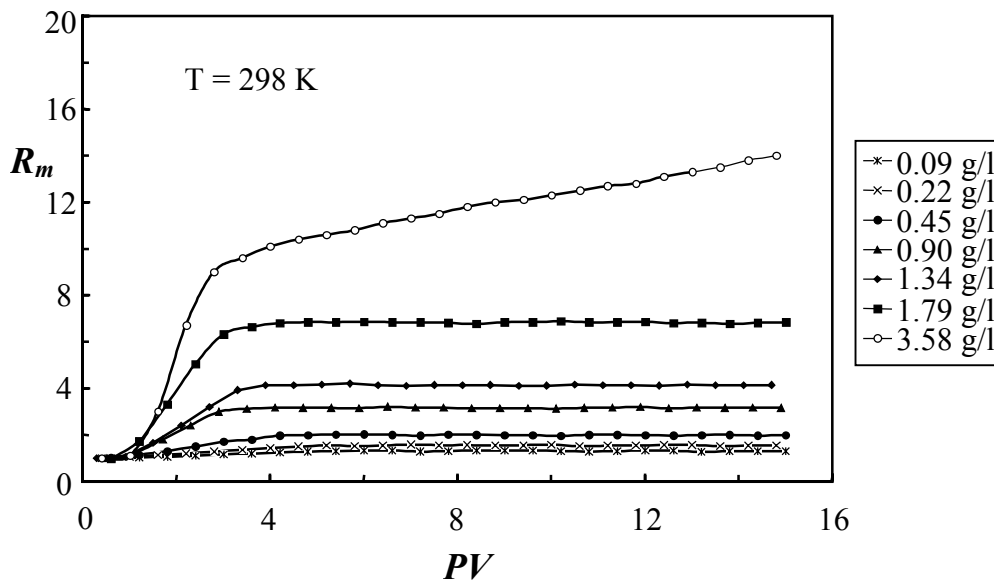


Figure 6.12 The evolution of R_m during injection of PAM1/brine solutions of different concentration in SiC 30 μm packs

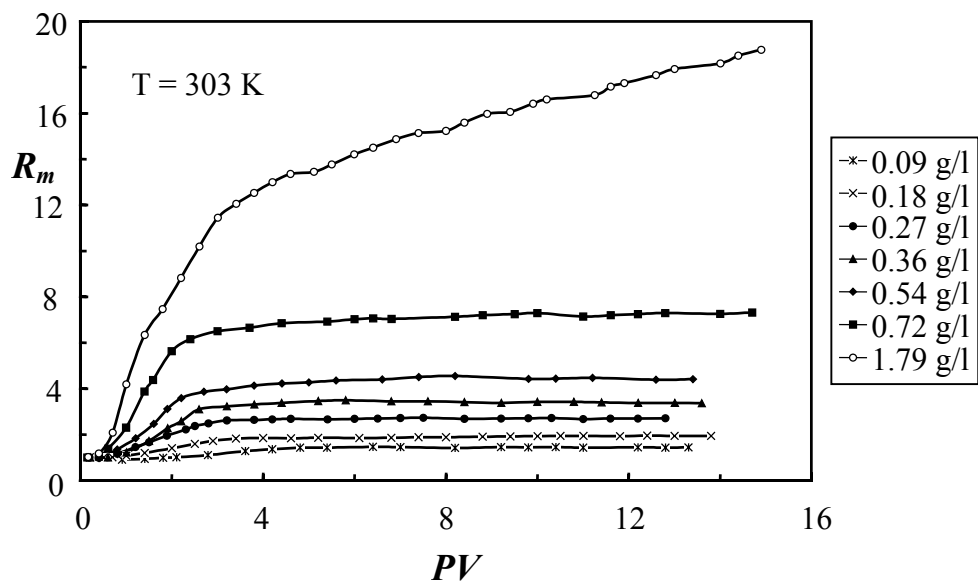


Figure 6.13 The evolution of R_m during injection of PAM2/brine solutions of different concentration in SiC 30 μm packs

At the highest polymer concentrations in Figures 6.12 and 6.13, the mobility reduction R_m continues to increase in time. It appears that in the semi-dilute regime another retention mechanism becomes important. A more or less similar effect has been described earlier in literature by Barham and Keller [52] and Hikmet et al. [53], who attributed this to an entanglement interaction between flowing chains and the

adsorbed layer causing the adsorbed layer to grow. These authors showed that high molecular weight polymers in solution could form adsorption entanglement multilayers whose thickness could grow with polymer concentration. Tables 6.4 and 6.5 show the core permeability k , injected polymer concentration c , pore radius R_p (Eq. 6.9), plateau mobility reduction R_{mp} (Eq. 2.21), permeability reduction R_k (Eq. 2.22) and hydrodynamic adsorbed layer thickness ε_h (Eq. 6.8) resulting from the coreflood experiments. The values of the relative viscosity η_r were taken from appendix D.

Core	k [10^{-13} m]	R_p [μm]	c [g/l]	R_{mp}	R_k	$R_k \eta_r / R_{mp}$	ε_h [μm]
A	5.2	3.6	0.09	1.30	1.14	0.96	0.12
B	4.9	3.5	0.22	1.55	1.30	1.02	0.22
C	5.0	3.5	0.45	1.99	1.42	1.03	0.29
D	5.3	3.6	0.90	3.15	1.60	0.97	0.40
E	5.2	3.6	1.34	4.20	1.68	1.01	0.44
F	4.7	3.4	1.79	6.82	2.28	1.10	0.63
G	4.8	3.4	3.58	-	6.20	-	1.25

Table 6.4 Injection characteristics of PAM1/brine corefloods

Core	k [10^{-13} m]	R_p [μm]	c [g/l]	R_{mp}	R_k	$R_k \eta_r / R_{mp}$	ε_h [μm]
H	5.7	3.7	0.09	1.43	1.21	0.99	0.17
I	5.0	3.5	0.18	1.94	1.37	0.96	0.26
J	4.8	3.4	0.27	2.70	1.74	1.00	0.44
K	4.9	3.5	0.36	3.38	1.91	1.00	0.52
L	5.0	3.5	0.54	4.40	1.95	0.96	0.54
M	5.7	3.7	0.72	7.25	2.80	1.15	0.85
N	4.9	3.5	1.79	-	5.40	-	1.20

Table 6.5 Injection characteristics of PAM2/brine corefloods

By making use of the dynamic adsorption method described in Appendix F, the adsorption level was estimated to equal 0.5–0.9 mg/m² for both polymers (tendency:

values gradually increase with concentration). Note that the difference in static and dynamic adsorption levels is common in literature [54]. This generally results from variances in specific surfaces, inaccessibility of portions of the pore space or other retention mechanisms acting in the dynamic experiment.

As can be deduced from the tables, the increase in R_{mp} with the polymer concentration is not only a viscosity effect, but also a result of an increasing R_k . From Tables 6.4 and 6.5 it follows that $R_k \eta_r / R_{mp} \approx 1$. This is quite remarkable since usually the apparent viscosity R_{mp} / R_k in the porous medium is smaller than the relative viscosity η_r measured in a rheometer [55]. This phenomenon, called polymer depletion or excluded volume effect, is a result of the fact that polymer molecules are sterically hindered by the pore wall due to their size. As a result the polymer concentration is smaller in the vicinity of the wall than in the bulk [56]. Under non-adsorbing conditions the size of the depleted layer δ_d is known to be of the order of the radius of gyration, in the dilute regime, while decreasing rapidly in size at increasing polymer concentrations due to osmotic forces [56]. Under adsorbing conditions free polymers can partially interpenetrate the adsorbed layer, resulting in a smaller depleted layer effect [45].

Most probably the absence of the depleted layer effect in our case is a result of the fact that brine is a “mediocre-quality” solvent for PAM (Section 6.2.2). As a result an attractive force exists between the adsorbed layer and the free polymer molecules reducing the depleted layer effect considerably. The absence of the polymer depletion effect has been evidenced earlier for the system Polystyrene/cyclohexane under Θ -conditions [57]. The depleted layer effect is discussed more extensively in Chapter 7. The structure of an adsorbed polymer molecule on the substrate can be subdivided into trains (sequence of segments, which contact the substrate), loops (no substrate contact, connecting two trains) and tails (non-adsorbed chain ends). From literature it is known that the segments in the periphery of the adsorbed layer, the tails, are the dominant factor in disturbing fluid flow, meaning that they have the biggest impact on the value of the hydrodynamic adsorbed layer thickness ε_h [45]. Consequently the value of ε_h increases with molecular weight [58]. Gramain and Myard [59] found an increase in ε_h with concentration without any change in the adsorbed amount suggesting a change of the conformation of the adsorbed layer. This increase in ε_h continued until a plateau was reached. Figure 6.14 shows for both polymer samples

the adsorbed layer thickness ε_h (Eq. 6.8) vs. the polymer concentration. As can be seen ε_h increases progressively, then goes through a region, which resembles a plateau, and afterwards increases again with increasing polymer concentration. Qualitatively the same type of behaviour as Gramain and Myard [59] has been found. However, at concentrations higher than studied by these authors, a new sudden increase in ε_h was observed. Most probably this behaviour is related to the continuously increasing values of R_m during injection at high polymer concentrations (Figures 6.12 and 6.13). Note that the plateau region in Figure 6.14 coincides with the coil overlap values due to the Simha criterion (Section 6.2.2).

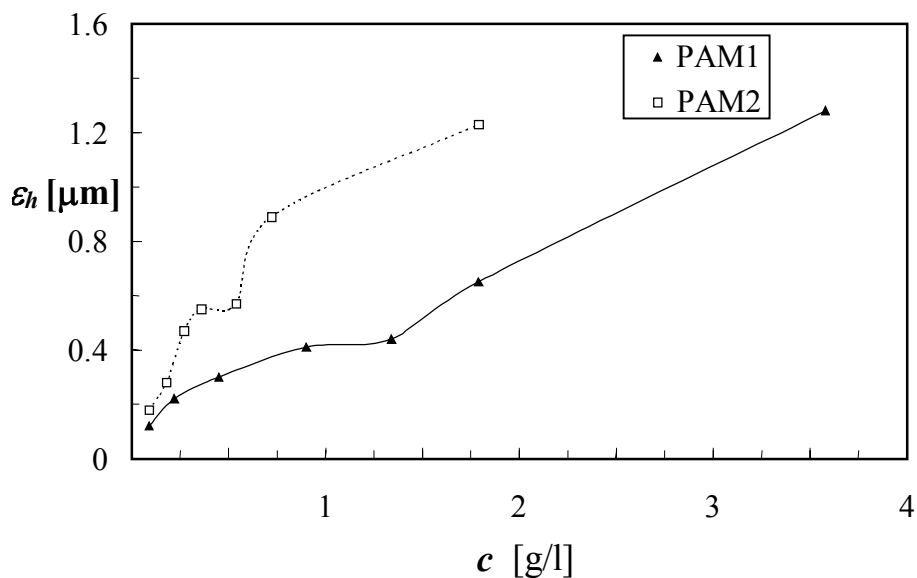


Figure 6.14 The hydrodynamic thickness of the adsorbed layer vs. polymer concentration

After the polymer injections described, oil has been injected into packs C, D, E and F to obtain estimations of the permeability to oil after polymer adsorption. For all packs stable values were found after about 20 PV yielding very small values of the permeability reduction to oil ($1.0 < R_{ko} < 1.1$). Reinjection of brine into the core, displacing oil, resulted in very irregular displacement curves due to fingering- and capillary entrapment effects with a general trend of increasing pressure drop in time up to R_k values as found directly after polymer injection. The conclusion is that the DPR effect was confirmed for this system meaning that adsorption decreases the relative permeability to water while having little or no effect on the relative permeability to oil.

6.5 Summary

1. As fields mature, water production is globally an increasing problem for oil operators. Consequently the money spent in the world on development of new water shut-off technologies is on the rise.
2. Polyacrylamides are widely used in the industry for water shut-off, but are also common in polymer flooding. Knowledge of its propagation- and retention behaviour in porous media is required to improve treatment effectiveness.
3. Often times injecting a polymer system without any zonal isolation, the so-called bullheading, is the only valid option for a well engineer. Frequent causes are a poor identification of the different zones around the wellbore, an unfavourable completion (gravel pack, slotted liners etc.) or excessive workover costs (offshore wells, marginal wells). Also the recent development of horizontal, multilateral wells calls for more future bullhead treatments.
4. DPR systems are considered to be attractive bullhead systems since it is often claimed that they do not harm the permeability of the pay zones. In this study this is confirmed for the non-ionic Polyacrylamide system, which shows very small values of the permeability reduction to oil ($1.0 < R_{ko} < 1.1$) after adsorption.
5. Concerning PAM rheology in porous media, it was shown that $R_k \eta_r / R_{mp} \approx 1$ indicating an absence of the depleted layer effect [55]. This is in contrast with results on HPAM/brine or CPAM/brine solutions [29] and seems to be caused by the fact that brine is only a “mediocre-quality” solvent for PAM resulting in an attractive force between the adsorbed layer and the free polymer molecules.
6. In the coreflood studies it is observed that, at concentrations in the semi-dilute regime, the mobility reduction R_m does not stabilise during polymer injection, as one expects for monolayer adsorption. This seems to be related to the formation of an adsorption-entangled multilayer [52,53] whose thickness grows during injection.
7. The DPR phenomenon is often explained by the concept that adsorbed layers tend to swell in the presence of water and tend to collapse in the presence of oil. As R_{kw} is related to the hydrodynamic adsorbed layer thickness, effective DPR systems should be designed to produce at least $R_{kw} = 5$. This can be obtained by modifying molecular weight, chain charges (see Chapter 7) and possibly also concentration.

References (Chapter 6)

1. Product information Haliburton company (1998)
2. P. Janssen, PhD thesis, Delft, The Netherlands (2000)
3. C. Matthews, SPE conference paper 35817, New Orleans (1996)
4. A. Zaitoun, N. Kohler, Y. Guerinni, *J. of Pet. Techn.*, 862 (1991)
5. European Union WELGEL Consortium, final report (2000)
6. P. Moffitt, A. Moradhi-Araghi, I. Ahmed et al., SPE conference paper 35173, Midland (1996)
7. R. Boreng, O. Birger Svendsen, SPE conference paper 37466, Oklahoma City (1997)
8. J. Bergem, R. Fulleylove, J. Morgan et al., SPE conference paper 38833, San Antonio (1997)
9. H. Nasr-El-Din, G. Bitar, F. Bou-Khamsin et al., SPE conference paper 39615, Tulsa (1998)
10. M. Faber, G. Joosten, K. Hashmi et al., SPE conference paper 39633, Tulsa (1998)
11. A. Zaitoun, N. Kohler, K. Denys et al., SPE conference paper 56740, Houston (1999)
12. G. Chauveteau, K. Denys, A. Zaitoun, SPE conference paper 75183, Tulsa, (2002)
13. M. Bartosek, A. Menella, T. Lockhart et al., SPE conference paper 27828, Tulsa (1994)
14. A. Zaitoun, B. Potie, SPE conference paper 11785, Denver (1983)
15. P. Albonico, T. Lockhart, *J. of Pet. Sci. and Eng.* **18**, 61 (1997)
16. P. Albonico, M. Bartosek, T. Lockhart et al., SPE conference paper 27609, Aberdeen (1994)
17. A. Moradhi-Araghi, P. Doe, *Soc. Pet. Eng. Reservoir Eng.*, 2, 189 (1987)
18. F. Garver, M. Sharma, G. Pope, SPE conference paper 19632, San Antonio (1989)
19. G. Sanders, M. Chambers, R. Lane, SPE conference paper 28502, New Orleans (1994)
20. R. Seright, J. Liang, SPE conference paper 24190, Tulsa (1992)
21. G. Chauveteau, R. Tabary, M. Renard et al., SPE conference paper 50752, Houston (1999)
22. J. Liang, R. Lee, R. Seright, SPE conference paper 20211, Tulsa (1990)
23. S. Plahn, D. Stevens, P. Enkababian et al., SPE conference paper 38194, The Hague (1997)
24. M. Miller, K. Chan, SPE conference paper 38325, Long Beach (1997)
25. A. Jones, F. van der Bas, M. Hardy, SPE conference paper 38199, The Hague (1997)
26. A. Zaitoun, N. Kohler, *In Situ* **13**, 55 (1989)
27. P. Barreau, H. Bertin, D. Lasseux et al., *SPE Res. Eng.*, 234 (1997)
28. A. Manella, L. Chiappa, S. Bryant et al., SPE conference paper 39634, Tulsa (1998)
29. K. Denys, C. Fichen, A. Zaitoun, SPE conference paper 64984, Houston (2001)
30. R. Dawe, Y. Zhang, *J. of Pet. Sci and Eng.* **12**, 113 (1994)
31. S. Nilsson, A. Stavland, H. Jonsbraten, SPE conference paper 39635, Tulsa (1998)
32. J. Liang, H. Sun, R. Seright, *SPE Res. Eng.* 282 (1995)
33. A. Zaitoun, H. Bertin, SPE conference paper 39631, Tulsa (1998)
34. B. Zimm, *J. Chem. Phys.* **16**, 1099 (1948)
35. W. Kulicke, R. Kniewski, J. Klein, *Prog. Polym. Sci.*, **8**, 373 (1982)
36. D. van Krevelen, "Properties of Polymers", Elsevier, Amsterdam (1976)
37. T. Schwartz, J. Sabbadin, J. Francois, *Polymer* **22**, 609 (1981)

38. P. Flory, T. Fox, *J. Am. Chem. Soc.* **73**, 1909 (1951)
39. J. Kirkwood, J. Riseman, *J. Chem. Phys.* **16**, 565 (1948)
40. W. Kulicke, R. Haas, *Ind. Eng. Chem. Fundam.* **23**, 308 (1984)
41. P. Carreau, PhD thesis, University of Wisconsin (1968)
42. P. Zitha, PhD thesis, University Paris VI (1994)
43. S. Sigal, *J. Mater. Sci.*, **11**, 1246 (1976)
44. J. Lecourtier, L. Lee, G. Chauveteau, *Colloids and Surfaces* **47**, 219 (1990)
45. G. Fleer, M. Cohen Stuart, J. Scheutjens et al., "Polymers at Interfaces", Chapman & Hall, London (1993)
46. J. Dijt, PhD thesis, University of Wageningen (1993)
47. J. Dijt, M.A. Cohen Stuart, J. Hofman et al., *Colloids Surfaces* **51**, 141 (1990)
48. M. Page, J. Lecourtier, C. Noik et al., *J. Colloid and Interface Science* **161**, 450 (1993)
49. Y. Guevellou, C. Noik, J. Lecourtier et al., *Colloids and Surfaces* **100**, 173 (1995)
50. O. Griot, J. Kitchener, *Trans. Faraday Soc.* **61**, 1026 (1965)
51. D. Broseta, F. Medjahed, *J. Colloid and Interface Science* **170**, 457 (1995)
52. P. Barham, A. Keller, *Macromolecules* **23**, 303 (1990)
53. R. Hikmet, K. Narh, P. Barham, A. Keller, *Progress in Colloid and Pol. Sci* **71**, 32 (1985)
54. I. Lakatos, J. Lakatos-Szabo, J. Toth, *Symp. EOR Surface Phenomena*, Stockholm (1979)
55. G. Chauveteau, M. Tirrell and A. Omari, *J. Colloid and Interface Science*, **100**, 41 (1984)
56. J. Joanny, L. Leibler, P. de Gennes, *J. Pol. Sci. Pol. Phys. Ed.* **17**, 1073 (1979)
57. J. Englert, PhD thesis, University of Minnesota (1983)
58. M. Cohen Stuart, F. Waaijen, T. Cosgrove et al., *Macromolecules* **17**, 1825 (1984)
59. P. Gramain, P. Myard, *J. of Colloid and Interface Science* **84**, 114 (1981)

CHAPTER 7 - NEW INSIGHTS ON POLYMER RETENTION AND RHEOLOGY IN POROUS MEDIA; THE GELANT DIVERSION PROCESS³³

7.1 Introduction

Operators of mature oil and gas fields are more and more often faced with a high water production coming from a water source or due to water injection. Excessive water production causes economic and operational problems and decreases the economical lifetime of a well. Treatments aiming to reduce water production are called water shut-off- or conformance treatments. Due to the increasing need for treatments without zonal isolation, oilfield operators have focused on DPR systems (see Chapter 6). These systems can be bullheaded downhole, reducing selectively the permeability to water with respect to the permeability to oil or gas. Due to this property polymers or weak gels were thought to be general purpose magic products. The relatively low success rate of DPR bullhead treatments, typically only 30%, shows reality is less favourable. In the following the reasons for this low success rate are discussed by using an example of a DPR treatment on a two-layer well with 1/10 permeability contrast (Figure 7.1). Here the high permeability layer is swept first, either by an active aquifer or by water injection. The low permeability layer is still producing at high oil cut, although water production from the high permeability layer is overtaking its oil production:

- Saturation effect. If DPR is injected into the whole open interval, it will invade more deeply into the high-permeability layer. Since it reduces the relative permeability to water more than the relative permeability to oil, the skin built by the polymer on the water zone should be larger than on the oil zone. This is true

³³ The work described in this chapter was done at Institut Français du Pétrole in an EU research project. It has been published in three SPE papers: 1) A. Zaitoun, N. Kohler, D. Bossie-Codreanu, K. Denys, SPE 56740, Houston (1999), 2) K. Denys, C. Fichen, A. Zaitoun, SPE 64984, Houston (2001) and 3) G. Chauveteau, K. Denys, A. Zaitoun, SPE 75183, Tulsa (2002)

when the fraction of water produced from the oil zone is negligible. However, when the fraction of water is significant, the reduction of the relative permeability to water results in an increase in water saturation. This induces a reduction in the relative permeability to oil. This saturation effect has been described by Liang et al. [1] a few years ago. They showed that even a perfect DPR, which is supposed to reduce strongly the relative permeability to water and not at all the relative permeability to oil, loses its selectivity as soon as also water is produced along with oil.

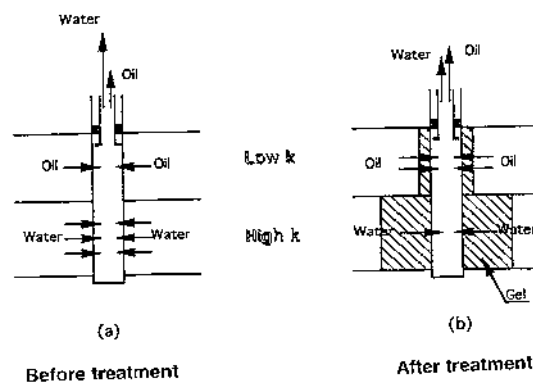


Figure 7.1 DPR bullhead treatment on a two-layer well

- Placement. In linear flow, the depth of DPR penetration in layers of the same thickness is proportional to the permeability ratio. In the example of the two-layer well (Figure 7.1) this means that, when DPR penetrates 10 meters into the high-permeability layer, it penetrates 1 meter into the low permeability layer. In radial flow, relevant around the wellbore, the penetration depth ratio is proportional to the square root of the permeability ratio. This means that when DPR penetrates 10 meters into the high permeability layer, it penetrates more than 3 meters into the low permeability layer causing a severe damage. Another frequent reason for unfavourable placement is communication between the layers. The coupling of the saturation effect and the unfavourable placement can eventually lead to an accentuation of the permeability contrast instead of a correction.
- Irreducible water saturation. Due to hydration water and plugging of the narrowest pore channels, polymers and weak gels induce an increase in the irreducible water saturation. This phenomenon combined with the saturation effect reduces the permeability to oil [2].

Surprisingly, DPR bullhead treatments have been successfully applied in the field whereas theory did not predict any favourable effect. Lately, this was the case for treatments consisting of single Cationic Polyacrylamide (CPAM) injections in gas wells [3] and in oil wells [4]. Such a result calls for physical phenomena preventing deep invasion of oil- or gas-bearing zones by the polymer. Recent studies on polymer behaviour have shown that near-wellbore polymer rheology can be very different from what occurs deeper in the reservoir (see Section 2.4). Experiments on non-ionic polyacrylamide (PAM) showed that, under conditions of high flow rate and for intermediate permeability porous media, polymer injection leads to unsteady state behaviour in which the mobility reduction increases progressively in time due to a continuous decrease in core permeability. The authors explained the observed phenomena by the so-called bridging adsorption mechanism (see Section 2.4) [5,6]. This project was initiated after realising that such a mechanism could prevent further polymer penetration in low permeability, oil saturated layers, diverting polymer towards high permeability watered out layers.

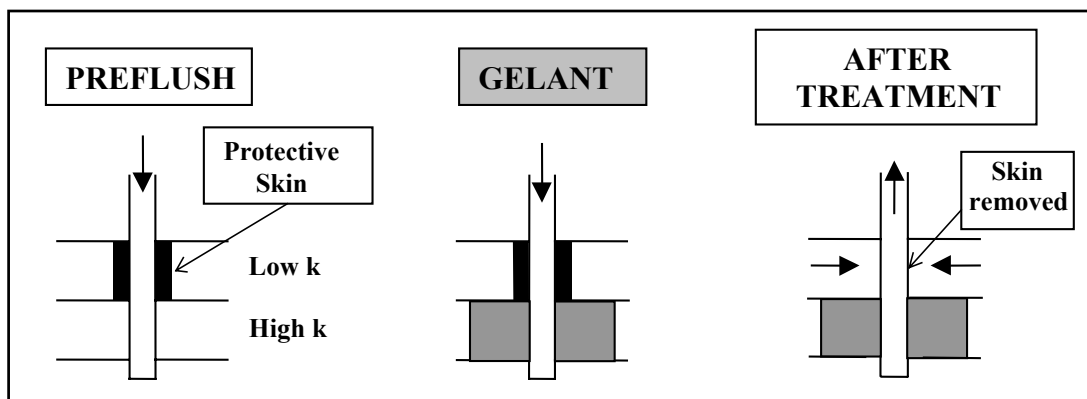


Figure 7.2 Concept behind the two-step gelant diversion process

The idea was to develop a two-step gelant diversion process (Figure 7.2). In the first step a preflush of diverter is injected, which aims at creating a skin on oil-bearing zones. In the second step a main flush of gelant is injected aiming at treating the water-bearing zone. After production release, the skin created on the oil-bearing zone has to be destroyed to recover productivity. The easiest way would be self-destruction by thermal degradation. Another possibility is a post-flush of cleaning agent, like a polymer breaker or desorber. Note that this diversion technique works on the opposite

of classical diverters used in stimulation, which aim at diverting flow from high- to low permeability zones. A first analysis showed that technically the gelant step was not a problem, since experience with reliable systems with proven effectiveness in the field was available. The main issue was to find out which conditions were needed for the skin formation in the first step.

In this chapter coreflood experiments on SiC packs and Berea sandstones are discussed which were done to address this issue. The polymer solutions studied were Cationic Polyacrylamide (CPAM)/ brine solutions. The idea was that, as the positively charged polymer has a higher energy of adsorption on a negatively charged surface than non-ionic PAM, its plugging tendency in the first process step should be much better. In addition, new findings on polymer rheology and retention in porous media will be discussed.

7.2 Experimental

7.2.1 Brine and polymer solution

The brine was prepared in the same manner as described in Section 6.2.1. Experimental work has been done on two different CPAM types, ADAMETM (CPAM1) and APTACTM (CPAM2), both produced by SNF Floerger. Figure 7.3 shows their molecular structure. Concerning the experiments on CPAM1, polymer samples having a cationicity, ranging between 5 and 50% ($0.05 \leq m \leq 0.50$ in Figure 7.3) have been studied. For those on CPAM2, only one sample with a cationicity of 12% ($p = 0.12$ in Figure 7.3) has been studied. The polymer was dissolved in the brine at a concentration of 0.36 g/l (determined by Total Organic Carbon, 0.40 g/l of solid material was dissolved). 0.05 g/l KI was added as a tracer. Before injection the polymer solutions were filtered at 6 ml/h through a set of MilliporeTM membranes (filter diameter: 12 cm, pore diameter 8, 3 and 1.2 μm in series) in order to remove microgels. Table 7.1 lists some important CPAM solution properties. The rheological behaviour of the CPAM2 solution, in the actual range of shear rates, is Newtonian. The viscosity is 1.50 mPas at 303 K, yielding a relative viscosity $\eta_r = 1.84$. The Huggins constant, determined from the slope of the specific viscosity curve $(\eta_r - 1)/c$

vs. concentration c , equals 0.44 indicating good solvent conditions. The Simha criterion for coil touching, $[\eta]c^* = 1$, gives a critical overlap concentration $c^* \approx 0.57$ g/l. Consequently, a 0.36 g/l CPAM2 is a dilute solution.

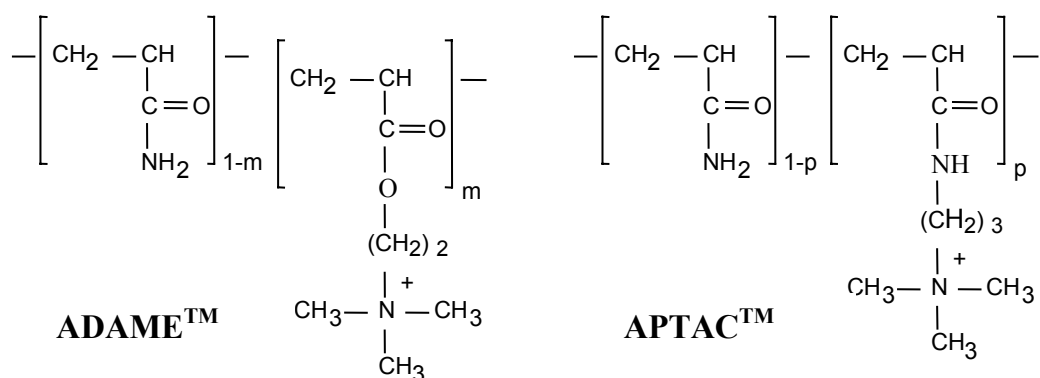


Figure 7.3 The molecular structure of the CPAM's ADAME™ and APTAC™

	CPAM1	CPAM2
Commercial name	ADAME™	APTAC™
M_w [10^6 g/mole]	8	6
Cationicity	$0.05 \leq m \leq 0.50$	$p = 0.12$
Polymer solutions		
c [g/l]	0.36	0.36
$[\eta]$ [l/g]	*	1.75
η_r	*	1.84
R_g [μm]	*	0.14

Table 7.1 CPAM solution characteristics at $T = 303$ K, * indicates that value depends on sample cationicity

7.2.2 Coreflood set-up and procedures

The coreflood set-up used was very similar to the one described in Chapter 6. The set-up consisted of a positive displacement pump, a core and a fraction collector, all set in series. The core was immersed in a thermostatic bath with water held at 303 K. Differential pressure transducers (0-15 mbar or 0-2000 mbar) were set in between the inlet and the outlet of the core to monitor the pressure drop during injection. The data

were recorded on a computer. Different were the dimensions of the porous media. The SiC grain packs had a diameter of 1.50 cm and a length of 3 cm. The Berea cores had a diameter of 2.25 cm and a length of 3 cm. Small cores have been used to be able to inject a large number of pore volumes in order to simulate near well-bore conditions. Table 7.2 summarises SiC pack and Berea sandstone characteristics.

Porous Media	k [10^{-12} m^2]	ϕ	R_p (Eq. 6.9) [μm]	S_{sp} [m^2/g]
SiC packs				
SiC 18 μm	0.13	0.43	1.79	0.25
SiC 30 μm	0.40	0.41	3.21	0.13
SiC 50 μm	1.05	0.39	5.34	0.08
Berea sandstones				
Berea A	0.16	0.19	”3.0”	-
Berea B	0.23	0.19	”3.6”	-

Table 7.2 SiC and Berea core characteristics. Shown are the permeability k , the porosity ϕ , the effective pore radius R_p and the specific surface S_{sp}

The concept of the effective pore radius R_p (Eq. 6.9) is less appropriate for Berea sandstones since this is a medium with a large distribution in pore sizes. The procedure in the corefloods consisted of injection of a large slug of polymer solution and subsequently brine, starting with the lowest rate of 1 ml/hr, and increasing the rate step by step. The pressure drop was monitored during either polymer- or brine injection. Plots of the mobility reduction R_m (Eq. 2.21) and the permeability reduction R_k (Eq. 2.22) vs. the number of injected pore volumes PV were determined from the pressure drop measurements. At the lowest injection rate, the adsorbed amount Γ was determined from the delay of the carbon front (by a Shimadzu TOC Analyzer) with respect to the tracer front (UV spectrometry at 230 nm). After polymer injection, oil was injected to evaluate the permeability reduction to oil. A mineral oil (Marcol™), having a viscosity of 8.3 mPas at 303 K, was used. The oil injection rate was 20 ml/h.

7.3 Coreflood results

7.3.1 CPAM1 experiments

SiC and Berea corefloods

CPAM1 series of coreflood experiments at a flow rate of 1 ml/h aimed at evaluating the influence of the cationicity on adsorption. Figure 7.4 gives the CPAM1 adsorbed amount in 18 μm SiC packs and in Berea sandstone's as a function of the cationicity. As can be seen a maximum adsorption is reached at a cationicity of 10-15%. The existence of a maximum adsorption is thought to be a result of a competition between adsorption energy and pore wall accessibility. A higher cationicity creates a stronger polymer-rock interaction but prevents adsorption of new polymer molecules due to a quicker coverage of the pore walls as well.

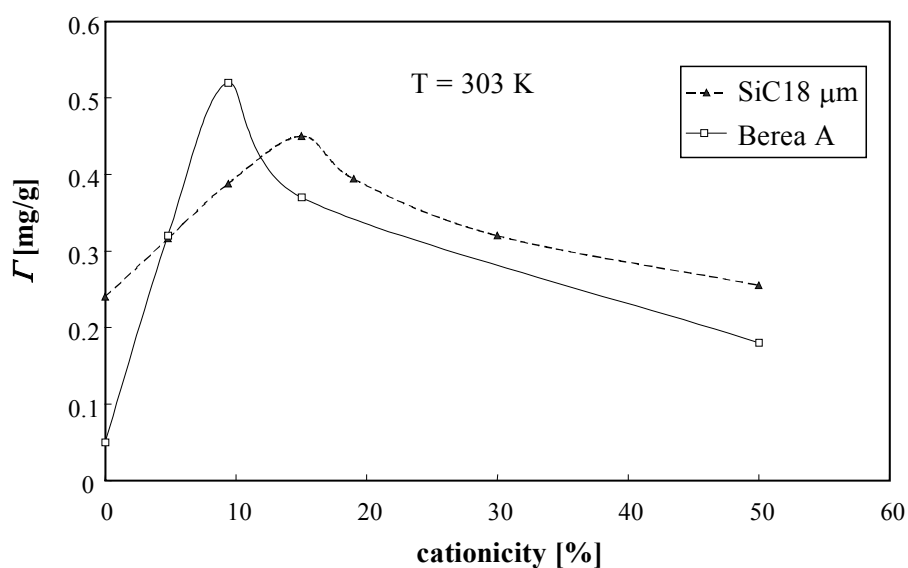


Figure 7.4 The adsorbed amount Γ vs. polymer cationicity after injection of CPAM1 solutions into SiC packs and Berea A sandstones

It has to be noted that, above a cationicity of 15%, in both media an unexpected plugging tendency was observed at low rate injection. This was attributed to aggregate formation by weak intermolecular bonding between the positive polymer charges present and negative charges, which result from hydrolysis of some acrylamide groups. As confirmed by the manufacturer, CPAM1 cationic groups have a tendency to hydrolyse in time into (anionic) acrylic acid and choline. A basic pH

and/or higher temperature favour this reaction [7]. Although the instability of CPAM1 could be advantageous with respect to field applications, e.g. for diversion, it hinders rheological interpretation of the corefloods. To overcome this problem, it was decided to work on the more stable Cationic Polyacrylamide, CPAM2 (see Table 7.1).

7.3.2 CPAM2 experiments

SiC corefloods at small shear rates

As can be seen in Figure 7.5, the mobility reduction R_m tends to a stable value when full surface coverage is obtained by monolayer adsorption and the polymer effluent concentration equals the initial solution concentration. Table 7.3 shows the resulting values of plateau mobility reduction R_{mp} , permeability reduction R_k , adsorbed layer thickness ε_h (Eq. 6.8) and adsorbed amount Γ . An adsorbed amount of $\Gamma \approx 1 \text{ mg/m}^2$ CPAM2 on SiC has been found. This adsorption level is about twice the value found for PAM on SiC (see Section 6.3). The values for the adsorbed layer thickness ε_h are more or less constant indicating that the macroscopic approach of Eq. 6.8 holds.

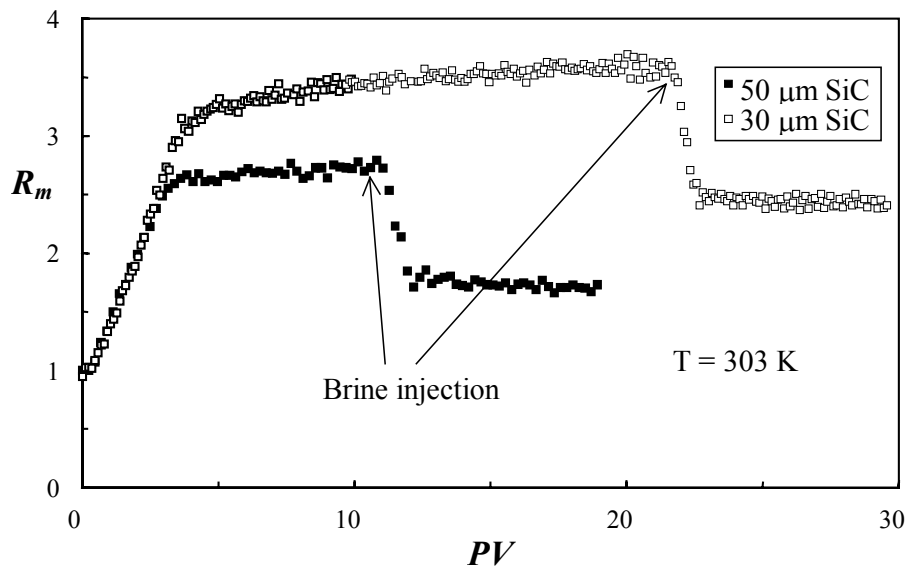


Figure 7.5 Evolution of the mobility reduction during injection of a CPAM2 solution and during subsequent brine injection into SiC packs at 1 ml/h

From Table 7.3 follows that $\varepsilon_h/(2R_g) \approx 2.2$ indicating that the adsorbed layer thickness is much larger than its regular size of $\varepsilon_h/(2R_g) \approx 1$. CPAM2 adsorbed layer thickness

on SiC is also more than two times larger than the layer thickness of neutral PAM on SiC [5,8]. Apparently the high adsorption energy results in an adsorption layer, which is extended by osmotic forces and charge repulsion due to the high segment density.

The values for the depleted layer factor $R_k \eta_r / R_{mp}$ (Table 7.3), being the ratio between the bulk viscosity and the apparent viscosity in the porous medium, are found to increase with decreasing pore size or permeability. In fact, all $R_k \eta_r / R_{mp}$ values exceed one. This well-established depletion effect is caused by the fact that the polymer molecules are sterically hindered by the pore wall due to their size resulting in a smaller polymer concentration at the wall than in the bulk (see Section 2.4.4).

D_p [μm]	R_{mp}	R_k	ε_h [μm]	$R_k \eta_r / R_{mp}$	$1 - \left(1 - \frac{\delta_d}{R_p - \varepsilon_h}\right)^4$	Γ [mg/m^2]
18	6.79	5.23	0.61	1.42	0.48	1.1
30	3.58	2.39	0.63	1.23	0.25	0.9
50	2.74	1.71	0.67	1.15	0.14	0.9

Table 7.3 Experimental results for low rate CPAM2 injection into SiC packs

Chauveteau et al. [9] modelled polymer solution flow through a cylindrical pore (radius R_p) with a depleted layer near the wall (thickness δ_d) and non-adsorbing conditions as a coaxial flow of two immiscible fluids. The fluid flowing in the centre has a bulk relative viscosity η_r . The fluid near the wall, in the depleted zone, has a lower concentration and thus a relative viscosity $\eta_{rw} < \eta_r$. Assuming that $\delta_d / R_p \ll 1$, that the velocity at the wall is zero and that the velocity is equal for both fluids at the fluid boundary, then results for the plateau mobility reduction R_{mp} :

$$\frac{\eta_r}{R_{mp}} = 1 + (\chi - 1) \left[1 - \left(1 - \frac{\delta_d}{R_p} \right)^4 \right] \quad (7.1)$$

where $\chi = \eta_r / \eta_{rw}$. Note that the term between square brackets at the right hand side is well approximated by $4\delta_d / R_p$ at small values of δ_d / R_p and that $\delta_d \approx 1.24 R_g$ for dilute solutions which was determined experimentally [9].

Chauveteau et al. [9] adapted Eq. 7.1 to adsorbing conditions, i.e. polymer flow in the presence of an adsorbed layer. So on top of the impermeable adsorbed layer of

thickness ε_h there is a depleted layer of thickness δ_d . When multiplying the left term by the permeability reduction R_k and by diminishing R_p by the adsorbed layer thickness ε_h , the following depletion model is obtained:

$$\frac{R_k \eta_r}{R_{mp}} = 1 + (\chi - 1) \left[1 - \left(1 - \frac{\delta_d}{R_p - \varepsilon_h} \right)^4 \right] \quad (7.2)$$

Figure 7.6 combines our data on CPAM solutions with previous data on HPAM solutions [9] in terms of the co-ordinates suggested by Eq. 7.2. All data, on different polymer systems and porous media, lay on the same line. Note that the result on Nuclepore™ membranes is under non-adsorbing conditions.

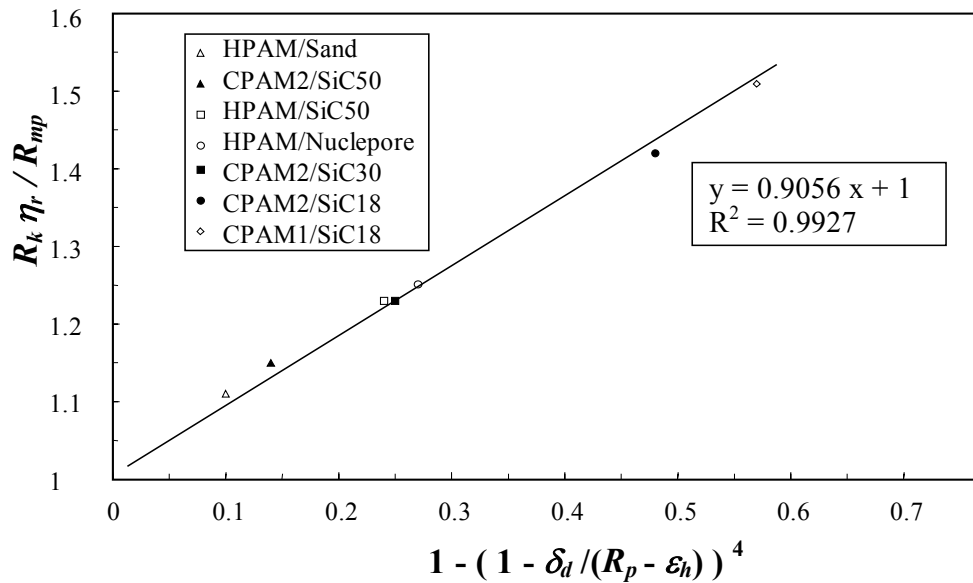


Figure 7.6 Experimental results on HPAM/brine [9] and CPAM/brine in terms of the depletion model coordinates (Eq. 7.2)

When using Eq. 7.2 and the least-square, linear relation shown in Figure 7.6, one obtains: $\chi = \eta_r / \eta_{rw} \approx 1.9$. The values of χ and η_r of the CPAM2 solution (Table 7.1) are nearly the same. Consequently one can conclude that the polymer concentration in the depleted layer must be very small. Logically the depleted layer effect is a function of solvent quality. Since the CPAM2/brine system behaves similarly as HPAM/brine (Figure 7.6), known to be under “good-solvent” conditions [7], these conditions also apply for CPAM2/brine. On the contrary, experiments on PAM/brine on SiC (see

Chapter 6 and [5]) have shown that the depleted layer effect for this system is negligible. The experimental results confirm the model assumption that the presence of an adsorbed polymer layer affects a polymer solution flowing over it in the same way as if there would be an impermeable non-adsorbing wall. Thus the simplistic depletion model of Eq. 7.2 gives a good description of the porous medium rheology of any polymer/solvent system at low flow rates, provided that the medium is homogeneous and that the solution is under “good-solvent” conditions.

SiC corefloods at higher shear rates

Figure 7.7 shows the influence of shear rate on the evolution of R_m during polymer injection in a 30 μm SiC pack. As can be seen unsteady state plugging was observed i.e. continuously increasing values of R_m at a shear rate $\dot{\gamma}_p \approx 59 \text{ s}^{-1}$ and higher. At lower rates, R_m is nearly constant in time.

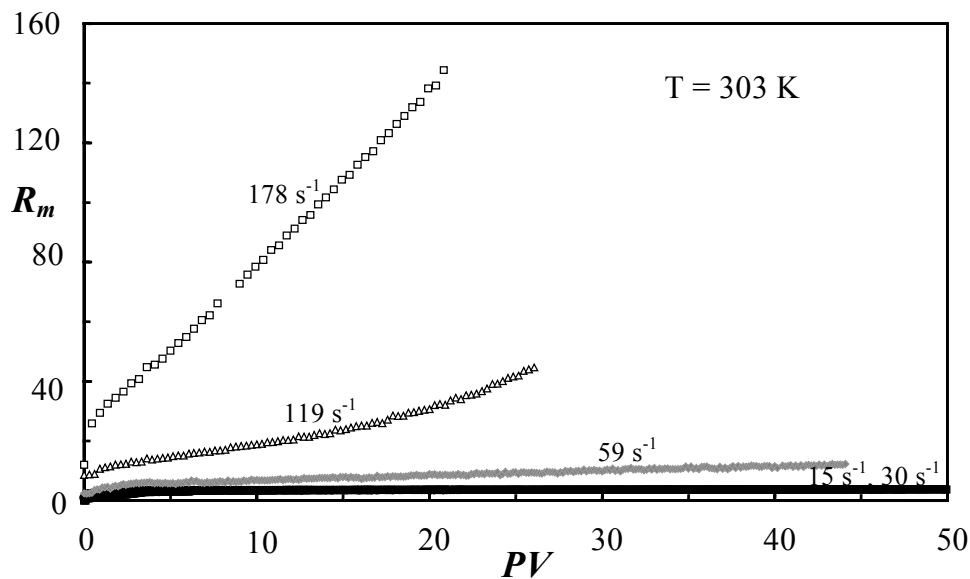


Figure 7.7 Evolution of the mobility reduction at different shear rates during injection of a CPAM2 solution into a 30 μm SiC pack

Table 7.4 shows the plugging rate $\delta R_m / \delta PV$ at different shear rates for all SiC packs. When comparing these data with PAM data in 18 and 30 μm SiC, it is found that the plugging rate on SiC is stronger for the cationic system [5,8]. In 50 μm SiC a weak plugging tendency was found during CPAM2 solution injection. This was also observed during the injection of PAM solutions in 50 μm SiC, for which a plugging rate $\delta R_m / \delta PV \approx 0.08$ was found at $\dot{\gamma}_p \approx 85 \text{ s}^{-1}$ [8].

Grain size [μm]	Flow rate Q [ml/h]				
	1	2	4	8	12
Shear rate $\dot{\gamma}_p$ [s^{-1}]					
18	31	62	124	–	–
30	15	30	59	119	178
50	9	17	34	69	103
Plugging rate $\delta R_m / \delta PV$					
18	0	5.5	30	–	–
30	0	0.006	0.16	1.9	5.9
50	0	0.002	0.002	0.005	0.010

Table 7.4 The plugging rate during injection of a CPAM2 solution into SiC packs at different shear rates

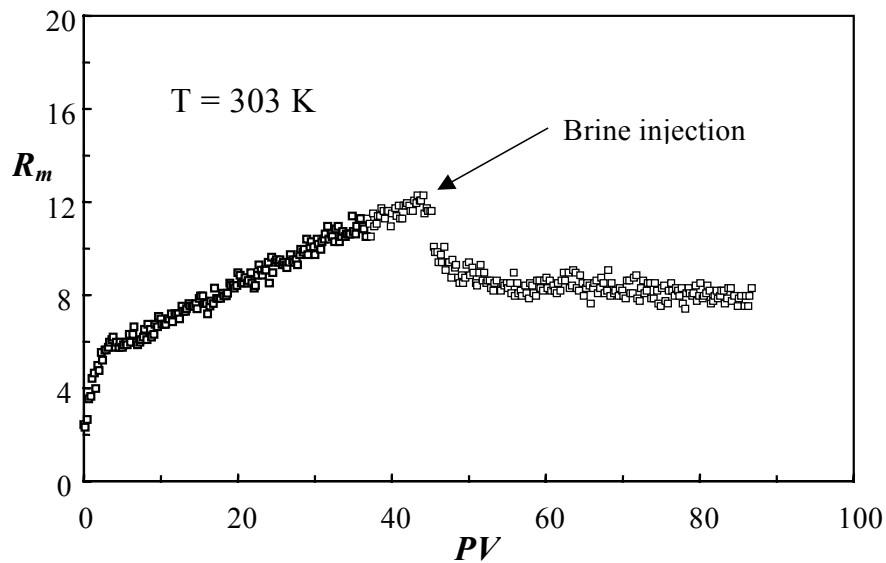


Figure 7.8 Evolution of the mobility reduction during 0.36 g/l CPAM2 injection and subsequent brine injection into a 30 μm SiC pack ($\dot{\gamma}_p \approx 59 \text{ s}^{-1}$)

Figure 7.8 shows a typical result for brine injection after unsteady state plugging has taken place. After a fast decrease in R_m due to the removal of non-adsorbed polymer, R_m decreases slowly in time, levelling off to a constant value. Similar behaviour was found for PAM [8]. It shows that the skin can persist under flowing conditions.

Berea corefloods at small shear rates

Figure 7.9 shows the mobility reduction R_m during CPAM2 injection and subsequent brine injection into Berea A at 1 ml/h ($\dot{\gamma}_p \approx 13 \text{ s}^{-1}$). As can be seen, R_m does not stabilize in time as was observed in the SiC experiments (Figure 7.5) and in the PAM/Berea experiments [8]. However, it was observed that for injections at 2 ml/h, R_m did stabilize during polymer injection. It is thought that this phenomenon, which was only observed at 1 ml/hr, is caused by electrostatic interactions between adsorbed and free polymer molecules causing a temporary retention, which can only persist at small flow rates. The same type of behavior has been found in Berea B (Table 7.2).

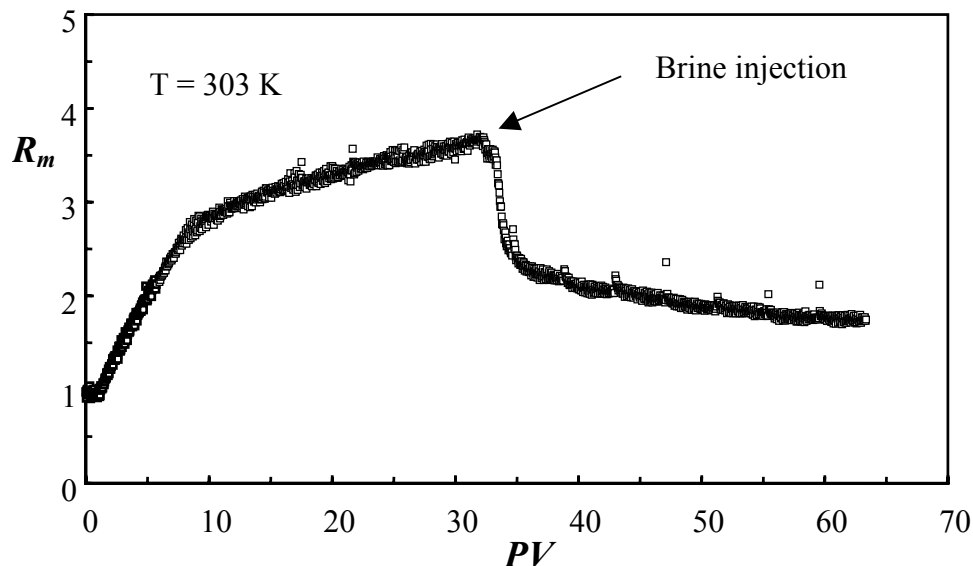


Figure 7.9 Evolution of the mobility reduction during CPAM2 injection and subsequent brine injection into Berea A at 1 ml/h ($\dot{\gamma}_p \approx 13 \text{ s}^{-1}$)

When estimating $R_k \approx 1.7$ from Figure 7.9, a layer thickness of $\varepsilon_h \approx 0.4 \mu\text{m}$ is obtained by Eq. 6.8, which is of the same order as found for adsorption on SiC. Note that the estimation of layer thickness has to be taken with caution, since it was calculated by using a mean pore size R_p while the porous medium has a large distribution in pore sizes. The adsorbed amount of CPAM2 was 0.2 mg/g Berea, which is smaller than value for CPAM1 on Berea, but larger than PAM adsorption level (Figure 7.4).

Berea corefloods at higher shear rates

Figure 7.10 shows the evolution of R_m during CPAM2 solution injection in the Berea A core. At a constant shear rate, R_m increases slowly in time. When increasing the

flow rate, R_m continues to increase progressively. Note that the experiments in Figure 7.10 have been done on a single core, starting with the smallest rates. After each polymer injection, brine was injected at the same rate to determine the permeability reduction. The behavior shown is very similar to the behaviour of PAM in Berea sandstone [8].

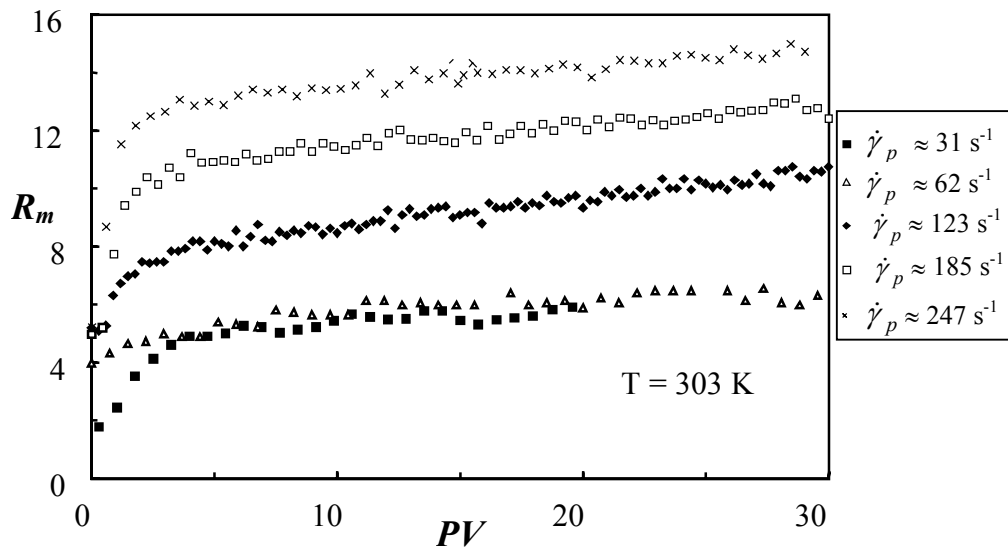


Figure 7.10 Evolution of the mobility reduction during CPAM2 injection into Berea A at different shear rates

Q [ml/h]	$\dot{\gamma}_p$ [s ⁻¹]	R_m (after 20 PV)	R_k (after 5 PV)	$\delta R_m / \delta PV$
Berea A				
1	15	3.6	2.2	0.02
2	31	6.0	4.6	0.02
4	62	6.0	5.2	0
8	123	9.5	7.5	0.09
12	185	12.0	7.3	0.06
16	247	14.2	7.0	0.06
Berea B				
1	12	4.3	2.5	0.04
2	25	5.4	3.3	0.03
4	49	10.7	7.8	0.06
8	99	11.8	8.5	0.12
12	148	14.0	9.6	0.07
16	197	16.4	11.4	0.08

Table 7.5 Experimental results for CPAM2 corefloods in Berea cores

Table 7.5 summarizes the experimental results obtained for CPAM2 corefloods in the Berea cores. Since the permeability of the cores does not differ much, the behavior is qualitatively the same. The differences in results can be explained by the fact that both the pore distributions and the CPAM2 injection history are not exactly the same.

Oil injection after unsteady state plugging

For all SiC packs studied, even for those which had experienced severe unsteady-state plugging up to R_k values above 50 (Figure 7.7), subsequent oil injection yielded small values of the permeability reduction to oil ($1.1 < R_{ko} < 1.3$). Although the origin of this well-known DPR phenomenon [10] is still a matter of debate, this effect strongly reduces the risk of well damage after a DPR treatment. For both experiments on Berea, oil injection after plugging gave $R_{ko} \approx 1.1$, while the final values of R_k for Berea A and B exceeded 6 and 9 respectively.

It can be concluded that injection of CPAM solutions at high shear rates (roughly above 70 s^{-1}) into SiC packs and Berea sandstones induces unsteady-state flow behaviour resulting in a skin formation i.e. a reduction of the core permeability. After a few pore volumes the plugging rate $\delta R_m / \delta PV$ becomes roughly constant. As for non-ionic PAM solutions, $\delta R_m / \delta PV$ increases strongly as the permeability decreases, which is important for the selectivity of the proposed shut-off technology. In this manner the oil containing, low permeability layers would be temporarily protected by the created skin, while the high permeability water producing layers, which do not have this skin, will be fully invaded by the strong gel system in the second step of the process. Note that the plugging rate $\delta R_m / \delta PV$ increases with flow rate and is stronger in SiC packs than in Berea. Remarkably, permeability to oil is never much affected.

7.4 Unsteady-state plugging behaviour; Flow-induced adsorption

The unsteady state plugging behaviour, which has been often observed when polymer solutions were injected into intermediate permeability porous media above a critical shear rate (Section 2.4.4, Section 7.3) has been explained in literature by a mechanism called bridging adsorption [5,8]. This mechanism consists of stretching of polymer

molecules under an elongational flow field and subsequent adsorption of these molecules by forming bridges across pore throats. It is consistent with the following observations: 1) rate of plugging increases as permeability decreases, 2) rate of plugging increases with the presence of residual oil, 3) rate of plugging decreases in cores having a broad size distribution and 4) rate of plugging increases with adsorption energy. However this mechanism cannot very well explain the following observations: I) the critical shear rate (around 70 s^{-1}) is lower than the onset of the coil-stretch transition [7,11], II) more than 99% of polymer molecules can easily flow through highly bridged pore throats. III) the permeability reduction to oil remains always close to 1. Because of these discrepancies it was decided to perform corefloods on high permeability porous media, of which the pore throat size was simply too large to allow polymer bridging. In these experiments 110 μm SiC grain packs have been used having an average pore diameter size of approximately 24 μm , which is about 85 times larger than the polymer coil size (Table 7.1). The permeability of these packs was $5.2 \times 10^{-12} \text{ m}^2$ and the porosity $\phi \approx 0.38$. The CPAM2 solution, the set-up and the filtration procedure used were exactly the same as described before.

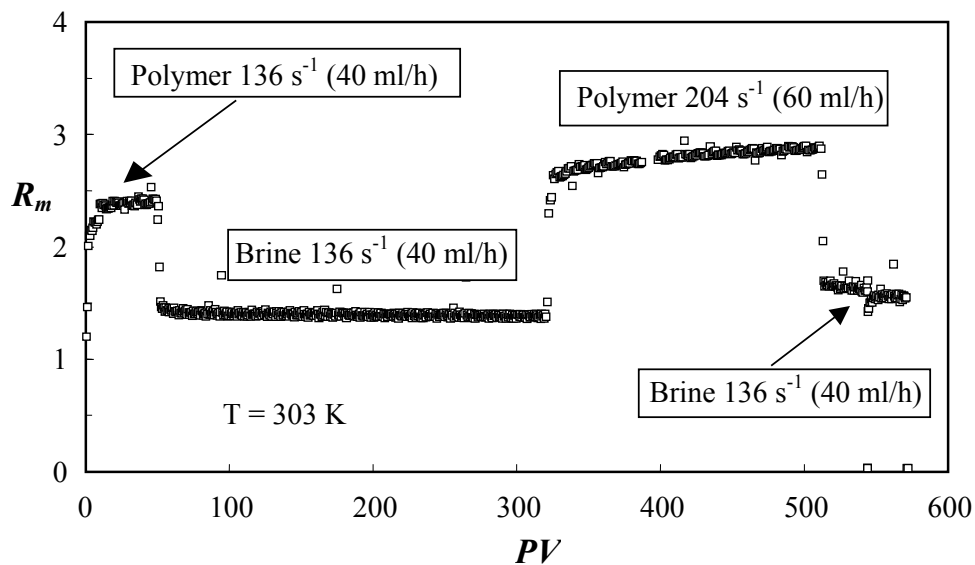


Figure 7.11 Injection of CPAM2 solution and brine into 110 mm SiC

In the first pack two polymer slugs have been injected separated by brine slugs. The first injection was done at a shear rate of 136 s^{-1} (flow rate 40 ml/h) and the second one at 204 s^{-1} (flow rate 60 ml/h). Figure 7.11 shows that the mobility reduction R_m

increases slowly but progressively during both polymer injections. The values of the permeability reduction R_k (at 136 s^{-1}) were respectively, 1.4 after the first and 1.6 after the second polymer injection. Note that the final R_k after monolayer adsorption (based on $\varepsilon_h \approx 0.6 \text{ }\mu\text{m}$, Table 7.3) should normally equal 1.2 (Eq. 6.8). The result of this study was not considered strong enough evidence as it is well-known effect that, after polymer retention in a core, R_k values can increase with increasing flow rate due to elongation of the adsorbed layer. Therefore another more extensive study was needed to be able to draw conclusions. In this experiment a polymer injection of at least 25 PV was done at a constant flow rate (starting with 5 ml/h) and the permeability reductions was measured by injecting brine at the same flow rate. The procedure was repeated for polymer injection rates of 10, 20, 40, 80 and 160 ml/h respectively.

Rate during polymer injection		R_m	R_k (5 ml/h) (17 s^{-1})	R_k (10 ml/h) (34 s^{-1})	R_k (20 ml/h) (68 s^{-1})	R_k (40 ml/h) (136 s^{-1})	R_k (80 ml/h) (272 s^{-1})
[ml/h]	[s^{-1}]						
5	17	2.16	1.25	1.26	1.29	1.42	1.84
10	34	2.25	1.29	1.28	1.32	1.42	1.86
20	68	2.42	1.32	1.31	1.32	1.41	1.80
40	136	2.98	1.40	1.39	1.39	1.47	2.13
80	272	4.33	1.54	1.51	1.51	1.69	1.92
160	544	11.7	1.71	1.70	1.67	1.86	2.88

Table 7.6 Mobility reduction and permeability reductions at different flow rates after subsequent CPAM2 solution injections into a 110 μm SiC pack

Table 7.6 shows the measured values of R_m and R_k . Both R_m and R_k show more or less the same trend. The values are more or less constant at low shear rate and then suddenly increase with an onset at around 70 s^{-1} . For the polymer solution injections the sudden increase in R_m values is due to a plugging effect (Figure 7.12). For the brine injections the sudden increase in R_k values is a consequence of deformation of the adsorbed layer. Apart from this one notes that after every polymer treatment (especially after 136 s^{-1} and 272 s^{-1}) the value of R_k (at 17 s^{-1}) has increased indicating that a progressive plugging is taking place. As bridging is not possible in this case, another mechanism than bridging adsorption must be responsible and the increase in

R_k must be related to an increase in adsorbed layer thickness ε_h . This increase is clearly related to the increase in shear rate, thus to hydrodynamic forces applied on polymer molecules close to the wall. At low rates ε_h remains constant when hydrodynamic forces are too small to affect macromolecule conformation i.e. the polymer adsorbs under static conditions. This means that the attachment is static, but the kinetics of adsorption depend on convection. In this regime, when adsorption energy is low, ε_h is close to the diameter of the polymer coil in solution. When adsorption energy is high, as for the cationic polymers studied here, ε_h is expected to be larger than the coil diameter in solution. Generally ε_h will be constant with the polymer covering homogeneously the surface of the pores.

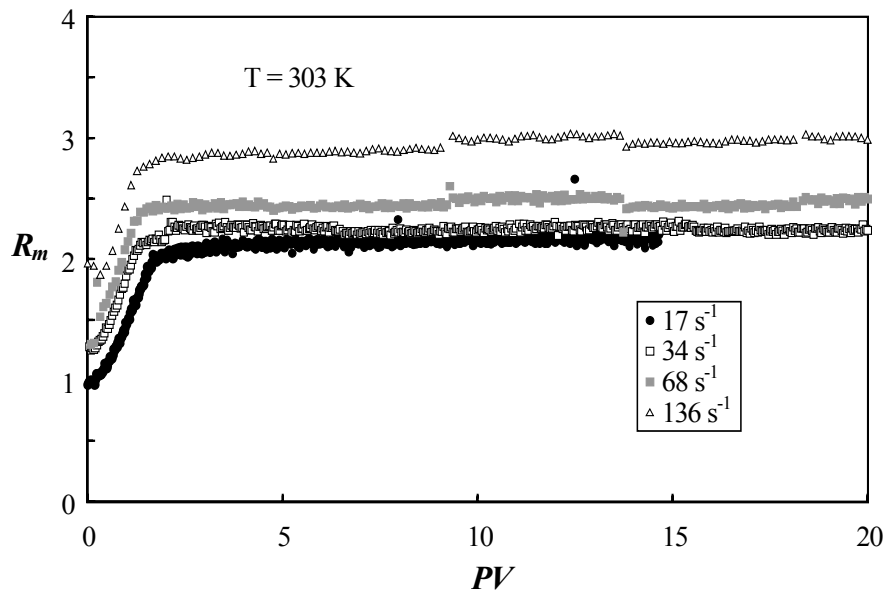


Figure 7.12 CPAM2 solution injection into a 110 μm SiC pack. R_m values increase progressively above 68 s^{-1}

The mechanism which is proposed here, is that, above a critical shear rate, which is around 70 s^{-1} , an additional adsorption occurs whose magnitude increases with hydrodynamic forces. In this “flow-induced adsorption” regime, the hydrodynamic forces lead to penetration of new polymer molecules inside the adsorption layer, despite the existing osmotic barrier. Consequently the density and size of the adsorbed polymers increases. By using the R_k values measured under low shear rate conditions, where the thickness of the adsorbed layer is not affected by hydrodynamic forces, the values of an effective adsorbed layer thickness ε_h can be calculated (Eq. 6.8) and

plotted versus shear rate (Figure 7.13). If the polymer solution is injected at low shear rates, the same adsorbed layer thickness of $\varepsilon_h \approx 0.65 \mu\text{m}$ is measured as before (Table 7.3). Above a shear rate of around 70 s^{-1} the effective adsorbed layer grows strongly with the shear rate up to a value of about $1.5 \mu\text{m}$.

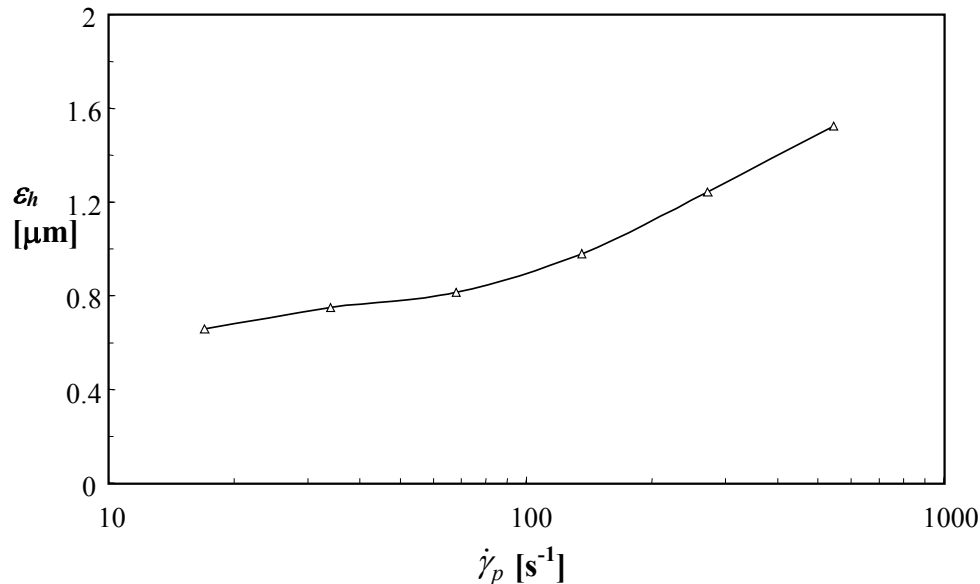


Figure 7.13 Adsorbed layer thickness ε_h vs. shear rate applied during polymer injection $\dot{\gamma}_p$

Apart from the consistency with the previously mentioned general observations on unsteady state plugging, this mechanism is also consistent with the high values of R_m and R_k obtained in low permeability media and the absence of plugging when adsorption is inhibited. Also the hypothesis of a thicker adsorbed layer gives a better idea why polymer penetration in low permeability zones can be reduced strongly without affecting oil permeability.

For this system, a cationic polymer with a strong affinity to adsorb on a negatively charged surface, it appears to be justified to exclude the concept of bridging adsorption as the pore throats are simply too large. However, based on this evidence, it is not (yet) justified to rule out the mechanism of bridging adsorption. For example Zitha et al. [5] did not observe any unsteady state plugging behaviour for corefloods using non-ionic PAM, a polymer with a smaller adsorption tendency, using exactly the same porous media (Figure 2.5). The answer on the questions, which mechanism actually takes place during unsteady state plugging and whether this depends on the adsorption energy, should still come from focussed experimental work in future.

7.5 Summary

1. CPAM adsorption is maximum for a cationicity in between 10 and 15%. This maximum is due to a competition between adsorption energy and pore wall accessibility.
2. Due to higher adsorption energy, CPAM adsorption level and plugging rate in porous media are higher than for a non-ionic polyacrylamide (PAM) at similar molecular weight.
3. For CPAM the adsorbed layer thickness is much larger than the hydrodynamic coil size due to extension by osmotic forces and charge repulsion resulting from the high segment density. On the contrary, for non-ionic PAM's and other uncharged polymers, the adsorbed layer thickness and coil size are roughly equal.
4. Low flow rate polymer solution rheology in a porous medium is well described by Chauveteau's depletion model of Eq. 7.2, provided that the medium is homogeneous and that the solution is under "good-solvent" conditions.
5. As for aqueous PAM solutions, injection of a CPAM solution at higher flow rates, in both SiC packs and Berea sandstone's, induces unsteady-state plugging whose magnitude increases as permeability decreases. This is important with respect to the selectivity to low permeability layers. Generally, plugging becomes notable above a shear rate $\dot{\gamma}_p \approx 70 \text{ s}^{-1}$ and its rate increases with flow rate.
6. A new retention mechanism, called flow induced adsorption, is proposed to explain the sudden unsteady state plugging phenomena which occur in intermediate permeability porous media above a critical flow rate. It is based on the fact that large enough hydrodynamic forces can push free polymer molecules over the osmotic energy barrier resulting in a denser and thicker adsorbed layer. The mechanism is consistent with all former observations and trends found.
7. In all cases skin formation in the lab was easily obtained. Field trials should give conclusive information whether the gelant diversion shut-off technology can work in practice.
8. After plugging, as the permeability reduction to water has reached to very high values, permeability to oil is remarkably preserved. This confirms the DPR phenomenon for this specific system.

References (Chapter 7)

1. J. Liang, R. Lee and R. Seright, SPEPF 276 (1993)
2. A. Zaitoun, N. Kohler, K. Denys et al., SPE conference paper 56740, Houston (1999)
3. G. Burrafato, E. Pitoni, G. Vietina et al. , SPE conference paper 54747, The Hague (1999)
4. R. Mota, C. de Holleben and L. Barbosa, conference paper IBP 20498, Rio de Janeiro (1998)
5. P. Zitha, G. Chauveteau and A. Zaitoun, SPE conference paper 28955, San Antonio (1995)
6. P. Zitha, C. Botermans, SPE conference paper 36665, Denver (1996)
7. G. Chauveteau and K. Sorbie, "Mobility Control by Polymers in Basic Concepts in Oil Recovery Processes", Ed. Marc Baviere, Elsevier (1991)
8. A. Zaitoun and G. Chauveteau, SPE conference paper 39674, Tulsa (1998)
9. G. Chauveteau, M. Tirrell and A. Omari, J. of Colloid and Interface Science **100**, 41 (1984)
10. A. Zaitoun, D. Bertin and D. Lasseux, SPE conference paper 39631, Tulsa (1998)
11. A. Magueur, M. Moan, G. Chauveteau, Chem. Eng. Communic. **36**, 351 (1985)

CHAPTER 8 - ON THE PERMEABILITY REDUCTION DUE TO ADSORBED POLYELECTROLYTES³⁴

8.1 Introduction

Drilling is one of the most common operations in hydrocarbon exploration and production [1]. During drilling, fluids are permanently circulated downwards through the drilling pipe and upwards through the annulus. These fluids are complex mixtures, which must meet requirements like lubrication, cooling of the bit, displacement of rock cuttings to the surface and filtration control aiming to reduce formation damage in the near-wellbore [2]. Most drilling fluids are water-based dispersions containing polymer additives. Anionic polymers, such as Polyacrylates, reduce fluid loss i.e. penetration of fluid in the formation by effectively increasing viscosity. The performance of this type of polymer as filtration control agent is dependent on pH and salinity. Usually drilling fluids contain additives to ensure a high pH and a certain ionic strength intending to prevent washouts, corrosion and excessive dissolution of calcium. However, these properties can be modified by interaction with the formation or the formation water. This is particularly true in horizontal wells, where the drilling fluid can experience large changes in pH and salinity due to the extent of the borehole. Until now little attention has been paid to possible formation damage caused by retention of the anionic polymer and its dependency on pH and salinity.

Apart from this operators are looking for cheap systems, which could form layer barriers temporarily. The goal of these temporary barriers would be to:

- shut off oil producing layers, e.g. for temporary pay-zone protection
- shut off layers which produce a lot of water, but could be economical later on
- prevent communication between layers etc.

³⁴ A part of the work described in this chapter has been published in a SPE paper: K. Denys, P. Zitha, H. Hensens, K. te Nijenhuis, SPE 39465, Lafayette (1998)

Different materials like particle systems, polyelectrolytes or even low-melting alloys are being considered. Concerning these layer barriers the following routes could be used to destroy the barrier:

- thermal degradation
- acid/ solvent attack
- desorption agents
- melting
- combustion
- structure collapse by electrostatic effects

Although the study described here could well be relevant for pharmaceutical-, food-, environmental- and water treatment industry, it has been initiated from the above sketched perspective. The choice was made to study the influence of pH and ionic strength on the rheology and permeability reduction of aqueous Polyacrylic acid (PAA) solutions, a weak polyelectrolyte. Coreflood experiments have been done on packs of Polymethylmethacrylate (PMMA) beads. This porous medium, which was chosen to eliminate ion release effects, made it possible to do well controlled studies on polyelectrolyte behaviour.

8.2 Polymer solution characterisation

8.2.1 PAA solution preparation

The water used was double distilled (pH \approx 7, conductivity $<$ 2 μ S/cm). Element analysis on the water gave the following results: $[\text{Na}^+] < 5 \times 10^{-5}$ g/l, $[\text{K}^+] < 5 \times 10^{-5}$ g/l, $[\text{Ca}^{2+}] < 1 \times 10^{-5}$ g/l and $[\text{Mg}^{2+}] < 1 \times 10^{-5}$ g/l. Alterations of pH and/or ionic strength of water or polymer solution were done by addition of sodiumhydroxide (NaOH) or hydrochloric acid (HCl) and/or sodiumchloride (NaCl). All fluids were degassed before core flooding to remove dissolved gases.

The PAA studied (Figure 8.1) is a commercial product of Polysciences (cat. 6501) which has an average molecular weight of 4×10^6 g/mole and $M_w/M_n \approx 2$. Aqueous solutions of PAA were prepared by adding the polymer grains to a vortex that was created by vigorous stirring of the appropriate amount of water. After the grains were distributed well, the dissolution process was prolonged for 24 hours under gentle stirring at room temperature. The solutions used for core flooding experiments were subsequently filtered with a flow rate of 6 ml/h through three cellulose nitrate filters of 8, 3 and 1.6 μm pore size placed in series. This procedure to remove microgels has been described previously in the literature [3].

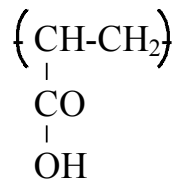


Figure 8.1 The molecular structure of Polyacrylic acid (PAA)

8.2.2 PAA conformation in the dilute state

PAA is a weak polyacid, which means that on dissolution in water only a few percent of the protons dissociates from the chain ($\text{pH} < 4$). When increasing pH, e.g. by adding NaOH, more protons become dissociated rendering it in a charged polymer, a polyelectrolyte. Consequently, the degree of dissociation α_d , the ratio between the amount of dissociated acid groups and the total amount of acid groups, increases with increasing pH. Proton dissociation results in negative charges on the polymer segments, which are located relatively close to each other. The mutual repulsion of the charges causes chain stiffening, as the internal repulsion is minimal for a straight-line charge. Besides, the intermolecular repulsion between chain sections, which are distant along the chain but can be close in space, i.e. the excluded volume, increases. These phenomena can have an enormous impact on PAA conformation, as the intrinsic stiffness of its main-chain is small.

Polymer chain rigidity is usually expressed by C_∞ (Eq. 6.2) or by the intrinsic persistence length q_i (where $q_i = C_\infty b_c/2$ and b_c is the C-C bonding length = 0.154

nm), which is the characteristic length along the chain over which the directional correlation between the segments disappears. The increase in chain rigidity due to charges on a polyelectrolyte chain, can be accounted for by adding an electrostatic contribution q_e [4] to the persistence length:

$$q_{tot} = q_i + q_e \quad (8.1)$$

A charged body immersed in an electrolyte solution, will attract counter ions and repel co-ions. The ions, influenced by the electrical field and thermal motion, will adopt a Boltzmann distribution, inducing a layer of counter charge. As a result of this the electrical field is screened by the presence of the small ions. The Poisson-Boltzmann (PB) equation describes the local electrostatic potential resulting from such a system of ionic species and is of fundamental importance in the study of electrolytes [5]. By approximating the non-linear PB equation by a linear form, Debye and Huckel [6] found that the electrical field decays rapidly with distance due to ion screening. The characteristic length of decay, the Debye length λ_d , is defined by:

$$\lambda_d = \sqrt{\frac{\varepsilon_o \varepsilon_r kT}{2e^2 N_A I}} \quad (8.2)$$

where ε_o is the permittivity in vacuum, ε_r is the relative permittivity, k is the constant of Boltzmann, T is temperature, e is the elementary charge and N_A is the constant of Avagadro. The ionic strength I is defined by:

$$I = \frac{1}{2} \sum_i z_i^2 c_i \quad (8.3)$$

where z_i is the valence of the i -th species and c_i is its bulk concentration in mole per m^3 . λ_d decreases from 9.7 nm at $I = 0.001$ M to 0.31 nm at $I = 1$ M at 298 K. Many data on simple salt systems have been successfully interpreted by the Debye-Huckel theory. Although objections are evident, this theory is frequently used in theoretical- and simulation work on polyelectrolytes to model the interaction between charges.

The Bjerrum length λ_b is the distance between two monovalent ions at which their electrostatic energy equals the thermal energy kT :

$$\lambda_b = \frac{e^2}{4\pi\epsilon_0\epsilon_r kT} \quad (8.4)$$

λ_b equals 0.71 nm in water at 298 K.

Researchers on polyelectrolytes [7] currently agree that two regimes can be distinguished. At low charge density ($l_e > z_c\lambda_b$), the Debye-Huckel theory can be used and the electrostatic persistence length q_e can be calculated by the OSF theory (Odijk [8], Skolnick and Fixman [9]):

$$q_e = \frac{\lambda_b \lambda_d^2}{4l_e^2} \quad (\text{for } l_e > z_c\lambda_b) \quad (8.5)$$

where l_e is the mean distance between two charges, z_c is the valency of the charge on the chain and λ_b is the Bjerrum length. At high charge density, i.e. for $l_e \leq z_c\lambda_b$, it becomes favourable for a fraction of counter ions to be “condensed” [10]. This means that they become located within very short distances from the polyelectrolyte chain. In this way they are gaining energy by electrostatic interaction but losing entropy. As a result the apparent charge on the chain is reduced to the maximum linear charge density of e/λ_b . Hence for monovalent polyelectrolytes the Bjerrum length λ_b is equivalent to the smallest distance between two elementary charges. The fraction of counter ions which condenses on the chain is $1 - l_e / z_c\lambda_b$. The electrostatic persistence length q_e in this regime is described by:

$$q_e = \frac{\lambda_d^2}{4z_c^2 \lambda_b} \quad (\text{for } l_e \leq z_c\lambda_b) \quad (8.6)$$

Eqs. 8.2 and 8.6 show that the electrostatic persistence length increases inversely proportionally with the ionic strength. Experiments have shown that this dependence works well for double-stranded DNA, which is a relatively rigid polyelectrolyte [4]. A discussion has been going on for quite some time whether or not this theory is

applicable for intrinsically flexible polyelectrolytes [11]. By translating the expression for the excluded volume of neutral polymers (Eq. 6.3) in an equivalent for polyelectrolytes, one obtains [12]:

$$\alpha_{ie}^5 - \alpha_{ie}^3 = q_{tot}^{-3} \lambda_d L_c \frac{1}{2} \quad (8.7)$$

where $L_c = Nb_c$ is the contour length ($N = 2M/M_m$ for vinyl polymers), α_{ie} is a factor to account for polymer-solvent interactions, excluded volume effects and electrostatic effects and q_{tot} is the total persistence length, which is equal to the sum of q_e and q_i . From Eq. 8.7 it follows that at high ionic strength, the polyelectrolyte behaves as a neutral polymer, which can only be swollen due to regular excluded volume effects. At intermediate salt concentrations, the electrostatic excluded volume becomes important and the radius of gyration in dilute solutions can be estimated by:

$$R_g \approx \alpha_{ie} \sqrt{\frac{q_{tot} L_c}{3}} \quad (8.8)$$

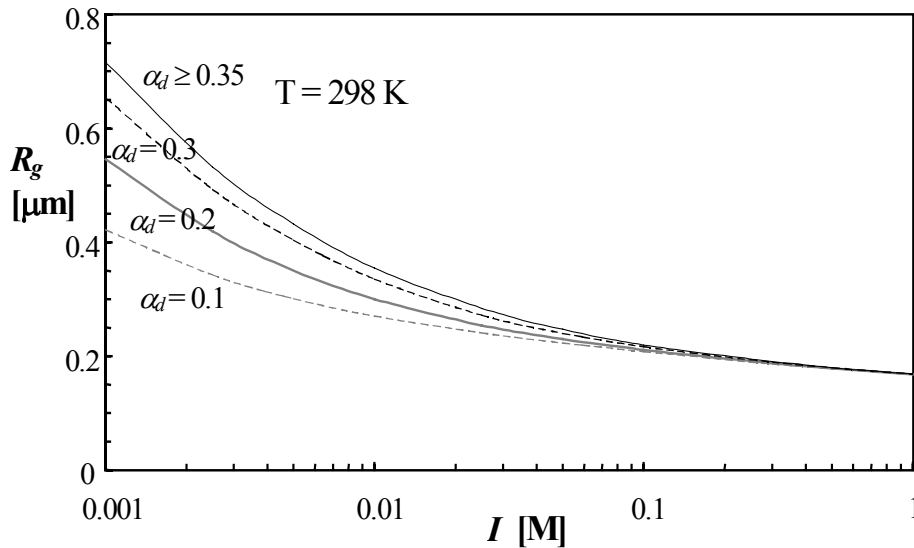


Figure 8.2 Radius of gyration of our PAA sample as a function of ionic strength I and degree of dissociation α_d

At low ionic strength coil swelling due to the increase in the electrostatic persistence length q_e becomes much larger than the excluded volume effect. The radius of

gyration can be estimated by Eq. 8.8 where $\alpha_{ie} = 1$ and $q_{tot} = q_e$. In Figure 8.2 the estimated radius of gyration of our PAA sample is calculated by OSF theory as a function of ionic strength and degree of dissociation. Above an ionic strength of 0.1 M a change of α_d does not affect R_g , since electrostatic interactions are fully screened. The OSF theory predicts that on decreasing the ionic strength from 1 M to 0.001 M, R_g of our sample increases a factor 4 at most. Note that for PAA, a weak polyacid of the vinyl type, the mean distance between two charges equals $l_e = 0.25/\alpha_d$ nm and that counter ion condensation occurs above $\alpha_d \approx 0.35$.

8.2.3 PAA titrations

For polyelectrolytes, pH titrations give information on the degree of functionalization, the acidity constants and possible conformational changes. By using ion-selective electrodes or conductometric titrations it is even possible to distinguish between condensed and non-condensed counterions.

General considerations on titrations

Let us consider the equilibrium for a weak acid: $HA + H_2O \leftrightarrow H_3O^+ + A^-$. Then follows for the equilibrium constant K_a :

$$K_a = \frac{[H_3O^+][A^-]}{[HA]} \quad (8.9)$$

and

$$pK_a = pH - \log \frac{[A^-]}{[HA]} = pH - \log \frac{\alpha_d}{1 - \alpha_d} \quad (8.10)$$

where $\alpha_d = \frac{[A^-]}{[A^-] + [HA]}$.

The bracket terms in Eqs. 8.9 and 8.10 represent concentrations. Eq. 8.10 is called the Henderson-Hasselbalch relation.

For a monoprotic acid the pK_a is independent of the degree of dissociation α_d . During a titration [4] α_d can be determined by:

$$\alpha_d = \frac{c_t V_t - (V_o + V_t) (K_w 10^{pH} - 10^{-pH})}{c_o V_o} \quad (8.11)$$

where c_o is the concentration of groups to be titrated, c_t the concentration of the titrant added, V_o is the initial volume of the solution to be titrated, V_t is the volume of titrant added and K_w is the autoprotolysis constant of water.

PAA titrations

Figures 8.3 and 8.4 show titration results on a PAA/water solution and a PAA/saline water solution at $T = 298$ K. The salt concentration of the saline solution was 0.11 mol/l NaCl. For comparison, curves for Acrylic acid (AA) are added too. The titrated solutions contained 0.50 g/l PAA solution (i.e. $c_o = 0.0070$ mol/l) and had a volume V_o of 0.037 l. The titrant concentration c_t was 0.10 mol/l NaOH.

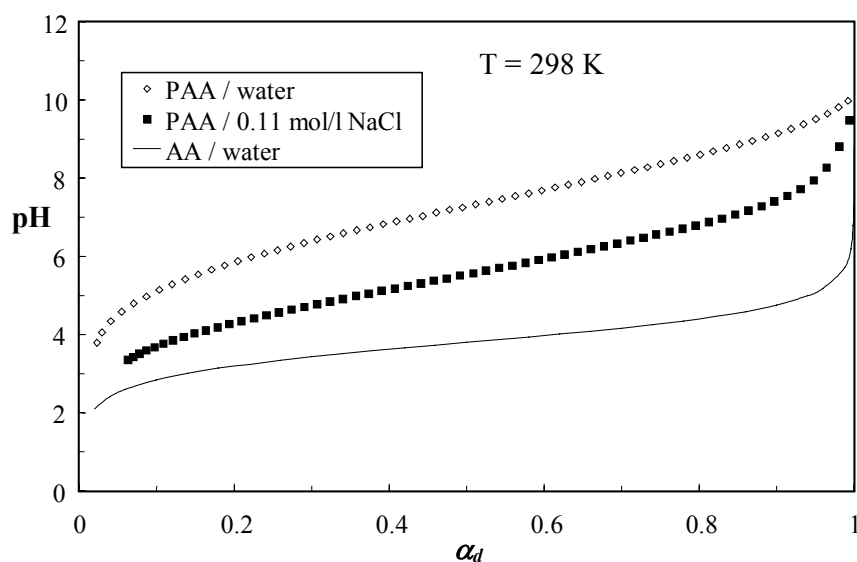


Figure 8.3 pH as a function of α_d (Eq. 8.11) for an AA solution and a saline and non-saline PAA solution

By titrations it was found that 6% of polymer weight was either due to bounded water or due to the presence of acrylamide monomers. Freeze-drying experiments showed that about 5% of polymer weight was due to bounded water, meaning that nearly all

structure units of the polymer are AA monomers. Proton dissociation of PAA is easier in the saline solution since the sodium ions screen the electrostatic potential between proton and polymer chain. For example at $\text{pH} = 6$, AA is fully dissociated, the saline PAA solution is about 60% dissociated and the non-saline PAA solution only about 20%. Figure 8.3 shows that when PAA electrostatic effects become important i.e. at low salinity, determination of the equivalence point becomes more difficult due to the fact that the titration curve is less steep, a well-known peculiarity of polyelectrolytes.

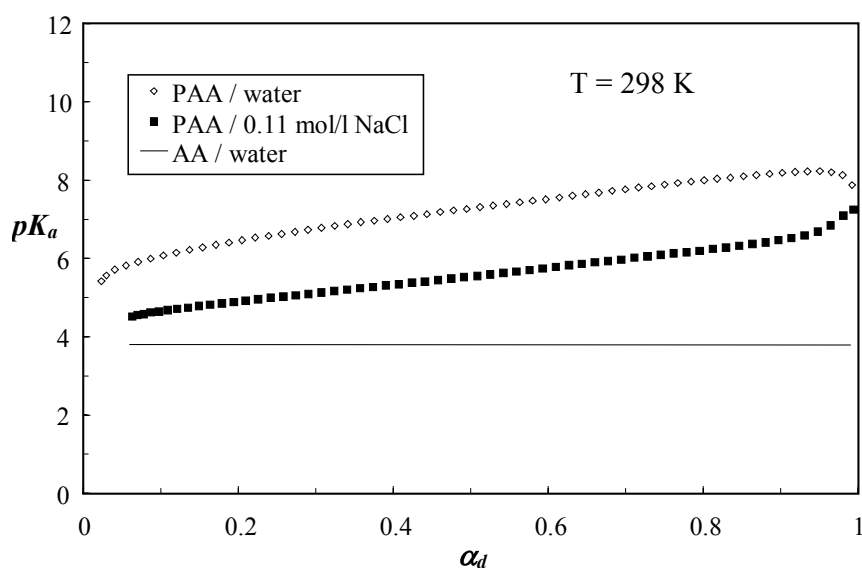


Figure 8.4 pK_a as a function of α_d (Eq. 8.11) for an AA solution and a saline and non-saline PAA solution

Figure 8.4 shows that the pK_a of PAA is increasing with α_d more or less linearly over a very long range, while for monoprotic acids the pK_a is independent of α_d . This is a result of the fact that ongoing dissociation becomes more difficult due to the increase of electrostatic potential of the polymer chains.

8.2.4 Rheological measurements

Stationary measurements

Stationary rheological measurements have been performed to characterise the flow behaviour of PAA solutions and the influence of ionic strength I and pH , i.e. the degree of dissociation α_d , on polymer conformation. These properties were determined with a Contraves LS40 Couette rheometer. This rheometer allows

accurate viscosity measurements at small shear rates. Figure 8.5 shows the viscosity of PAA/water solutions as a function of shear rate for different polymer concentrations. No salt and no NaOH were added. The pH of the solutions was in the range 3 to 5 depending on polymer concentration. Newtonian flow behaviour results for all concentrations.

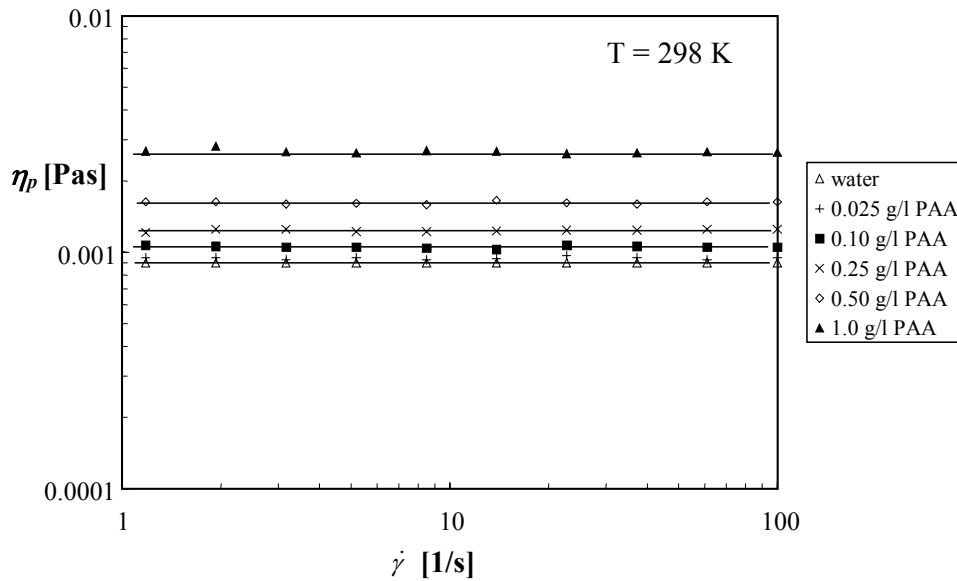


Figure 8.5 Polymer solution viscosity η_p as a function of shear rate $\dot{\gamma}$ for PAA/water solutions, no added salt

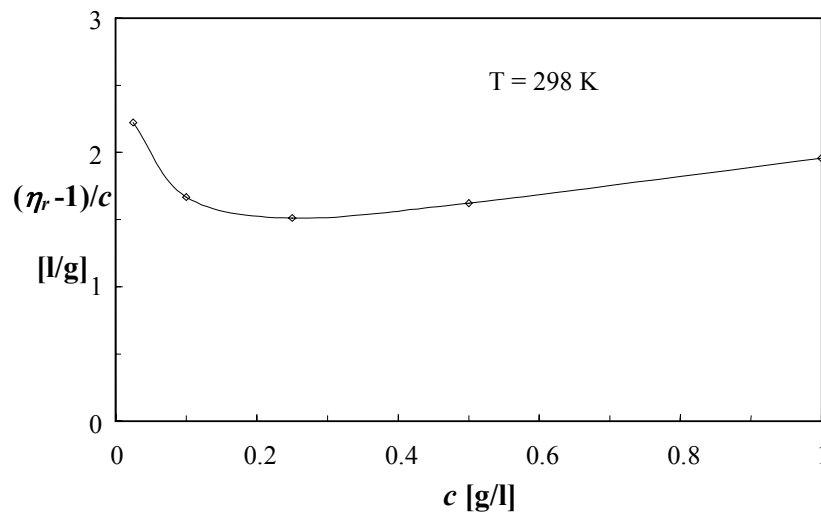


Figure 8.6 $(\eta_r - 1)/c$ vs. polymer concentration c for PAA/water solutions, no added salt

Figure 8.6 shows the relation between $(\eta_r - 1)/c$ and c . As follows from Eq. 6.1, for neutral polymers, extrapolation of $(\eta_r - 1)/c$ to $c = 0$ gives the intrinsic viscosity $[\eta]$. However, for a polyelectrolyte whose electrostatic effects are not screened, no linear relation exists between $(\eta_r - 1)/c$ and c and consequently the intrinsic viscosity cannot be determined under these conditions.

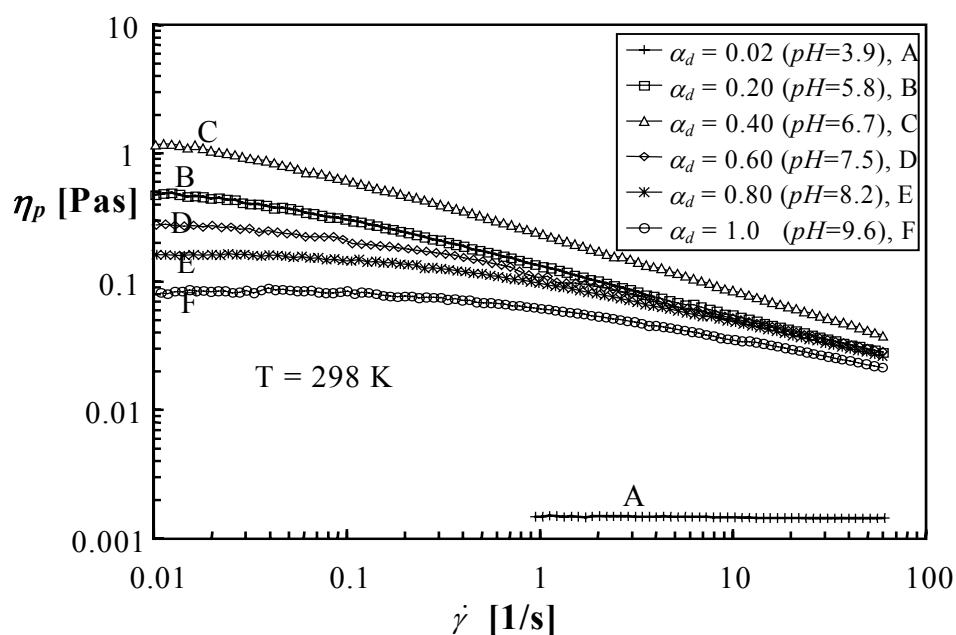


Figure 8.7 Viscosity η_p vs. shear rate $\dot{\gamma}$ for a 0.50 g/l PAA solution in water at different pH's

Rheological measurements have been done on PAA solutions to characterise the influence of pH i.e. the degree of dissociation α_d . Figure 8.7 shows rheological experiments on a 0.50 g/l PAA/water solution (no added salt). Polymer dissolution results in a dilute solution of pH = 3.9 ($\alpha_d = 0.02$) and a viscosity slightly higher than water and Newtonian flow behaviour over the range of shear rates studied. Striking is the drastic viscosity increase in the range $3.9 < \text{pH} < 5.8$. Shear-thinning behaviour is obtained at pH = 5.8 ($\alpha_d = 0.20$) having a plateau viscosity about 330 times higher than at pH = 3.9. Upon further increasing pH a viscosity maximum seems to occur at pH = 6.7 ($\alpha_d = 0.40$). Additional measurements have indicated that the actual maximum viscosity is in the vicinity of pH = 6.5 ($\alpha_d = 0.35$).

The huge increase in stationary viscosity upon raising pH from 3.9 to 6.5 is a consequence of the large coil expansion resulting in a high number of physical entanglements between the polymer coils i.e. a semi-dilute state. The occurrence of

shear-thinning is related to the presence of physical entanglements. It is a peculiarity of polyelectrolytes that one can pass from the dilute regime, i.e. isolated coils, into the semi-dilute regime, i.e. multiple entanglements, without changing the polymer concentration.

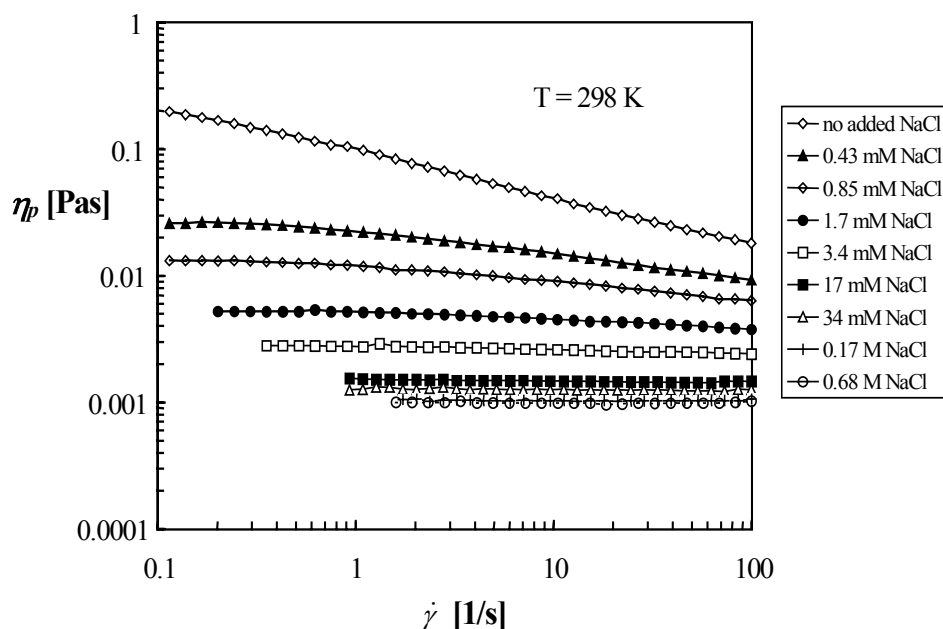


Figure 8.8 The shear viscosity η_p vs. shear rate $\dot{\gamma}$ for a 0.50 g/l PAA solution in water at pH = 5.8 ($\alpha_d = 0.20$) at varying ionic strength

Although not found back in literature, evidence is provided here that the viscosity maximum in Figure 8.7 can most probably be associated with the phenomenon of counterion condensation [10]. Above a certain chain charge density it is energetically favourable for positive counterions to condense near the chain. Consequently the distance between the chain charges cannot be reduced anymore. The Bjerrum length λ_b (Eq. 8.5), the smallest distance between two elementary chain charges for monovalent polyelectrolytes, is about 0.71 nm at 298 K. This corresponds with the mean distance between chain charges at $\alpha_d = 0.35$ i.e. pH = 6.5, which appears to be exactly the degree of dissociation at which the maximum viscosity was observed. It seems that increasing pH above 6.5 results in a higher fraction of condensed counterions with no change in the distance between chain charges. The increasing amount of sodium ions as a result of NaOH addition leads to a higher charge screening and consequently to a decrease in viscosity.

The influence of the salinity on the shear viscosity of an aqueous solution of 0.50 g/l PAA at pH = 5.8 ($\alpha_d = 0.20$) is shown in Figure 8.8. The sodium ion concentration in these experiments resulting from pH modification by NaOH was equal to 1.4 mM. Especially at small concentrations of added NaCl, the salinity has a strong influence on the viscosity of the PAA solution. In the absence of excess salt the semi-dilute polyelectrolyte solutions are known to form a transient network in which charge screening depends on counterions and monomer concentration [11]. On raising salinity the charge screening becomes gradually independent on monomer concentration and finally only dependent on ionic strength. In this regime an increase of the salt concentration leads to a decrease of the chain size, the amount of physical entanglements and thus the viscosity. High ionic strength results in a dilute state, in which the magnitude of viscosity is governed by coil contraction as a result of charge screening and a decrease in solvent quality.

Visco-elasticity studies

Polymeric materials behave visco-elastic, which means that their stress response will have both fluid- and solid-like characteristics. The visco-elastic behaviour of polymeric materials can be characterised by small amplitude oscillatory measurements [13]. Here a small sinusoidal deformation in time is imposed and the stress response is measured. The imposed deformation γ can be described by:

$$\gamma = \gamma_0 \sin \omega t \quad (8.12)$$

where γ_0 is the deformation amplitude, ω is the angular frequency and t is time. For Newtonian fluids the shear stress response is in phase with the shear rate and thus 90° ahead of shear while for solid materials the stress response is immediate and thus in phase with shear. Visco-elastic materials behave in between these two extremes.

This yields for the shear stress σ_{sh} of visco-elastic materials:

$$\sigma_{sh} = \sqrt{(G'^2 + G''^2)} \gamma_0 \sin(\omega t + \delta) = G' \gamma_0 \sin(\omega t) + G'' \gamma_0 \cos(\omega t) \quad (8.13)$$

where G' is the storage modulus, G'' is the loss modulus and δ is the loss angle with which the stress is ahead of shear for which holds $\delta = \arctan(G''/G')$. These linear visco-elastic material properties are a function of ω . G' gives information about the elastic character of the fluid i.e. energy storage while G'' gives information on the viscous character of the fluid i.e. energy dissipation. For a Hookean solid G' equals the shear modulus G and $G'' = 0$. For a Newtonian fluid $G' = 0$ and $G'' = \eta\omega$.

The visco-elastic behaviour of PAA/water solutions was characterised by oscillatory measurements using a Rheometrics RMS-800 rheometer (Fluids Option) and a Couette geometry (cup diameter 34 mm, bob diameter 32 mm, $\gamma_0 = 0.5\%$). For accuracy reasons, studies were done on 2 g/l PAA/water solutions.

Figure 8.9 and 8.10 show the results for the influence of α_d on G' and G'' vs. ω . After dissolving (pH = 3.1) G' and G'' are of the same order of magnitude. The fluid is behaving like a regular dilute polymer solution. When increasing pH progressively the emerging chain charges result in multiple entanglements, i.e. in a physical network. As a result the stress response is much more solid-like. Consequently $G' \gg G''$ and G' is constant over a wide range of frequencies.

Figures 8.11 and 8.12 show the results for the influence of salinity on G' and G'' vs. ω of 2 g/l PAA/water at pH = 5.8. The sodium ion concentration resulting from pH modification by NaOH equals 5.6 mM. On NaCl addition the physical network collapses quickly due to the increased screening of the chain charges. As a result G' and G'' become of the same order of magnitude, which is characteristic for dilute polymer solutions.

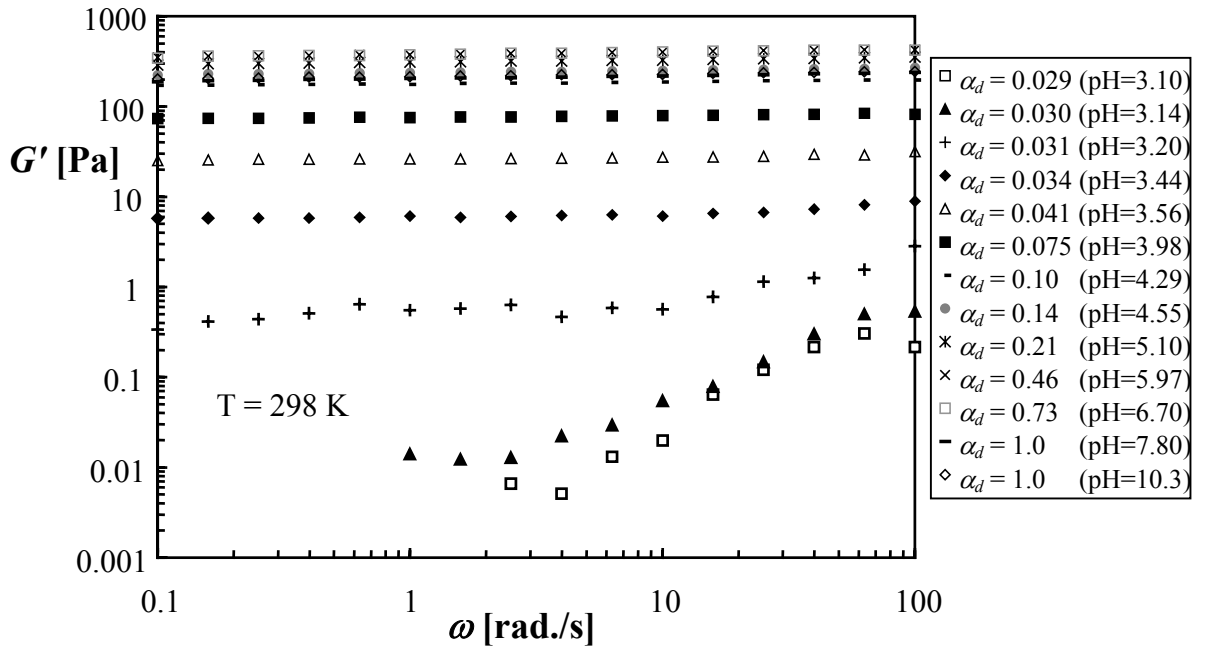


Figure 8.9 G' vs. ω at various pH values for 2 g/l PAA/water, no added salt

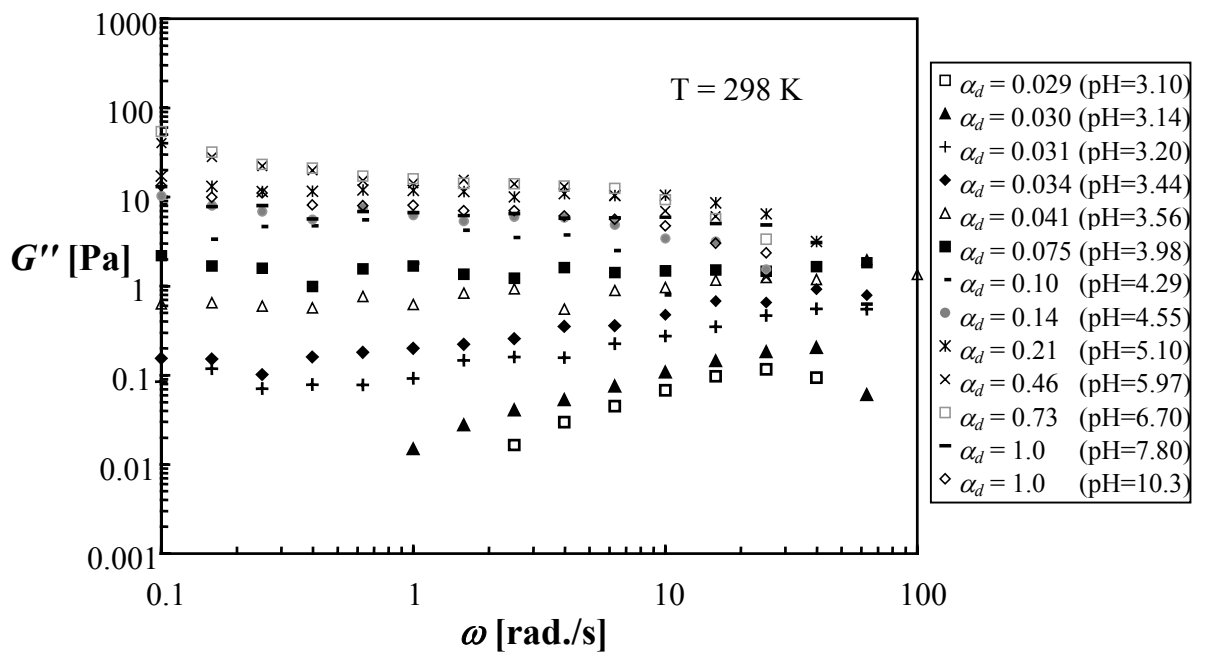


Figure 8.10 G'' vs. ω at various pH values for 2 g/l PAA/water, no added salt

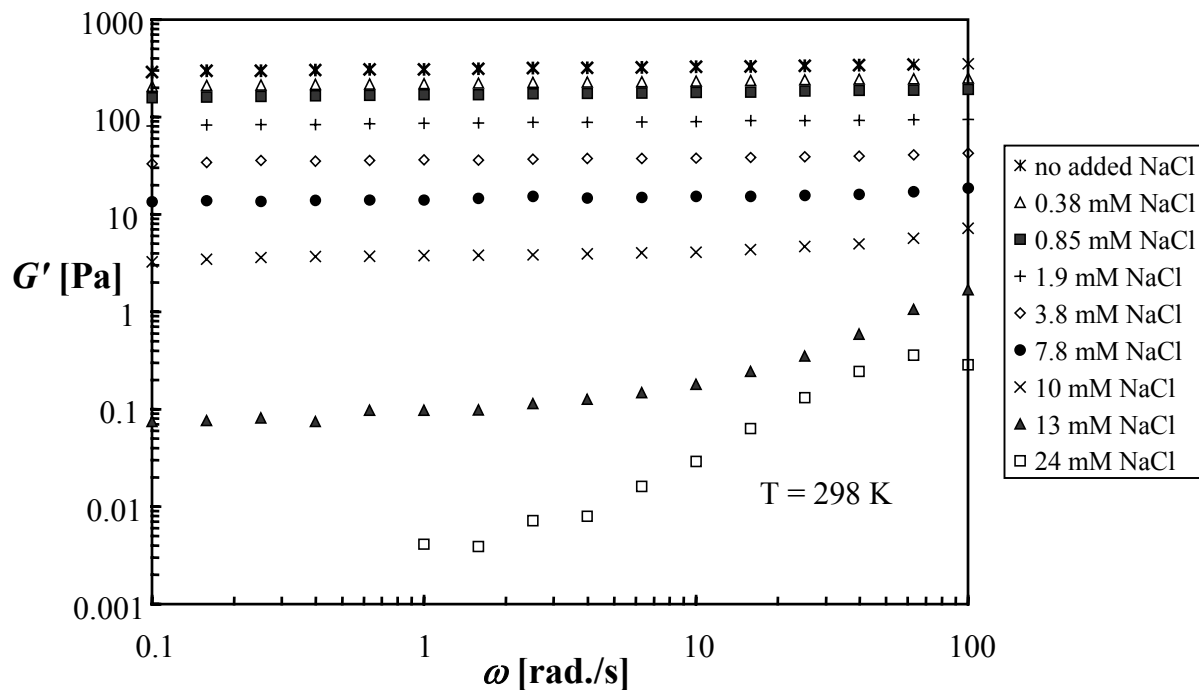


Figure 8.11 G' vs. ω at various concentrations of added NaCl for 2 g/l PAA/water, pH = 5.8

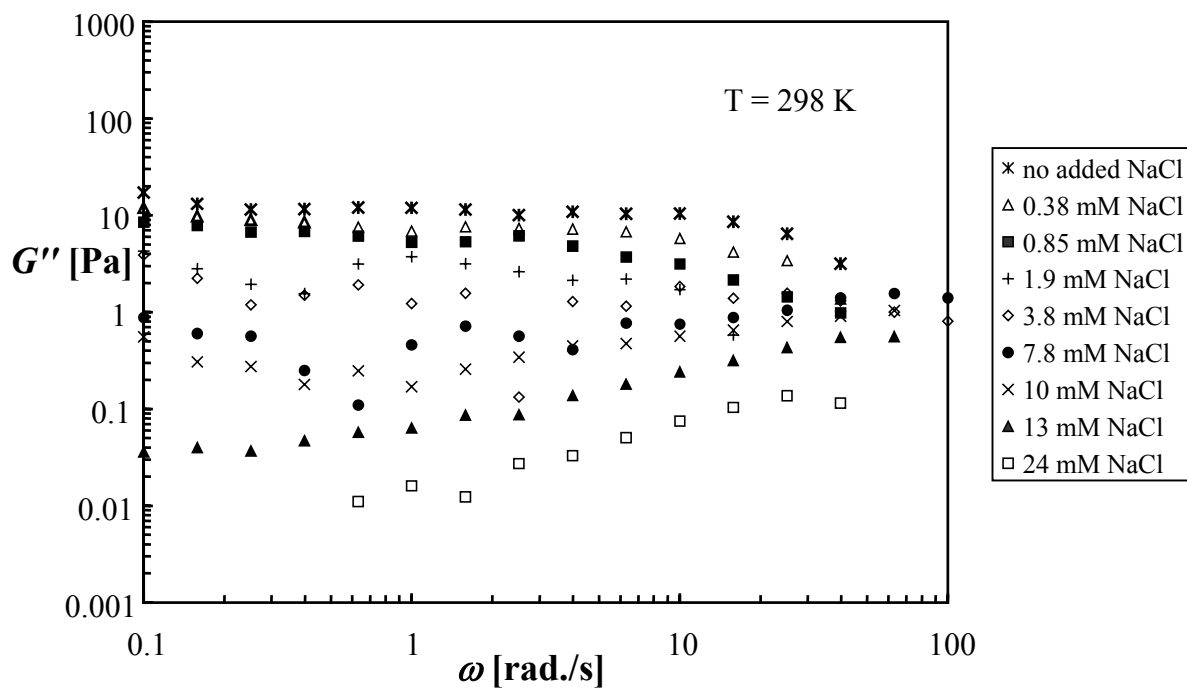


Figure 8.12 G'' vs. ω at various concentrations of added NaCl for 2 g/l PAA/water, pH = 5.8

8.3 Coreflood studies

8.3.1 Set-up, materials and procedures

In general, interpretation of porous media flow experiments using polyelectrolyte solutions is complex because rheological behaviour and retention effects are dependent on parameters like pH, ionic strength, surface charge, molecular weight, polymer concentration, quality of the solvent etc. Because in literature no data were available on this specific polymer/adsorbent system, it was decided not to vary the conditions under which polymer injection occurred.

The coreflood set-up used is described in Section 6.4.1. The core holder is a cylindrical tube made of Polymethylmethacrylate (PMMA) with an internal diameter of 2.62 cm. The pressure drop can be measured over three sections separately (Figure 6.11). The advantage of this is that non-linear entrance effects cannot disturb the measurements and that local permeability or viscosity changes can be monitored. The length of each section is 2.67 cm.

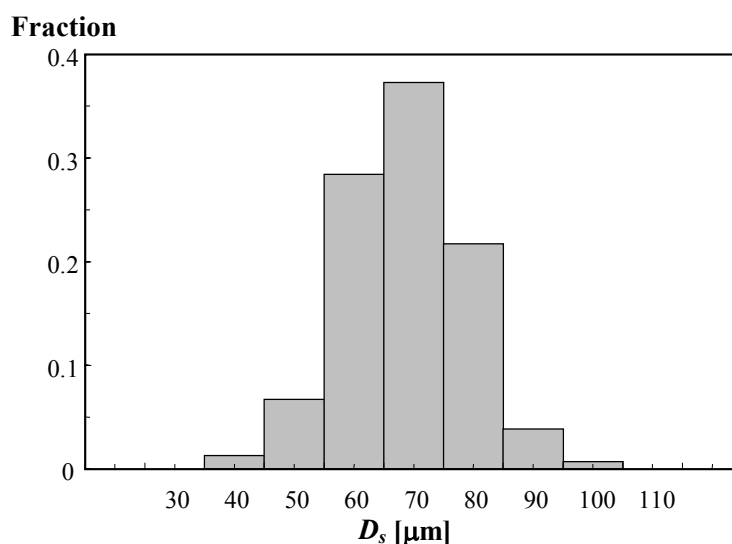


Figure 8.13 Bead diameter distribution

The porous media were obtained by dry packing spherical PMMA beads in the core holder. The PMMA beads have been sieved carefully to obtain a narrow distribution of bead diameters. Figure 8.13 shows the bead diameter distribution determined by light microscopy. The average bead diameter was 69 μm . During filling, the core

holder was gently shaken resulting in an average porosity of 0.375. The permeability of packs was determined by water injection: $k = 4.3 \times 10^{-12} \text{ m}^2$. This value was very reproducible and is in good agreement with the prediction based on the Carman-Kozeny equation (Eq. 2.16) with $A = 150$ giving a value of $4.4 \times 10^{-12} \text{ m}^2$. An estimation of the effective pore radius (Eq. 6.9, $\alpha_s = 1$) gives $R_p = 9.6 \text{ }\mu\text{m}$. Before every experiment water was injected in the PMMA bead packing until no change in conductivity and pH of the injected water could be noticed. Control experiments with water under respectively acid, neutral and alkaline conditions and water with different amounts of added salt showed no change in core permeability.

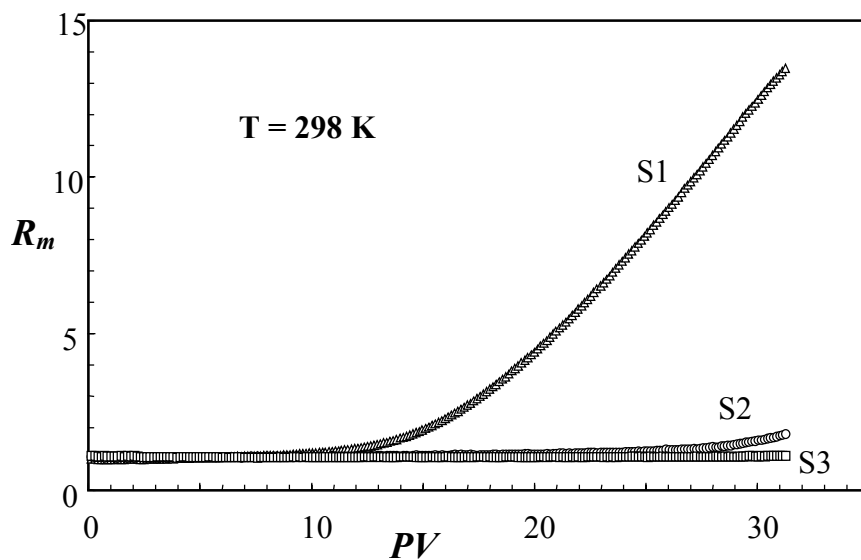


Figure 8.14 Plugging of the first section during injection of 0.21 g/l PAA/water

The polymer solution used was a 0.50 g/l PAA/water solution with no added NaCl, which was prepared and filtered (Section 8.2.1). After filtration the solution was diluted by a factor 2. The resulting polymer concentration, determined by Total Organic Carbon analysis was 0.21 g/l (pH = 4.3, conductivity = 0.05 mS/cm). The polymer solution was injected at a flow rate of 26 ml/h yielding $\dot{\gamma}_p \approx 25 \text{ s}^{-1}$ (Eq. 2.23), meaning that only retention due to adsorption was expected. The same flow rate was used when injecting fluids in subsequent steps.

8.3.2 Coreflood results

Figure 8.14 shows a severe plugging of the first core section (S1) and to a smaller extent of the second core section (S2) during injection of the polymer solution. A subsequent injection of acid water (pH = 3.2, conductivity = 0.30 mS) resulted in an immediate decrease of R_k (S1) to a value of 3 and R_k (S2) to a value of 1.4 (see Figure 8.15). The pressure drop over S3 did not show any change.

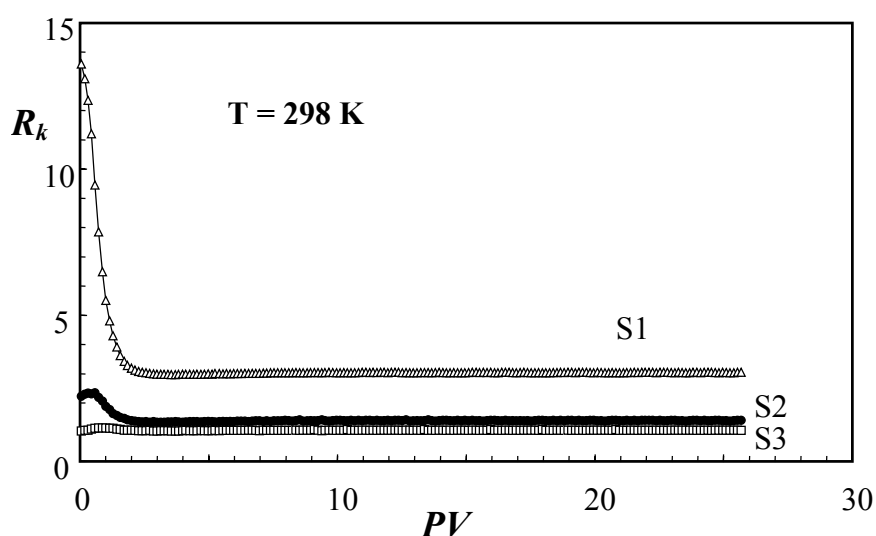


Figure 8.15 Injection of acid water (pH = 3.2) in the plugged core

Subsequently the acid water was displaced by alkaline water (pH = 9.8, conductivity = 0.13 mS) and the experiment had to be stopped after 9 PV to prevent pressure transducer overload. R_k (S1) was increasing linearly in time and had reached a value of 21. R_k (S2) was equal to 4 and constant in time. R_k (S3) did not show any change. A repetition of the injection of acid water (pH = 3.2) and alkaline water (pH = 9.8) had a corresponding outcome. Finally, the alkaline water was displaced by water with the same pH but high salinity (0.34 mol/l added NaCl). This resulted in R_k (S1) = 2.4, R_k (S2) = 1.1 and R_k (S3) = 1, all were constant in time. In addition, pH at the outlet had changed to a value of 4.4 and conductivity had decreased from 32 mS/cm to 24 mS/cm. Apparently the polymer phase present in the core acted as an ion exchanger. A repeat experiment on another core using a fresh polymer solution resulted in similar plugging effects and influences of pH and salinity on the permeability reduction.

So, despite the high core permeability and the extensive filtration procedure, core plugging took place. The fact that the pressure drop over section S3 did not change at all and that no polymer phase could be determined by TOC analysis in the fluid flowing out of the core, indicated that a filtration process was taking place, predominantly in the first section of the core. This could only be a result of trapped polyelectrolyte aggregates. These aggregates, which must have formed after filtration, become stuck in pore throats and their size is dependent on pH and salinity. A literature search revealed that polyelectrolytes can easily form aggregates in the presence of small amounts of divalent or trivalent ions (like Ca^{2+} , Mg^{2+} and Al^{3+}) [14,15]. These ions can be released from glassware used during preparation or degassing.

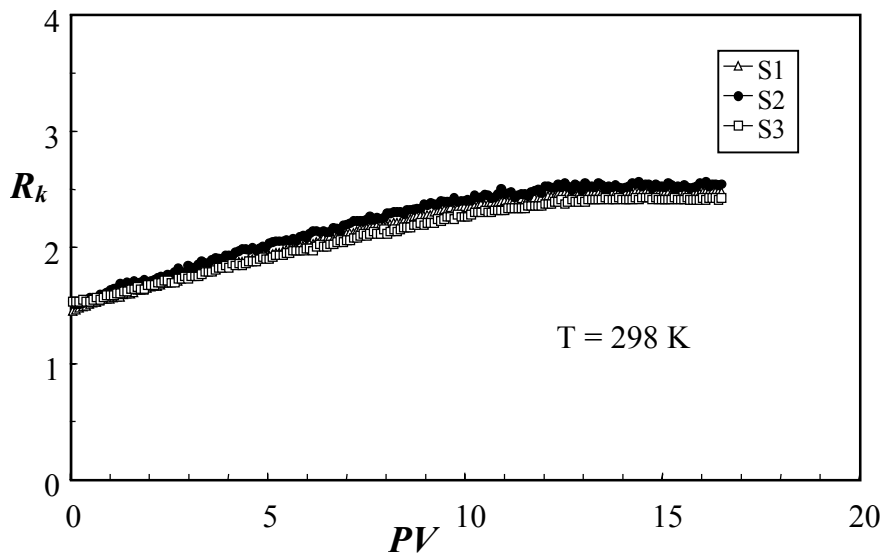


Figure 8.16 Injection of water in a core saturated with water containing 0.003 M Na_3PO_4

In an attempt to remove this aggregate plugging effect, water containing some phosphate (0.003 M Na_3PO_4) was injected in a plugged core. The idea was that phosphate could act as a multivalent ion scavenger. Indeed injection resulted in an immediate disappearance of the plugging in sections S1 and S2. Finally, the same permeability reductions were obtained for all core sections, namely $R_k = 1.5$. TOC measurements revealed that some polymer had left the core during phosphate injection. A subsequent injection of millipore water (pH = 6.5) without added salt lead to a slow but equal increase of R_k for all core sections (Figure 8.16). The permeability

reduction was constant after 13 PV at $R_k = 2.5$. water (pH = 6.5) without added salt lead to a slow but equal increase of R_k for all core sections (Figure 8.16). The permeability reduction was constant after 13 PV at $R_k = 2.5$.

A following injection with salted water (pH = 6.5, 0.009 M NaCl) gave an equal decrease of the permeability reduction for all core sections to R_k (S1,S2,S3) = 1.6 (Figure 8.17). Further experiments on this core using water of varying pH and/or salinity resulted in equal values of R_k for all sections and in fully reversible behaviour of R_k . Thus a porous medium was made of which the permeability could be controlled and regulated by pH and ionic strength suggesting that changes in R_k were only due to a change in the adsorbed layer thickness.

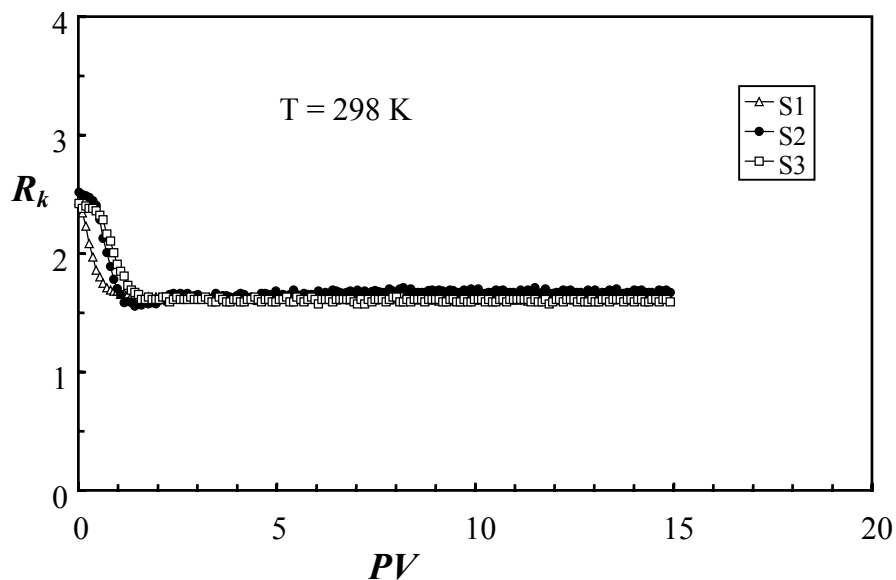


Figure 8.17 Injection of salted water (0.009 M NaCl) in a core saturated with water

Based on the previous result the solution preparation was changed. After filtration, 0.0006 M Na_3PO_4 was added to the polymer solution. The result was that during injection of the polymer solution in a new core the previously reported plugging effect had vanished. The mobility reductions of all sections were equal to 1.6. An attempt to measure by TOC analysis the amount of polymer adsorbed failed, probably due to a combination of a small specific surface and low adsorbed amount. Because reproducible results could be obtained in this way the relationship between R_k of a pre-adsorbed core and the ionic strength of the injected water was determined. Measurements have been performed at pH = 4, pH = 6.5 and pH = 9 (Figure 8.18). In

all cases the permeability reduction reacted fully reversibly on changes in ionic strength. It follows that 0.1 M NaCl is the limiting concentration, as predicted by the OSF theory. On decreasing salinity below this value, R_k increases due to a reduction of charge screening leading to an increase in the size of the adsorbed polymer layer. At pH = 4 the number of chain charges is too small to cause growth of the size of the adsorbed layer. Above the limiting concentration, R_k was equal to 1.36 for all core sections. Note that $R_k = 2.5$ was obtained for water injection with no added salt at pH = 6.5. Presumably, R_k at pH = 9 is smaller than R_k at pH = 6.5 due to the equal distance between chain charges while due to the NaOH addition to obtain the higher pH, ionic strength is effectively higher.

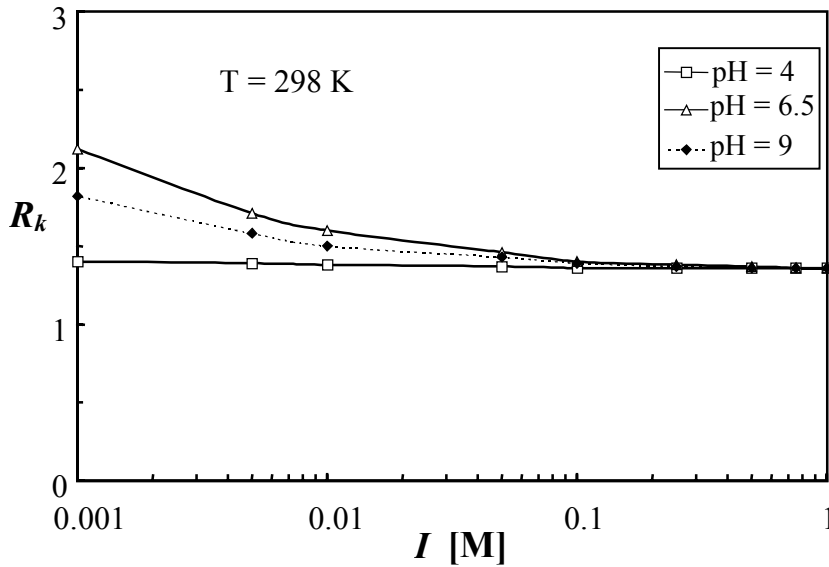


Figure 8.18 R_k of the pre-adsorbed core vs I of the injected brine at different values of pH

When combining Eqs. 6.8, 6.9 (with $\alpha_s = 1$) and 8.8 and assuming that the size of the adsorbed layer equals $2R_g$, one can estimate the permeability reduction as a function of ionic strength I and degree of dissociation α_d on the basis of the OSF theory:

$$R_k = \left(I - \frac{2\alpha_{ie} \sqrt{q_{tot} L_c}}{R_p \sqrt{3}} \right)^{-4} \quad (8.14)$$

Figure 8.19 shows R_k predictions as a function of I and α_d from Eq. 8.14. On the basis of the results described in Section 8.2.4, the adsorbed layer is expected to have a

maximum size at pH = 6.5 meaning that the curve at $\alpha_d \geq 0.35$ should correspond. A comparison between the model and experiments (Figures 8.18 and 8.19) shows that the order of magnitude and the shape of the curves can be reasonably predicted by the model. In both cases the limiting concentration for electrostatic effects is 0.1 M. However, the real polyelectrolyte system appears to be more efficient in restraining flow than would be expected from the model predictions. Possible explanations for this behaviour are the fact that the real size of the adsorbed layer is probably larger than $2R_g$, as was observed in Chapter 7 for positively charged polymers. Other reasons could be polydispersity effects and inadequacies in the OSF coil size prediction.

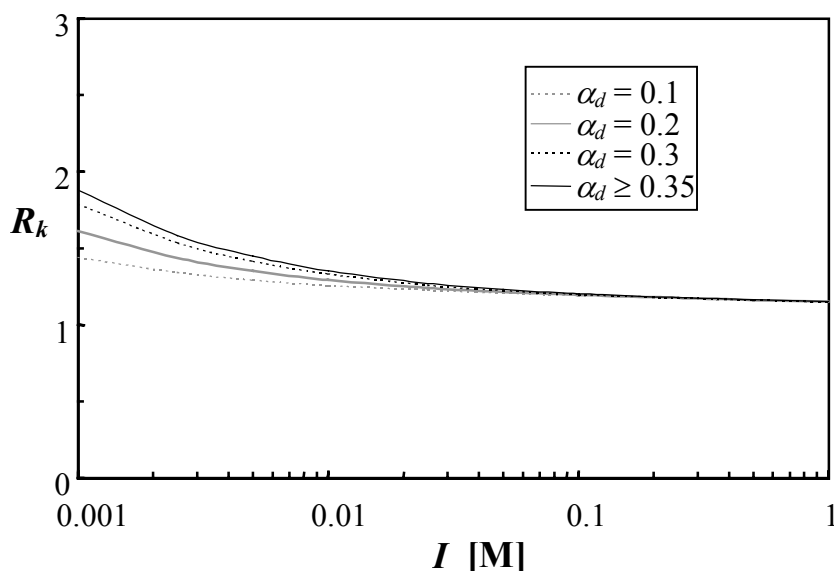


Figure 8.19 Predicted R_k as a function of I and α_d by OSF theory (Eq. 8.14)

8.4 Downhole application as reversible barrier

Due to the high ionic strength environment, present under reservoir conditions, and the low limiting value above which electrostatic effects are screened ($I = 0.1$ M), it is concluded that there is no scope to use polyelectrolytes as downhole permeability tuners or reversible plugs or barriers. Note that polyacrylate systems are also known for phase separation effects, in particular at high ionic strength, low pH, divalent ion presence and high temperatures, i.e. typical conditions experienced downhole [16].

8.5 Summary

1. The rheological studies on aqueous PAA solutions have shown a huge increase in viscosity upon raising pH from the acid to the neutral regime. This increase is a consequence of the large coil expansion resulting in a high number of physical entanglements between the polymer coils i.e. a semi-dilute state. Oscillatory measurements show a solid-like response in this regime ($G' \gg G''$ and G' is constant over a wide range of frequencies).
2. For semi-dilute aqueous solutions of PAA without excess salt, a viscosity maximum was observed at $\text{pH} = 6.5$. Most probably the viscosity maximum can be associated with the start of counterion condensation as the mean distance between chain charges at the viscosity maximum is equal to the Bjerrum length.
3. This work suggests that even for relatively high permeability cores the formation of polymer aggregates can result in plugging. The resulting permeability reduction was strongly dependent on pH and salinity. It is therefore recommended to use multiple pressure readings along the core to prevent disputable interpretations.
4. Phosphate appears to act as a multivalent ion scavenger leading to a destabilisation of aggregates. Small additions to aqueous PAA solutions resulted in removal of plugging effects and equal R_k values for all sections during corefloods.
5. Both rheological experiments and corefloods confirm the fact that $I = 0.1 \text{ M}$ is the limiting value for electrostatic effects. Above this value charge repulsion is fully screened and the polyelectrolyte is behaving as a neutral polymer.
6. The studies show that viscosity and permeability reduction of aqueous PAA solutions show very similar dependencies on pH and ionic strength. Both are “high” at neutral and alkaline conditions and “low” under acid conditions. Both are “low” at high ionic strength.
7. The model based on OSF theory (Eq. 8.14) gives reasonable predictions of the influence of pH and ionic strength on the resulting permeability reduction.
8. Due to the high salinity environment and the low ionic strength threshold above which no coil expansion occurs, the application of polyelectrolyte systems as downhole permeability tuners, selective barriers or reversible plugs will not be very successful. They might work well in lower salinity industrial applications.

References (Chapter 8)

1. F. Giuliano, "Introduction to Oil and Gas Technology", 2nd Ed. (1983)
2. A. Bourgoyne, M. Chenevert, K. Millhem et al., "Applied Drilling Engineering", Chapter II, SPE Text Book Series, Vol. 2 (1985)
3. G. Chauveteau, SPE conference paper 10060, San Antonio (1981)
4. T. Odijk, Ned. Tijdschr. Natuurk. A50, 53 (1984)
5. P. Atkins, "Physical Chemistry", Oxford University Press, 4th Ed. (1990)
6. P. Debye, Ann. Phys. **46**, 809 (1915)
7. P. De Gennes, P. Pincus, R. Velasco et al., J. Physique **37**, 1461 (1976)
8. T. Odijk, J. Polymer Sci., Polym. Phys. Ed. **15**, 477 (1977)
9. J. Skolnick, M. Fixman, Macromolecules **10**, 944 (1977)
10. G. Manning, J. Chem. Phys. **51**, 934 (1969)
11. H. Dautzenberg, W. Jaeger, J. Kötzt et al., "Polyelectrolytes, Formation, Characterization and Application", Carl Hanser Verlag (1994)
12. G. Fleer, M. Cohen Stuart, J. Scheutjens et al., "Polymers at Interfaces", Chapman & Hall, London (1993)
13. R. Bird, R. Armstrong, O. Hassager, "Dynamics of Polymeric Liquids", John Wiley & Sons, New York (1987)
14. R. Skouri, F. Schosseler, J. Munch et al., "Swelling and Elastic Properties of polyelectrolyte gels", Macromolecules **28**, 197, 1995
15. T. Tanaka, "Polyelectrolyte gels", ACS Symposium Series, 480, Am. Chem. Soc., 1992
16. I. Sabbagh, PhD thesis, University Denis Diderot, Paris (1997)

CHAPTER 9 - CONCLUSIONS

This chapter summarises the main conclusions of this thesis:

- The flow resistance in porous media flow is strongly related to the packing structure. This packing structure, which determines the flow path of minimum resistance, can vary considerably, even for packed beds of monodisperse spheres. Consequently permeability can only be predicted with a fairly high inaccuracy and therefore it is usually measured (Chapters 2 and 3).
- Modelling a porous medium by a bundle of tubes with diameter variations in the axial direction provides an improvement over the well-known capillary bundle model with straight tubes. In this way one is able to account for elongational dissipation effects and for capillary pressure effects in two-phase flow problems (Chapters 4 and 5).
- Based on a continuum rheological approach analytical predictions for different geometries and various types of fluids have been derived using the lubrication approximation method (LAM). The resulting predictions are in good agreement with both measurements and numerical predictions and have been converted into corrugated capillary bundle models (Chapters 4 and 5).
- Elongational dissipation is especially relevant in porous media flow of polymer solutions where, due to coil stretching effects, it can exceed dissipation due to shear (Chapters 4 and 5, Appendices A and B).
- The newly developed LAM with spherical co-ordinates allows an improved definition of the deformation rates during flow in tubes with a varying diameter (Chapter 5).
- Concerning the rheology of aqueous Polyacrylamide (PAM) solutions in porous media, a full absence of the depleted layer effect was observed. This is in contrast with results on other acrylamide based polymer systems and seems to be caused by the fact that brine is only a “mediocre-quality” solvent for PAM resulting in an attractive force between the adsorbed layer and the free polymer molecules (Chapter 6).

- Coreflood experiments on PAM/brine solutions in SiC grain packs at low flow rates show that, above a certain concentration in the semi-dilute regime, the mobility reduction does not stabilise during injection, as it does at lower concentrations. This behaviour can be explained by the formation of entangled multi-layers whose thickness grow during injection. The induced layer thickness is the governing parameter for the resulting permeability reduction and for the magnitude of the DPR phenomenon (Chapter 6).
- Lab studies on aqueous Cationic Polyacrylamide (CPAM) solutions in SiC grain packs and Berea sandstone's have proven the concept of using polymer solution injection to create selectively a protective skin on low permeability zones. As for PAM solutions, injection of CPAM solutions at high flow rates induces unsteady-state plugging behaviour. Field trials have to give conclusive information whether the envisaged gelant diversion process can work in practice (Chapter 7).
- Due to the higher adsorption energy, CPAM's adsorption level, adsorbed layer thickness and plugging rate are higher than for non-ionic PAM (Chapter 7).
- A new retention mechanism, called flow-induced adsorption, was proposed to explain the well-established phenomenon of unsteady state plugging behaviour at high flow rates in intermediate permeability porous media. This mechanism, based on the concept that at high rates hydrodynamic forces become large enough to push extra molecules over the osmotic energy barrier, formed by the adsorbed layer, to adsorb is consistent with all previous experimental results (Chapter 7).
- Low flow rate polymer solution rheology in porous media is well described by Chauveteau's depletion model, provided that the medium is homogeneous and that the solution is under "good-solvent" conditions (Chapter 7).
- Coreflood and rheological studies on aqueous solutions of the weak polyelectrolyte Polyacrylic acid (PAA) confirm that viscosity and permeability reduction show similar dependencies on pH and ionic strength. Both are governed by the phenomena of electrostatic charge repulsion and screening (Chapter 8).
- The permeability reduction after adsorption of a weak polyelectrolyte can be regulated by changing pH and ionic strength of the injected fluid. A new model based on the OSF theory gives a reasonable description of the magnitude of these effects (Chapter 8).

- Most probably the maximum in the viscosity of solutions of weak polyelectrolytes with no excess salt, which occurs at a certain pH, can be associated with the start of counterion condensation as the mean distance between the chain charges at the viscosity maximum appears to be equal to the Bjerrum length (Chapter 8).
- Application of polyelectrolyte systems downhole as permeability tuners or reversible plugs does not seem an option due to the high salinity environment present. Above an ionic strength of 0.1 M charge repulsion is fully screened and polyelectrolytes behave like neutral polymers. Experiments show that the concept could work for other industrial applications which involve a lower ionic strength (Chapter 8).

APPENDIX A COIL-STRETCH TRANSITION

In a pure shear flow the velocity gradient is perpendicular to the flow direction i.e. the axial velocity v_z is only a function of the radial co-ordinate r . In a pure elongational flow a velocity gradient in the flow direction exists and the axial velocity v_z is only a function of the axial co-ordinate z . However in practice, any geometry, which involves a diameter change, will generate a flow field with elongational characteristics. Therefore in most flow problems the flow field is complex involving both shear- and elongational components.

The most simple pure elongational flow is uniaxial elongation which can be described by: $v_z = \dot{\epsilon} z$, $v_x = -\frac{1}{2} \dot{\epsilon} x$ and $v_y = -\frac{1}{2} \dot{\epsilon} y$ where $\dot{\epsilon}$ is a constant elongational strain rate. As elongational flow is fundamentally different from shear, the material property characterizing flow is not the viscosity η , but the elongational viscosity η_{elo} . The associated stress distribution in uniaxial elongation is: $T_{ik} = 0$ for $i \neq k$ and $T_{zz} - T_{xx} = T_{zz} - T_{yy} = \dot{\epsilon} \eta_{elo}$. For Newtonian fluids η_{elo} is a constant only depending on the type of elongational deformation. For example, in a simple uniaxial elongational flow $\eta_{elo} = 3\eta$ while in a steady biaxial elongational flow $\eta_{elo} = 6\eta$. For polymeric materials the flow behaviour is more complex and η_{elo} is a function of elongational rate $\dot{\epsilon}$ and time. In dilute polymer solutions, a polymer coil, which is exposed to an elongational flow field, can undergo a sudden transition from a coil conformation into an elongated state, at a critical rate $\dot{\epsilon}_c$. As the stretched state induces a big increase in polymer-solvent interaction, the friction and thus η_{elo} can increase orders of magnitude. This coil-stretch transition was predicted in the seventies by de Gennes [A1] and Hinch [A2]. Theoretical considerations lead to the conclusion that the coil-stretch transition is due to hysteresis of the molecular relaxation time with chain extension [A1]. As a result the critical strain rate is related to the longest relaxation time of the polymer molecule as follows: $\dot{\epsilon}_c = \tau_r^{-1}$, where τ_r is the longest relaxation time.

The coil-stretch transition was studied extensively by Odell et al. [A3, A4] using an opposed jet device. This apparatus is composed of two narrow capillary jets that face each other, immersed in the polymer solution. As solution is sucked simultaneously into both jets, an elongational flow field is created between the tubes. Based on the

geometry and flow rate the elongational rate in such a device can be estimated and a pressure drop over the tubes can be measured to obtain an estimation of the elongational viscosity. The coil-stretch transition can be visualized by flow induced birefringence measurements using laser light in combination with two polarisators placed perpendicularly. Above a certain flow rate a sudden line of light between the opposed jets becomes visible, which indicates orientation due to stretching of the flowing polymer molecules. The model experiments of Odell et al. [A3, A4] resulted in the following general conclusions:

- The relaxation time increases with molecular weight and is usually in the range of 10^{-5} - 10^{-3} s for polymers with a molecular weight of one million.
- The measured relaxation times correspond to Zimm's non-free draining model and as a result $\dot{\epsilon}_c \propto kTM^{-3/2}\eta_s^{-1}$. Surprisingly enough experiments show that this relation holds, independent of the solvent quality.
- The relaxation time characterizing contraction is usually more than one order of magnitude longer compared to the one governing stretching.
- Apart from the critical rate $\dot{\epsilon}_c$, also the time the coil is experiencing that critical rate is an important parameter in the stretching phenomenon.
- As the strain rate is increased progressively beyond $\dot{\epsilon}_c$, the stretched chains become increasingly stressed until they rupture. The critical strain rate for fracture i.e. mechanical degradation is found to obey $\dot{\epsilon}_f \propto M^2$. So very high molecular weight polymer chains stretch and break immediately.
- Rupture due to mechanical stresses usually occurs exactly in the middle of a chain, where the stresses on the chain are the highest.

As porous media flow involves elongational flow components, the coil-stretch transition phenomenon can also take place during injection of polymer solutions. It is generally thought that in porous media flow the stretching process occurs in a much more gradual way than in the above described model experiments. This is a consequence of the fact that the residence time in each contraction is very limited and that the polymer passes "low velocity" regions, where it can, at least partly, relax back to a less stretched state. Consequently full stretching can only occur after passing a large number of pore constrictions in the porous medium.

A systematic study on flow induced polymer stretching in porous media has been done by Haas et al. [A5, A6]. These authors used Polyacrylamide solutions in packs of randomly packed glass spheres. The size of the spheres were typically in the order of a few hundred microns to avoid the disturbing influence of polymer retention phenomena. Their results are summarised here by using an onset Reynolds number for stretching (Re_o), which is indicated by a sudden increase in the pressure drop. The maximum pressure drop obtained as a result of coil stretching is expressed here in terms of the maximum flow resistance (A_{max}). For their definitions see Chapter 2. The results of Haas et al. [A5, A6] are expressed here in a qualitative, concise manner, dealing with the important influence parameters, avoiding going into too many details:

- Molecular weight: This is the main controlling factor for both Re_o and A_{max} . Increasing the molecular weight decreases Re_o and increases A_{max} strongly.
- Sphere diameter: For a given polymer solution decreasing the sphere diameter will shift Re_o to smaller numbers. A_{max} remains unchanged.
- Solvent viscosity/quality: For a given sample, increasing the solvent viscosity decreases Re_o but does not affect A_{max} . Increasing the solvent quality decreases Re_o and increases A_{max} slightly.
- Polymer concentration: For a given polymer solution increasing the concentration, increases A_{max} , but does not affect Re_o (except for the effect of changed viscosity).
- Temperature: A decrease in temperature changes the onset to smaller values of Re_o but does not influence A_{max} . The influence of temperature can be explained by the change in solvent viscosity and the changing quality of the solution.

Most of the observed trends in porous media flow can be explained directly by the results obtained from the opposed jet experiments of Odell et al. [A3, A4].

- A1. P. De Gennes, J. Chem. Phys **60**, 5030 (1974)
 A2. E. Hinch, Proceedings of Colloques Internationaux de CNRS **233**, 241 (1974)
 A3. A. Keller, J. Odell, Colloid Polymer Sci. **263**, 181 (1985)
 A4. J. Odell, A. Keller, A. Muller, Colloid Polymer Sci **270**, 307 (1992)
 A5. W. Kulicke, R. Haas, Ind. Eng. Chem. Fundam. **23**, 308 (1984)
 A6. R. Haas, F. Durst, Rheol. Acta **21**, 150 (1982)

APPENDIX B ELASTIC EFFECTS

Core-flow experiments have been done in the developed set-up (see Section 6.4.1) to be able to study elastic effects as a result of coil stretching (see Appendix A) separately over the three different core sections. The porous medium used was a monodisperse pack of glass beads of 110 μm size and had a porosity of 0.375. The permeability was equal to $9.0 \times 10^{-12} \text{ m}^2$. For these experiments Polyacrylamide/brine solutions have been used i.e. the PAM 1 sample which characterization is described in Section 6.2. Two polymer concentrations have been studied, 0.45 g/l and 0.90 g/l PAM1 in brine containing 20 g/l NaCl. Based on our characterization both solutions can be considered to be dilute. The temperature during the experiments was 303 K. To determine the impact of polymer adsorption, the experiment started with the injection of the polymer solution at a low flow rate. The permeability reduction R_k was subsequently determined by brine injection. The latter turned out to be 1.14.

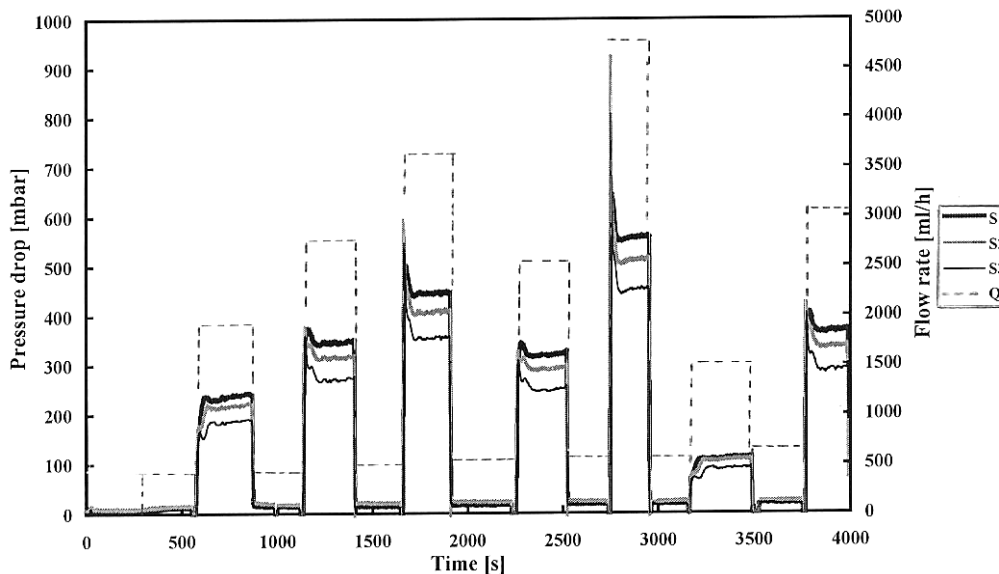


Figure B1 Pressure drop and flow rate vs. time for the three different core sections (0.90 g/l PAM1/brine, T = 303 K)

The experiments were carried out as follows. Fresh polymer solution was injected at a low flow rate for at least 3 pore volumes. After the flow was stopped, the injection was started at the desired flow rate and the pressure drops over the three different core section were recorded. This procedure was repeated for different flow rates.

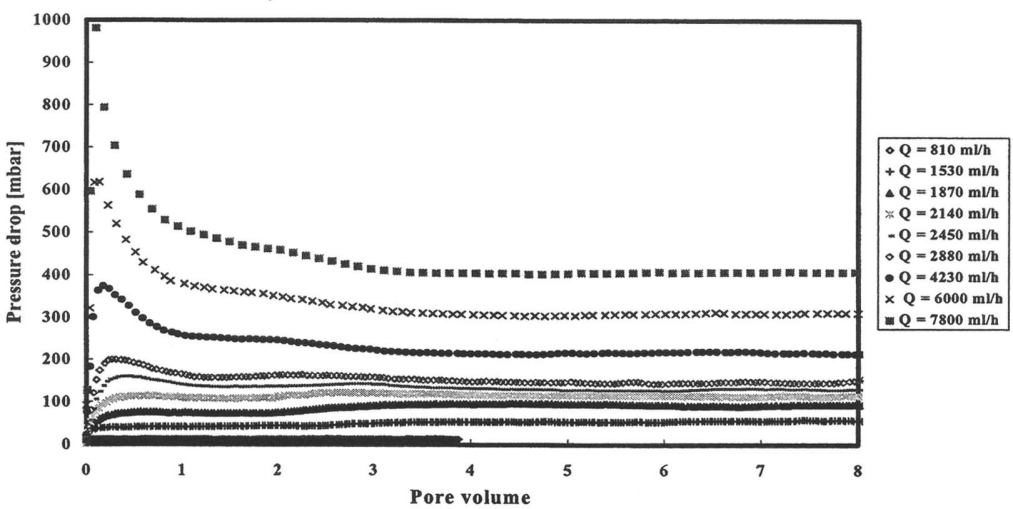
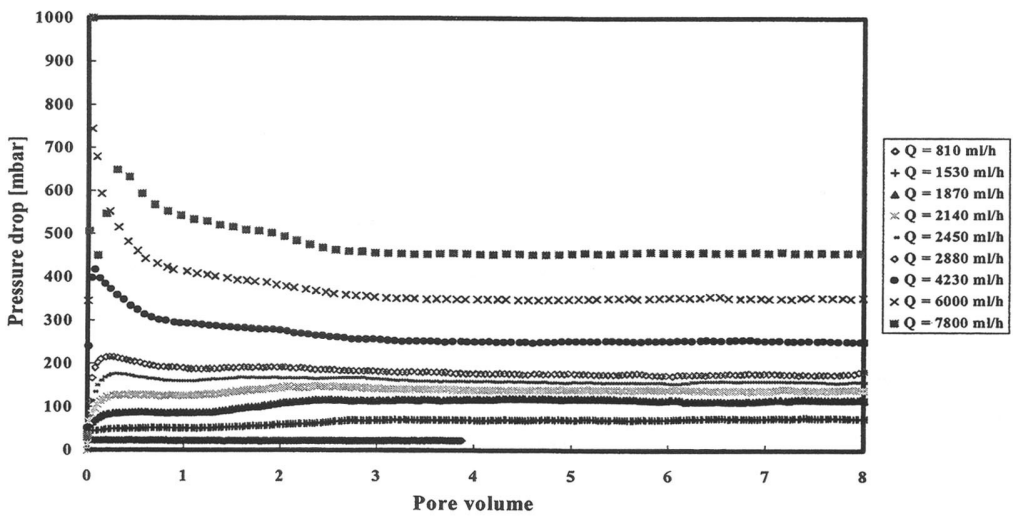
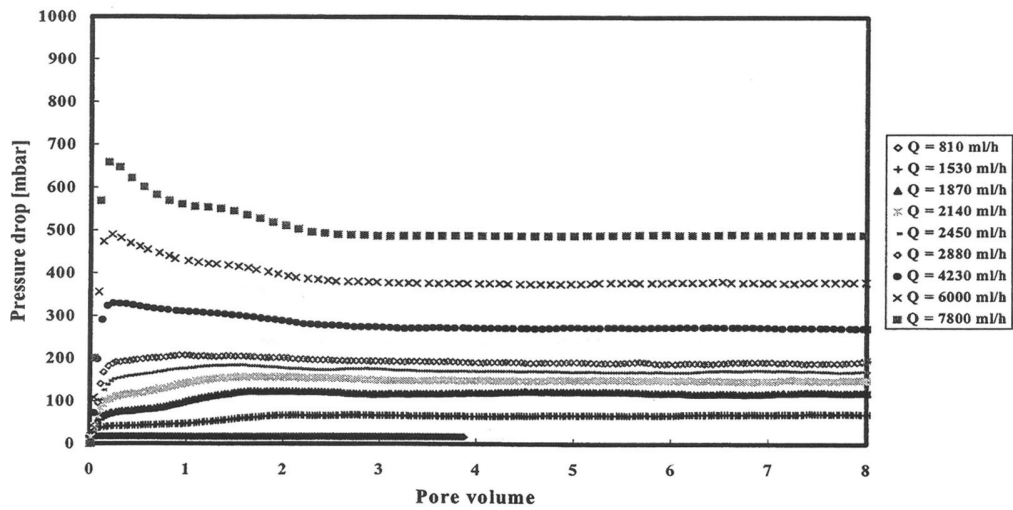


Figure B2 Pressure drop vs. pore volume in the core sections S1, S2 and S3 respectively for a 0.45 g/l PAM1/brine solution at different flow rates, T = 303 K

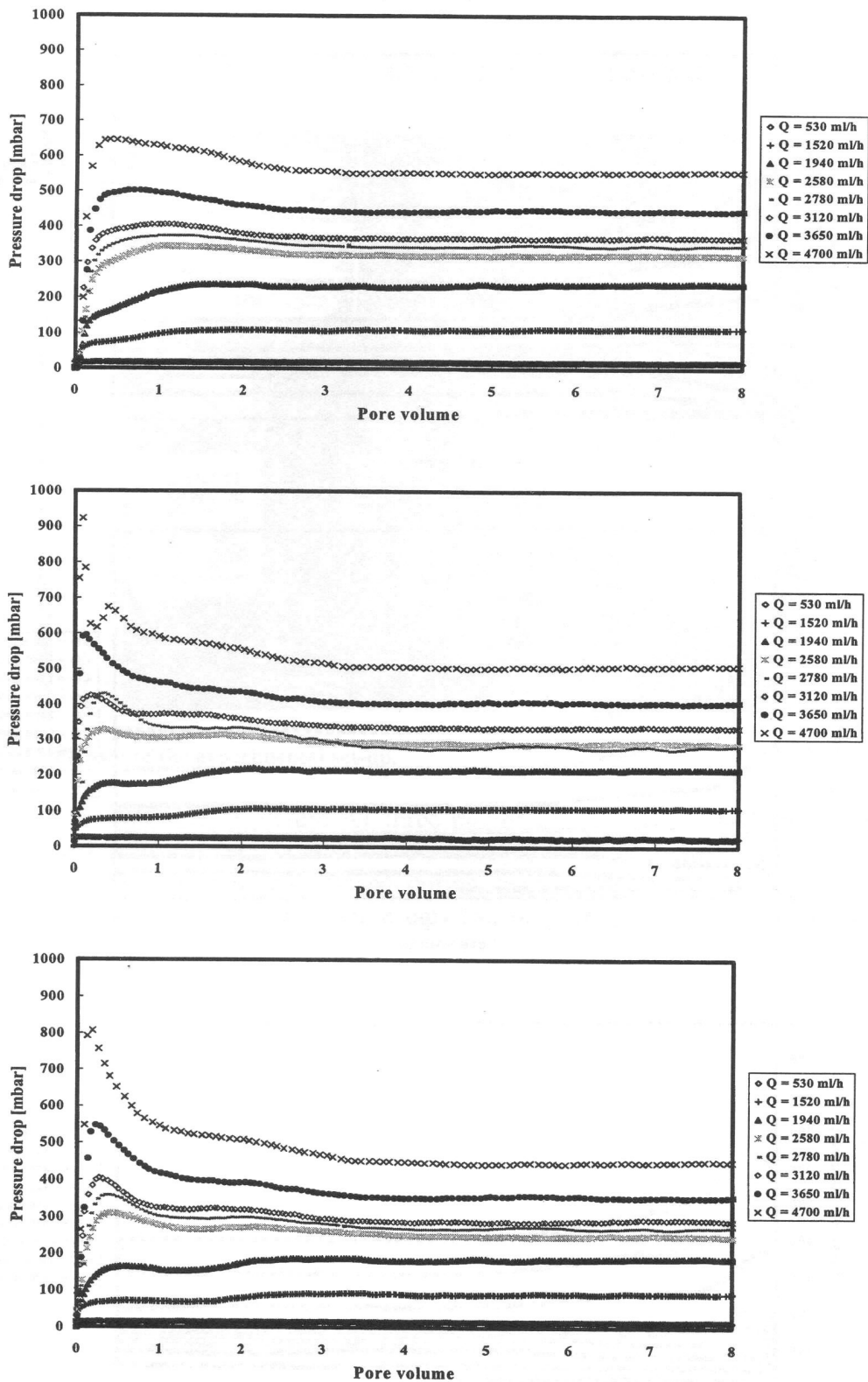


Figure B3 Pressure drop vs. pore volume in the core sections S1, S2 and S3 respectively for a 0.90 g/l PAM1/brine solution at different flow rates, T = 303 K

Figure B1 shows typical rawdata i.e. the pressure drop for the various sections and the flow rate as a function of experimental time for injection of the 0.90 g/l PAM1 solution. Figure B2 and B3 show the results of both experiments, the pressure drop of the different core sections versus the pore volume at different flow rates.

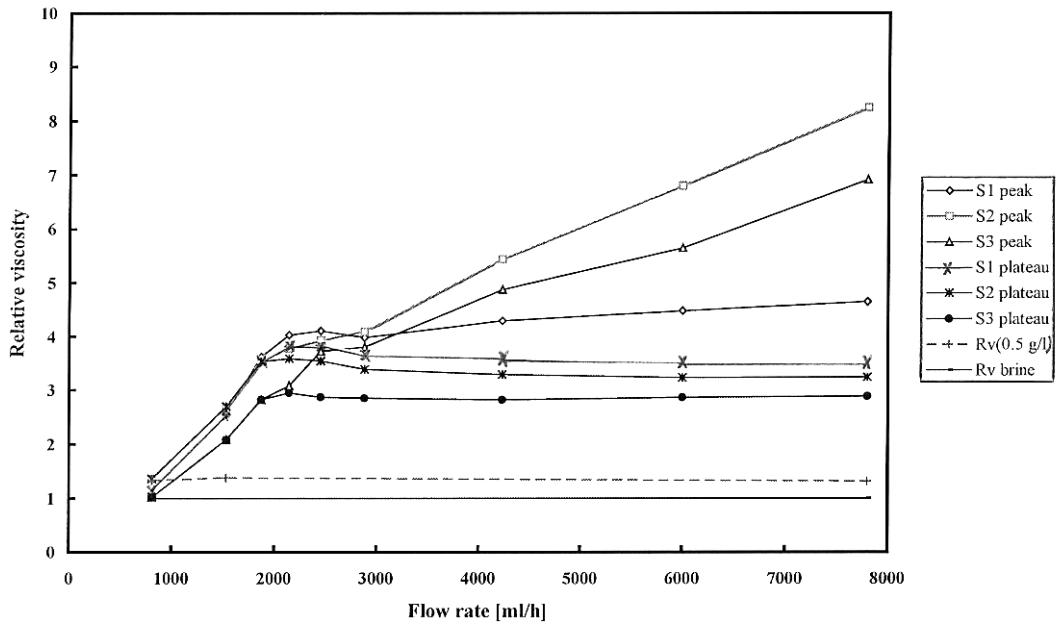


Figure B4 The relative viscosity vs. the flow rate for the 0.45 g/l PAM/brine solution. S1, S2, S3 represent the different core sections. The dashed line is the relative viscosity of the solution, while Rv brine is the relative viscosity of the brine, T = 303 K

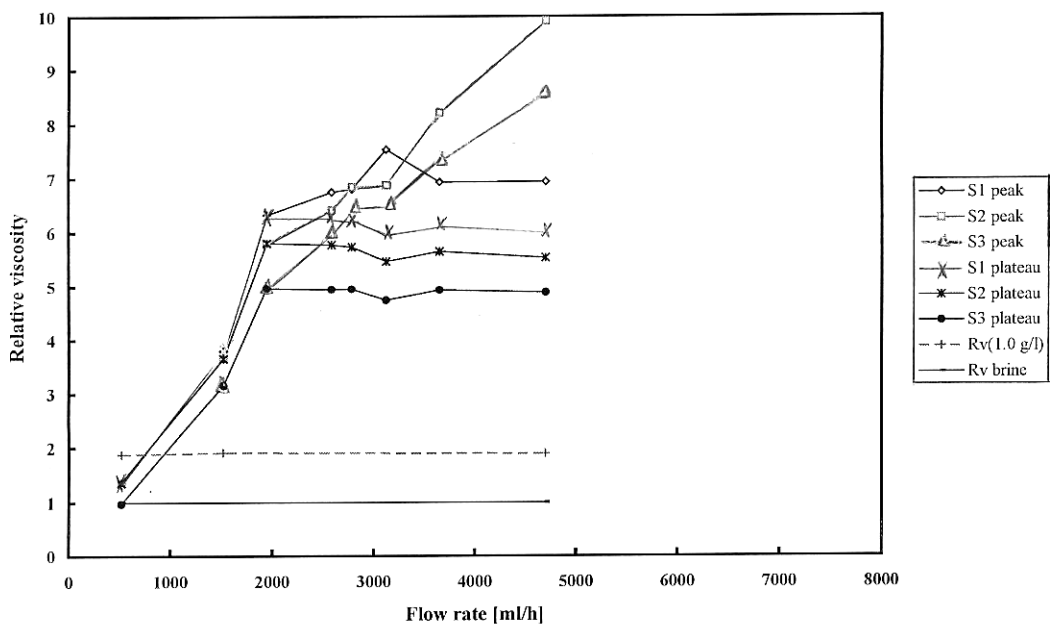


Figure B5 The relative viscosity vs. the flow rate for the 0.90 g/l PAM/brine solution. S1, S2, S3 represent the different core sections. The dashed line is the relative viscosity of the solution, while Rv brine is the relative viscosity of the brine, T = 303 K

Figure B4 and B5 compare the relative viscosities of the polymer solutions in the porous medium and in the rheometer. In the porous medium the relative viscosity is defined as the pressure drop during polymer solution injection divided by the pressure drop during to brine injection (after polymer adsorption). The shown peak values are based on the maximum pressure drop values measured during the experiment. The plateau values are based on the stationary value of the pressure drop after 4 pore volumes. The following trends are found:

- The polymer solutions show clear thickening effects related to coil stretching
- The peak values occur within the first pore volume and the peak position shifts to the left at increasing rates. Sequence of increasing values is S1, S3, S2.
- At low rates, no peaks occur and the pressure drop builds gradually
- For every flow rate a plateau value has developed within 4 pore volumes
- The plateau value decreases in magnitude from S1 to S3 in both experiments
- The plateau viscosity decreases at increasing flow rate

It turns out that two mechanisms play an important role during these experiments: coil stretching and mechanical degradation. The first one goes along with an increase in the pressure drop, the second one with a decrease. Mechanical fracture only coincides with coil stretching if a critical flow rate is exceeded. At a certain critical flow rate, a high molecular weight fraction can stretch causing an increased pressure drop. At an increasing rate a part of the stretched fraction can break mechanically as the molecules get overstretched during flow. As a result, after having reached a high peak value, this results in a decrease of the pressure drop. When the polymer solution reaches the second section, it already has a degradation history from the first section. Consequently the pressure drops in this section will be lower. The value of the plateau viscosity decreases at higher flow rates as a larger fraction of the macromolecules have been stretched and broken. The latter is also the reason for the higher peak values at higher rates. Coil stretching starts to occur around 1000 ml/h. Degradation effects become important above a flow rate of 2000 ml/h.

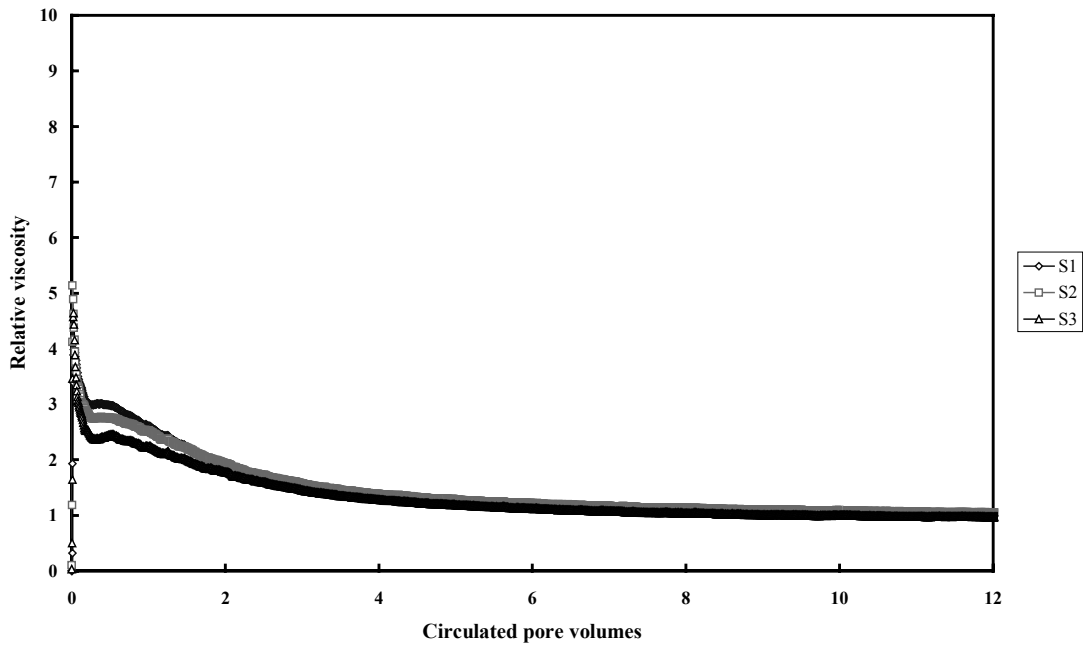


Figure B6 Relative viscosity vs. the circulated pore volume for the 0.45 g/l PAM/brine solution, $Q = 5800$ ml/h, $T = 303$ K. One circulated pore volume equals 230 ml.

A clear proof for the occurrence of mechanical degradation is the result shown in Figure B6, in which the polymer solution was circulated. So a closed system was formed connecting the inlet and the outlet. After three circulated volume the reaction in the sections is identical and the solution obtains the relative viscosity of a lower molecular weight PAM/brine solution during further circulation.

APPENDIX C TWO-PHASE IMMISCIBLE FLOW

The principles of immiscible, two-phase displacement in porous media are of great interest to the petroleum industry. A good understanding of the mechanisms affecting oil recovery allows the development of new techniques to improve the recovery process. In immiscible displacement the main forces acting on a droplet of fluid are hydrostatic-, viscous-, gravity-, inertial- and capillary forces. The capillary forces result from the combined action of surface forces acting on: i) the interface between the two fluids, ii) the interfaces between the two fluids and the solid medium. They find their origin in the uneven attraction by neighbour molecules at such an interface, which is quantified by the interfacial tension, the free surface energy per unit area. The interfacial tension causes a droplet of oil immersed in water to strive to a spherical shape, which is the geometry with the smallest surface/volume ratio and thus the smallest free surface energy. For such a droplet the pressure on the concave side of the droplet exceeds that on the convex side. This difference is known as the capillary pressure P_c for which holds $P_c = P_o - P_w = 2 \mu_{ow} / R$. Here P_o and P_w are the oil and water pressure respectively, μ_{ow} is the interfacial tension between oil and water and R is the droplet radius. When oil and water are in contact with a rock face (Figure C1), a contact angle γ_c exists for which holds $\cos \gamma_c = (\mu_{os} - \mu_{ws}) / \mu_{ow}$. If $\gamma_c < 90$ the rock is defined as being water wet. If $\gamma_c > 90$ the rock is oil wet. The wettability is a measure of which fluid preferentially adheres to the rock.

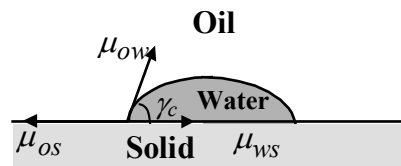


Figure C1 A water drop surrounded by oil which contacts a water wet solid surface

Consider a water wet porous medium, fully saturated with oil except for a small water fraction, the irreducible water saturation S_{wi} . In order to maintain this situation, a hydrostatic pressure equal to the capillary pressure P_c has to be applied. At a certain point of time water is injected into the medium (imbibition). Water will have the

tendency to invade the smallest pores first as this will lead to a stronger decrease in capillary pressure. When prolonging water injection, larger pores will be filled out and the decrease in capillary pressure will be slower (Figure C2). The oil phase loses its continuity at $S_w = 1 - S_{or}$, where S_{or} is the residual oil saturation. The reverse, water loses its continuity and P_c is maximum, occurs at $S_w = S_{wc}$ where S_{wc} is the irreducible water saturation. The relationship between the capillary pressure P_c and the water saturation S_w is called the capillary curve (Figure C2). The shape of this curve is a function of the pore diameter, the diameter distribution and the wettability.

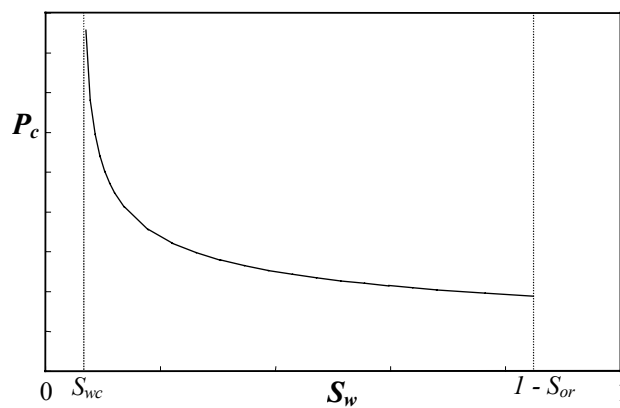


Figure C2 The capillary curve for water injection (imbibition) in a water wet porous medium, initially saturated with oil

Consider water injection (viscosity η_w) with a Darcy velocity $u (=Q/S)$ in a water wet porous medium (permeability k , porosity ϕ , cross-section S , length L) saturated with oil (viscosity η_o , capillary pressure $P_c = P_c(S_w) = P_o - P_w$). When oil and water are flowing through a porous medium simultaneously, the fluids will impede each other. Consequently oil and water have their own effective permeability, k_w and k_o , which both depend on the local water saturation S_w . These permeabilities are usually normalised by division through the absolute permeability k rendering the relative permeabilities to oil and water, k_{ro} resp. k_{rw} . The value of the relative permeability is a function of the fluid distribution in the porous medium and the shape of the pores. Figure C3 shows a typical curve of the relative permeabilities as a function of the water saturation in a water wet porous medium. Due to capillary force effects water tends to be present in small pores, while oil tends to occupy space in the middle of the larger pores. As a result of this water encounters more pore wall friction than oil.

Consequently the water saturation S_w at the intersection of oil- and water relative permeability curves is larger than 0.50.

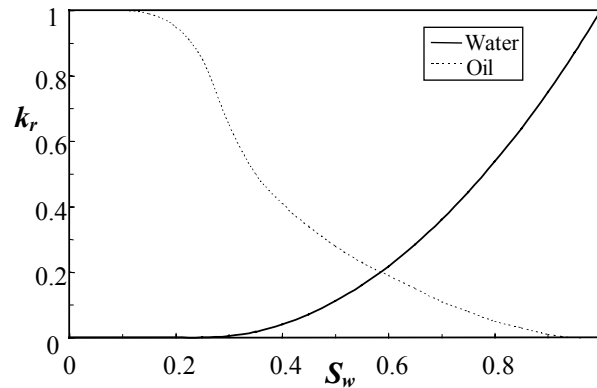


Figure C3 A typical curve of the relative permeabilities as a function of the water saturation in a water wet porous medium

In practice macroscopic equations are used to describe two-phase flow in porous media. At every point in time t and for every value of z ($0 < z < L$) must hold:

$$u_i = -\lambda_i \frac{\partial P_i}{\partial z} \quad (i = w, o) \quad (C1)$$

$$\lambda_i = \frac{k_i}{\eta_i} = \frac{k k_{ri}}{\eta_i} \quad (i = w, o) \quad (C2)$$

where $k_{ri} = k_{ri}(S_w)$, $\lambda_o = k_o/\eta_o$, $\lambda_w = k_w/\eta_w$. Now holds for the fractional water flow f_w :

$$f_w = \frac{u_w}{u_w + u_o} = \frac{1 + \frac{\lambda_o}{\lambda_w} \frac{\partial P_c}{\partial z}}{1 + \frac{\lambda_o}{\lambda_w}} \quad (C3)$$

where $P_c = P_o - P_w$

As $\frac{\partial P_c}{\partial z}$ is always positive, capillary pressure gradient tends to increase the fractional flow of water in a water wet medium. When neglecting the capillary pressure gradient $\frac{\partial P_c}{\partial z}$, f_w is strictly a function of the fluid viscosities and water saturation as related by the local relative permeabilities. For a good description of this problem, see Leverett's frontal displacement theory [C1], which is widely used in petroleum industry

C1. M.C. Leverett, Trans. AIME **146**, 107 (1942)

APPENDIX D CARREAU PARAMETERS

c [g/l]	η_{po} [mPas]	λ_l [s]	n	η_r
0.09	1.00	0	1	1.10
0.22	1.10	0	1	1.21
0.45	1.31	0	1	1.44
0.90	1.74	0	1	1.91
1.34	2.29	0	1	2.52
1.79	3.00	0.024	0.92	3.30
3.58	7.01	0.043	0.91	7.70
5.37	14.5	0.061	0.90	15.9
7.16	29.3	0.163	0.90	32.2
8.95	52.1	0.201	0.87	57.3

Table D1 Parameters of the Carreau model resulting from linear regression of the rheological measurements (T = 298 K) of the PAM1/brine solutions ($\eta_r = \eta_{po}/\eta_s$)

c [g/l]	η_{po} [mPas]	λ_r [s]	n	η_r
0.09	1.02	0	1	1.17
0.18	1.18	0	1	1.36
0.27	1.35	0	1	1.55
0.36	1.54	0	1	1.77
0.54	1.88	0.04	0.90	2.16
0.72	2.60	0.08	0.90	2.99
1.79	7.00	0.26	0.87	8.05

Table D2 Parameters of the Carreau model resulting from linear regression of the rheological measurements (T = 303 K) of the PAM2/brine solutions ($\eta_r = \eta_{po}/\eta_s$)

APPENDIX E COREFLOOD SET-UP

A coreflood set-up has been developed to measure the relationship between pressure drop and volumetric flow rate during fluid flow through a synthetic or natural porous medium. In fact this set-up was built after gaining experience with a previous set-up. The main drawbacks of the old set-up were:

- The pump was a batch-like piston displacement pump, which means that only discontinuous flow was possible. Besides the pump could only deliver small flow rates up to $0.056 \text{ cm}^3/\text{s}$.
- The pressure drop was determined externally, meaning that the pressure drop was measured over the whole core including short inlet and outlet tubes. For high permeability porous media ($k > 1 \times 10^{-11} \text{ m}^2$) the extra pressure loss over these tubes was not negligible and a correction was necessary.
- Measurements on water at high flow rates (using another pump) resulted in a non-linear relationship between pressure drop and flow rate due to an excess pressure loss at the inlet and outlet of the core. The flow rate was too small for inertial flow to be the cause. Figure E1 gives an example of this effect. It shows the relationship between pressure drop ΔP and flow rate Q for flow of water at 298 K through a monodisperse glass bead pack ($D_p \approx 390 \text{ }\mu\text{m}$). The triangles give the pressure drop measured externally i.e. with the old set-up. At small flow rates the pressure drop behaves linearly while at larger flow rates non-linear behaviour results.

Because of these drawbacks, a new set-up was built which was able to measure over a wide range of flow rate and permeability. Some modifications were the following: The diameter of the inlet and outlet tubes was increased, the pressure points were made inside the core-holder and the number of pressure points was increased to gain extra information. Measurements by the new set-up on the same glass beads resulted in a linear relationship between pressure drop and flow rate (Figure E1) in agreement with Darcy's law (Equation 2.1). At small flow rates, the external pressure drop

measurement gives slightly larger values than the internal measurements due to the extra pressure loss over the inlet and outlet tubes (Figure E1).

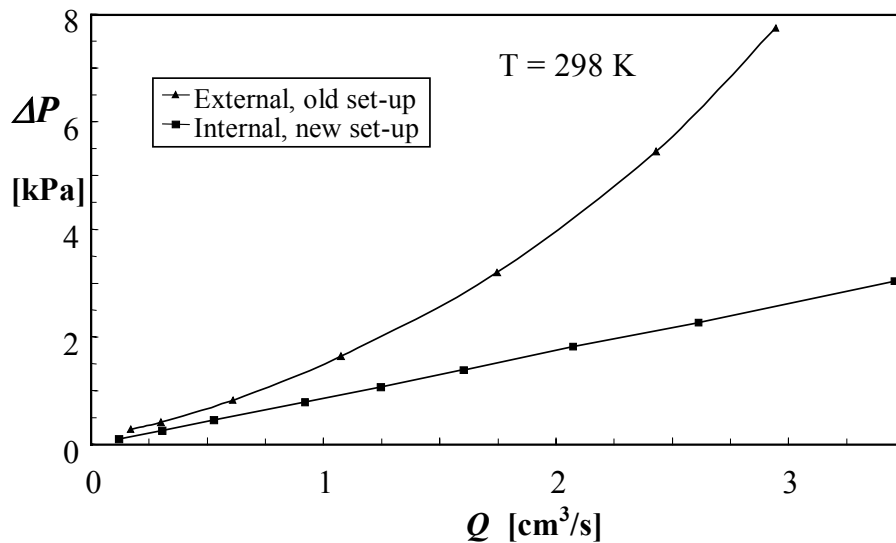


Figure E1 Pressure drop vs. flow rate for flow of water through a monodisperse glass bead pack. Same core material, but different placement of pressure points.

The permeability found was $k \approx 1.14 \times 10^{-10} \text{ m}^2$ ($\phi \approx 0.375$). This result is in good agreement with the Carman-Cozeny prediction (Equation 2.16) when using $A = 180$.

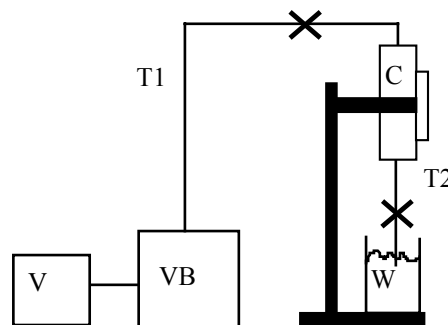


Figure E2 The saturation set-up. V = Vacuum pump, VB = Vacuum barrel, C = Core-holder, W = Water barrel, T1 & T2 are PTFE tubes with precision valve

The saturation procedure

From previous experience was known that the saturation procedure is crucial and has to be performed with great care. This is especially true for low permeability porous media because air can remain trapped due to capillary forces. To obtain a good and reproducible saturation, a small set-up was built (Figure E2). It consists of a vacuum

pump, a vacuum barrel with pressure-meter, a water barrel, a vertical standard with grab-bucket and some PTFE tubes and precision valves.

The saturation procedure was done as follows: First all pressure point channels of the core-holder were closed by four covers and the core-holder was placed vertically in the standard. A tube with closed valve (T1) was connected between the upper end of the core-holder and the vacuum barrel. Another tube with closed valve (T2) was connected between the lower end of the core-holder and the water barrel. This barrel contained water that was degassed before during 1 hour by connecting it to a vacuum pump. The upper valve was opened and the core-holder was evacuated. Subsequently the lower valve was opened gradually until the water started to move slowly in the direction of the core-holder. After the waterfront had passed the core-holder and upper valve, both valves were closed. Finally, the saturated core-holder, still connected to T1 and T2 (closed valves), was transported to the coreflood set-up.

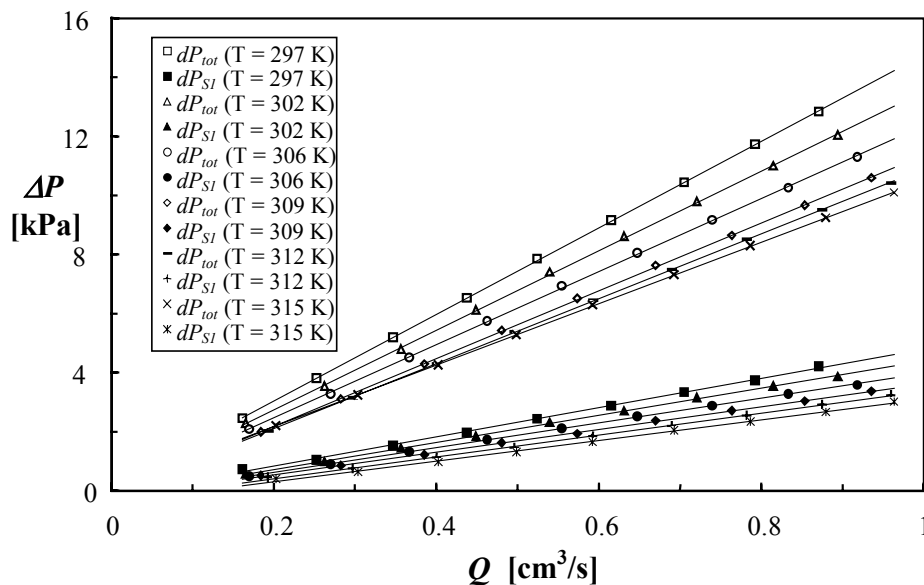


Figure E3 Pressure drop vs. flow rate during water flow through a glass bead pack
 dP_{tot} is the total pressure drop, dP_{S1} is the pressure drop over section S1

During transportation the pressure point channels were kept vertically (rectangular block up) to ensure that no air present in the pressure point channels could intrude in the porous medium. In the coreflood set-up the core-holder was held vertically and T1 was removed. A small amount of degassed water was added by a hypodermic syringe to fill up the open end (connector). Then degassed water was pumped very slowly through the feed tubing of the coreflood set-up while connecting the core-holder to it.

Then T2 was removed and the outlet tubing of the coreflood set-up was connected to the core-holder. Finally, degassed water was pumped through the core for some minutes. Using this procedure, the pressure point channels were still not saturated with water. This was obtained in the following manner: First the valve at the outlet tubing was closed and the cover at pressure point channel D (Figure 6.10) was removed, while degassed water was pumped slowly through the core. Now water flowed out of pressure point channel D. The desired PTFE tube of the pressure system was filled up totally with water from a long needle syringe and was connected to channel D. Then the cover of pressure point channel C (Figure 6.10) was removed and the procedure was repeated. The same was done for channel B and A. After channel A had been connected, the valve at the outlet-pipe was opened and the set-up was ready for a measurement.

dP_{tot}/Q [kPa s/cm ³]	η_w (exp.) [mPas]	η_w (lit.) [mPas]
14.645	0.885	0.890
13.487	0.815	0.815
12.363	0.747	0.749
11.476	0.697	0.705
10.987	0.664	0.665
10.401	0.629	0.629

Table E1 The dP_{tot}/Q slopes and experimental- and literature viscosity values

Testing the set-up

The set-up was tested extensively to verify its potential and measurement window (permeability, flow rate, fluid viscosity). Figure E3 shows measurements on water flow at different temperatures through a pack of monodisperse glass beads ($D_p \approx 110 \mu\text{m}$, $\phi \approx 0.375$). The permeability found was $k \approx 8.97 \times 10^{-12} \text{ m}^2$, in good agreement with the Carman-Kozeny relation when $A = 180$ (Equation 2.16). Measurements are shown for the pressure drop over all sections (dP_{tot}) and over section S1. Table E1 shows dP_{tot}/Q slopes from Figure E3 and experimental- and literature viscosity values. As can be seen the viscosity values from the experiments correspond well with those from literature, indicating that the coreflood set-up measures correctly.

APPENDIX F DYNAMIC ADSORPTION

The delay in the polymer front displacement can give information on the amount of polymer adsorbed [F1]. Suppose a polymer front is moving at a steady Darcy velocity u (flow rate Q , cross-section S) in a core (length L) initially saturated with brine. Since adsorption of the polymer delays the front, the polymer front velocity v_p is smaller than the velocity of brine filtration $v_b = u/\phi$. Thus $v_p = v_b - v_a$ where v_a depends on the rate of adsorption, i.e. the rate at which the polymers leave the front to adhere onto the pore walls. When the flow rate is sufficiently low, adsorption only depends on attractive interactions and is instantaneous. The infinitesimal amount of polymer dW_a that is adsorbed in time dt is given by:

$$dW_a = (1 - \phi)\rho_s S_{sp} \Gamma v_p S dt \quad (\text{F1})$$

where ρ_s is solid density, S_{sp} is specific surface and Γ is adsorbed amount. Also holds:

$$dW_a = \phi S c v_a dt \quad (\text{F2})$$

Combining F1 and F2 gives:

$$v_a = \zeta_a v_p \quad (\text{F3})$$

where $\zeta_a = [(1 - \phi)\rho_s S_{sp} \Gamma] / (\phi c)$ equals the dimensionless time to fill up the surface with adsorbed molecules. Combining the total pressure drop $\Delta P = \Delta P_w + \Delta P_p$ with Darcy's law (Eq. 2.1) and the expression for R_m (Eq. 2.21) gives for $PV < 1 + \zeta_a$:

$$R_m(t) = I + \left[\frac{R_{mp} - I}{1 + \zeta_a} \right] PV \quad (\text{F4})$$

where R_{mp} is the plateau mobility reduction. By taking $\delta R_m / \delta PV$ after injection the retardation factor (Eq. F4) and the adsorbed amount (Eq. F3) can be determined.

F1. P. Zitha, PhD thesis, University Paris VI (1994)

NOMENCLATURE

Greek

α	= Geometry parameter widening tube ($\alpha = R_{min}/R_{max}$)	
α^*	= Darcy parameter in dimensionless Forchheimer's law	
α_l	= Darcy parameter	[m ⁻²]
α_d	= Degree of dissociation (= ratio between amount of dissociated acid groups and total amount of acid groups)	
α_g	= Dimensionless factor depending on porous medium structure	
α_i	= Dimensionless factor to account for polymer-solvent interactions and excluded volume effects on polymer coil size	
α_{ie}	= Same as α_i but now also including electrostatic effects	
α_s	= Dimensionless factor depending on porous medium structure	
β	= Dimensionless radial coordinate sinusoidal tube ($\beta = r/R$)	
β^*	= Inertia parameter in dimensionless Forchheimer's law	
β_l	= Inertia parameter	[m ⁻¹]
γ	= Imposed deformation	
γ_0	= Deformation amplitude	
γ_c	= Contact angle	[rad]
$\dot{\gamma}$	= Shear rate	[s ⁻¹]
$\dot{\gamma}_r$	= Radial shear rate	[s ⁻¹]
$\dot{\gamma}_p$	= Average shear rate in porous medium	[s ⁻¹]
Γ	= Adsorbed amount	[kg m ⁻²]
δ	= Loss angle	[rad]
δ_d	= Depleted layer thickness	[m]
$\frac{\partial P}{\partial z}$	= Component of gradient of fluid pressure	[kg m ⁻² s ⁻²]
$\frac{\partial P}{\partial r}$	= Component of gradient of fluid pressure	[kg m ⁻² s ⁻²]
ΔP	= Pressure drop	[kg m ⁻¹ s ⁻²]
ΔP_{ela}	= Pressure drop due to elasticity	[kg m ⁻¹ s ⁻²]
ΔP_{elo}	= Pressure drop due to elongation	[kg m ⁻¹ s ⁻²]
ΔP_m	= Pressure drop over model	[kg m ⁻¹ s ⁻²]
ΔP_{sur}	= Surface term of pressure drop	[kg m ⁻¹ s ⁻²]
ΔP_{tot}	= Total pressure drop	[kg m ⁻¹ s ⁻²]
ΔP_p	= Pressure drop during polymer flow after adsorption	[kg m ⁻¹ s ⁻²]
ΔP_{s0}	= pressure drop during solvent flow before adsorption	[kg m ⁻¹ s ⁻²]
ΔP_{s1}	= pressure drop during solvent flow after adsorption	[kg m ⁻¹ s ⁻²]
$\dot{\epsilon}$	= Elongational rate	[s ⁻¹]
$\dot{\epsilon}_c$	= Critical elongational rate for coil-stretching	[s ⁻¹]
$\dot{\epsilon}_f$	= Critical elongational rate for chain rupture	[s ⁻¹]
$\dot{\epsilon}_r$	= Radial elongational rate	[s ⁻¹]
ϵ_0	= Permittivity in vacuum = 8.85×10^{-12}	[C ² N ⁻¹ m ⁻²]
ϵ_h	= Hydrodynamic adsorbed layer thickness	[m]
ϵ_r	= Relative permittivity	

ζ_a	=	Dimensionless time to fill up the surface	
η	=	Fluid viscosity (i.e. shear viscosity)	[kg m ⁻¹ s ⁻¹]
η_o	=	Oil viscosity	[kg m ⁻¹ s ⁻¹]
η_w	=	Water viscosity	[kg m ⁻¹ s ⁻¹]
η_{elo}	=	Elongational viscosity	[kg m ⁻¹ s ⁻¹]
η_{sh}	=	Shear viscosity	[kg m ⁻¹ s ⁻¹]
η_p	=	Polymer solution viscosity	[kg m ⁻¹ s ⁻¹]
η_{po}	=	Polymer solution zero shear rate viscosity	[kg m ⁻¹ s ⁻¹]
η_r	=	Relative viscosity polymer solution = η_{po}/η_s	
η_{rw}	=	Relative viscosity polymer solution near the wall	
η_s	=	Solvent viscosity	[kg m ⁻¹ s ⁻¹]
$\eta_{p\infty}$	=	Polymer solution infinite shear rate viscosity	[kg m ⁻¹ s ⁻¹]
η_{sp}	=	Specific viscosity = $(\eta_p - \eta_s)/\eta_s$	
$[\eta]$	=	Intrinsic viscosity	[kg ⁻¹ m ³]
$[\eta]_{\Theta}$	=	Intrinsic viscosity under Θ conditions	[kg ⁻¹ m ³]
θ	=	Angle coordinate in spherical coordinate system	[rad]
Θ	=	Widening angle of widening tube	[rad]
κ	=	Rheological parameter (only function of power law index n)	
λ	=	Wavelength distortion on sinusoidal tube	[m]
λ_b	=	Bjerrum length	[m]
λ_d	=	Debye length	[m]
λ_r	=	Relaxation time	[s]
λ_o	=	Mobility of oil = k_o/η_o	[kg ⁻¹ m ³ s]
λ_w	=	Mobility of water = k_w/η_w	[kg ⁻¹ m ³ s]
A_p	=	Flow resistance in porous medium	
A_{max}	=	Maximum flow resistance	
μ_{ws}	=	Interfacial tension between water and solid rock face	[kg s ⁻²]
μ_{os}	=	Interfacial tension between oil and solid rock face	[kg s ⁻²]
μ_{ow}	=	Interfacial tension between oil and water	[kg s ⁻²]
ξ	=	Area porosity	
π	=	Pi = 3.14159	
ρ	=	Length coordinate in spherical coordinate system	[m]
ρ_f	=	Fluid density	[kg m ⁻³]
ρ_s	=	Solid density	[kg m ⁻³]
ρ_w	=	Water density	[kg m ⁻³]
σ_{elo}	=	Elongational stress	[kg m ⁻¹ s ⁻²]
σ_{sh}	=	Shear stress	[kg m ⁻¹ s ⁻²]
τ	=	Tortuosity factor porous medium	
τ_t	=	Tortuosity factor tube	
τ_p	=	Tortuosity factor packed bed	
τ_r	=	Longest relaxation time polymer coil	[s]
ϕ	=	Porosity	
χ	=	Relative viscosity ratio i.e. bulk vs. near wall ($\chi = \eta_r/\eta_{rwall}$)	
ψ_1	=	First normal stress coefficient	[kg m ⁻¹]
ω	=	Angular frequency	[rad s ⁻¹]
Ω	=	Total number of widening and converging segments	

Latin

a	=	Normalized amplitude sinusoidal tube ($= R_s/R_t$)	
a_m	=	Mark-Houwink index	
A	=	Carman-Kozeny constant	
A_c	=	Dimensionless inflow cross-section	
A_s	=	Area available for adsorption	$[m^2]$
$A_1...A_4$	=	Functions describing average cross section model	
b	=	Geometry parameter sinusoidal tube ($= \lambda/R_t$)	
b_c	=	Length of statistical chain unit, C-C bonding length	$[m]$
B	=	Inertia constant	
$B(x,y)$	=	Beta function	
c	=	Polymer concentration	$[kg\ m^{-3}]$
c^*	=	Critical overlap concentration	$[kg\ m^{-3}]$
c_o	=	Concentration of groups to be titrated	$[mol\ m^{-3}]$
c_i	=	Concentration of the i-th species	$[mol\ m^{-3}]$
c_t	=	Concentration of titrant added	$[mol\ m^{-3}]$
C_∞	=	Chain rigidity parameter	
CN	=	Co-ordination number	
CV	=	Unit cell volume	$[m^3]$
d_p	=	Shape factor porous medium	
d_t	=	Shape factor tube	
\underline{D}	=	Rate of deformation tensor	$[s^{-1}]$
D_h	=	Hydraulic diameter	$[m]$
D_p	=	Charact. length scale in medium (particle diameter)	$[m]$
D_s	=	Sphere diameter	$[m]$
e	=	Elementary charge = 1.60×10^{-19}	$[C]$
f_p	=	Friction factor in medium	
f_e	=	Fluid property dependent on type of elongational flow field	
f_w	=	Fractional flow of water	
$F_1...F_4$	=	Dimensionless functions describing model flow resistance	
g	=	Power law parameter	$[kg\ m^{-1}\ s^{h-2}]$
G'	=	Storage modulus	$[kg\ m^{-1}\ s^{-2}]$
G''	=	Loss modulus	$[kg\ m^{-1}\ s^{-2}]$
G_1, G_4	=	Dimensionless functions describing permeability of model	
h	=	Power law index	
H	=	Parameter dependent on the shape of the particles	
I	=	Ionic strength	$[mol\ m^{-3}]$
J_1, J_2	=	Parameters characterizing pore geometry in sphere packs	
k	=	Permeability	$[m^2]$
k_b	=	Boltzmann constant = 1.38×10^{-23}	$[N\ m\ K^{-1}]$
k_o	=	Permeability to oil	$[m^2]$
k_p	=	Permeability packed bed	$[m^2]$
k_t	=	Permeability tube	$[m^2]$
k_w	=	Permeability to water	$[m^2]$
k_{ro}	=	Relative permeability to oil = k_o/k	
k_{rw}	=	Relative permeability to water = k_w/k	
K	=	Parameter accounting for shape and tortuosity	

K_a	=	Acid equilibrium constant	[mol m ⁻³]
K_o	=	Parameter depending on cross-sectional shape	
K_w	=	Autoprotolysis constant water	[mol m ⁻³]
l_o	=	Distance between two sphere layers	[m]
l_e	=	Mean distance between two chain charges	[m]
l_i	=	Length of i-th tube segments	[m]
L	=	Length porous medium or tube	[m]
L_c	=	Contour length polymer molecule	[m]
L_e	=	Effective length flow path in porous medium	[m]
m	=	Power law parameter	[kg m ⁻¹ s ⁿ⁻²]
M	=	Molecular weight	[kg mol ⁻¹]
M_m	=	Monomer weight	[kg mol ⁻¹]
M_n	=	Number average molecular weight	[kg mol ⁻¹]
M_v	=	Viscosity average molecular weight	[kg mol ⁻¹]
M_w	=	Weight average molecular weight	[kg mol ⁻¹]
MR	=	Mobility ratio	
n	=	Power law index	
n_t	=	Number of tubes	
N	=	Number of chain units	
N_s	=	Number of tube segments	
N_t	=	Number of tubes	
N_a	=	Number of tubes in model	
N_A	=	Constant of Avogadro = 6.022 x 10 ²³	[mol ⁻¹]
N_1	=	First normal stress difference	[kg m ⁻¹ s ⁻²]
N_2	=	Second normal stress difference	[kg m ⁻¹ s ⁻²]
NP	=	Number of principal directions in conduit element	
p	=	Power law parameter	[kg m ⁻¹ s ^{q-1}]
P_c	=	Capillary pressure	[kg m ⁻¹ s ⁻²]
P_o	=	Oil pressure	[kg m ⁻¹ s ⁻²]
P_w	=	Water pressure	[kg m ⁻¹ s ⁻²]
PV	=	Number of injected pore volumes	
q	=	Power law index	
q_e	=	Electrostatic persistence length	[m]
q_i	=	Intrinsic persistence length	[m]
q_{tot}	=	Total persistence length = $q_e + q_i$	[m]
q_p	=	Persistence length (= chain rigidity parameter)	[m]
Q	=	Volumetric flow rate	[m ³ s ⁻¹]
Q_s	=	Specific volumetric flow rate	[m ³ s ⁻¹]
r	=	Radial place co-ordinate	[m]
R	=	Tube radius	[m]
R_g	=	Characteristic polymer coil radius = radius of gyration (= $\langle R_g^2 \rangle^{1/2}$)	[m]
R_h	=	Hydrodynamic polymer coil radius	[m]
R_i	=	Radius of i-th tube or i-th tube segment	[m]
R_k	=	Permeability reduction	
R_{ko}	=	Permeability reduction to oil	
R_m	=	Mobility reduction	
R_{mp}	=	Plateau value of the mobility reduction	
R_p	=	Characteristic pore radius	[m]

R_s	=	Amplitude distortion on sinusoidal tube	[m]
R_t	=	Average tube radius sinusoidal tube	[m]
R_{av}	=	Average radius widening or converging tube	[m]
R_{min}	=	Minimum radius widening or converging tube	[m]
R_{max}	=	Maximum radius widening or converging tube	[m]
Re_p	=	Reynolds number in porous medium	
Re_o	=	Reynolds number at onset of coil stretching	
S	=	Cross-sectional area porous medium or tube	[m ²]
S_u	=	Wetted surface per unit volume	[m ⁻¹]
S_v	=	Volumetric specific surface	[m ⁻¹]
S_w	=	Water saturation	
S_{or}	=	Residual oil saturation	
S_{sp}	=	Specific surface	[m ² kg ⁻¹]
S_{wi}	=	Irreducible water saturation	
t	=	Time	[s]
T	=	Temperature	[K]
$\underline{\underline{T}}$	=	Stress tensor (components T_{zr} , T_{zz} etc.)	[kg m ⁻¹ s ⁻²]
u	=	Darcy or filtration velocity = Q/S	[m s ⁻¹]
u_o	=	Darcy velocity of oil	[m s ⁻¹]
u_w	=	Darcy velocity of water	[m s ⁻¹]
U	=	Sphere volume centered at arbitrary point in medium	[m ³]
U_v	=	Volume of void space within U	[m ³]
v_a	=	Velocity loss front due to polymer adsorption	[m s ⁻¹]
v_b	=	Velocity of brine filtration	[m s ⁻¹]
v_i	=	Average interstitial velocity in porous medium	[m s ⁻¹]
v_p	=	Polymer front velocity	[m s ⁻¹]
v_ρ	=	Velocity in ρ direction	[m s ⁻¹]
v_r	=	Velocity in r direction	[m s ⁻¹]
v_z	=	Velocity in z direction	[m s ⁻¹]
V_o	=	Initial volume of solution to be titrated	[m ³]
V_p	=	Polymer solution volume used	[m ³]
V_t	=	Volume of titrant added	[m ³]
VV	=	Unit void volume	[m ³]
W	=	Condition parameter for use of lubrication approximation	
Y	=	Volumetric ratio = U_v/U	
z	=	Axial place co-ordinate	[m]
z_c	=	Valency of the charge on the chain	
z_d	=	Dimensionless place coordinate = z/D_s	
z_i	=	Valency of the i -th species	
Z	=	Interfacial angles	[°]

PUBLICATION LIST

- [I] K.F.J. Denys
Formation, Stability and Properties of in-situ composites made of thermotropic LCP/thermoplast blends, Msc thesis, Delft University of Technology (1993)
- [II] A.G.C. Machiels, K.F.J. Denys, J. van Dam, A. Posthuma de Boer
Formation and morphological stability of in situ composites based on blends of thermotropic liquid crystalline polymers and thermoplastic polymers, paper for the annual meeting of the Polymer Processing Society, Eindhoven, Netherlands (1994)
- [III] A.G.C. Machiels, K.F.J. Denys, J. van Dam, A. Posthuma de Boer
Formation, stability and properties of in situ composites based on blends of a thermotropic liquid crystalline polymer and a thermoplastic elastomer.
Polymer Engineering and Science 36, 2451 (1996)
- [IV] A.G.C. Machiels, K.F.J. Denys, J. van Dam, A. Posthuma de Boer
Effect of processing history on the morphology and properties of polypropylene/ thermotropic liquid crystalline polymer blends.
Polymer Engineering and Science 37, 59 (1997)
- [V] K. Denys, Y. Slagmulder, K. te Nijenhuis, W. Botermans, P. Zitha
Effects of Adsorption on the Rheology of Linear Flexible Polymers in Permeable Materials, Paper for the 68th Annual meeting of the Society of Rheology, Galveston (USA), 16-20 February (1997)
- [VI] K.F.J. Denys, P.L.J. Zitha, H.C. Hensens, K. te Nijenhuis
Near-wellbore formation damage by polyacrylates: Effects of pH and salinity, SPE 39465, Paper for the SPE International Symposium on Formation Damage Control, Lafayette (USA), 18-19 February (1998)
- [VII] P.L.J. Zitha, K.G.S. van Os, K.F.J. Denys
Adsorption of linear flexible polymers during laminar flow through porous media; effect of the concentration, SPE 39675, Paper for the SPE/DOE Eleventh symposium on Improved Oil Recovery, Tulsa (USA) 19-22 April (1998)
- [VIII] A. Zaitoun, N. Kohler, D. Bossie-Codreanu and K. Denys
Water shutoff by relative permeability modifiers: Lessons from several field applications, SPE 56740, Paper for the SPE Annual Technical Conference and Exhibition, Houston (USA), 3-6 October (1999)
- [IX] K. Denys, C. Fichen, A. Zaitoun
Bridging adsorption of cationic polyacrylamides in porous media, SPE 64984, Paper for the SPE International Symposium on Oilfield Chemistry, Houston (USA), 13-16 February (2001)
- [X] G. Chauveteau, K. Denys, A. Zaitoun
New insight on polymer adsorption under high flow rates, SPE 75183, Paper for the SPE/DOE Thirteenth Symposium on Improved Oil Recovery, Tulsa, Oklahoma, 13-17 April (2002)

SUMMARY

These days leading oil and gas producing companies are investing increasing amounts of money into the development of non-fossil energy sources like wind-, solar-, biomass energy and forestry. On the other hand these companies are persisting in developing techniques to make energy recovery more efficient intending to stretch the life span of fossil resources. One of the more mature techniques to improve recovery efficiency is polymer flooding. Herein polymer solutions are injected in injector wells to pressurise producers thereby sweeping oil. The high viscosity attained by dissolving polymers in water makes oil displacement more efficient compared to conventional water injection.

More generally, efficiency can be enhanced by reducing the water production, which is worldwide an increasing problem for operators. In mature oil fields, as oil depletion induces a rise in the oil-water contact, water breaks through in the production wells at a certain moment. Breakthrough can also result from stimulation by water injection. Depending on the specific situation water production can be decreased by shutting off the bottom of the well or plugging certain water producing layers by using polymer gels or cements, the so-called water shut-off treatments. Other shut-off treatments involve disproportionate permeability reducers (DPR's), which are usually polymer solutions. DPR working is based on the fact that adsorption of hydrophilic polymers can strongly decrease the permeability to water while having little effect on the permeability to oil.

For an effective application of the above-mentioned technologies knowledge of polymer flow behaviour and retention behaviour, both in porous media, is indispensable. Apart from oil-related applications this field is important to many other industries and technologies, but nevertheless it is still not well understood. The main reason for this is the complex relationship between rheology and retention behaviour. Both are depending on porous medium structure and are clearly different from bulk behaviour. The aim in this work was to contribute to the understanding of this field, while focussing on systems based on aqueous polymer solutions.

Chapter 1 is the introduction of this thesis. Chapter 2 provides an overview of current knowledge on the flow of Newtonian fluids and polymer solutions in porous media.

Chapter 3 deals with the relation between permeability and packing structure in packed beds of monodisperse spheres. It shows that, even for Newtonian fluids in well-defined porous media, the prediction of dissipation is not straightforward at all as it is a complex function of wall- and internal friction, velocity gradients and tortuosity, all strongly related to flow path geometry.

Chapters 4 and 5 deal with pressure drop predictions for laminar flow of Newtonian- and polymeric fluids through tubes with diameter variations in the axial direction. Modelling a porous medium by a bundle of these tubes is conceptually an improvement over the well-known capillary bundle model with straight tubes. The presence of diameter variations gives the possibility to account for elongational dissipation effects, which contribute to the measured permeability. Analytical predictions for different geometries and various fluid types have been derived by using the Lubrication Approximation Method (LAM). Our newly developed LAM involving spherical co-ordinates allows a good definition of deformation rates during

flow. The resulting predictions are in good agreement with both measurements and numerical predictions and have been converted in capillary models, which do take into account elongational dissipation.

Chapter 6 describes the results of coreflood studies on aqueous non-ionic Polyacrylamide (PAM) solutions in silicon carbide grain packs at low flow rates. PAM is the most frequently used system in polymer flooding- and water shut-off treatments. The experiments show that, above a certain concentration in the semi-dilute regime, the mobility reduction R_m does not stabilise during injection, as it does at lower concentrations in the dilute regime. This behaviour seems to be related to the formation of adsorption entangled multilayers whose thickness can grow during injection. The layer thickness is an important parameter as, together with the effective pore size, it determines the resulting permeability reduction and the magnitude of the so-called disproportionate permeability reduction (DPR) effect. In our studies on PAM, the DPR effect has been confirmed. Concerning PAM rheology in porous media, a full absence of the depleted layer effect was measured, in contrast with previous results on other water-soluble polymers. This absence is due to the fact that brine is only a “mediocre-quality” solvent for PAM resulting in an attractive force between the adsorbed layer and the free polymer molecules.

Chapter 7 shows the results of coreflood studies on aqueous Cationic Polyacrylamide (CPAM) solutions in silicon carbide grain packs and Berea sandstones. The goal in these studies was to explore whether there is scope for a water shut-off process, called two-step gelant diversion, based on the following idea; In a first step a polymer solution is injected to create a protective skin on the oil-bearing zones. In a second step a main flush of gelant is injected to treat the water-bearing zone, while being diverted from oil-bearing zones. Finally the protective skin is destroyed by degradation or by a cleaning agent to restart oil production. As for PAM solutions, injection of CPAM solutions at high flow rates induces unsteady-state flow behaviour i.e. a plugging effect. It was found that plugging rate increases as permeability decreases which is important with respect to the selectivity to low permeability layers. Besides due to the higher adsorption energy CPAM adsorption level, adsorbed layer thickness and plugging rate were higher than for PAM. In all cases skin formation in the lab was easily obtained. Field trials should give conclusive information whether the gelant diversion process can work in practice. Based on experimental evidence a new retention mechanism, called flow-induced adsorption, has been proposed to explain unsteady state plugging behaviour at high flow rates. This mechanism, based on the fact that at high rates hydrodynamic forces become large enough to push extra polymer molecules over the osmotic energy barrier (due to the adsorbed layer) to adsorb, is consistent with all previous experimental results. Another conclusion obtained is that low flow rate polymer solution rheology in a porous medium is well described by Chauveteau’s depletion model, provided that the medium is homogeneous and that the solution is under “good-solvent” conditions.

Chapter 8 gives the results of rheological- and coreflood studies on aqueous Polyacrylic acid (PAA) solutions. Since PAA is a weak polyelectrolyte, both rheology and adsorption are strongly dependent on pH and ionic strength. Particularly interesting is the fact that after adsorption the permeability reduction can be regulated by changing pH or ionic strength of the injected fluid. The studies show that viscosity and induced permeability reduction show similar dependencies on pH and ionic strength and that the model based on OSF theory gives reasonable predictions.

Chapter 9 describes the main conclusions of the thesis.

SAMENVATTING

Tegenwoordig investeren de belangrijkste olie- en gas producerende bedrijven steeds meer geld in de ontwikkeling van alternatieve energiebronnen zoals wind-, zonne-, biomassa energie en bosbouw. Aan de andere kant blijven deze bedrijven technologieën ontwikkelen die de energiewinning efficiënter maken teneinde het tijdperk van de fossiele brandstoffen te verlengen.

Eén van de rijpere technieken die de efficiëntie van de winning kan verbeteren is “polymer flooding”. Hierbij worden polymeeroplossingen in injectieputten geïnjecteerd om productieputten onder druk te zetten en zo olie te verdringen. De hogere viscositeit, die bereikt wordt door het oplossen van polymeren in water, maakt de olieverdringing efficiënter dan in de conventionele waterinjectie.

Een meer algemene manier om de efficiëntie te verbeteren is om waterproductie tegen te gaan, hetgeen een wereldwijd toenemend probleem is voor olie producerende bedrijven. In oudere olievelden zorgt olie depletie voor een stijging van het olie-water contact en dus voor water doorbraak in de productieputten. Waterproductie kan ook een gevolg zijn van stimulatie door waterinjectie. Afhankelijk van de specifieke situatie kan waterproductie tegengegaan worden door bepaalde lagen of de onderkant van de put af te sluiten met polymeer gels of cement, de zgn. “water shut-off treatments”. Andere “shut-off treatments” gaan uit van “disproportionate permeability reducers” (DPR’s), veelal polymeer oplossingen. De werking van DPR’s is gebaseerd op het feit dat adsorptie van hydrofiele polymeren de permeabiliteit voor water sterk kan verlagen zonder al te veel effect op de permeabiliteit voor olie.

Voor een effectieve toepassing van bovengenoemde technieken is kennis van het stromingsgedrag van polymeren (i.e. polymeer rheologie) en hun retentiegedrag, beide in poreuze media, onmisbaar. Afgezien van olie gerelateerde toepassingen, is dit vakgebied belangrijk in veel andere industrieën en technieken. Toch wordt het nog steeds niet goed begrepen. De belangrijkste reden hiervoor is de complexe relatie tussen rheologie en retentiegedrag. Beiden zijn afhankelijk van de structuur van het poreuze medium en zijn duidelijk verschillend van bulk gedrag. Het doel van dit werk was een bijdrage te leveren aan het begrip van dit gebied, ons beperkend tot waterachtige polymeeroplossingen.

Hoofdstuk 1 is de introductie van dit proefschrift.

Hoofdstuk 2 geeft een overzicht van de huidige kennis op het gebied van stroming van Newtonse vloeistoffen en polymeeroplossingen in poreuze media.

Hoofdstuk 3 gaat over de relatie tussen permeabiliteit en pakingsstructuur in monodisperse bolstapelingen. Het laat zien dat, zelfs voor stroming van Newtonse vloeistoffen in goed gedefinieerde poreuze media, de voorspelling van dissipatie een complexe functie is van fricties, snelheidgradiënten en tortuositeit, allen sterk gerelateerd aan de geometrie van het stromingspad.

Hoofdstuk 4 en 5 gaan over drukvalvoorspellingen tijdens laminaire stroming van Newtonse- en polymere vloeistoffen door buizen met diameter variaties in de axiale richting. Het modelleren van een poreus medium door een bundel van deze buizen is conceptueel een verbetering over het welbekende “capillary bundle model” met rechte buizen. De aanwezigheid van diameterveranderingen geeft de mogelijkheid om elongationele dissipatie, welke bijdraagt tot de gemeten permeabiliteit, in rekening te brengen. Analytische voorspellingen voor verschillende geometrieën en verschillende

typen vloeistoffen zijn verkregen door gebruik te maken van de “Lubrication Approximation Method” (LAM). De nieuw ontwikkelde LAM met sferische coördinaten laat een goede definitie van de snelheidsgradiënten toe tijdens stroming. De gedane voorspellingen zijn in goede overeenstemming met metingen en numerieke voorspellingen en zijn vertaald in “capillary bundle models”, die ook elongationele dissipatie meenemen.

Hoofdstuk 6 beschrijft coreflood studies aan Polyacrylamide (PAM)/water oplossingen in gepakte bedden van siliciumcarbide (SiC) deeltjes bij lage stroomsnelheden. PAM is het meest gebruikte systeem in “polymer flooding-” en “water shut-off treatments”. De experimenten laten zien dat boven een bepaalde concentratie in het semi-verdunde regime de mobiliteitsreductie R_m niet meer stabiliseert gedurende polymeerinjectie zoals het dat wel doet bij lagere concentraties in het verdunde regime. Dit gedrag lijkt te zijn gerelateerd aan de vorming van geadsorbeerde multi-lagen wier omvang kan groeien tijdens injectie. De laagdikte is een belangrijke parameter daar deze, samen met de poriegrootte, de resulterende permeabiliteitsreductie bepaalt en ook de grootte van het DPR effect.

Wat betreft PAM rheologie in poreuze media werd een volledige afwezigheid van het “depleted layer effect” gemeten, in tegenstelling tot eerdere resultaten voor andere water/polymeeroplossingen. Dit is te wijten aan het feit dat zout water kwalitatief een minder goed oplosmiddel is voor PAM dan voor de andere systemen, resulterend in grotere attractieve krachten tussen geadsorbeerde laag en vrije polymeermoleculen.

Hoofdstuk 7 laat resultaten zien van coreflood experimenten aan cationisch Polyacrylamide (CPAM)/water oplossingen in met SiC gepakte bedden en in Berea zandstenen. Het doel hier was na te gaan of een nieuw type “water shut-off treatment”, het zgn. “two-step gelant diversion” haalbaar is; In een eerste stap wordt een polymeeroplossing geïnjecteerd om een beschermende laag op de laagpermeabele, olieproducerende lagen te vormen. In een tweede stap wordt een sterk gelerend systeem geïnjecteerd om de waterproducerende laag volledig dicht te stoppen. Vervolgens wordt de beschermende vernietigd, door degradatie of een chemische stof, om de olieproductie te kunnen hervatten.

Net als bij andere polymeersystemen, induceert injectie van CPAM oplossingen bij hoge stroomsnelheden een verstoppend effect. De snelheid van verstopping blijkt toe te nemen als de permeabiliteit afneemt wat belangrijk is voor de selectiviteit voor laagpermeabele lagen. Daarnaast is als gevolg van de hogere adsorptie-energie, de hoeveelheid geadsorbeerd polymeer en de geïnduceerde laagdikte groter dan bij PAM. In alle experimenten kon een beschermende laag moeiteloos worden verkregen in het lab. Testen in het veld moeten nu bewijzen of dit procédé kan werken in de praktijk.

Gebaseerd op experimenten wordt een nieuw retentiemechanisme voorgesteld om het welbekende “unsteady state plugging effect” te verklaren wat optreedt bij injectie van polymeeroplossingen in poreuze media boven een bepaalde injectiesnelheid. Dit mechanisme is gebaseerd op de veronderstelling dat bij hoge snelheden de hydrodynamische krachten groot genoeg worden om extra polymeermoleculen over de osmotische barrière, ten gevolge van de adsorptielaag, te kunnen duwen. Het mechanisme is consistent met alle eerder experimentele resultaten en lijkt een plausibele verklaring te geven. Een andere conclusie is dat de rheologie van polymeeroplossingen in poreuze media bij lage stroomsnelheden goed beschreven wordt door Chauveteau’s depletie model, mits het medium homogeen is en het oplosmiddel kwalitatief goed is.

Hoofdstuk 8 geeft de resultaten van rheologische- en coreflood studies met waterachtige Polyacrylzuur (PAA) oplossingen. Daar PAA een zwak polyelectrolyet is, zijn zowel rheologie als adsorptie sterk afhankelijk van pH en ionensterkte. Met name interessant is het feit dat na adsorptie de permeabiliteitsreductie gereguleerd kan worden door de pH of de ionensterkte van de geïnjecteerde vloeistof te veranderen. De studies laten zien dat het rheologisch gedrag en de permeabiliteitsreductie vergelijkbare afhankelijkheden vertonen van pH en ionensterkte en dat het model gebaseerd op OSF theorie redelijke voorspellingen geeft. Hoofdstuk 9 beschrijft de belangrijkste conclusies van de thesis.

DANKWOORD

Velen hebben bijgedragen aan de realisatie van dit proefschrift en daarom wil ik hen hiervoor bedanken. Ik wou beginnen bij de vakgroep Polymer Materials and Engineering. Ik bedank in eerste instantie mijn directe begeleider Klaas te Nijenhuis en mijn promotor Abe Posthuma de Boer. Hun enthousiasme en kritische houding hebben uiteindelijk hun vruchten afgeworpen. Bedankt ook Jaap van Dam voor zijn steun en de vervlogen rekenuurtjes achter zijn compu. Dank aan Job Ubbink die mij ingeleid heeft in de wereld van de polyelectrolieten. Bedankt Alexandros Gotsis en Ben Norder voor hun ondersteuning op het gebied van de rheologie. Gerard de Vos en Nol van Keeken wil ik bedanken voor hun hulp bij de experimenten. Piet Droppert dank ik voor de goede hulp in de allerlaatste fase bij de totstandkoming van dit boekje. Tonny Verheul en Maria Rodenburg dank ik voor de mentale ondersteuning. Verder wil ik alle oud AIO's bedanken voor de gezellige tijd. Een laatste dank gaat uit naar Yves Slagmulder die in het kader van zijn afstuderen bij het onderzoek geholpen heeft.

De vakgroep Petroleum Engineering wil ik als geheel bedanken voor de geboden gastvrijheid. Met name de gezellige sfeer en beruchte vrijdagmiddag borrels staan in mijn geheugen gegriefd. Als eerste wil ik Hans Bruining bedanken voor zijn rol als initiator van dit project. Ik houd goede herinneringen over aan zijn groot wetenschappelijk enthousiasme. Bedankt ook Pacelli Zitha en Peter Currie voor hun hulp en aanhoudende interesse in het project. Goede technische ondersteuning bij de experimenten kreeg ik van Jan Etienne, Bert Meijer, Henk van Asten, Peter de Vreede, Ton van Leeuwen en Leo Vogt. Dank gaat ook uit naar Karel Heller die er altijd in bleef geloven dat ik het boekje zou afmaken. Hij heeft gelijk gekregen ! Ook de goede sfeer op het Dietzlab met kamergenoten Mark van der Zande, Marco Verlaan, Cas Berentsen, Alies Bartelds, Saskia Blom en Buu-Long Nguyen vergeet ik nooit. Tot slot wil ik afstudeerders Hans Hensens en Bas van Os bedanken voor hun goede bijdrage.

In mijn Parijse periode (1999–2001) wil ik Paul Janssen, Ana Cristina Puga en Paul en Catherine van Lingen bedanken voor hun vriendschap en mentale steun bij het schrijven aan dit boekje. Dank gaat ook uit naar Alain Zaitoun en Guy Chauveteau van Institut Français du Pétrole voor de gastvrijheid en de vruchtbare werksfeer resulterend in hoofdstuk 7.

Tevens wil ik alle doctoren en professoren bedanken die zo vriendelijk waren zitting te willen nemen in mijn promotiecommissie. Aan het einde van dit verhaal wil ik mijn broers en met name mijn ouders bedanken voor hun niet aflatende steun en tenslotte Ouahiba voor de gezellige afgelopen 3 jaar.

CURRICULUM VITAE

Karl Denys werd geboren op 23 januari 1969 te Mohammadia, Algerije. Enkele maanden later verhuisde hij naar Nederland, waar hij zijn jeugd doorbracht in Leiden en Noordwijkerhout. De middelbare school werd doorlopen aan het Sancta Maria Lyceum te Haarlem, waar hij in 1987 slaagde voor Gymnasium Beta. Vervolgens koos hij voor een studie Materiaalkunde aan de TU Delft. De propedeuse werd behaald in 1988. Afstudeeronderzoek in de vakgroep Polymer Materials and Engineering werd verricht aan composieten op basis van mengsels van een thermoplast met een vloeibaar kristallijn polymeer. Het doctoraal diploma werd behaald eind 1993. In 1994 startte hij een promotieonderzoek bij diezelfde vakgroep. Daar in de vakgroep Petroleum Engineering meer ervaring en apparatuur aanwezig was om de gewenste “coreflood experimenten” uit te voeren, verhuisde hij in 1996 zijn bureau naar het Dietz laboratorium. Naar aanleiding van een publicatie werd hij in 1998 benaderd door Institut Français du Pétrole om een voorstel te schrijven voor een EU onderzoeksproject op het gebied van “water shut-off”. Dit voorstel werd gehonoreerd en na het afronden van het experimentele werk verhuisde hij half 1999 naar Frankrijk met het idee het heilige boekje wel af te schrijven in de avonden. Door het goede Parijse leven en de drukke baan verdween dit streven echter tijdelijk naar de achtergrond. Na afloop van dit project ging hij half 2001 werken voor Shell Exploratie en Productie in Rijswijk in een team dat zich bezighoudt met het tegengaan van waterproductie in olieputten, waterinjectie en het opschonen van water. In 2002 schreef hij in de weekends dit proefschrift af.